Understanding Phonon Transport in Extended Solids Using First Principles Calculations

Thesis submitted in partial fulfilment of the requirement for the award of the degree of

DOCTOR OF PHILOSOPHY

by

S CHAND RAKESH ROSHAN

(Roll No:719109)

Supervisor:

Dr. R. RAKESH KUMAR

DEPARTMENT OF PHYSICS

NATIONAL INSTITUTE OF TECHNOLOGY WARANGAL

HANUMAKONDA-506 004, (T. S.), INDIA

February 2024

Dedicated to

THE OMNISCIENT

THE OMNIPRESENT &

THE OMNIPOTENT

CERTIFICATE

This is to certify that the work presented in the thesis entitled "Understanding Phonon Transport in Extended Solids Using First Principles Calculations" is being submitted by Mr. S Chand Rakesh Roshan (Roll No. 719109) to the Department of Physics, National Institute of Technology (NIT) Warangal, for the award of degree Doctor of Philosophy, is a record of bonafide research work carried out by him under my supervision/guidance. I further state that this work has not been submitted to any other University or Institution in part or full for the award of any degree.

R. Rakesh Kumar 14/12/23

(Dr. R. RAKESH KUMAR)

Supervisor

(Prof. T. VENKATAPPA RAO)

Professor& Head, Physics Dept

Date: 14th December 2023

Place: NIT Warangal

DECLARATION

This is to certify that the work presented in the Ph.D. thesis entitled "Understanding Phonon Transport in Extended Solids Using First Principles Calculations" is a bonafide work done by me under the supervision of Dr. R. Rakesh Kumar in the Department of Physics, National Institute of Technology (NIT) Warangal and was not submitted elsewhere for the award of any degree. I declare that this written submission represents my ideas in my own words and where others' ideas or words have been included, I have adequately cited and referenced the original sources. I also declare that I have adhered to all principles of academic honesty and integrity and have not misrepresented or fabricated or falsified any idea/data/fact/source in my submission. I understand that any violation of the above will be a cause for disciplinary action by the Institute and can also invoke penal action from the sources which have thus not been properly cited or from whom proper permission has not been taken when needed.

S.C. Rakesh Roshan

(Mr. S CHAND RAKESH ROSHAN)

Ph.D. Scholar

Date: 14th December 2023

Place: NIT Warangal

CONTENTS

Acknowledgments

I would like to express my sincere gratitude to **Dr.R. Rakesh Kumar**, Assistant Professor, Department of Physics, NIT Warangal, my supervisor for his constant guidance, motivation and encouragement throughout. His zeal for research and his good nature are indeed very contagious. He had been highly supportive.

My Thanks to **Prof. T. Venkatappa Rao** garu, Professor and Head, Department of Physics, NIT Warangal for his immense support from day one towards my research work, he has been a pillar of strength throughout my research journey so far.

My sincere thanks to the DSC members**, Prof. D. Srinivasa Charya** garu, Student welfare Dean and Professor, Department of Mathematics, NIT Warangal, **Prof. T. Venkatappa Rao** garu and **Prof. D. Haranath** garu, Professors, Department of Physics, NIT Warangal for their highly valuable inputs, crucial comments during the DSC meetings and their constant encouragement eventually leading to extracting the best out of me.

Many Thanks to **Prof. Venugopal Reddy** garu and **Prof. D. Dinakar** garu, former Heads, Department of Physics, NIT Warangal for their support towards my research work.

I would like to extend my sincere thanks to **Prof. Bidyadhar Subudhi**, Hon'ble Director, NIT Warangal. Also, my sincere gratitude to **Prof. N V Ramana Rao** garu, former Director, NIT Warangal for his full-fledged support towards my research.
I would like to express my sincere thanks to **all the Faculty Members**, Department of Physics, NIT Warangal for their encouragement.
Thanks to **Dr. Ajoy Kumar Pandey,** Associate Professor, Dept. of MME, NIT Warangal, my former colleague for his support, hospitality and love.
Thanks to my young research scholar friends, **Mr. Nikhil V, Mr.Prasad, Ms. Lavanya, Ms. Mahalaxmi, Dr.Siju Mishra, Dr.Jayaram** for their support. I wish all my friends the best. I thank **Non-Teaching Staff** members and **other Ph.D. scholars** of the Department of Physics for their support.

Special thanks to my lab-mates at NIT Warangal, **Ms. P Supraja, Mr. Navaneeth and Mr. Mahesh** for their continuous help and support. I wish all of them the very best.

Words wouldn't suffice for all the help and support extended by **Dr. Neelam Yedukondalu**, Research Assistant Professor, Stony Brook University, US, a very good friend of mine and God-given brother, he has been instrumental in sowing the seeds of research in my career and also in setting up a computational physics research lab from scratch, I extend my heartfelt gratitude for the mentoring he has been providing throughout.

Thanks to **Prof. Lars Ehm, Prof. John Parise**, Stony Brook University, US for their help and support. Sincere thanks to **Dr. Tribhuvan Pandey,** University of Antwerp, Belgium and **all research collaborators** for their support.

Sincere thanks to **Prof. Srihari** garu, former AO, Dean R&D, RGUKT Basar for his huge support and encouragement, he has gone out of his way to help me during my initial days of Ph.D at NIT Warangal.
Thanks are due to **Prof. M Sainath**, Professor of Physics, IcfaiTech, IFHE and former Dean, IIED, RGUKT Basar and **Prof. Sirasani Satyanarayana**, Former Vice Chancellor, RGUKT Basar for their immense support and help in setting up a Computational Physics Research Lab at RGUKT Basar. Today, I believe, I could stand up to their trust and belief.
My Thanks to **Former Vice-Chancellors, Former Directors, Former AO's**, RGUKT Basar for their support.
My Sincere thanks to the current administration of RGUKT Basar for their support.
Thanks so much to my friends at RGUKT Basar for their support, **Mr. Srinivas Sagar, Mr.Ranadheer Sagi, Mr. Laxman Mutyam** to name a few and to all others who remain supportive.

My Sincere thanks to **all my teachers** and **my friends, Sai brothers and sisters (SSS-SAI-Tech group)** back home at Prasanthi Nilayam/Whitefield.

I would like to thank my Parents **S A Rahiman, P Anasuyamma** for their unconditional support thorough out my studies and career, they have always given me the liberty to choose what I love. Thanks to my brother **S Mukesh** for his love. Thanks to my in-laws **K Venkata Reddy** garu and **K Venkataramana** garu for their unwavering love and affection. Thanks to **K Karthik Reddy** and family for the support. Many Thanks to **Mrs. Hyndavi** and **N Parvathamma** garu for their support.

Finally, A Huge thanks to my better-half **Dr. Lavanya Kunduru** for her Unflinching Love and trust in me and my abilities, I am nothing without her by my side. Love and blessings to my lovely kids **Bhargava Sai** and **Sahasra Hamsini** who remain everything to me/us.

Abstract

Materials with an extreme lattice thermal conductivity (κ_L) are indispensable for thermal energy management applications. Therefore, microscopic understanding of phonon transport is critically important for designing functional materials. In the present thesis, a systematic investigation has been made for in-depth understanding of phonon transport in binary and ternary compounds using first principles calculations in combination with Boltzmann transport theory. In contrast to the expected trend based on their atomic mass, anomalous trends for κ_L are observed in binary systems, namely Alkaline-earth chalcogenides and Alkali halides. It has been shown how atomic mass contrast can tune the contribution of optical phonons to κ_L and its implications on scattering rates either enhancing or suppressing κ_L. Ternary alkaline-earth halofluorides and Bismuth halooxides provide an avenue for designing functional materials with low κ_L due to their intrinsic bonding heterogeneity. Investigation of iso-structural layered materials with varying average atomic mass is intriguing because they allow to make structure-property correlations by exploring the interplay between bonding heterogeneity and atomic mass and their implications on lattice dynamics thereby tailoring the phonon transport properties. Overall, the present thesis focused on understanding interplay amongst crystal structure, atomic mass, chemical bonding, mechanical properties, lone pair activity, and their role in phonon transport properties, which would aid in designing extremely low κ_L materials. This is indispensable for the development of sustainable energy conversion devices for future thermal energy management applications.

The Thesis consists of six chapters, the finer details are provided below.

Chapter 1: It provides an introduction to the domain of phonon transport in extended solids and why low κ_L plays a crucial role in thermal management applications. It also provides a comprehensive view of the various mechanisms affecting the phonon transport, both extrinsic and intrinsic with a comprehensive literature survey of the mechanisms to lower κ_L.

Chapter 2: This chapter provides the theoretical background for the current work and the computational methodology utilized for this work.

The Density Functional Theory (DFT) formalism and an overview of first principles calculations are discussed. Both harmonic and anharmonic approximations concerning the phonons and phonon transport has been discussed followed by the Boltzmann transport theory for obtaining κ_L, phonon-phonon scattering mechanism has been discussed, specifically three phonon scattering, as the same has been considered in the current work. The methodology employed in the present study, known as Temperature Dependent Effective Potential (TDEP), is elaborated upon, this is followed by an overview of list of packages utilized for the current work.

Chapter 3: The first part of the chapter focuses on a detailed and comparative study on phonon transport of Alkaline Earth Chalcogenides (AEC's) MCh (M = Mg, Ca, Sr, Ba and Ch = O, S, Se,Te) compounds in order to provide insights to achieve low κ_L materials through phonon engineering. More light is shed on understanding lattice dynamics, phonon transport, and mechanical properties of 16 MCh (M = Mg, Ca, Sr, Ba and Ch = O, S, Se, Te) compounds. The second part of this chapter deals with another set of isostructural binary systems, Alkali Halides (AH's), consisting of 20 MX (M = Li, Na, K, Rb, Cs and X = F, Cl, Br, I) compounds and presented in comparison with the results obtained with AEC's. This chapter provides an in-depth understanding of atomic mass and its effect on phonon transport properties of AH's and AEC's. Furthermore, this reveals that by manipulating the atomic masses, one can engineer materials with both high and low values of κ_L, providing exciting possibilities for tailored thermal conductivity in various applications.

Chapter 4: This chapter explores layered materials which are bonded through strong covalent/ionic bonds within the plane (in-plane) and coupled by weak van der Waals (vdW) interactions in the perpendicular (out-of-plane) direction i.e., bonding heterogeneity, thus resulting in a strong structural anisotropy. Therefore, through bonding heterogeneity, these layered materials provide an avenue for tailoring phonon transport properties. Investigation of iso-structural layered materials with varying average atomic mass is intriguing because they allow structure-property correlations by exploring the inter-play between bonding heterogeneity and atomic mass and their implications on lattice dynamics, thereby fine-tuning the phonon transport properties. Consequently, for layered materials, a microscopic understanding of crystal structure,

bonding, anharmonic lattice dynamics, and phonon transport properties is of the utmost importance.

Alkaline-earth halofluorides, MXF (M = Ca, Sr, Ba and X = Cl, Br, I) belong to the class of matlockite (PbClF)-type layered materials and they provide an avenue to explore the interplay between crystal structure, atomic mass, and bonding heterogeneity and thereby to fine tune their phonon transport properties. The outcomes of the chapter are that structural anisotropy and/or bonding plays a crucial role along with atomic mass in determining the κ_L in these iso-structural MXF compounds. This study on MXF compounds provides an in-depth understanding on interplay among crystal structure, atomic mass and bonding heterogeneity, which would aid in designing extreme κ_L materials by manipulating in-plane and out-of-plane bonding for future thermal energy management applications.

Chapter 5: This chapter explores another family of layered materials known as Bismuth halooxides, BiXO (X= Cl, Br, I). BiXO is composed of a series of ionically bonded X-Bi-O-O-Bi-X layers stacked perpendicular to the c-axis. These layers are held together by weak van der Waals (vdW) interactions; consequently, these compounds exhibit bonding heterogeneity, featuring in-plane ionic bonding and out-of-plane weak vdW bonding. The rattling mechanism owing to bonding heterogeneity that results in an ultralow κ_L has been described.

Chapter 6: This chapter summarizes the results that are obtained and consolidates the same by proposing few design principles for obtaining low κ_L materials followed by the future scope of work.

LIST OF FIGURES

LIST OF TABLES

CHAPTER-1

INTRODUCTION

1.1. Thermal Transport

Solid state materials, in particular semiconductors and metals play a key role in designing functional devices, which has profound applications in our day-to-day life. Therefore, understanding the electronic and/or phonon transport is critically important for enhancing the performance of electronic and energy conversion devices. Phonons play a significant role in determining the thermal properties of solid-state materials, serving as the primary carriers of thermal energy, and contributing to both thermal conductivity and heat capacity. In the context of semiconductors and insulators, phonons play a dominant role in facilitating heat transport, whereas in metals, electrons are primary carriers for thermal transport. Therefore, it is crucial to have a thorough understanding of heat transport in solid state materials to aid for discovering advanced functional materials to design efficient devices for thermal energy management applications.

1.2. Why Lattice Thermal Conductivity

Thermal conductivity is an extremely important parameter for the semiconductor industry. Many electronic and opto-electronic applications demand high thermal conductivity materials because they efficiently disperse heat from the material and lower device temperature, enhancing performance and durability, whereas thermoelectric conversion and thermal insulation [1] require materials with low lattice thermal conductivity.

From the local cooling of electronics [2] to the provision of electricity for deep-space probes [3], thermoelectric devices are used in a wide range of solid-state power generating [4] and refrigeration applications [5]. Many novel materials have been studied as potential thermoelectric materials during the past few years [6]. Despite the thorough examinations of new and traditional materials, there is always a need to study new classes of materials, with unique physical features that may result in higher thermoelectric performance with extremely low lattice thermal conductivity.

When heat is transferred via a thermoelectric material, an electric potential difference is produced as a result of the movement of charge carriers. This phenomenon may be used for the purpose of power generation. The efficiency [7] of the conversion process

is considered favorable when the thermoelectric figure of merit (ZT) exhibits a high value.

$$ZT = \frac{\sigma S^2}{\kappa} T$$

The Seebeck coefficient is denoted by the symbol S, the thermal conductivity is represented by κ, the electrical conductivity is represented by σ, and the temperature is denoted by T. Semiconductors exhibit a high potential for attaining the desired value due to their characteristic combination of lower lattice thermal conductivity and favorable electrical conductivity. It is crucial to comprehend that the thermal conductivity k has two distinct constituents ($\kappa = \kappa_e + \kappa_L$): an electronic component κ_e, which arises from the diffusion of charge carriers, and a lattice component κ_L, which arises from lattice vibrations, simply called as phonons.

The Wiedemann-Franz law postulates that the thermal conductivity resulting from electronic contributions is directly proportional to the electrical conductivity (σ) due to the fact that the charge carriers responsible for electrical conduction also heat transport. One of the challenges in optimizing the figure of merit for a material lies in the fact that a thermal conductivity typically accompanies a high electrical conductivity. Notwithstanding this issue, the identification of optimal thermoelectric materials may be achieved through the search for materials characterized by a lower lattice thermal conductivity. Suppressing the lattice thermal conductivity without compromising electrical characteristics can improve the figure of merit of thermoelectric materials.

In numerous applications, materials possessing an exceptionally low lattice thermal conductivity are indispensable. Thermal barrier coatings (TBCs) [8], [9] applied on gas turbine engine blades serve to enhance their efficiency and power generation capabilities. This necessitates the use of multifunctional materials that possess desirable attributes such as low thermal conductivity, thermomechanical stability, and chemical resistance. These materials are crucial in safeguarding the blades from the adverse effects of high temperatures [10]. Solid-state energy conversion devices, such as thermoelectrics, necessitate the use of materials with low thermal conductivity. The combination of this requirement with the need for certain electrical properties presents a complex and intriguing problem. Effective thermal insulation materials are essential in order to minimize parasitic heat transfers across various heat engines, heat pumps,

refrigerators, and air conditioning systems. The utilization of low- k materials for thermal insulation is of utmost importance in order to minimize the dissipation of heat from the storage unit to the surrounding environment, hence ensuring a high level of storage efficiency. One other noteworthy application of thermal insulation material in the context of energy storage is its utilization as thermal barriers inside battery packs [11]. This particular usage aims to impede or delay the spread of thermal runaway from a single cell to the entire pack, hence mitigating the potential consequences of accidents.

This research focuses on phonon-based thermal transport in extended non-metallic systems as many thermoelectric materials are semiconducting. Discovering materials with low lattice thermal conductivity and/or finding mechanisms to achieve low lattice thermal conductivity is the main goal of the present thesis work.

1.3. Phonon Transport

Gaining a comprehensive understanding of phononic behaviour is of paramount importance in order to make informed decisions on the management of heat conduction in electrical devices.

Phonons, being the oscillations of the periodic lattice of atoms in crystals come together to produce a spectrum of permitted frequencies, {f}, for atom vibrations that are harmonics of one another. The harmonic term refers to the lowest order term that characterizes variations in potential energy resulting from the displacement of an atom from its equilibrium position. This term may be utilised to determine the fundamental frequencies of vibration. The highest frequency, which is usually on the scale of several THz, is associated with the fast vibrational motion that occurs when two nearby atoms travel in different directions from one another. The basic resonant mode of the macroscopic crystal is the sound wave, which has the lowest frequency, usually in the tens or hundreds of Hz range. One way to visualise a perfect crystal is as a three-dimensional ball-and-spring lattice, where the atoms are represented by balls with mass m and the interatomic forces by springs with spring constant K. The force on each atom is $F(\delta) = K\delta$, if one further assumes that the springs are perfect, meaning that K does not rely on the displacement, δ, of the atoms from their typical position. Atomic vibrations in such a lattice have a spectrum of frequencies, {f}, that depends only on K, mass of atom, m, and the propagation velocity, v; it is not dependent on δ.

A real system's deviation from this assumption is measured by its anharmonicity: in an anharmonic solid, the force is not proportional to the displacement, transforming K and the resonant frequency spectrum into functions of δ, the distance between atoms, and the volume, V, of the crystal's unit cell. The lowest order harmonic approximation is limited to linear forces between atoms and is therefore considered inadequate for elucidating phenomena such as thermal conductivity and expansion, which are attributable to non-linear anharmonic interactions, referred to as phonon anharmonicity (more details provided in Chapter-2).

In the realm of condensed matter physics, the thermal conductivity (κ_L) primarily arises from two fundamental factors: the anharmonicity of atomic bonding and the presence of crystal defects that possess various dimensions and scales [12], [13]. In the context of solid materials, the constituent atoms exhibit vibrational motion in the vicinity of their equilibrium locations. In the context of anharmonicity, when phonon transport occurs and atoms experience deviations from their equilibrium positions, the relationship between the applied force and the atomic displacement is no longer linear. This phenomenon results in the occurrence of non-equilibrium phonon transport and enhances the scattering between phonons, thus leading to a substantial reduction in the lattice thermal conductivity (κ_L) [14], [15] , the atomic bonding in the majority of materials exhibits anharmonicity, characterized by varying degrees of anharmonicity [16]. The presence of significant anharmonicity in a material leads to the occurrence of intrinsic phonon scattering, mostly caused by Umklapp processes [17]. This anharmonicity plays a crucial role in determining the inherently low thermal conductivity (κ_L) observed in materials with multidimensional crystal structures.

The mechanisms for reducing the lattice thermal conductivity in thermoelectric systems may be categorized into two distinct parts: (a) Extrinsic mechanisms - the inducement of extrinsic phonon scattering by the introduction of crystal defects with numerous dimensions and high-range scales into the matrix, and (b) Intrinsic mechanisms - the realisation of inherently low κ_L in diverse crystal structures.

1.3.1 Extrinsic Mechanisms

In order to augment the anharmonicity of a given material, it is imperative to induce significant lattice distortion within that material, hence compelling the atoms to stray from their state of equilibrium. The introduction of different crystal defects into the material enables the realization of this phenomenon [18], [19]. Concurrently, these

external imperfections significantly contribute to enhancing phonon scattering and diminishing the lattice thermal conductivity (κ_L) [20], [21]

Point defects with zero dimensions (0D), such as atomic substitutions, vacancies, and interstitial and filling atoms in particular structures, have the ability to significantly scatter high-frequency phonons. This scattering occurs due to the induction of atomic-scale lattice distortions and the presence of high-density strains in the vicinity of these defects. As a result, the thermal conductivity, κ_L, is reduced [22]–[24]. Thermoelectric materials mostly exhibit one-dimensional (1D) linear defects, predominantly in the form of edge dislocations, which effectively disperse mid-frequency phonons [25], [26]. Two-dimensional (2D) planar defects, such as stacking faults and boundaries between grains and phases, have been seen to cause scattering of low frequency phonons in the presence of dislocation arrays [27], [28]. The scattering of phonons with a wide range of frequencies is successfully achieved by three-dimensional (3D) body defects, which arise from variations in the diameters of nanoprecipitates, secondary phases, and porous structures [29]–[31].

The use of multiscale extrinsic defects as a means to decrease the lattice thermal conductivity, $\kappa_{L,}$ has emerged as a highly sophisticated technique within the realm of thermoelectric research [32]–[35]. Furthermore, recent research has demonstrated the efficacy of atomic ordering and high-entropy engineering in reducing κ_L and improving the ZT values of several materials [36]. The transfer of heat inside the lattice is facilitated by phonons, which are quantized vibrations with various modes and frequency. The thermal conductivity of the lattice, κ_L, is the aggregate of all individual thermal conductivities. In order to reduce the κ_L of specific materials, it is common practice to introduce extrinsic scattering centers consisting of defects of various sizes and dimensions into the matrix [37], [38].

Nevertheless, the use of extrinsic approaches often results in the scattering of the carriers, a phenomenon that can have detrimental effects on electrical transport and impede the improvement of thermoelectric efficiency. One potential approach to enhance the thermoelectric efficiency is the exploration of materials possessing inherently low κ_L.

1.3.2 Intrinsic Mechanisms

The relationship expressing the phonon thermal conductivity, κ_L, has been established and validated by both kinetic theory and the Boltzmann transport equation [39].

$$\kappa_L = \frac{1}{3}\int C_v(\omega) \cdot \nu(\omega) \cdot l(\omega)\mathrm{d}\omega$$

Here, C_v represents the specific heat capacity, $\nu(\omega)$ denotes the phonon group velocity, $l(\omega)$ represents the phonon mean free path (or the scattering processes), and ω signifies the phonon frequency. C_v is defined as the partial derivative of the total energy with respect to temperature. It quantifies the amount of energy contained in the excitations of phonons. Now, in order to get a low κ_L, which is a desirable characteristic for thermal management applications, it is expected that a low specific heat, a brief relaxation period, and a slower propagation velocity would be essential. The focus is on approaches to reduce the phonon thermal conductivity. These approaches are classified into various categories and often involve the synergistic effects of multiple strategies. For instance, DiSalvo [7] and Slack [40] postulated that compounds characterized by a low melting point, heavy elements, and a large unit cell could exhibit a reduction in thermal conductivity. A low elastic modulus is associated with a low melting point, resulting in a correspondingly low sound velocity, or phonon group velocity. The sound velocity is also diminished by the heavy elements. The proportion of energy transmitted via acoustic modes is diminished when the unit cell is large, a consequence that is associated with the specific heat.

1.3.2.1. Specific Heat: A crystal unit cell composed of p atoms contains three acoustic branches and 3p-3 optical branches [41]. The acoustic branch makes a greater contribution to phonon thermal conductivity than the optical branch due to the higher phonon group velocities in the former relative to the latter. Therefore, in a crystal characterized by a significant number of atoms per unit cell, specifically a large unit cell, the acoustic branch carries only a minute portion of the overall thermal energy contained within the solid, as evidenced in zinc antimonides [42].

Many high-frequency phonons might not be sufficiently excited by the quantity of heat energy present at low temperatures, resulting in a low specific heat. Conversely, elevated temperatures induce the activation of the majority of accessible phonon modes, resulting in a state of specific heat (C_v) saturation referred to as the Dulong–Petit limit

($3k_BT$ per atom). Thermal expansion may cause the specific heat at high temperatures to marginally surpass this limit.

Given that the operational temperatures of thermoelectrics are typically sufficient to induce excitation of the majority of phonons, resulting in a specific heat that approaches this threshold, there are only a limited number of proven methods to decrease κ_L by decreasing the overall specific heat. Nevertheless, a significant proportion of the specific heat that contributes to κ_L is generated by acoustic phonons due to their considerably greater group velocity in comparison to optical phonons [40], [43]. For a low κ_L, an augmentation in the complexity of the crystal structure results in a corresponding decrease in the specific heat.

Few methods have been shown to effectively reduce C_v in thermoelectrics when operating at high temperatures. This is because, at high temperatures in bulk materials, the energy transported by each atom approaches $3k_BT$, as predicted by classical statistical theory [44].

This makes it challenging to manipulate the specific heat of thermoelectric materials, since the high-temperature specific heat approaches the Dulong-Petit limit.

1.3.2.2. Liquid like conduction: Cu_2X (X = S, Se) compounds containing liquid Cu ions have been shown to have a specific heat at high temperatures that is lower than the Dulong-Petit limit [45], [46]. It is the Se(S) ions that build a stiff framework in these copper chalcogenides, whereas the Cu ions are very disordered and diffusive at high temperatures. Liquid-like ions are thought to prevent the propagation of shear vibrations, which results in a lower specific heat of transverse mode(s) and, consequently, a lower specific heat of the system as a whole [45], [46]. The poor lattice thermal conductivity is primarily due to the presence of liquid-like species. The above approach confirms the poor lattice thermal conductivity of a family of materials containing liquid-like ions [45], [47].

1.3.2.3. Group Velocities: The lattice thermal conductivity is influenced by the group velocity (v_g), which is frequency dependent in practice. However, for simplicity, it is commonly approximated as the sound velocity (v_s). This approximation is convenient for measurement purposes and is equivalent to the group velocity at the Γ point in the Brillouin zone. By employing the sound velocity as an approximation for the overall

group velocity, it is shown that a decrease in sound velocity corresponds to a decrease in lattice thermal conductivity.

As mentioned before, the lattice can be represented by atoms of average mass M, which are interconnected by spring-like chemical bonds with a restoring force of F. In this simplified model, the sound velocity is approximately proportional to the square root of the ratio of F to M. This suggests that a low sound velocity can be achieved by the presence of a weak restoring force and/or a heavy atomic mass of the component atoms. Determining the atomic mass of component elements in a material is a relatively basic task, however quantifying the strength of chemical bonds, which may be seen as the restoring force, is a more complex challenge.

In experimental studies, it has been observed that weak chemical bonds and/or the presence of heavy component elements have a significant role in the reduction of thermal conductivity κ_L in several high-performance thermoelectric materials [48] . The presence of weak chemical bonds in α-MgAgSb results in a comparatively low sound velocity of around thereby leading to a low κ_L [49]. The $(Bi,Sb)_2Se_3$ alloys exhibit a reduction in sound velocity to due to chemical bond softening caused by a structural transition. This is in contrast to the sound velocities of the parent compounds, Bi_2Se_3 and Sb_2Se_3 [50] . In addition, several novel thermoelectric materials that possess inherently low lattice thermal conductivity have remarkably low sound velocities as observed in argyrodite compounds (Ag_8MX_6, M = Si, Ge, Sn and X = S, Se, Te) [51].

1.3.2.4. Phonon Relaxation times: To minimize κ_L for thermoelectric applications, the phonon relaxation period must be as short as feasible. When phonons are disrupted by a temperature gradient, the phonon system relaxes towards its equilibrium distribution, which takes time (relaxation time). As a result, relaxation time measures the time intervals between phonon collisions [52], Because the rate of change in the distribution function is the core of phonon scattering [53],phonon scattering owing to lattice anharmonicity and the related thermal resistance is inherent in all materials [54].

1.3.2.5. Intrinsic Vacancies: There are naturally occurring vacancies in some of the sample materials, which results in a significant amount of phonon scattering. For instance, it was discovered that Cu_2SnSe_4, which has intrinsic cation vacancies, shows a relatively low value for κ_L [55]. In contrast to the other similar materials ($Cu_2SnCdSe_4$

and $Cu_2SnZnSe_4$) that are devoid of vacancies, Cu_2SnSe_4 exhibits the lowest κ_L and, thus, the greatest ZT across the board across all temperature ranges. Similarly, the presence of a large concentration of intrinsic cation vacancies in Ga_2Te_3 results in a lattice thermal conductivity that is exceedingly low [56] .

1.3.2.6. Lone Pair Electrons: A lone pair of outermost valence electrons (LPEs) are those that are not shared by any other elements. The correlation between phonon anharmonicity and non-bonding LPEs is due to the fact that the LPEs are anticipated to generate a shell with a comparatively large radius, thereby inducing the bonding asymmetry. During thermal vibration, when atoms approach each other, a nonlinear repulsive electrostatic force is generated due to the overlapping wave functions of nearby valence electrons and non-interacting LPEs. This force causes structural instability and anharmonic atomic displacements, which ultimately results in phonon anharmonicity [57], [58]. Typically, an intense interaction between the p orbitals of cations and anions and the crystal structure perturbation is required for the formation of LPEs [59]. To illustrate, consider an atom with the valence configuration ns^2np^x. If a single valence electron from the np orbitals forms a bond with the anion, the bond will not require the ns^2 electron pair to transition to an isolated state known as the "lone pair" state; thus, the LPEs are produced. Very recent studies pertaining to the contribution of LPEs to thermal conductivity are provided [60]–[62] .

1.3.2.7. Resonant Bonding: Strong anharmonicity is induced in a variety of substances by LPEs, including ternary oxides,[63]ternary chalcogenides [64], [65], and binary oxides [66], [67] Rocksalt and rocksalt-like structures [68]are examples of highly symmetric structures that can nonetheless exhibit lattice anharmonicity due to resonant bonding [69]. Resonant bonding is characterized by extraordinary electron delocalization, which significantly increases electronic polarizability. Strong anharmonicity of long-range interatomic force constants may be regularly induced by resonant bonding in rocksalt formations [70]. Latest studies on obtaining low lattice thermal conductivity through chemical bonding are as follows [71]–[74].

1.3.2.8. Rattling: The phenomenon known as rattling vibration can be defined as follows: within an oversized atomic cage, the guest atoms (or molecules) are only

loosely bonded and relatively autonomous from the other atoms; these atoms vibrate anharmonically with significant displacements. Sievers and Takeno [75] were the first to report this rattling behavior. One of the most prominent characteristics of guest atoms causing rattling vibrational behaviors is that the restoring pressures on them weaken when the available space in the host cages is bigger than their ionic radii. In a more localized location, the phonon frequencies will drop and act in an inharmonic fashion. This results in the flattening and lowering of the dispersion of these guest phonons [76], [77]. The size of the cage in relation to the guest atom determines whether the rattling guest atom is on or off centre in the cage [78]. There will be a disparity in phonon dispersion [79] between on-center and off-center atoms. Materials having cage structures (such as skutterudite [80]and clathrate [81], [82], non-cage structures (such as $CsPbI_3$ [83]and $Cu_{12}Sb_4S_{13}$ [84]), and even 2D-layered structures such as Mg_3Sb_2 [85] have all been shown to exhibit rattling vibration. Rattling mechanism is observed in the recent works [86]–[89].

1.3.2.9. Atomic Mass: Atomic mass of constituent elements of a compound has a role in the phonon transport. Lindsay et al. showed that compounds with high mass ratios result in substantial frequency differences between acoustic and optic phonons (such as BSb, BAs, BeTe, BeSe) show a decrease in thermal conductivity (k) when pressure (P) increases [90]. The abnormal dependency of κ on P is due to the fundamentally distinct nature of the intrinsic scattering mechanisms for heat-carrying acoustic phonons in compounds with large mass ratios compared to those with small mass ratios. Also, in contrast to the view that thermal conductivity often decreases with increasing atomic mass, Chang et al. demonstrated that for some compounds within a family of compounds, trends in thermal conductivity with rising atomic mass deviate substantially [91]. More works on effect of mass/mass ratios on phonon transport are provided [92]–[96].

1.3.2.10. Ferroelectric Instability: The manifestation of ferroelectric instability in a solid material is characterized by the occurrence of a softening phenomenon in transverse optical (TO) phonons at the center of the Brillouin zone. This softening causes the energy of TO phonons to approach the energy level of the acoustic phonons responsible for heat conduction. Consequently, a robust optical-acoustic phonon coupling arises, resulting in a significant enhancement of the scattering of acoustic

phonons responsible for heat transport. Hence, the implementation of ferroelectric instability in a material can serve as a viable approach to decrease κ_L [97]–[99].

1.3.2.11. Bond Heterogeneity: The presence of heterogeneous bonding adversely impacts the transmission of phonons in a solid. A strong bond works as a smooth channel for phonon transmission, whereas a weak bond suggests that the atoms will vibrate at a higher frequency on thermal agitation and operate as phonon scattering centers. Therefore, the presence of various forms of bonding within a solid disrupts the uniformity needed for the propagation of phonons, resulting in a significant reduction in the κ_L of the material. Bonding heterogeneity within the crystal lattice of the cubic rocksalt $AgBiS_2$ has only recently come to light [100] . Similar bonding heterogeneity has been observed in a number of other compounds, including $BaAgYTe_3$,$Cu_{17.6}Fe_{17.6}S_{32}$ Zintl phases and $CdTe_2$ that have intrinsically extremely low κ_L [101]–[103]. Recent works on impact of bonding heterogeneity on phonon transport are as follows [104]–[106].

In some cases, there might be an interplay of two or more factors of the above mentioned intrinsic mechanisms [107]–[110] affecting the phonon transport.

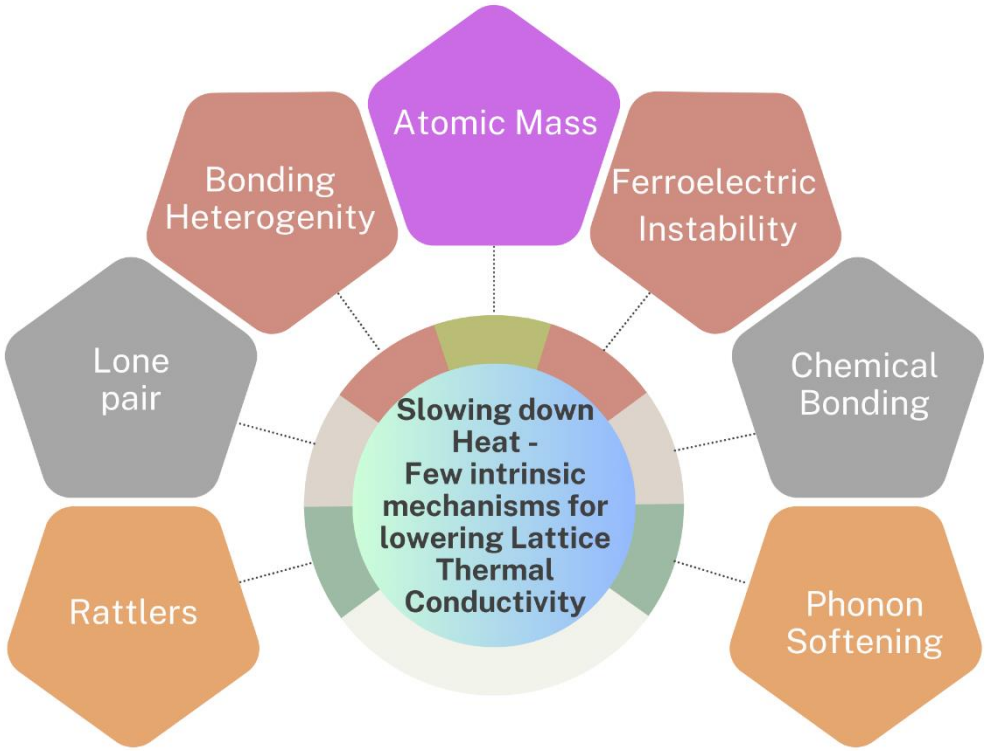

Fig 1.1: Few Intrinsic mechanisms for lowering lattice thermal conductivity

Having looked at various mechanisms for lowering κ_L , the focus of this thesis pertains to the phenomenon of thermal transport by phonons in extended non-metallic systems (isostructural families), as the majority of thermoelectric materials exhibit semiconducting properties, and the key focus is to look for materials with low or ultralow lattice thermal conductivity (κ_L) with intrinsic mechanisms.

The compounds that are explored in the current work are Alkaline Earth Chalcogenides, MCh (M = Mg, Ca, Sr, Ba and Ch = O, S ,Se, Te), Alkali Halides, MX (M = Li, Na, K, Rb, Cs and X = F, Cl, Br, I) Alkaline Earth Halo Fluorides, MXF (M = Ca, Sr, Ba and X = Cl, Br, I) & Bismuth Halooxides, BiXO (X = Cl, Br, I) (more details in the following chapters).

1.3 Objectives of the current work

- Understanding phonon transport and proposing designing principles to achieve low κ_L in known materials.
- Exploring the reasons for the anomalous behaviour in κ_L trends in Alkaline Earth Chalcogenides (AEC's) and Alkali Halides (AH's).
- In-depth understanding of various factors like atomic mass, interatomic bonding, crystal structure, and anharmonicity to κ_L.
- Exploring the tensile lattice strain-dependent phonon transport properties for binary compounds and disclose the dominant factor(s) to influence κ_L.
- Investigation of iso-structural layered materials (Alkaline earth halo fluorides & Bismuth halooxides) with varying average atomic mass for structure-property correlations by exploring the interplay between bonding heterogeneity, atomic mass, lone pair induced anharmonicity, rattling behavior and their implications on lattice dynamics thereby tailoring the phonon transport properties.

The current thesis is divided into six chapters, consisting of an introduction (this chapter) with a comprehensive literature survey followed by theoretical background with computational details, results and discussion concerning on κ_L in binary Alkaline Earth Chalcogenides (AEC's) and Alkali Halides (AH's), followed by κ_L in ternary layered materials like Alkaline earth halo fluorides and Bismuth halooxides and then

followed by the summary, conclusions and future scope emerging from the present thesis work.

References:

[1] E. Bsaibess, F. Delorme, I. Monot-Laffez, and F. Giovannelli, "Ultra-low thermal conductivity in scheelite and A-deficient scheelite ceramics," *Scr Mater*, vol. 201, p. 113950, Aug. 2021, doi: 10.1016/j.scriptamat.2021.113950.

[2] J. R. Sootsman, D. Y. Chung, and M. G. Kanatzidis, "New and Old Concepts in Thermoelectric Materials," *Angewandte Chemie International Edition*, vol. 48, no. 46, pp. 8616–8639, Nov. 2009, doi: 10.1002/anie.200900598.

[3] Y. Tu, W. Zhu, T. Lu, and Y. Deng, "A novel thermoelectric harvester based on high-performance phase change material for space application," *Appl Energy*, vol. 206, pp. 1194–1202, Nov. 2017, doi: 10.1016/j.apenergy.2017.10.030.

[4] F. Odobel and Y. Pellegrin, "Recent Advances in the Sensitization of Wide-Band-Gap Nanostructured p-Type Semiconductors. Photovoltaic and Photocatalytic Applications," *J Phys Chem Lett*, vol. 4, no. 15, pp. 2551–2564, Aug. 2013, doi: 10.1021/jz400861v.

[5] Z. Tian, S. Lee, and G. Chen, "COMPREHENSIVE REVIEW OF HEAT TRANSFER IN THERMOELECTRIC MATERIALS AND DEVICES," *Annual Review of Heat Transfer*, vol. 17, no. N/A, pp. 425–483, 2014, doi: 10.1615/AnnualRevHeatTransfer.2014006932.

[6] M. Zebarjadi, K. Esfarjani, M. S. Dresselhaus, Z. F. Ren, and G. Chen, "Perspectives on thermoelectrics: from fundamentals to device applications," *Energy Environ. Sci.*, vol. 5, no. 1, pp. 5147–5162, 2012, doi: 10.1039/C1EE02497C.

[7] F. J. DiSalvo, "Thermoelectric Cooling and Power Generation," *Science (1979)*, vol. 285, no. 5428, pp. 703–706, Jul. 1999, doi: 10.1126/science.285.5428.703.

[8] Z.-Y. Wei *et al.*, "Progress in ceramic materials and structure design toward advanced thermal barrier coatings," *Journal of Advanced Ceramics*, vol. 11, no. 7, pp. 985–1068, Jul. 2022, doi: 10.1007/s40145-022-0581-7.

[9] B. Liu *et al.*, "Advances on strategies for searching for next generation thermal barrier coating materials," *J Mater Sci Technol*, vol. 35, no. 5, pp. 833–851, May 2019, doi: 10.1016/j.jmst.2018.11.016.

[10] D. R. Clarke, M. Oechsner, and N. P. Padture, “Thermal-barrier coatings for more efficient gas-turbine engines,” *MRS Bull*, vol. 37, no. 10, pp. 891–898, Oct. 2012, doi: 10.1557/mrs.2012.232.

[11] Wen Xiaoyan, Ling Ziye, Fang Xiaoming, and Zhang Zhengguo, “Wen Xiaoyan 2016 Preparation of RT28/fumed silica composite phase change materials and research on the thermal insulation performance of lithium-ion batteries,” *Journal of Chemical Engineering in Colleges and Universities*, vol. 30, pp. 1178–1183, 2016.

[12] T. Ghosh *et al.*, “Ultrathin Free-Standing Nanosheets of Bi_2O_2Se: Room Temperature Ferroelectricity in Self-Assembled Charged Layered Heterostructure,” *Nano Lett*, vol. 19, no. 8, pp. 5703–5709, Aug. 2019, doi: 10.1021/acs.nanolett.9b02312.

[13] C. Chang and L.-D. Zhao, “Anharmoncity and low thermal conductivity in thermoelectrics,” *Materials Today Physics*, vol. 4, pp. 50–57, Mar. 2018, doi: 10.1016/j.mtphys.2018.02.005.

[14] M. Hong *et al.*, “Strong Phonon–Phonon Interactions Securing Extraordinary Thermoelectric $Ge_{1-x}Sb_xTe$ with Zn-Alloying-Induced Band Alignment,” *J Am Chem Soc*, vol. 141, no. 4, pp. 1742–1748, Jan. 2019, doi: 10.1021/jacs.8b12624.

[15] C. W. Li *et al.*, “Orbitally driven giant phonon anharmonicity in SnSe,” *Nat Phys*, vol. 11, no. 12, pp. 1063–1069, Dec. 2015, doi: 10.1038/nphys3492.

[16] M. Li *et al.*, “Crystal symmetry induced structure and bonding manipulation boosting thermoelectric performance of GeTe,” *Nano Energy*, vol. 73, p. 104740, Jul. 2020, doi: 10.1016/j.nanoen.2020.104740.

[17] “Solid State Physics. Von N. W. Ashcroft und N. D. Mermin; Holt, Rinehart and Winston, New York 1976, XXII, 826 Seiten, $19,95,” *Physik in unserer Zeit*, vol. 9, no. 1, pp. 33–33, Jan. 1978, doi: 10.1002/piuz.19780090109.

[18] Z. Chen *et al.*, “Mechanical alloying boosted SnTe thermoelectrics,” *Materials Today Physics*, vol. 17, p. 100340, Mar. 2021, doi: 10.1016/j.mtphys.2021.100340.

[19] Y. Zhang, J. Sun, J. Shuai, X. Tang, and G. Tan, “Lead-free SnTe-based compounds as advanced thermoelectrics,” *Materials Today Physics*, vol. 19, p. 100405, Jul. 2021, doi: 10.1016/j.mtphys.2021.100405.

[20] H. Wang, A. D. LaLonde, Y. Pei, and G. J. Snyder, “The Criteria for Beneficial Disorder in Thermoelectric Solid Solutions,” *Adv Funct Mater*, vol. 23, no. 12, pp. 1586–1596, Mar. 2013, doi: 10.1002/adfm.201201576.

[21] H. Wang *et al.*, “Band flattening and phonon-defect scattering in cubic SnSe–AgSbTe2 alloy for thermoelectric enhancement,” *Materials Today Physics*, vol. 16, p. 100298, Jan. 2021, doi: 10.1016/j.mtphys.2020.100298.

[22] J. Li *et al.*, “Point defect engineering and machinability in n-type Mg3Sb2-based materials,” *Materials Today Physics*, vol. 15, p. 100269, Dec. 2020, doi: 10.1016/j.mtphys.2020.100269.

[23] Z. Yao *et al.*, “Solute manipulation enabled band and defect engineering for thermoelectric enhancements of SnTe,” *InfoMat*, vol. 1, no. 4, pp. 571–581, Dec. 2019, doi: 10.1002/inf2.12044.

[24] C. Xu *et al.*, “Scalable synthesis of n-type Mg3Sb2-xBix for thermoelectric applications,” *Materials Today Physics*, vol. 17, p. 100336, Mar. 2021, doi: 10.1016/j.mtphys.2020.100336.

[25] X.-L. Shi, J. Zou, and Z.-G. Chen, “Advanced Thermoelectric Design: From Materials and Structures to Devices,” *Chem Rev*, vol. 120, no. 15, pp. 7399–7515, Aug. 2020, doi: 10.1021/acs.chemrev.0c00026.

[26] S. Chandra and K. Biswas, “Realization of High Thermoelectric Figure of Merit in Solution Synthesized 2D SnSe Nanoplates via Ge Alloying,” *J Am Chem Soc*, vol. 141, no. 15, pp. 6141–6145, Apr. 2019, doi: 10.1021/jacs.9b01396.

[27] W.-W. Liao *et al.*, “Realizing Bi-doped α-Cu2Se as a promising near-room-temperature thermoelectric material,” *Chemical Engineering Journal*, vol. 371, pp. 593–599, Sep. 2019, doi: 10.1016/j.cej.2019.04.081.

[28] Y. Wang *et al.*, “Enhanced thermoelectric properties of nanostructured n-type Bi2Te3 by suppressing Te vacancy through non-equilibrium fast reaction,”

Chemical Engineering Journal, vol. 391, p. 123513, Jul. 2020, doi: 10.1016/j.cej.2019.123513.

[29] S. Chandra, P. Dutta, and K. Biswas, "Enhancement of the Thermoelectric Performance of 2D SnSe Nanoplates through Incorporation of Magnetic Nanoprecipitates," *ACS Appl Energy Mater*, vol. 3, no. 9, pp. 9051–9057, Sep. 2020, doi: 10.1021/acsaem.0c01448.

[30] J. Chen *et al.*, "Nanostructured monoclinic Cu_2Se as a near-room-temperature thermoelectric material," *Nanoscale*, vol. 12, no. 39, pp. 20536–20542, 2020, doi: 10.1039/D0NR05829G.

[31] G. Tan, L.-D. Zhao, and M. G. Kanatzidis, "Rationally Designing High-Performance Bulk Thermoelectric Materials," *Chem Rev*, vol. 116, no. 19, pp. 12123–12149, Oct. 2016, doi: 10.1021/acs.chemrev.6b00255.

[32] L. D. Zhao *et al.*, "All-scale hierarchical thermoelectrics: MgTe in PbTe facilitates valence band convergence and suppresses bipolar thermal transport for high performance," *Energy Environ Sci*, vol. 6, no. 11, p. 3346, 2013, doi: 10.1039/c3ee42187b.

[33] L. You *et al.*, "Boosting the thermoelectric performance of PbSe through dynamic doping and hierarchical phonon scattering," *Energy Environ Sci*, vol. 11, no. 7, pp. 1848–1858, 2018, doi: 10.1039/C8EE00418H.

[34] R. Tranås, O. M. Løvvik, and K. Berland, "Attaining Low Lattice Thermal Conductivity in Half-Heusler Sublattice Solid Solutions: Which Substitution Site Is Most Effective?," *Electronic Materials*, vol. 3, no. 1, pp. 1–14, Jan. 2022, doi: 10.3390/electronicmat3010001.

[35] S. N. H. Eliassen, A. Katre, G. K. H. Madsen, C. Persson, O. M. Løvvik, and K. Berland, "Lattice thermal conductivity of $Ti_xZr_yHf_{1-x-y}NiSn$ half-Heusler alloys calculated from first principles: Key role of nature of phonon modes," *Phys Rev B*, vol. 95, no. 4, p. 045202, Jan. 2017, doi: 10.1103/PhysRevB.95.045202.

[36] S. Roychowdhury *et al.*, "Enhanced atomic ordering leads to high thermoelectric performance in $AgSbTe_2$," *Science (1979)*, vol. 371, no. 6530, pp. 722–727, Feb. 2021, doi: 10.1126/science.abb3517.

[37] H.-C. Chang, T.-H. Chen, R. Sankar, Y.-J. Yang, L.-C. Chen, and K.-H. Chen, "Highly improved thermoelectric performance of BiCuTeO achieved by decreasing the oxygen content," *Materials Today Physics*, vol. 15, p. 100248, Dec. 2020, doi: 10.1016/j.mtphys.2020.100248.

[38] Z. Chen *et al.*, "Vacancy-induced dislocations within grains for high-performance PbSe thermoelectrics," *Nat Commun*, vol. 8, no. 1, p. 13828, Jan. 2017, doi: 10.1038/ncomms13828.

[39] R. Peierls, "Zur kinetischen Theorie der Wärmeleitung in Kristallen," *Ann Phys*, vol. 395, no. 8, pp. 1055–1101, Jan. 1929, doi: 10.1002/andp.19293950803.

[40] G. A. Slack, "The Thermal Conductivity of Nonmetallic Crystals," 1979, pp. 1–71. doi: 10.1016/S0081-1947(08)60359-8.

[41] Charles Kittel, *Introduction to Solid State Physics.*, 7th ed. New York: Wiley, 1996.

[42] E. S. Toberer, A. F. May, and G. J. Snyder, "Zintl Chemistry for Designing High Efficiency Thermoelectric Materials," *Chemistry of Materials*, vol. 22, no. 3, pp. 624–634, Feb. 2010, doi: 10.1021/cm901956r.

[43] M. Roufosse and P. G. Klemens, "Thermal Conductivity of Complex Dielectric Crystals," *Phys Rev B*, vol. 7, no. 12, pp. 5379–5386, Jun. 1973, doi: 10.1103/PhysRevB.7.5379.

[44] S H Simon, *The Oxford Solid State basics*, 1st ed. UK: Oxford University Press, 2013.

[45] Y. He *et al.*, "High Thermoelectric Performance in Non-Toxic Earth-Abundant Copper Sulfide," *Advanced Materials*, vol. 26, no. 23, pp. 3974–3978, Jun. 2014, doi: 10.1002/adma.201400515.

[46] H. Liu *et al.*, "Copper ion liquid-like thermoelectrics," *Nat Mater*, vol. 11, no. 5, pp. 422–425, May 2012, doi: 10.1038/nmat3273.

[47] W. Qiu, L. Xi, P. Wei, X. Ke, J. Yang, and W. Zhang, "Part-crystalline part-liquid state and rattling-like thermal damping in materials with chemical-bond hierarchy," *Proceedings of the National Academy of Sciences*, vol. 111, no. 42, pp. 15031–15035, Oct. 2014, doi: 10.1073/pnas.1410349111.

[48] Y. Eckstein, A. W. Lawson, and D. H. Reneker, “Elastic Constants of Bismuth,” *J Appl Phys*, vol. 31, no. 9, pp. 1534–1538, Sep. 1960, doi: 10.1063/1.1735888.

[49] P. Ying *et al.*, “Hierarchical Chemical Bonds Contributing to the Intrinsically Low Thermal Conductivity in α-MgAgSb Thermoelectric Materials,” *Adv Funct Mater*, vol. 27, no. 1, Jan. 2017, doi: 10.1002/adfm.201604145.

[50] S. Wang *et al.*, “High thermoelectric performance in Te-free $(Bi,Sb)_2Se_3$ via structural transition induced band convergence and chemical bond softening,” *Energy Environ Sci*, vol. 9, no. 11, pp. 3436–3447, 2016, doi: 10.1039/C6EE02674E.

[51] T. J. Zhu, S. N. Zhang, S. H. Yang, and X. B. Zhao, “Improved thermoelectric figure of merit of self-doped $Ag_{8-x}GeTe_6$ compounds with glass-like thermal conductivity,” *physica status solidi (RRL) – Rapid Research Letters*, vol. 4, no. 11, pp. 317–319, Nov. 2010, doi: 10.1002/pssr.201004278.

[52] J. D. Chung, A. J. H. McGaughey, and M. Kaviany, “Role of Phonon Dispersion in Lattice Thermal Conductivity Modeling,” *J Heat Transfer*, vol. 126, no. 3, pp. 376–380, Jun. 2004, doi: 10.1115/1.1723469.

[53] C. L. Julian, “Theory of Heat Conduction in Rare-Gas Crystals,” *Physical Review*, vol. 137, no. 1A, pp. A128–A137, Jan. 1965, doi: 10.1103/PhysRev.137.A128.

[54] P. G. Klemens, “Thermal Conductivity and Lattice Vibrational Modes,” 1958, pp. 1–98. doi: 10.1016/S0081-1947(08)60551-2.

[55] W. Li, S. Lin, X. Zhang, Z. Chen, X. Xu, and Y. Pei, “Thermoelectric Properties of Cu_2SnSe_4 with Intrinsic Vacancy,” *Chemistry of Materials*, vol. 28, no. 17, pp. 6227–6232, Sep. 2016, doi: 10.1021/acs.chemmater.6b02416.

[56] C. Kim, K. Kurosaki, M. Ishimaru, H. Muta, and S. Yamanaka, “Effect of Vacancy Distribution on the Thermal Conductivity of Ga_2Te_3 and Ga_2Se_3,” *J Electron Mater*, vol. 40, no. 5, pp. 999–1004, May 2011, doi: 10.1007/s11664-010-1479-7.

[57] M. D. Nielsen, V. Ozolins, and J. P. Heremans, “Lone pair electrons minimize lattice thermal conductivity,” *Energy Environ. Sci.*, vol. 6, no. 2, pp. 570–578, 2013, doi: 10.1039/C2EE23391F.

[58] M. K. Jana, K. Pal, U. V. Waghmare, and K. Biswas, “The Origin of Ultralow Thermal Conductivity in InTe: Lone-Pair-Induced Anharmonic Rattling,” *Angewandte Chemie*, vol. 128, no. 27, pp. 7923–7927, Jun. 2016, doi: 10.1002/ange.201511737.

[59] A. Walsh, D. J. Payne, R. G. Egdell, and G. W. Watson, “Stereochemistry of post-transition metal oxides: revision of the classical lone pair model,” *Chem Soc Rev*, vol. 40, no. 9, p. 4455, 2011, doi: 10.1039/c1cs15098g.

[60] I. Maria, R. Arora, M. Dutta, S. Roychowdhury, U. V. Waghmare, and K. Biswas, “Metavalent Bonding-Mediated Dual 6s ^{2} Lone Pair Expression Leads to Intrinsic Lattice Shearing in n-Type TlBiSe $_{2}$,” *J Am Chem Soc*, vol. 145, no. 16, pp. 9292–9303, Apr. 2023, doi: 10.1021/jacs.3c02146.

[61] Y. Zhu *et al.*, “Giant phonon anharmonicity driven by the asymmetric lone pairs in Mg3Bi2,” *Materials Today Physics*, vol. 27, p. 100791, Oct. 2022, doi: 10.1016/j.mtphys.2022.100791.

[62] N. Yedukondalu, T. Pandey, and S. C. Rakesh Roshan, “Effect of Hydrostatic Pressure on Lone Pair Activity and Phonon Transport in Bi $_{2}$ O $_{2}$ S,” *ACS Appl Energy Mater*, vol. 6, no. 4, pp. 2401–2411, Feb. 2023, doi: 10.1021/acsaem.2c03725.

[63] A. Farid Ul Islam, M. Nurul Huda Liton, H. Tariqul Islam, M. Al Helal, and M. Kamruzzaman, “Mechanical and thermodynamical stability of $BiVO_4$ polymorphs using first-principles study,” *Chinese Physics B*, vol. 26, no. 3, p. 036301, Mar. 2017, doi: 10.1088/1674-1056/26/3/036301.

[64] E. J. Skoug and D. T. Morelli, “Role of Lone-Pair Electrons in Producing Minimum Thermal Conductivity in Nitrogen-Group Chalcogenide Compounds,” *Phys Rev Lett*, vol. 107, no. 23, p. 235901, Nov. 2011, doi: 10.1103/PhysRevLett.107.235901.

[65] C. Chang and L.-D. Zhao, “Anharmoncity and low thermal conductivity in thermoelectrics,” *Materials Today Physics*, vol. 4, pp. 50–57, Mar. 2018, doi: 10.1016/j.mtphys.2018.02.005.

[66] A. E. Whitten, B. Dittrich, M. A. Spackman, P. Turner, and T. C. Brown, “Charge density analysis of two polymorphs of antimony(iii) oxide,” *Dalton Transactions*, no. 1, p. 23, 2004, doi: 10.1039/b312550e.

[67] A. Walsh and G. W. Watson, “The origin of the stereochemically active Pb(II) lone pair: DFT calculations on PbO and PbS,” *J Solid State Chem*, vol. 178, no. 5, pp. 1422–1428, May 2005, doi: 10.1016/j.jssc.2005.01.030.

[68] Y. Yu, M. Cagnoni, O. Cojocaru-Mirédin, and M. Wuttig, “Chalcogenide Thermoelectrics Empowered by an Unconventional Bonding Mechanism,” *Adv Funct Mater*, vol. 30, no. 8, Feb. 2020, doi: 10.1002/adfm.201904862.

[69] L Pauling, *The Nature of the Chemical Bond—An Introduction to Modern Structural Chemistry*, 3rd ed. Ithaca, New York,: Cornell University Press, 1960.

[70] Y. Zhang, X. Ke, P. R. C. Kent, J. Yang, and C. Chen, “Anomalous Lattice Dynamics near the Ferroelectric Instability in PbTe,” *Phys Rev Lett*, vol. 107, no. 17, p. 175503, Oct. 2011, doi: 10.1103/PhysRevLett.107.175503.

[71] J. He *et al.*, “Accelerated Discovery and Design of Ultralow Lattice Thermal Conductivity Materials Using Chemical Bonding Principles,” *Adv Funct Mater*, vol. 32, no. 14, Apr. 2022, doi: 10.1002/adfm.202108532.

[72] A. Das, K. Pal, P. Acharyya, S. Das, K. Maji, and K. Biswas, “Strong Antibonding I (p)–Cu (d) States Lead to Intrinsically Low Thermal Conductivity in $CuBiI_4$,” *J Am Chem Soc*, vol. 145, no. 2, pp. 1349–1358, Jan. 2023, doi: 10.1021/jacs.2c11908.

[73] J. Zhang, H. Jiang, X. Xia, Y. Gao, and Z. Huang, “Antibonding p-d and s-p Hybridization Induce the Optimization of Thermal and Thermoelectric Performance of $MGeTe_3$ (M = In and Sb),” *ACS Appl Energy Mater*, vol. 5, no. 12, pp. 15566–15577, Dec. 2022, doi: 10.1021/acsaem.2c03138.

[74] J. Ji *et al.*, “Functional-Unit-Based Material Design: Ultralow Thermal Conductivity in Thermoelectrics with Linear Triatomic Resonant Bonds,” *J Am*

Chem Soc, vol. 144, no. 40, pp. 18552–18561, Oct. 2022, doi: 10.1021/jacs.2c08062.

[75] A. J. Sievers and S. Takeno, "Isotope Shift of a Low-Lying Lattice Resonant Mode," *Physical Review*, vol. 140, no. 3A, pp. A1030–A1032, Nov. 1965, doi: 10.1103/PhysRev.140.A1030.

[76] J. S. Tse and M. A. White, "Origin of glassy crystalline behavior in the thermal properties of clathrate hydrates: a thermal conductivity study of tetrahydrofuran hydrate," *J Phys Chem*, vol. 92, no. 17, pp. 5006–5011, Aug. 1988, doi: 10.1021/j100328a036.

[77] Y. Takasu, T. Hasegawa, N. Ogita, M. Udagawa, M. A. Avila, and T. Takabatake, "Raman scattering of type-I clathrate compounds," *Physica B Condens Matter*, vol. 383, no. 1, pp. 134–136, Aug. 2006, doi: 10.1016/j.physb.2006.03.079.

[78] T. Takabatake, K. Suekuni, T. Nakayama, and E. Kaneshita, "Phonon-glass electron-crystal thermoelectric clathrates: Experiments and theory," *Rev Mod Phys*, vol. 86, no. 2, pp. 669–716, Jun. 2014, doi: 10.1103/RevModPhys.86.669.

[79] T. Nakayama and E. Kaneshita, "Significance of Off-Center Rattling for Emerging Low-Lying THz Modes in Type-I Clathrates," *J Physical Soc Japan*, vol. 80, no. 10, p. 104604, Oct. 2011, doi: 10.1143/JPSJ.80.104604.

[80] B. C. Sales, D. Mandrus, B. C. Chakoumakos, V. Keppens, and J. R. Thompson, "Filled skutterudite antimonides: Electron crystals and phonon glasses," *Phys Rev B*, vol. 56, no. 23, pp. 15081–15089, Dec. 1997, doi: 10.1103/PhysRevB.56.15081.

[81] M. Christensen *et al.*, "Avoided crossing of rattler modes in thermoelectric materials," *Nat Mater*, vol. 7, no. 10, pp. 811–815, Oct. 2008, doi: 10.1038/nmat2273.

[82] M. A. Avila, K. Suekuni, K. Umeo, H. Fukuoka, S. Yamanaka, and T. Takabatake, "Ba 8 Ga 16 Sn 30 with type-I clathrate structure: Drastic suppression of heat conduction," *Appl Phys Lett*, vol. 92, no. 4, Jan. 2008, doi: 10.1063/1.2831926.

[83] W. Lee *et al.*, "Ultralow thermal conductivity in all-inorganic halide perovskites," *Proceedings of the National Academy of Sciences*, vol. 114, no. 33, pp. 8693–8697, Aug. 2017, doi: 10.1073/pnas.1711744114.

[84] W. Lai, Y. Wang, D. T. Morelli, and X. Lu, "From Bonding Asymmetry to Anharmonic Rattling in $Cu_{12}Sb_4S_{13}$ Tetrahedrites: When Lone-Pair Electrons Are Not So Lonely," *Adv Funct Mater*, vol. 25, no. 24, pp. 3648–3657, Jun. 2015, doi: 10.1002/adfm.201500766.

[85] W. Peng, G. Petretto, G.-M. Rignanese, G. Hautier, and A. Zevalkink, "An Unlikely Route to Low Lattice Thermal Conductivity: Small Atoms in a Simple Layered Structure," *Joule*, vol. 2, no. 9, pp. 1879–1893, Sep. 2018, doi: 10.1016/j.joule.2018.06.014.

[86] M. Dutta, D. Sarkar, and K. Biswas, "Intrinsically ultralow thermal conductive inorganic solids for high thermoelectric performance," *Chemical Communications*, vol. 57, no. 39, pp. 4751–4767, 2021, doi: 10.1039/D1CC00830G.

[87] Y. Wang, Q. Gan, M. Hu, J. Li, L. Xie, and J. He, "Anharmonic lattice dynamics and the origin of intrinsic ultralow thermal conductivity in AgI materials," *Phys Rev B*, vol. 107, no. 6, p. 064308, Feb. 2023, doi: 10.1103/PhysRevB.107.064308.

[88] M. Dutta, M. Samanta, T. Ghosh, D. J. Voneshen, and K. Biswas, "Evidence of Highly Anharmonic Soft Lattice Vibrations in a Zintl Rattler," *Angewandte Chemie*, vol. 133, no. 8, pp. 4305–4311, Feb. 2021, doi: 10.1002/ange.202013923.

[89] T. Jia, X. Liu, Y. Zhang, and S.-H. Wei, "Origin of the variation in lattice thermal conductivities in pyrite-type dichalcogenides," *Phys Rev B*, vol. 107, no. 11, p. 115204, Mar. 2023, doi: 10.1103/PhysRevB.107.115204.

[90] L. Lindsay, D. A. Broido, J. Carrete, N. Mingo, and T. L. Reinecke, "Anomalous pressure dependence of thermal conductivities of large mass ratio compounds," *Phys Rev B*, vol. 91, no. 12, p. 121202, Mar. 2015, doi: 10.1103/PhysRevB.91.121202.

[91] Z. Chang *et al.*, “Anomalous Thermal Conductivity Induced by High Dispersive Optical Phonons in Rubidium and Cesium Halides,” *ES Energy & Environment*, 2022, doi: 10.30919/esee8c653.

[92] X. Yu, H. Shao, X. Wang, Y. Zhu, D. Fang, and J. Hong, “Anomalous lattice thermal conductivity in layered MNCl (M = Zr, Hf) materials driven by lanthanide contraction,” *J Mater Chem A Mater*, vol. 8, no. 6, pp. 3128–3134, 2020, doi: 10.1039/C9TA12600G.

[93] T. Pandey, C. A. Polanco, L. Lindsay, and D. S. Parker, “Lattice thermal transport in --- : Interplay of anharmonicity and scattering phase space,” *Phys Rev B*, vol. 95, no. 22, p. 224306, Jun. 2017, doi: 10.1103/PhysRevB.95.224306.

[94] J. Ding *et al.*, “Soft anharmonic phonons and ultralow thermal conductivity in Mg $_3$ (Sb, Bi) $_2$ thermoelectrics,” *Sci Adv*, vol. 7, no. 21, May 2021, doi: 10.1126/sciadv.abg1449.

[95] E. Al Dawood, A. Shafique, and U. Schwingenschlögl, “Anomalous Ultralow Lattice Thermal Conductivity in Mixed-Anion Ba $_4$ Sb $_2$ Se and Ba $_4$ Sb $_2$ Te,” *ACS Appl Electron Mater*, vol. 5, no. 8, pp. 4268–4274, Aug. 2023, doi: 10.1021/acsaelm.3c00542.

[96] J. Sun, G. Chen, S. Li, and X. Liu, “Light Atomic Mass Induces Low Lattice Thermal Conductivity in Janus Transition-Metal Dichalcogenides MSSe (M═Mo, W),” *The Journal of Physical Chemistry C*, vol. 127, no. 35, pp. 17567–17574, Sep. 2023, doi: 10.1021/acs.jpcc.3c03201.

[97] D. Sarkar *et al.*, “Ferroelectric Instability Induced Ultralow Thermal Conductivity and High Thermoelectric Performance in Rhombohedral *p* -Type GeSe Crystal,” *J Am Chem Soc*, vol. 142, no. 28, pp. 12237–12244, Jul. 2020, doi: 10.1021/jacs.0c03696.

[98] D. Sarkar *et al.*, “Metavalent Bonding in GeSe Leads to High Thermoelectric Performance,” *Angewandte Chemie International Edition*, vol. 60, no. 18, pp. 10350–10358, Apr. 2021, doi: 10.1002/anie.202101283.

[99] Y. Zhang, X. Ke, P. R. C. Kent, J. Yang, and C. Chen, “Anomalous Lattice Dynamics near the Ferroelectric Instability in PbTe,” *Phys Rev Lett*, vol. 107, no. 17, p. 175503, Oct. 2011, doi: 10.1103/PhysRevLett.107.175503.

[100] E. Rathore *et al.*, “Origin of Ultralow Thermal Conductivity in n-Type Cubic Bulk $AgBiS_2$: Soft Ag Vibrations and Local Structural Distortion Induced by the Bi $6s^2$ Lone Pair,” *Chemistry of Materials*, vol. 31, no. 6, pp. 2106–2113, Mar. 2019, doi: 10.1021/acs.chemmater.9b00001.

[101] K. Pal, Y. Xia, J. He, and C. Wolverton, “High thermoelectric performance in BaAgYTe3 via low lattice thermal conductivity induced by bonding heterogeneity,” *Phys Rev Mater*, vol. 3, no. 8, p. 085402, Aug. 2019, doi: 10.1103/PhysRevMaterials.3.085402.

[102] H. Xie *et al.*, “Origin of Intrinsically Low Thermal Conductivity in Talnakhite $Cu_{17.6}Fe_{17.6}S_{32}$ Thermoelectric Material: Correlations between Lattice Dynamics and Thermal Transport,” *J Am Chem Soc*, vol. 141, no. 27, pp. 10905–10914, Jul. 2019, doi: 10.1021/jacs.9b05072.

[103] B. Wan *et al.*, “Bonding Heterogeneity Inducing Low Lattice Thermal Conductivity and High Thermoelectric Performance in 2D $CdTe_2$,” *ACS Appl Energy Mater*, vol. 5, no. 8, pp. 9549–9558, Aug. 2022, doi: 10.1021/acsaem.2c01176.

[104] X. Jin *et al.*, “Bonding Heterogeneity Leads to Hierarchical and Ultralow Lattice Thermal Conductivity in Sodium Metavanadate,” *J Phys Chem Lett*, vol. 13, no. 48, pp. 11160–11168, Dec. 2022, doi: 10.1021/acs.jpclett.2c03061.

[105] Y. Grin, “Inhomogeneity and anisotropy of chemical bonding and thermoelectric properties of materials,” *J Solid State Chem*, vol. 274, pp. 329–336, Jun. 2019, doi: 10.1016/j.jssc.2018.12.055.

[106] J. Hu *et al.*, “Breaking the Minimum Limit of Thermal Conductivity of Mg_3Sb_2 Thermoelectric Mediated by Chemical Alloying Induced Lattice Instability,” *Small*, vol. 19, no. 33, Aug. 2023, doi: 10.1002/smll.202301382.

[107] Y. Li, Y. Luo, Z. Tian, J. Wang, and J. Wang, “Theoretical exploration of the abnormal trend in lattice thermal conductivity for monosilicates RE2SiO5

(RE = Dy, Ho, Er, Tm, Yb and Lu)," *J Eur Ceram Soc*, vol. 38, no. 10, pp. 3539–3546, Aug. 2018, doi: 10.1016/j.jeurceramsoc.2018.04.014.

[108] N. Yedukondalu *et al.*, "Lattice Instability and Ultralow Lattice Thermal Conductivity of Layered PbIF," *ACS Appl Mater Interfaces*, vol. 14, no. 36, pp. 40738–40748, Sep. 2022, doi: 10.1021/acsami.2c01135.

[109] O. Cherniushok, R. Cardoso-Gil, T. Parashchuk, R. Knura, Y. Grin, and K. T. Wojciechowski, "Lone-Pair-Like Interaction and Bonding Inhomogeneity Induce Ultralow Lattice Thermal Conductivity in Filled β-Manganese-Type Phases," *Chemistry of Materials*, vol. 34, no. 14, pp. 6389–6401, Jul. 2022, doi: 10.1021/acs.chemmater.2c00915.

[110] B. Qin, D. Wang, and L. Zhao, "Slowing down the heat in thermoelectrics," *InfoMat*, vol. 3, no. 7, pp. 755–789, Jul. 2021, doi: 10.1002/inf2.12217.

CHAPTER-2

Theoretical Background & Computational Methodology

2.1. First Principles Calculations

During the transition from the 19th to the 20th century, significant progress was made in formulating a theoretical framework that elucidates the behaviour of matter at the microscopic level. In the year 1926, Erwin Schrödinger developed his renowned equation [1], which, upon solving, enables the comprehensive description of any physical system existing at the atomic level. The development of this approach has enabled the modelling of a system without the need for empirical parameters. This category of calculations is commonly referred to as first principles calculations.

2.2 Density functional theory

Consider a system with N electrons and M nuclei, the Schrodinger wave equation can be written as:

$$\hat{H}\Psi = E\Psi \qquad ----- \quad 2.1$$

Here,

$$\Psi = \Psi(\mathbf{r}_1, \dots, \mathbf{r}_N, \mathbf{r}_1^n, \dots, \mathbf{r}_M^n) \qquad ----- \quad 2.2$$

Ψ is a wavefunction which is dependent upon the position of all the electrons $\{\mathbf{r}\}$ as well as nuclei $\{\mathbf{r}^n\}$, the Hamiltonian can be written as:

$$\hat{H} = -\frac{\hbar^2}{2m_e}\sum_i \nabla_i^2 - \frac{\hbar^2}{2}\sum_k \frac{\nabla_k^2}{M_k} + \frac{1}{2}\sum_{i\neq j} \frac{e^2}{|\mathbf{r}_i - \mathbf{r}_j|} + \frac{1}{2}\sum_{k\neq l} \frac{Z_k Z_l}{|\mathbf{r}_k^n - \mathbf{r}_l^n|} - \sum_{i,k} \frac{eZ_k}{|\mathbf{r}_i - \mathbf{r}_k^n|}. \qquad ----- \quad 2.3$$

The above terms describe the kinetic energy of the electrons and nuclei, as well as the electrostatic interactions involving the electrons, nuclei and the interactions between nuclei and electrons respectively.

With the exception of the hydrogen atom, solving the many-body problem within a quantum mechanical framework is a challenging task. This difficulty arises from the intricate multi-body structure of the system and the two-body nature of the Coulomb interaction, which results in the inseparability of the Schrodinger equation mentioned above. To address this issue, researchers have devised a range of approximations that

are carefully controlled and applicable to a diverse set of problems. The incorporation of the significant disparities in the masses of electrons and nuclei may lead to a simplification of the many body Hamiltonian. The Born-Oppenheimer (BO) approximation is a phenomenon where the electrons move in the field of stationary nuclei due to the significant weight difference between protons and electrons. This weight difference causes the nucleus to move at a slower pace compared to the electrons, with the proton weighing approximately 1800 times more than the electron.

One implication of the nuclear objects remaining stationary in space is that their kinetic energy can be approximated as zero. So, the Hamiltonian can now be written as

$$\widehat{H} = -\frac{\hbar^2}{2m_e}\sum_i \nabla_i^2 + \frac{1}{2}\sum_{i\neq j}\frac{e^2}{|\mathbf{r}_i - \mathbf{r}_j|} - \sum_{i,k}\frac{eZ_k}{|\mathbf{r}_i - \mathbf{r}_k^n|} \quad ------ \; 2.4$$

These terms correspond to the kinetic energy, the electron-electron interaction and the external potential (electron-nucleus interaction). The utilisation of the Born-Oppenheimer approximation leads to a notable reduction in the overall complexity of the system. Nevertheless, the complexity of the problem persists as a result of the interactions between electrons.

Although electrons in solid systems are generally regarded as non-interacting classical particles, they do exhibit certain interactions, primarily through Coulomb two-body forces. The probability of electron localization within an atom, which contains Z electrons, is dependent upon the spatial arrangement of (Z-1) additional electrons. Hence, it is not appropriate to consider the single electron as an individual and distinct entity. This is commonly denoted as correlation. Consequently, in numerous instances, the applicability of one-particle wave functions isn't considered viable. In order to solve this many body problem, in 1964 Hohenberg and Kohn [2] had formulated the density functional theory (DFT). The mechanism provided henceforth is as detailed by Eshrig [3].

The key idea here is to rewrite equation 2.4 so that it contains an equation for the electron density rather than the many-body problem. Because it is a function of all three spatial dimensions, the density will also contain the electronic degrees of freedom

implicitly. Their first formulation includes two theorems that state this is doable, and they are as follows:

The ground state density n, up to some arbitrary constant, is the only thing that can definitively determine the potential V_{ext}. A universal total energy functional, denoted F_{HK}, is associated with every external potential. The exact density of the ground state would result in minimization of total energy functional $E_{\text{t}}[n]$.

The Hohenberg-Kohn functional is defined as follows

$$F_{\text{HK}}[n] = E_{\text{t}}[n] - \int V_{\text{ext}}[n] n dr \qquad ----- \ 2.5$$

where $E_{\text{t}}[n]$ is the total energy functional.

DFT was formulated as a theoretical framework for addressing many-body systems and is capable of addressing systems with interacting particles, drawing upon the foundational theorems proposed by Kohn and Hohenberg. The Kohn and Hohenberg density functional theory (DFT) theorems assert that the properties of a system can be calculated by incorporating the density of the ground state. Nevertheless, this approach does not offer a means of ascertaining the electronic densities of the system. The Kohn-Sham equations [4] offer a practical method to compute the energy density of the ground state. The primary idea revolves around replacing a complex many-body problem with a simplified system of non-interacting particles subject to a suitable external potential.

The fundamental concept involves substituting actual electrons with non-interacting quasiparticles that yield the accurate ground state density, while consolidating all unknown terms into a single term referred to as exchange and correlation. With this, the universal functional assumes the form

$$F_{\text{HK}}[n] = T[n] + E_{\text{H}}[n] + E_{\text{xc}}[n] - \int V_{\text{ext}}[n] n dr \qquad ----- \ 2.6$$

The terms involved above are the kinetic energy (T), Hartree energy (E_{H}), the external potential (V_{ext}) and a single term that contains all the many-body terms, E_{xc}. The exact

form of the exchange-correlation is not known, but later it can be observed that it could be approximated. The total energy functional can now be written as

$$E_{\mathrm{t}}[n] = T[n] + E_{\mathrm{H}}[n] + E_{\mathrm{xc}}[n] + \int V_{\mathrm{ext}}(\mathbf{r})n(\mathbf{r})dr \quad ----- \ 2.7$$

The objective is to determine the density that minimises the energy functional. To do this, a restricted search is conducted to identify the stationary spots. The restriction is imposed by maintaining a fixed particle number N, while the Lagrange multipliers ϵ_i are utilised:

$$\mathcal{L} = E_{\mathrm{t}}[n] - \epsilon_i \left(\int n(\mathbf{r})dr - N \right), \qquad ----- \ 2.8$$
$$\delta\mathcal{L} = \int \frac{\delta\mathcal{L}}{\delta n}\delta n dr = 0$$

Now, Ψ^0 stands for the ground state many-body wavefunction for the quasiparticles that do not interact with one another. This may invariably be expressed as a determinantal condition of one-particle wavefunctions, as follows:

$$\Psi^0 = \frac{1}{\sqrt{N!}}\|\phi_i(\mathbf{r}_j)\|, \ \langle \phi_i \mid \phi_j \rangle = \delta_{ij} \qquad ----- \ 2.9$$

The density could be expressed in orbitals as below:

$$n = \sum_i \phi_i^* \phi_i \qquad ----- \ 2.10$$
$$\delta n = \sum_i \delta\phi_i^* \phi_i + \phi_i^* \delta\phi$$

So, the kinetic energy functional can now be defined as,

$$T[n] = \frac{1}{2}\sum_i \langle \phi_i | \hat{\mathrm{T}} | \phi_i \rangle \qquad ----- \ 2.11$$

Now, a variation on T with respect to ϕ_j^* makes this

$$\begin{aligned}\delta T &= T\left[n+\delta\phi_j^*\right]-T[n]= \\ &=\left\langle\phi_j+\delta\phi_j^*|\hat{\mathrm{T}}|\phi_j\right\rangle-\left\langle\phi_j|\hat{\mathrm{T}}|\phi_j\right\rangle= \\ &=\int\hat{\mathrm{T}}\phi_j\delta\phi_j^*dr=\int\frac{\delta T}{\delta\phi_j^*}\delta\phi_j^*dr\end{aligned} \qquad -----\ 2.12$$

So,

$$\frac{\delta T}{\delta\phi_i^*}=\hat{\mathrm{T}}\phi_i=\int\frac{\delta T}{\delta n(\mathbf{r}')}\frac{\delta n(\mathbf{r}')}{\delta\phi_i^*(\mathbf{r})}dr'=\frac{\delta T}{\delta n}\phi_i \qquad -----\ 2.13$$

Putting equation 2.11 into 2.9 gives

$$\delta\mathcal{L}=\sum_i\int\underbrace{\frac{\delta\mathcal{L}}{\delta n}\phi_i}_{=0}\delta\phi_i^*dr+\sum_i\int\underbrace{\frac{\delta\mathcal{L}}{\delta n}\phi_i^*}_{=0}\delta\phi dr=0 \quad -----\ 2.14$$

This results in the constraints on the orbitals.

$$\frac{\delta\mathcal{L}}{\delta n}\phi_i=\left(\frac{\delta T}{\delta n}+\frac{\delta E_{\mathrm{H}}}{\delta n}+\frac{\delta E_{\mathrm{xc}}}{\delta n}+V_{\mathrm{ext}}-\epsilon_i\right)\phi_i=0 \qquad -----\ 2.15$$

With these terms, the Hartree potential is

$$\frac{\delta E_{\mathrm{H}}[n]}{\delta n}=\int\frac{n(\mathbf{r}')}{|\mathbf{r}'-\mathbf{r}|}dr'=V_{\mathrm{H}}[n] \qquad -----\ 2.16$$

and

$$\frac{\delta E_{\mathrm{xc}}[n]}{\delta n}=V_{\mathrm{xc}}[n] \qquad -----\ 2.17$$

$V_{\mathrm{xc}}[n]$ is the exchange-correlation potential. Putting all these together,

$$\left(\hat{\mathrm{T}}+V_{\mathrm{H}}+V_{\mathrm{xc}}+V_{\mathrm{ext}}-\epsilon_i\right)\phi_i=0 \qquad -----\ 2.18$$

Considering the potentials into one term as shown, $V_{\mathrm{eff}}=V_{\mathrm{H}}+V_{\mathrm{xc}}+V_{\mathrm{ext}}$, the Schrodinger-like Kohn-Sham equations for the quasiparticle orbitals ϕ_i, which are responsible for obtaining the ground state density, are as follows

$$\left(\hat{\mathrm{T}}+V_{\mathrm{eff}}[n]\right)\phi_i=\epsilon_i\phi_i \qquad -----\ 2.19$$

Then, the total energy functional can be written as

$$E_{\mathrm{t}}[n] = \sum_{i} \epsilon_i + \int n(\mathbf{r}) V_{\mathrm{eff}}[n] dr \qquad ----- \ 2.20$$

It is now possible to obtain the electronic ground state density by solving equations 2.10, 2.19, and 2.20 in a self-consistent manner.

Currently, Spin-polarized densities have not yet been addressed. In the event that the precise E_{xc} is known and the Kohn-Sham equations are successfully solved for an oxygen atom, density functional theory would accurately provide the ground state energy and density. However, it would not provide any insights on spin polarisation. In practical applications, the use of approximate exchange-correlation energy (E_{xc}) necessitates the explicit incorporation of spin-polarized densities and spin-dependent E_{xc} in order to achieve precise characterization of the electronic structure in magnetic systems. The Kohn-Sham equations for this may be derived using a similar approach.

2.2.1 Exchange-correlation

Until this point, no approximations have been employed, and the theory remains exact. In order to effectively solve the equations, it is necessary to provide a suitable definition for the unknown variable V_{xc}. The local density approximation (LDA) was concurrently introduced with the Kohn-Sham equations and looks like this;

$$E_{\mathrm{xc}}^{\mathrm{LDA}} = \int \epsilon(n(\mathbf{r})) n(\mathbf{r}) dr \quad ----- \ 2.21$$

Here, ϵ is the exchange-correlation of a uniform electron gas, which could be obtained using quantum Monte Carlo method. The previously mentioned approximation demonstrates a high degree of success, producing favourable results over a wide spectrum of materials. An appropriate progression in this context involves including the density gradient and deriving the exchange and correlation effects from a uniform electron gas with a gradient. This leads to the generalized gradient approximation (GGA) [5], which looks like;

$$E_{\mathrm{xc}}^{\mathrm{GGA}} = \int f(n(\mathbf{r}), \nabla n(\mathbf{r})) n(\mathbf{r}) dr \quad ----- 2.22$$

Since there is no one foolproof method for calculating the gradient dependency of the uniform electron gas, various variants of GGA have been developed, each one optimised for a specific use case. The usefulness of these functions is severely constrained. For example, the band gap of semiconductors is frequently underestimated (and, in extreme cases, completely absent, indicating a metallic state). Furthermore, lattice parameters are under-estimated by the LDA and over-estimated by the GGA.

2.2.2. Pseudopotentials

In the process of solving the Kohn-Sham equations for a crystalline solid, it is seen that the resultant wavefunctions exhibit fast oscillations in the vicinity of the nuclei, while displaying slower variations in the interstitial areas. In order to get numerical solutions for the equations, it is necessary to employ a basis set. The identification of basis functions capable of accurately describing both the vicinity around the nucleus, where atomic orbitals are effective, and the interstitial area, where plane waves are more appropriate, is a significant challenge. It would be advantageous to devise a method for disregarding the deep core states as well. These states provide a negligible contribution to bonding and are only mildly impacted by it.

The computational complexity often exhibits an $\mathcal{O}(N^3)$ scaling, where N represents the quantity of electrons. The omission of any electron would significantly enhance computing efficiency.

The pseudopotential methodology was initially proposed by Hellmann [6], and then refined into its contemporary version by Phillips and Kleinman [7] . It was shown that one could construct a modified valence wave function $\tilde{\phi}_v$ with the true core ϕ_c and valence wave functions ϕ_v

$$|\tilde{\phi}_v\rangle = |\phi_v\rangle + \sum_c a_{cv}|\phi_c\rangle,\ a_{cv} = \langle\phi_c \mid \tilde{\phi}_v\rangle \quad ----- \ 2.23$$

The pseudo-wavefunction must satisfy

$$\left(\hat{H} + \sum_c (\epsilon_v - \epsilon_c)|\phi_c\rangle\langle\phi_c|\right)|\tilde{\phi}_v\rangle = \epsilon_v|\tilde{\phi}_v\rangle \quad ----- \ 2.24$$

The eigenvalues of the pseudowave functions are equivalent to those of real wavefunctions. An additional term is incorporated into the Hamiltonian. This initial endeavour demonstrated the feasibility of distinguishing between core and valence states, and employing predetermined core states significantly reduces the number of electrons involved in the task. There exist several pseudopotential methodologies that are specifically tailored to address diverse tasks [8].

The Normconserving and Ultrasoft pseudopotentials are widely recognised as the predominant types of pseudopotentials. The concept of norm-conserving pseudopotentials [9] was proposed by D. Hamann, M. Schlüter, and C. Chiang in 1979. The primary objective of these pseudopotentials is to enhance the transferability of the pseudopotential. In contrast to previous methodologies that need orthogonalization to the core states and renormalization for charge densities outside the core area, the approach ensures the continued effectiveness and representativeness of the pseudopotential in diverse chemical environments. Ultrasoft pseudopotentials [10] have the advantage of not needing norm-conservation, hence enabling the use of a reduced basis set and significantly smaller cut-off values. The effects seen cannot be adequately described using non-interacting quasiparticles. The materials encompassed within this category consist of transition metal oxides, Mott insulators among others. The initial attempts to address these issues were presented by Hubbard [11], [12]. Currently, the most often employed approaches include LDA+U [13] , hybrid functionals [14], [15], and dynamical mean-field theory (DMFT) [16].

The projector augmented wave (PAW) [17]method was utilised in this thesis. This method is a contemporary method that maintains the all-electron wave function by the use of a linear transformation.

$$\mathcal{T} = 1 + \sum_c \mathcal{T}_c \qquad \text{-----} \ 2.25$$

in which $\mathcal{T}_c$ only exerts its influence inside a zone centred on nuclei c.

This transformation may be performed to any operator $\tilde{A} = \mathcal{T}^{-1}\hat{A}\mathcal{T}$, which makes it possible for it to act on smooth pseudowaves while preserving the information from the entire wavefunction. This results in an increase in the transferability of the potentials.

2.3 Harmonic and Anharmonic approximations

The dynamical theory of lattices was developed by Born and von Kármán [18]. It focuses on figuring out what occurs when the lattice is heated [19] and how the system reacts to a displaced atom and the resultant vibrations.

The free energy criteria are often employed in the analysis of crystalline materials to establish the direction of spontaneity. This necessitates equilibrium with a minimum free energy F.

$$F = U - TS \qquad ----- \ 2.26$$

the atomic configuration at absolute zero temperature $T = 0$ K corresponds to the position that minimises the total internal energy U. This may be mathematically represented by a Taylor series expansion with respect to displacement of the atoms from their equilibrium position, this serves as the basis for understanding lattice dynamics.

$$U = U_0 + \sum_{i=1} \frac{\partial U}{\partial x_i} dx_i + \frac{1}{2} \sum_{i,j=1} \frac{\partial^2 U}{\partial x_i \, \partial x_j} dx_i dx_j$$

$$+ \frac{1}{6} \sum_{i,j,k=1} \frac{\partial^3 U}{\partial x_i \, \partial x_j \, \partial x_k} dx_i dx_j dx_k + \cdots \quad ----- \ 2.27$$

where i goes to to 3N , where N is the total number of atoms in the system. The first term may be seen as zero, and the second term is likewise zero when assessed in the state of equilibrium. The term with the highest degree that remains is the second order derivative. When higher order components are ignored, the resulting approximation is known as the harmonic approximation.

The total kinetic energy of the system can be written as:

$$T = \frac{1}{2} \sum_{i=1} m_i \dot{x_l}^2 \qquad ----- \ 2.28$$

where x_i denotes dx_i for simplicity. Under the Harmonic approximation, Hamiltonian can be written as

$$H = U + T = \frac{1}{2}\sum_{i=1} m_i \dot{x}_i^2 + \frac{1}{2}\sum_{i,j=1} \frac{\partial^2 U}{\partial x_i\, \partial x_j} dx_i dx_j \quad ------ \ 2.29$$

Using the canonical Hamiltonian equation, one can write

$$\begin{aligned} m_k \ddot{x_k} = \dot{p}_k &= -\frac{\partial H}{\partial x_k} = -\frac{1}{2}\sum_{i,j=1} \frac{\partial^2 U}{\partial x_i\, \partial x_j} \frac{\partial (x_i x_j)}{\partial x_k} \\ &= -\frac{1}{2}\sum_{i,j=1} \frac{\partial^2 U}{\partial x_i\, \partial x_j} \delta_{ik} x_j - \frac{1}{2}\sum_{i,j=1} \frac{\partial^2 U}{\partial x_i\, \partial x_j} \delta_{jk} x_j = \quad ------ \ 2.30 \\ &-\frac{1}{2}\sum_{j} \frac{\partial^2 U}{\partial x_k\, \partial x_j} x_j - \frac{1}{2}\sum_{j} \frac{\partial^2 U}{\partial x_k\, \partial x_i} x_i = -\sum_{j} \frac{\partial^2 U}{\partial x_k\, \partial x_i} x_i \end{aligned}$$

On rearranging equation 2.30,

$$\ddot{x_k} + \sum_{i} \frac{1}{m_i} \frac{\partial^2 U}{\partial x_i\, \partial x_j} x_j = 0 \qquad ------ \ 2.31$$

Under the assumption that the phonon mode is a plane wave, the following solution can be obtained:

$$x_i^{\alpha} = A e^{i(\boldsymbol{q}\cdot\boldsymbol{x} - \omega t)} \widehat{e^{\alpha}} \qquad ------ \ 2.32$$

where α takes x, y and z. $\widehat{e^{\alpha}}$ is the normal vector in α direction. Then, Equation 2.31 can be rewritten as,

$$\ddot{x}_k^{\alpha} + \sum_{\beta} \sum_{j=1}^{N} \frac{1}{m_i} \frac{\partial^2 U}{\partial x_i^{\alpha}\, \partial x_j^{\beta}} x_j^{\beta} = 0 \qquad ------ \ 2.33$$

Now considering equations 2.32 and 2.33,

$$\omega^2 \widehat{e^{\alpha}} - \sum_{\beta} \sum_{j=1}^{N} \frac{1}{m_i} \frac{\partial^2 U}{\partial x_i^{\alpha}\, \partial x_j^{\beta}} e^{iq\cdot(x_j - x_i)} \widehat{e^{\beta}} = 0 \quad ------ \ 2.34$$

Let's define

$$D_{\alpha\beta}(\boldsymbol{q}) = \sum_{j=1}^{N} \frac{1}{m_i} \frac{\partial^2 U}{\partial x_i^{\alpha}\, \partial x_j^{\beta}} e^{i\boldsymbol{q}\cdot(\boldsymbol{x}_j - \boldsymbol{x}_i)} \qquad ------ \ 2.35$$

to be the dynamical matrix, Equation 2.34 can be written as:

$$\omega^2 \widehat{e^{\alpha}} - \sum_{\beta} D_{\alpha\beta}(\boldsymbol{q}) \widehat{e^{\beta}} = 0 \qquad ----- \ 2.36$$

Based on the principles of linear algebra, it is necessary to establish the following secular equation in order to obtain a nontrivial solution for $\widehat{e^{\alpha}}$.

$$\det \left| D_{\alpha\beta}(\boldsymbol{q}) - \omega^2 \delta_{\alpha\beta} \right| = 0 \qquad ----- \ 2.37$$

The phonon dispersion relation is defined as the solved eigenvalue ω as a function of $\boldsymbol{q}$. Phonons can be thought of as the decoupled lattice vibration mode with some frequencies as indicated by Equation 2.32. For all crystalline materials, more generically, the following relation holds good;

$$\omega^2 \widehat{e^{\alpha}(s)} - \sum_{\beta} \sum_{s'} D_{\alpha\beta}(\boldsymbol{q}, s, s') e^{\widehat{\beta}(s')} = 0 \qquad ----- \ 2.38$$

here the dynamical matrix is

$$D_{\alpha\beta}(\boldsymbol{q}, s, s') = \sum_{j=1}^{N} \frac{1}{\sqrt{m(s)m(s')}} \frac{\partial^2 U}{\partial x_i^{\alpha}(s) \, \partial x_j^{\beta}(s')} e^{i\boldsymbol{q}\cdot(x_j - x_i)} ----- \ 2.39$$

The calculation of the dynamical matrix is the primary challenge for phonons since the phonon dispersion relation might result in complete information on the thermodynamic parameters of a system. One of the most important aspects to consider here is the second order force constants $\frac{\partial^2 U}{\partial x_i^{\alpha}(s) \, \partial x_j^{\beta}(s')} = \Phi_{\alpha\beta}(i - j, s, s')$. Given the knowledge of the crystal structure and the accessibility of second order force constants as an input, it becomes possible to compute several phonon harmonic properties, including but not limited to group velocity and specific heat.

The determination of second order force constants can be done through first-principles simulations utilising the crystal structure.

2.4 Boltzmann Transport Equation

2.4.1 Phonon-Phonon Scattering

The majority of quasiparticle transport properties are computed using the semiclassical Boltzmann transport equation, which treats electrons and phonons as particles and re-distributes the nonequilibrium state distribution function upon collision. Both electron and phonon Boltzmann transport equations have the following general form:

$$\frac{df_\alpha(\boldsymbol{r},\boldsymbol{k},t)}{dt}=\left(\frac{\partial f_\alpha}{\partial t}\right)_{\text{coll}}=\frac{\partial f_\alpha}{\partial t}+v(\boldsymbol{k})\cdot\nabla_{\boldsymbol{r}}f_\alpha+\frac{\boldsymbol{F}}{\hbar}\cdot\nabla_{\boldsymbol{k}}f_\alpha \quad ------ \ 2.40$$

Here, the distribution of electrons or phonons with band index α is denoted as $f(\boldsymbol{r},\boldsymbol{k},t)$ in the context of nonequilibrium. The wavevector is represented by $\boldsymbol{k}$, while the external field, denoted as $\boldsymbol{F}$, which is zero in the case of phonons and corresponds to the electrical field in electron transport. In a condition of equilibrium, the rate of change over time is equal to zero. In the vicinity of a state of near equilibrium, it is possible to expand the distribution function on the left-hand side and consider the lowest order terms. It is reasonable to make the assumption that the distribution function is solely dependent on spatial coordinates through temperature, and that the dependence of the momentum distribution is solely driven by the electrochemical potential gradient. This assumption is justified by the fact that in the case of heat transfer, the transport of phonons and electrons is primarily driven by temperature gradient and electrochemical potential gradient. By employing this approximation, one can get the linearized Boltzmann transport equation [20] for both phonons and electrons.

$$v_\alpha(\boldsymbol{k})\cdot\frac{\partial f_\alpha^0(\boldsymbol{k})}{\partial T}\nabla T-ev_\alpha(\boldsymbol{k})\cdot\frac{\partial f_\alpha^0(\boldsymbol{k})}{\partial E}\nabla\phi=\left(\frac{\partial f_\alpha}{\partial t}\right)_{coll} \quad ------ \ 2.41$$

and

$$v_\lambda(\boldsymbol{q})\cdot\frac{\partial n_\lambda^0(\boldsymbol{q})}{\partial T}\nabla T=\left(\frac{\partial n_\lambda}{\partial t}\right)_{coll} \quad ------ \ 2.42$$

where $f_\alpha^0(\boldsymbol{k})=\frac{1}{e^{(E_\alpha^0(k)-\mu)/kT}+1}$ and $n_\alpha^0(\boldsymbol{k})=\frac{1}{e^{\hbar\omega_\lambda^0(q)/kT}-1}$ is the equilibrium Fermi-Dirac distribution and Bose-Einstein distribution of electron band α in wavevector $\boldsymbol{k}$ and phonon mode λ in wavevector $\boldsymbol{q}$.

The single mode relaxation time approximation (SMRTA) is a widely used and straightforward method for solving the Boltzmann transport equation. In this technique,

the relaxation time associated with each phonon mode or electron band is considered as the average time interval between scattering events. The collision phrase on the right-hand side in the context of SMRTA can be expressed as:

$$\left(\frac{\partial n_\lambda}{\partial t}\right)_{\text{coll}} = -\frac{n_\lambda - n_\lambda^0}{\tau_\lambda(\boldsymbol{q})} \qquad ----- \ 2.43$$

Considering equations 2.43 and 2.42 together, one can solve the nonequilibrium distribution function:

$$n_\lambda(\boldsymbol{q}) = -\tau_\lambda(\boldsymbol{q}) v_\lambda(\boldsymbol{q}) \cdot \frac{\partial n_\lambda^0(\boldsymbol{q})}{\partial T} \nabla T \quad ----- \ 2.44$$

where the total heat flux contributed by a single phonon mode is $\boldsymbol{q}_{\lambda \boldsymbol{q}} = \frac{1}{V} v_{\lambda \boldsymbol{q}} \hbar \omega_{\lambda \boldsymbol{q}} \left(n_{\lambda \boldsymbol{q}} - n_{\lambda \boldsymbol{q}}^0\right)$, and $\boldsymbol{q}_{\lambda \boldsymbol{q}} = -\kappa_{\lambda \boldsymbol{q}} \nabla T$. One could obtain the expression for thermal conductivity in a single phonon mode.

$$\kappa_{\lambda \boldsymbol{q}} = c_{\lambda \boldsymbol{q}} v_\lambda^2 \tau_{\lambda \boldsymbol{q}} \qquad ----- \ 2.45$$

where $c_{\lambda \boldsymbol{q}} = \frac{\hbar \omega_{\lambda \boldsymbol{q}}}{V} \frac{\partial n_\lambda^0(\mathbf{q})}{\partial \mathrm{T}} = \frac{1}{V} \frac{\partial U_{\lambda q}}{\partial T}$ is the single mode specific heat. By aggregating the collective impact of all phonon modes and mitigating the influence of varying reciprocal space sampling, the lattice thermal conductivity is given by,

$$\boldsymbol{\kappa} = \frac{1}{N_q} \sum_{\boldsymbol{q}\lambda} c_{\boldsymbol{q}\lambda} v_{\boldsymbol{q}\lambda}^2 \tau_{\boldsymbol{q}\lambda} \quad ----- \ 2.46$$

This is under the assumption that distinct phonon modes are decoupled from one another and that they would decay separately. Here phonon velocity $v_{\lambda \boldsymbol{q}} = \frac{\partial \omega_{\lambda q}}{\partial \boldsymbol{q}}$ as well as specific heat $c_{\lambda \boldsymbol{q}}$ can both be calculated from the phonon dispersion relation but phonon relaxation time remains unknown so far.

The relaxation time approximation can also be employed to represent thermoelectric and electrical conductivity characteristics by utilising electron group velocity and the relaxation time [20], [21].

$$\sigma = -\frac{e^2}{NV}\sum_{n,\boldsymbol{k}} v_{n,\boldsymbol{k}}^2 \tau_{n,\boldsymbol{k}} \frac{\partial f_{n,\boldsymbol{k}}}{\partial E_{n,\boldsymbol{k}}}$$

$$S = -\frac{1}{eT}\frac{\sum_{n,\boldsymbol{k}} \left(E_{n,\boldsymbol{k}} - E_F\right) v_{n,\boldsymbol{k}}^2 \tau_{n,\boldsymbol{k}} \frac{\partial f_{n,\boldsymbol{k}}}{\partial E_{n,\boldsymbol{k}}}}{\sum_{n,\boldsymbol{k}} v_{n,\boldsymbol{k}}^2 \tau_{n,\boldsymbol{k}} \frac{\partial f_{n,\boldsymbol{k}}}{\partial E_{n,\boldsymbol{k}}}} \qquad ----- \ 2.47$$

$$\kappa_e = \frac{1}{NV}\sum_{n,\boldsymbol{k}} -\frac{\left(E_{n,\boldsymbol{k}} - E_F\right)^2}{T} v_{n,\boldsymbol{k}}^2 \tau_{n,\boldsymbol{k}} \frac{\partial f_{n,\boldsymbol{k}}}{\partial E_{n,\boldsymbol{k}}} - T \times S^2\sigma$$

Because all phonon modes are decoupled there would be no phonon-phonon scattering if simply harmonic approximation was used. However, the finite value of lattice thermal conductivity indicates that anharmonic factors might influence phonon transport. The second order force constant can be extended to third order force constants, where $\frac{\partial^3 U}{\partial x_0^{\alpha}(s)\,\partial x_m^{\beta}(s')\,\partial x_n^{\gamma}(s'')} = \Phi_{\alpha\beta\gamma}(0, m, n, s, s', s'')$. While omitting the derivation procedure, it is possible to obtain the three-phonon scattering matrix and the creation and annihilation operator form of the third order Hamiltonian [22] using the third order force constant.

$$\mathrm{V}_3(\boldsymbol{q}\lambda, \boldsymbol{q}'\lambda', \boldsymbol{q}''\lambda'') = \left(\frac{\hbar}{8N_0\omega_{\boldsymbol{q}\lambda}\omega_{\boldsymbol{q}'\lambda}\omega_{\boldsymbol{q}''\lambda}}\right)^{\frac{1}{2}} \sum_{m,n,s,s',s''} \frac{\Phi_{0,m,n,s,s',s''}^{\alpha\beta\gamma} e^{i\boldsymbol{q}\cdot\boldsymbol{m}} e^{i\boldsymbol{q}'\cdot\boldsymbol{n}} e_{\boldsymbol{q}\lambda}^{s\alpha} e_{\boldsymbol{q}'\lambda'}^{s'\beta} e_{\boldsymbol{q}''\lambda''}^{s''\gamma}}{\sqrt{m_s m_{s'} m_{s''}}}$$

$$\mathrm{V}_3 = \frac{i\hbar}{6}\sum_{\boldsymbol{q}\lambda,\boldsymbol{q}'\lambda',\boldsymbol{q}''\lambda''} \delta_{\boldsymbol{G},\boldsymbol{q}+\boldsymbol{q}'+\boldsymbol{q}''} \mathrm{V}_3(\boldsymbol{q}\lambda, \boldsymbol{q}'\lambda', \boldsymbol{q}''\lambda'')\left(a_{\boldsymbol{q}\lambda}^{\dagger} - a_{-\boldsymbol{q}\lambda}\right)\left(a_{\boldsymbol{q}'\lambda'}^{\dagger} - a_{-\boldsymbol{q}'\lambda'}\right)\left(a_{\boldsymbol{q}''\lambda''}^{\dagger} - a_{-\boldsymbol{q}''\lambda''}\right) \qquad ----- \ 2.48$$

Here, m_s is the atomic mass of this atom and $e_{\boldsymbol{q}\lambda}^{s\alpha}$ is the α-th Cartesian components in phonon eigenvector of mode with wavevector $\boldsymbol{q}$ and branch λ for atom s in the primitive cell.

From Equation 2.47, one could observe a quasi-momentum conservation relation $\boldsymbol{q} + \boldsymbol{q}' + \boldsymbol{q}'' = \boldsymbol{G}$ which is required in case of three-phonon scattering, where $\boldsymbol{G}$ is a reciprocal lattice vector. $\boldsymbol{G} = 0$ is the case of normal scattering, while a nonzero $\boldsymbol{G}$ implies the Umklapp scattering.

The phonon Boltzmann transport equation can incorporate the three-phonon scattering matrix by applying Fermi's Golden Rule, a principle that governs the probability of transitions in time-dependent perturbation theory.

$$P = \frac{2\pi}{\hbar}|\langle f|V_3|i\rangle|^2\delta(E_f - E_i) \quad -----2.49$$

where $|f\rangle$ and $|i\rangle$ are the final and initial states respectively and E_f and E_i are their corresponding energies.

Figure 2.1 illustrates two distinct forms of three-phonon scattering: one phonon mode can divide into two phonon modes, and two phonon modes can be combined to form one. Energy conservation (shown in Equation 2.49) and quasi-momentum conservation (shown in Equation 2.48) is obeyed. In these two cases, one could express the scattering process in terms of changing of phonon occupations: when $|i\rangle = |n_{\boldsymbol{q}\lambda}, n_{\boldsymbol{q}'\lambda'}, n_{\boldsymbol{q}''\lambda''}\rangle$ and $|f\rangle = |n_{\boldsymbol{q}\lambda} - 1, n_{\boldsymbol{q}'\lambda'} + 1, n_{\boldsymbol{q}''\lambda''} + 1\rangle$; These can be considered in equation (2.49). This leads
to

$$P_{q\lambda,}^{\boldsymbol{q}''\lambda'',\boldsymbol{q}'\lambda'} = \frac{2\pi}{\hbar}\left|\langle n_{\boldsymbol{q}\lambda} - 1, n_{\boldsymbol{q}'\lambda'} + 1, n_{\boldsymbol{q}''\lambda''} + 1|V_3|n_{\boldsymbol{q}\lambda}, n_{\boldsymbol{q}'\lambda'}, n_{\boldsymbol{q}''\lambda''}\rangle\right|^2\delta(\omega_{\boldsymbol{q}\lambda} - \omega_{\boldsymbol{q}'\lambda'} - \omega_{\boldsymbol{q}''\lambda''})$$

$$P_{q\lambda,\boldsymbol{q}'\lambda'}^{\boldsymbol{q}''\lambda''} = \frac{2\pi}{\hbar}\left|\langle n_{\boldsymbol{q}\lambda} - 1, n_{\boldsymbol{q}'\lambda'} - 1, n_{\boldsymbol{q}''\lambda''} + 1|V_3|n_{\boldsymbol{q}\lambda}, n_{\boldsymbol{q}'\lambda'}, n_{\boldsymbol{q}''\lambda''}\rangle\right|^2\delta(\omega_{\boldsymbol{q}\lambda} + \omega_{\boldsymbol{q}'\lambda'} - \omega_{\boldsymbol{q}''\lambda''}) \quad --- \quad 2.50$$

Since both these two are phonon scattering schemes, the net scattering rate for the these two processes are $P_{\boldsymbol{q}\lambda,\boldsymbol{q}'\lambda'}^{\boldsymbol{q}''\lambda''} - P_{\boldsymbol{q}''\lambda''}^{\boldsymbol{q}\lambda,\boldsymbol{q}'\lambda'}$, and $P_{q\lambda}^{\boldsymbol{q}'\lambda',\boldsymbol{q}''\lambda''} - P_{q'\lambda',\boldsymbol{q}''\lambda''}^{\boldsymbol{q}\lambda}$. By carefully taking the forms of the Equation 2.50 & 2.44 and counting the scattering contribution from phonon $\boldsymbol{q}'\lambda'$ and $\boldsymbol{q}''\lambda''$, the equation is:

$$v_\lambda(\boldsymbol{q}) \cdot \frac{\partial n_\lambda^0(\boldsymbol{q})}{\partial T}\nabla T =$$

$$= \sum_{q'\lambda',q''\lambda''}\left[\left(P_{q\lambda,\boldsymbol{q}'\lambda'}^{\boldsymbol{q}''\lambda''} - P_{\boldsymbol{q}''\lambda'',}^{\boldsymbol{q}\lambda,\boldsymbol{q}'\lambda'}\right) + \frac{1}{2}\left(P_{q\lambda}^{\boldsymbol{q}'\lambda',\boldsymbol{q}''\lambda''} - P_{\boldsymbol{q}'\lambda',\boldsymbol{q}''\lambda''}^{\boldsymbol{q}\lambda}\right)\right] \quad ----2.51$$

The full phonon BTE can be determined now by utilising Equation 2.48 as the form of the three-phonon scattering matrix and Equation 2.50 as an expression for the Fermi Golden Rule pertaining to the three phonon scattering rate.

Solving the problem becomes intricate due to the interdependence of the phonon distribution $n_{\boldsymbol{q}\lambda}, n_{\boldsymbol{q}'\lambda'}, n_{\boldsymbol{q}''\lambda''}$, which are connected on the right-hand side of equation 2.51. One often employed method involves utilising an iterative approach, wherein the nonequilibrium phonon distribution function is initially approximated by expanding it in the vicinity of its equilibrium counterpart.

$$n_{q\lambda} = n^0_{q\lambda} - \frac{k_B T}{\hbar} \frac{\partial n_{\boldsymbol{q}\lambda}}{\partial \omega_{\boldsymbol{q}\lambda}} \Lambda_{\mathbf{q}\lambda} \qquad ---- \ 2.52$$

Where the expansion coefficient $\Lambda_{\mathbf{q}\lambda}$ is unknown so far.

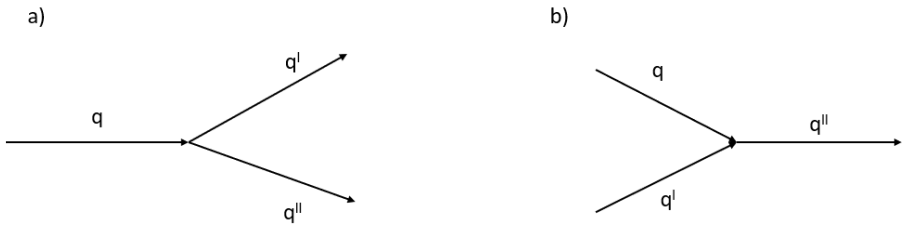

Fig. 2.1: Two types of three-phonon scattering process.

Phonons are shown as solid lines accompanied by arrows in figure 2.1. Here, a) illustrates the process wherein a phonon of high frequency undergoes decay, resulting in the production of two phonon modes. Conversely, (b) demonstrates the amalgamation of two phonons, leading to the formation of a single phonon with an elevated frequency.

When considering the whole phonon Boltzmann transport equation (BTE), neglecting the expansion component initially results in an analogous solution to the phonon relaxation time approximation (RTA) solution. By conducting a comparative analysis between the phonon relaxation time approximation (RTA) solution and the comprehensive three-phonon scattering rates, it is possible to derive the phonon relaxation time.

$$\frac{1}{\tau_{\boldsymbol{q}\lambda}} = 2\pi \sum_{\boldsymbol{q}'\lambda'\boldsymbol{q}''\lambda''} \Big[|V_3(\boldsymbol{q}\lambda, \boldsymbol{q}'\lambda', -\boldsymbol{q}''\lambda'')|^2 \big(n_{\boldsymbol{q}'\lambda'} - n_{\boldsymbol{q}''\lambda''}\big)\delta\big(\omega_{\boldsymbol{q}\lambda} + \omega_{\boldsymbol{q}'\lambda'} - \omega_{\boldsymbol{q}''\lambda''}\big)\delta(\boldsymbol{q} + \boldsymbol{q}' - \boldsymbol{q}'' + \boldsymbol{G}) + |V_3(-\boldsymbol{q}\lambda, \boldsymbol{q}'\lambda', \boldsymbol{q}''\lambda'')|^2 \big(n_{\boldsymbol{q}'\lambda'} + n_{\boldsymbol{q}''\lambda''} + 1\big)\delta\big(\omega_{\boldsymbol{q}\lambda} - \omega_{\boldsymbol{q}'\lambda'} - \omega_{\boldsymbol{q}''\lambda''}\big)\delta(\boldsymbol{q} - \boldsymbol{q}' - \boldsymbol{q}'' + \boldsymbol{G})\Big] \quad ----2.53$$

This expression pertains to the characterization of two important factors in three phonon scattering: the first one concerns the magnitude of the three-phonon scattering, which is specified by the V_3 scattering matrix. According to equation 2.48, the matrix exhibits a dependence on the third order force constants. In the absence of phonon anharmonicity, the scattering is inherently zero, thereby establishing a direct relationship between phonon anharmonicity and the strength of three-phonon scattering. Specifically, greater phonon anharmonicity corresponds to increased three-phonon scattering intensity. The second aspect pertains to the scattering phase space [23] for three phonon scattering, this factor quantifies the number of scattering channels that can occur while adhering to the conservation principles of energy and momentum.

The development of a comprehensive iterative solution extends beyond the RTA approach. RTA treats all scattering processes equally, which includes both the Umklapp process and the normal process, whereas the normal process does not contribute to thermal resistance. This is the rationale to go beyond RTA.

Equation 2.52 serves as the starting point for this iterative solution, in which the $\Lambda_{\mathbf{q}\lambda}$ is decomposed into three Cartesian components based on the temperature gradient:

$$\Lambda_{q\lambda} = \sum_{\alpha} \Theta^{\alpha}_{q\lambda} \nabla_{\alpha} T \quad ----2.54$$

By using this in the phonon BTE,

$$v^{\alpha}_{\lambda}(\boldsymbol{q}) \cdot \frac{\partial n^{0}_{\lambda}(\boldsymbol{q})}{\partial T} = \sum_{\boldsymbol{q}'\lambda', \boldsymbol{q}''\lambda''} \Big[\tilde{P}^{\boldsymbol{q}''\lambda''}_{q\lambda, \boldsymbol{q}'\lambda'} \Big(\Theta^{\alpha}_{\boldsymbol{q}''\lambda''} - \Theta^{\alpha}_{\boldsymbol{q}'\lambda'} - \Theta^{\alpha}_{\boldsymbol{q}\lambda}\Big) + \frac{1}{2}\tilde{P}^{\boldsymbol{q}''\lambda'', \boldsymbol{q}'\lambda'}_{q\lambda} \Big(\Theta^{\alpha}_{\boldsymbol{q}''\lambda''} + \Theta^{\alpha}_{\boldsymbol{q}'\lambda'} - \Theta^{\alpha}_{\boldsymbol{q}\lambda}\Big)\Big] \quad ----2.55$$

where $\tilde{P}^{q''\lambda''}_{q\lambda,q'\lambda'}$ is the transition probabilities corresponding to equilibrium probabilities (the RTA transition probability). In order to solve this equation, the first Brillouin zone is discretized into a uniform grid, and subsequently, the RTA solution is utilised as the basis for the iterative solution. In order to ensure numerical stability [24] ,the energy conservation principle is commonly represented as a Gaussian function with adaptive broadening, rather than a delta function.

2.5. Temperature Dependent Effective Potential (TDEP) Methodology

In order to calculate the Lattice thermal conductivity, it is necessary to acquire third-order force constants. The force constants as seen in above section is of a third-order expansion in the Taylor series representation of the lattice potential energy. Various software packages may be employed to derive force constants from ab initio computations. Examples of such software are Phono3py [25], [26], ShengBTE [27]. The temperature-dependent effective potential (TDEP) method, as established by Hellman et al. [28][29][30] , is a promising approach for conducting finite temperature lattice dynamics. The TDEP package comprises programmes designed for the extraction of effective force constants of second, third, or higher orders. Additionally, this computational tool may be employed to determine other parameters, including as phonon dispersions, free energies, and the lattice thermal conductivity (LTC), while considering various phonon scattering processes.

In the present study, the technique of TDEP employs atomic positions and forces obtained by Density Functional Theory (DFT) calculations as an input.

The TDEP approach is mostly utilized for the purpose of obtaining a model Hamiltonian in order to carry out lattice dynamics. When the Hamiltonian is expanded to the third order, the expression that follows is;

$$\hat{H} = U_0 + \sum_{i\alpha} \frac{p_{i\alpha}^2}{2m_i} + \frac{1}{2!}\sum_{i,j}\sum_{\alpha,\beta} \Phi_{ij}^{\alpha\beta} u_i^{\alpha} u_j^{\beta} + \frac{1}{3!}\sum_{i,j,k}\sum_{\alpha,\beta,\gamma} \Phi_{ijk}^{\alpha\beta\gamma} u_i^{\alpha} u_j^{\beta} u_k^{\gamma} \quad ----2.56$$

The first two components on the right-hand side pertain to the potential energy of the stationary lattice and the kinetic energy of the atoms. The displacement of equilibrium of atom i in a particular direction α is indicated by u_i^{α}, and $\Phi_{ij}^{\alpha\beta}$ and $\Phi_{ijk}^{\alpha\beta\gamma}$ are the

second- and third-order force constants respectively, accounting for two- and three-body atomic interactions. The force constants in question are commonly denoted as harmonic and anharmonic force constants. The force constant matrix for a two-body interaction consists of 3^2 variables and is given as

$$\Phi_{ij} = \begin{pmatrix} \Phi_{ij}^{\alpha\alpha} & \Phi_{ij}^{\alpha\beta} & \Phi_{ij}^{\alpha\gamma} \\ \Phi_{ij}^{\beta\alpha} & \Phi_{ij}^{\beta\beta} & \Phi_{ij}^{\beta\gamma} \\ \Phi_{ij}^{\gamma\alpha} & \Phi_{ij}^{\gamma\beta} & \Phi_{ij}^{\gamma\gamma} \end{pmatrix} \quad ----2.57$$

In the case of three-body interaction, the force constant matrix comprises a total of 3^3 variables. Various methodologies have been applied in the context of TDEP (Time-Dependent Effective Potential) to effectively minimise the number of fforce constants that need to be calculated. One strategy that can be employed involves the utilisation of constraints from the principles of crystal symmetry. The presence of symmetry constraints leads to the inclusion of both reducible (symmetry equivalent) and irreducible (inequivalent) components in the variable Φ, hence lowering the overall number of unknown variables. The cutoff radius, denoted as r_c, is an additional factor that influences the number of force constants. The variable r_c denotes a region of sphere that encompasses the two- or three-body interactions. In the region beyond the sphere, the interactions are assumed to be zero.

Convergence testing can yield an adequate choice for the r_c parameter, unless the simulation explicitly accounts for all potential interactions within the simulation cell. Depending on the material property to be calculated and the intended degree of precision, its value will vary. In the context of the TDEP framework, it is possible to assign distinct values to r_c for second- and third-order force constants. A detailed analysis can be found here [31].

The cumulative force acting on an atom arises from the collective influence of all potential n-body interactions. However, for the model, the force exerted on the atom is dependent upon two- and three-body interactions specifically involving the atom. The force exerted on atom i in the direction α can be mathematically represented as

$$f_{i\alpha}^{\mathrm{M}} = \sum_{j}\sum_{\beta} \Phi_{ij}^{\alpha\beta} u_j^{\beta} + \frac{1}{2}\sum_{jk}\sum_{\beta\gamma} \Phi_{ijk}^{\alpha\beta\gamma} u_j^{\beta} u_k^{\gamma} \quad ----2.58$$

The forces acting on the atoms within the cell may be collectively categorised as the force vector $\mathbf{F}_{\mathrm{M}}$. The TDEP methodology operates by aligning the forces of the model, denoted as $\mathbf{F}_{\mathrm{M}}$, with the forces computed using Density Functional Theory (DFT), represented as $\mathbf{F}_{\mathrm{DFT}}$ By reducing the difference between $\mathbf{F}_{\mathrm{M}}$ and $\mathbf{F}_{\mathrm{DFT}}$, one may derive force constants that most accurately depict the system. The minimization problem is given as

$$\min_{\Phi} \Delta \mathbf{F} = \frac{1}{N_{\mathrm{c}}} \sum_{i=1}^{N_{\mathrm{c}}} \left| \mathbf{F}_{\mathrm{DFT}}^{i} - \mathbf{F}_{\mathrm{M}}^{i} \right| \qquad ----2.59$$

here the sum is spread out over N_{c} configurations and a least-squares solution is used to minimize the force difference.

The idea is to create thermally excited configurations that are uncorrelated, which will serve as supercells for input in density functional theory (DFT) computations to determine the $\mathbf{F}_{\mathrm{DFT}}$. The selected configurations should exhibit a comprehensive and varied representation of the phase space. The use of ab initio molecular dynamics is frequently employed in order to acquire realistic configurations at the designated temperature. One limitation of this technique is that there exists a high degree of correlation among the various configurations obtained at each time step in the molecular dynamics simulation. Hence, it is advantageous to extract a subset of the molecular dynamics run, such as by selectively analyzing every fifth- or tenth-time step. Hence, only a portion of the computations proves to be valuable as input for TDEP. In the context of molecular dynamics, it is imperative to ensure that the system is equilibrated at the designated temperature prior to commencing the sampling process.

The process of acquiring a collection of thermally excited configurations is as follows: 1) In order to obtain the equilibrium positions, the primitive cell is relaxed. 2) The elastic tensor is computed. 3) The relaxed cell is utilized to construct an adequately sized supercell. 4) The configurations of thermally excited supercells are computed using the atomic displacements and velocities that were calculated. Then, the second- and third-order force constants at a designated temperature, T, could be obtained by gathering configurations from an ensemble existing at T [32].

TDEP is an efficient method for obtaining force constants of the second and third orders; however, it requires substantial computational resources. As a general rule, it is

specified [90] that convergence testing can commence with approximately ten equations per irreducible force constant. $3N_a$ equations are generated for every supercell configuration whose forces are computed using DFT, where N_a denotes the number of atoms.

2.6 Packages Utilized

The list of packages utilized in the current work are as follows: i) VASP ii) CASTEP iii) VESTA iv) TDEP

VASP: The Vienna Ab initio Simulation Package (VASP) [33] is a software package designed for the purpose of simulating materials at the atomic scale. Furthermore, it may be employed for the examination of quantum mechanical molecular dynamics. This computational method offers approximate solutions to the many-body Schrödinger equation through the resolution of the Kohn-Sham equations utilising plane wave basis sets. The Kohn-Sham equations allow for the determination of numerous physical parameters, including orbitals, electronic charge density, and local potential. In order to establish the interactions between ions and electrons, the use of norm-conserving pseudopotentials or a projector-augmented wave technique is often employed. The aforementioned is a licenced commercial product, and VASP has several applications including the calculation of frequency dependent dielectric function, band structures, structural optimisations, phonons, density of states, and optical characteristics. In the current investigation, the Vienna Ab initio Simulation Package (VASP) is utilised to conduct Density Functional Theory (DFT) analysei.

CASTEP: The CASTEP package [34], is extensively employed in the field of materials science for doing calculations based on density functional theory (DFT) to determine a range of material characteristics. This computational tool exhibits the capacity to do calculations pertaining to atomic structure, electronic response, and energetics. Furthermore, it has the capability to simulate several characteristics of atomic materials, including but not limited to optical qualities, band structure, and mechanical properties. The current investigation uses CASTEP as a tool for doing Raman Spectral analysis.

VESTA: The VESTA [35] software package is a freely available 3D visualisation tool designed for academic usage. It facilitates the examination and interpretation of diverse

structural models and data. The current investigation employs VESTA as a tool for visualising crystal structures.

TDEP: As mentioned, the TDEP Package (Temperature-Dependent Effective Potential Package) [28][29][30], is a comprehensive set of tools designed for the study of lattice dynamics under finite temperature conditions. The features encompassed comprise of obtaining temperature-dependent phonon frequencies, anharmonic free energy, and lattice thermal conductivity, amongst others. The current work employs the use of TDEP for performing lattice thermal conductivity analysis.

References:

[1] E. Schrödinger, “An Undulatory Theory of the Mechanics of Atoms and Molecules,” *Physical Review*, vol. 28, no. 6, pp. 1049–1070, Dec. 1926, doi: 10.1103/PhysRev.28.1049.

[2] P. Hohenberg and W. Kohn, “Inhomogeneous Electron Gas,” *Physical Review*, vol. 136, no. 3B, pp. B864–B871, Nov. 1964, doi: 10.1103/PhysRev.136.B864.

[3] H. Eschrig, *The Fundamentals of Density Functional Theory*, vol. 32. Wiesbaden: Vieweg+Teubner Verlag, 1996. doi: 10.1007/978-3-322-97620-8.

[4] W. Kohn and L. J. Sham, “Self-Consistent Equations Including Exchange and Correlation Effects,” *Physical Review*, vol. 140, no. 4A, pp. A1133–A1138, Nov. 1965, doi: 10.1103/PhysRev.140.A1133.

[5] J. P. Perdew *et al.*, “Atoms, molecules, solids, and surfaces: Applications of the generalized gradient approximation for exchange and correlation,” *Phys Rev B*, vol. 46, no. 11, pp. 6671–6687, Sep. 1992, doi: 10.1103/PhysRevB.46.6671.

[6] H. Hellmann, “A New Approximation Method in the Problem of Many Electrons,” *J Chem Phys*, vol. 3, no. 1, pp. 61–61, Jan. 1935, doi: 10.1063/1.1749559.

[7] J. C. Phillips and L. Kleinman, “New Method for Calculating Wave Functions in Crystals and Molecules,” *Physical Review*, vol. 116, no. 2, pp. 287–294, Oct. 1959, doi: 10.1103/PhysRev.116.287.

[8] J. Kohanoff, *Electronic Structure Calculations for Solids and Molecules*. Cambridge University Press, 2006. doi: 10.1017/CBO9780511755613.

[9] D. R. Hamann, M. Schlüter, and C. Chiang, “Norm-Conserving Pseudopotentials,” *Phys Rev Lett*, vol. 43, no. 20, pp. 1494–1497, Nov. 1979, doi: 10.1103/PhysRevLett.43.1494.

[10] D. Vanderbilt, “Soft self-consistent pseudopotentials in a generalized eigenvalue formalism,” *Phys Rev B*, vol. 41, no. 11, pp. 7892–7895, Apr. 1990, doi: 10.1103/PhysRevB.41.7892.

[11] “Electron correlations in narrow energy bands,” *Proc R Soc Lond A Math Phys Sci*, vol. 276, no. 1365, pp. 238–257, Nov. 1963, doi: 10.1098/rspa.1963.0204.

[12] “Electron correlations in narrow energy bands III. An improved solution,” *Proc R Soc Lond A Math Phys Sci*, vol. 281, no. 1386, pp. 401–419, Sep. 1964, doi: 10.1098/rspa.1964.0190.

[13] V. I. Anisimov, J. Zaanen, and O. K. Andersen, “Band theory and Mott insulators: Hubbard *U* instead of Stoner *I*,” *Phys Rev B*, vol. 44, no. 3, pp. 943–954, Jul. 1991, doi: 10.1103/PhysRevB.44.943.

[14] J. P. Perdew, M. Ernzerhof, and K. Burke, “Rationale for mixing exact exchange with density functional approximations,” *J Chem Phys*, vol. 105, no. 22, pp. 9982–9985, Dec. 1996, doi: 10.1063/1.472933.

[15] A. D. Becke, “A new mixing of Hartree–Fock and local density-functional theories,” *J Chem Phys*, vol. 98, no. 2, pp. 1372–1377, Jan. 1993, doi: 10.1063/1.464304.

[16] V. Anisimov and Y. Izyumov, *Electronic Structure of Strongly Correlated Materials*, vol. 163. Berlin, Heidelberg: Springer Berlin Heidelberg, 2010. doi: 10.1007/978-3-642-04826-5.

[17] P. E. Blöchl, “Projector augmented-wave method,” *Phys Rev B*, vol. 50, no. 24, pp. 17953–17979, Dec. 1994, doi: 10.1103/PhysRevB.50.17953.

[18] M. & von K. Born, *Über Schwingungen im Raumgittern*, vol. 13. Physikalische Zeitschrift, 1912.

[19] M. and K. H. Born, *Dynamical theory of crystal lattices*. Oxford university press, 1996.

[20] J. Zhou, B. Liao, and G. Chen, “First-principles calculations of thermal, electrical, and thermoelectric transport properties of semiconductors,” *Semicond Sci Technol*, vol. 31, no. 4, p. 043001, Apr. 2016, doi: 10.1088/0268-1242/31/4/043001.

[21] B. Qiu *et al.*, “First-principles simulation of electron mean-free-path spectra and thermoelectric properties in silicon,” *EPL (Europhysics Letters)*, vol. 109, no. 5, p. 57006, Mar. 2015, doi: 10.1209/0295-5075/109/57006.

[22] X. Gu and R. Yang, “First-principles prediction of phononic thermal conductivity of silicene: A comparison with graphene,” *J Appl Phys*, vol. 117, no. 2, Jan. 2015, doi: 10.1063/1.4905540.

[23] L. Lindsay and D. A. Broido, “Three-phonon phase space and lattice thermal conductivity in semiconductors,” *Journal of Physics: Condensed Matter*, vol. 20, no. 16, p. 165209, Apr. 2008, doi: 10.1088/0953-8984/20/16/165209.

[24] X. Gu and R. Yang, “First-principles prediction of phononic thermal conductivity of silicene: A comparison with graphene,” *J Appl Phys*, vol. 117, no. 2, Jan. 2015, doi: 10.1063/1.4905540.

[25] A. Togo, L. Chaput, and I. Tanaka, “Distributions of phonon lifetimes in Brillouin zones,” *Phys Rev B*, vol. 91, no. 9, p. 094306, Mar. 2015, doi: 10.1103/PhysRevB.91.094306.

[26] A. Togo and I. Tanaka, “First principles phonon calculations in materials science,” *Scr Mater*, vol. 108, pp. 1–5, Nov. 2015, doi: 10.1016/j.scriptamat.2015.07.021.

[27] W. Li, J. Carrete, N. A. Katcho, and N. Mingo, “ShengBTE: A solver of the Boltzmann transport equation for phonons,” *Comput Phys Commun*, vol. 185, no. 6, pp. 1747–1758, Jun. 2014, doi: 10.1016/j.cpc.2014.02.015.

[28] O. Hellman, I. A. Abrikosov, and S. I. Simak, “Lattice dynamics of anharmonic solids from first principles,” *Phys Rev B*, vol. 84, no. 18, p. 180301, Nov. 2011, doi: 10.1103/PhysRevB.84.180301.

[29] O. Hellman and I. A. Abrikosov, “Temperature-dependent effective third-order interatomic force constants from first principles,” *Phys Rev B*, vol. 88, no. 14, p. 144301, Oct. 2013, doi: 10.1103/PhysRevB.88.144301.

[30] O. Hellman, P. Steneteg, I. A. Abrikosov, and S. I. Simak, “Temperature dependent effective potential method for accurate free energy calculations of solids,” *Phys Rev B*, vol. 87, no. 10, p. 104111, Mar. 2013, doi: 10.1103/PhysRevB.87.104111.

[31] N. Shulumba, *Vibrations in solids: From first principles lattice dynamics to high temperature phase stability*. Linköping University Electronic Press, 2015. doi: 10.3384/diss.diva-122949.

[32] N. Shulumba, O. Hellman, and A. J. Minnich, “Intrinsic localized mode and low thermal conductivity of PbSe,” *Phys Rev B*, vol. 95, no. 1, p. 014302, Jan. 2017, doi: 10.1103/PhysRevB.95.014302.

[33] G. Kresse and J. Furthmüller, “Efficient iterative schemes for *ab initio* total-energy calculations using a plane-wave basis set,” *Phys Rev B*, vol. 54, no. 16, pp. 11169–11186, Oct. 1996, doi: 10.1103/PhysRevB.54.11169.

[34] S. J. Clark *et al.*, “First principles methods using CASTEP,” *Z Kristallogr Cryst Mater*, vol. 220, no. 5–6, pp. 567–570, May 2005, doi: 10.1524/zkri.220.5.567.65075.

[35] K. Momma and F. Izumi, “*VESTA* : a three-dimensional visualization system for electronic and structural analysis,” *J Appl Crystallogr*, vol. 41, no. 3, pp. 653–658, Jun. 2008, doi: 10.1107/S0021889808012016.

CHAPTER-3

Phonon transport and anomalous lattice thermal conductivity in Alkaline earth Chalcogenides and Alkali Halides.

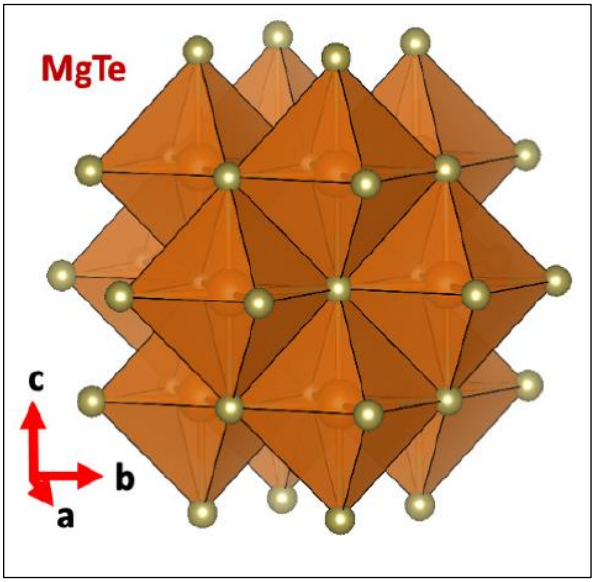

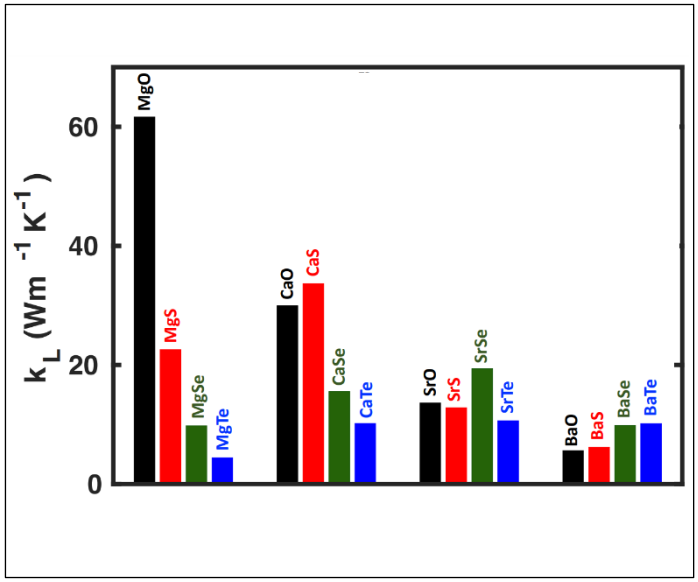

Publications from this chapter:

1. Anomalous Lattice Thermal Conductivity in Rocksalt IIA–VIA Compounds**, Rakesh Roshan, S. Chand ;** Yedukondalu, Neelam.; Muthaiah, R.; Lavanya, K.; Anees, P.; Rajaboina, Rakesh Kumar; Rao, T., Ehm, Lars; Parise, John B., ***ACS Applied Energy Materials,*** **(2022)** *5(1), 882-896.* **https://doi.org/10.1021/acsaem.1c03310**

2. Effect of Atomic Mass Contrast on Lattice Thermal Conductivity: A Case Study for Alkali Halides and Alkaline-Earth Chalcogenides, **Rakesh Roshan, S.Chand** ; Yedukondalu, Neelam; Pandey, Tribhuwan; Kunduru, Lavanya; Muthaiah, Rajmohan; Rajaboina, Rakesh Kumar; Ehm, Lars; Parise, John B., ***ACS Applied Electronic materials*** **(2023), 2023,** *5, 11, 5852–5863.* **https://doi.org/10.1021/acsaelm.3c00759**

The first part of this chapter focuses on a detailed and comparative study on phonon transport of Alkaline earth chalcogenides (AEC's) consisting of MCh (M = Mg, Ca, Sr, Ba and Ch = O, S, Se,Te) compounds in order to provide insights to achieve low κ_L materials through phonon engineering. More light is shed on understanding lattice dynamics, phonon transport, and mechanical properties of 16 MCh (M = Mg, Ca, Sr, Ba and Ch = O, S, Se, Te) compounds.

The second part of this chapter deals with another set of isostructural binary systems, Alkali Halides (AH's), consisting of MX (M = Li, Na, K, Rb, Cs and X = F, Cl, Br, I) compounds and presented in comparison with the results obtained with AEC's.

Materials exhibiting a low lattice thermal conductivity (κ_L) have garnered significant attention due to their potential applications in several fields such as thermoelectrics [1], [2], thermal barrier coatings [3], thermal insulation [4], and thermal energy management. Over the last decade, researchers have made significant efforts to create suitable materials for energy conversion applications. The binary systems of alkaline-earth chalcogenides, denoted as MCh (where M represents Mg, Ca, Sr, and Ba, and Ch represents O, S, Se, and Te), have garnered significant interest due to their applications in thermoelectrics [5]–[7]. Several materials have been identified as having promising thermoelectric properties, including Bulk MX and its 2D equivalents [5]–[8], p-type PbTe and MTe nanocrystals[9], CaTe-SnTe [10], highly doped SrTe with PbTe [11], [12], and BaTe-PbTe [13]. These materials have demonstrated outstanding thermoelectric figure of merit (ZT) values ranging from 0.5 to 1.32 [5], [14].

3.1. Alkaline Earth Chalcogenides, MCh (M = Mg, Ca, Sr, Ba and Ch = O, S, Se,Te)

The MCh (M = Mg, Ca, Sr, and Ba and Ch = O, S, Se, and Te) compounds are extensively studied from the theoretical perspective, which mainly focused on exploring the elastic [15], [16],lattice dynamics [17]–[20], thermodynamic [21], [22] and thermoelectric properties [5]–[7] at ambient and/or high-pressure conditions. Nevertheless, there has been limited work focused on understanding the phonon transport in compounds such as MgSe [23], MgTe [24], CaCh (where Ch represents O, S, Se, and Te) [25], and MTe (where M represents Mg, Ca, Sr, Ba, and Pb) [26]. Hence,

doing a comprehensive and comparative analysis of phonon transport in MCh compounds (where M represents Mg, Ca, Sr, and Ba, and Ch represents O, S, Se, and Te) offers valuable insights into the development of materials with significantly reduced thermal conductivity (referred to as (ultra)low κ_L) by phonon engineering which is of utmost importance in the quest for discovering high thermoelectric figure of merit (ZT) materials. This work aims to provide more insights into the lattice dynamics, phonon transport, and mechanical characteristics of 16 MCh compounds (where M represents Mg, Ca, Sr, and Ba, and Ch represents O, S, Se, and Te) under ambient conditions. It is noteworthy that there are anomalous patterns observed in the values of κ_L for the CaCh (CaS > CaO > CaSe > CaTe), SrCh (SrSe > SrO > SrS > SrTe), and BaCh (BaTe > BaSe > BaS > BaO) series. In particular, the observed anomalous [27] trend in the BaCh (and to some extent in SrCh and CaCh [25]) series deviates from the trend predicted by their atomic mass. In our study, it is observed that BaO, BaS, and MgTe, which are among the 16 compounds analysed, demonstrated a low κ_L behaviour during the temperature range of 300−800 K. This observation is noteworthy considering their relatively low atomic mass and their crystalline structure, which resembles that of rocksalt NaCl-type (B1). The calculated lattice dynamics, phonon lifetimes, scattering rates, phonon group velocities at 300 K, and mechanical characteristics are used to comprehensively analyse the underlying processes for such abnormal trends and low κ_L behaviour. Additionally, the impact of tensile strain on the phonon transport properties and lattice dynamics of the compounds BaO, BaS, and MgTe has been examined and thoroughly discussed.

3.1.1 Computational Details

All first-principles calculations for MCh (Mg, Ca, Sr, and Ba with Ch = O, S, Se, and Te) compounds were performed using the Vienna Ab initio Simulation Package (VASP) [28]. The PBEsol functional was utilised to analyse the exchange-correlation, while the pseudopotential based projected augmented wave (PAW) method was employed to examine the electron−ion interactions. As plane wave basis orbitals, 10 and 6 valence electrons were used for alkaline-earth metals (Mg, Ca, Sr, and Ba) and chalcogens (O, S, Se, and Te). For the expansion of the plane wave basis set, a cutoff energy of 520 eV was used. In the irreducible Brillouin zone, a spacing of $2\pi \times 0.024$ Å^{-1} was utilised for the k-mesh. MCh compounds (where M represents Mg, Ca,

Sr, and Ba and Ch represents O, S, Se, and Te) are classified as polar semiconductors, in order to account for dipole−dipole interactions, Born effective charges and dielectric constants are computed utilizing density functional perturbation theory. The temperature-dependent effective potential (TDEP) [29]–[31] approach is used to determine the lattice dynamics and thermal conductivity of MCh compounds (M = Mg, Ca, Sr, and Ba; Ch = O, S, Se, and Te), taking into consideration harmonic (second) and anharmonic (third) interatomic force constants (IFCs). The expansion of interatomic force constants (IFCs) was considered up to the third order in the current study, and the corresponding model Hamiltonian is shown below:

$$H = U_0 + \sum_i \frac{p_i^2}{2m_i} + \frac{1}{2!}\sum_{ij}\sum_{\alpha\beta} \Phi_{ij}^{\alpha\beta} u_i^{\alpha} u_j^{\beta} + \frac{1}{3!}\sum_{ijk}\sum_{\alpha\beta\gamma} \psi_{ijk}^{\alpha\beta\gamma} u_i^{\alpha} u_j^{\beta} u_k^{\gamma} \qquad ----3.1$$

where p_i^1 and u_i^{α} are the momentum and displacement of atom i, respectively. $\Phi_{ij}^{\alpha\beta}$ and $\psi_{ijk}^{\alpha\beta\gamma}$ are second- and third-order force constant matrices, respectively. In order to calculate the harmonic (second) and anharmonic (third) interatomic force constants (IFCs), ab initio molecular dynamics (AIMD) simulations at 300 K were conducted using the VASP. The AIMD calculations were performed for all the compounds under investigation for 5000 MD steps with a time-step of 1 fs (equivalent to 5 ps) and a supercell of 128 atoms (4 × 4 × 4). To assure convergence of calculated lattice dynamics and phonon transport properties, interactions up to the ninth nearest neighbour were incorporated for second and third order IFCs. A Nose−Hoover thermostat [32], [33] was utilised to regulate the temperature. The calculation of lattice thermal conductivity involves the iterative solution of the complete Boltzmann transport equation (BTE), which takes into account isotope and three-phonon scatterings originating from the natural distribution on a 25 ×25 × 25 q-point grid.

The thermal conductivity tensor is given by

$$k^{\alpha\beta} = \frac{1}{(2\pi)^3}\sum_s \int dq C_\lambda v_{\lambda\alpha} v_{\lambda\beta} \tau_{\lambda\beta} \qquad ----3.2$$

where C_λ is the contribution per mode λ= *(s, q)* to specific heat, α and β are Cartesian components, and v_β and τ_β are phonon velocity and scattering time, respectively. The scattering rates are calculated from a full inelastic phonon Boltzmann equation which is given by

$$k_B T v_\lambda \nabla T \frac{\partial n_{0\lambda}}{\partial T} = \sum_{\lambda'\lambda''} \left[P^{+}_{\lambda\lambda'\lambda''} (\Psi_{\lambda''} - \Psi_{\lambda'} - \Psi_{\lambda}) + \frac{1}{2} P^{-}_{\lambda\lambda'\lambda''} (\Psi_{\lambda''} + \Psi_{\lambda'} - \Psi_{\lambda}) \right] \quad ----3.3$$

The left-hand side represents the phonon diffusion induced by the thermal gradient ∇T and $n_{0\lambda}$ is the equilibrium phonon distribution function. The right-hand side corresponds to the collision term for three-phonon interactions. v_λ is the phonon velocity in mode $\lambda, P^{+}_{\lambda\lambda'\lambda''}$, and $P^{-}_{\lambda\lambda'\lambda''}$are three phonon scattering rates for absorption $(\lambda + \lambda' \rightarrow \lambda'')$ and emission $(\lambda \rightarrow \lambda' + \lambda'')$ processes, respectively.

3.1.2 Results and discussion

3.1.2.1 Crystal structure

Binary alkaline-earth chalcogenides, denoted as MCh (where M represents Mg, Ca, Sr, and Ba and Ch represents O, S, Se, and Te), crystallize in the face-centered cubic (FCC) structure of NaCl (B1)-type rocksalt structure having a space group of Fm3m with Z =4 formula units (f.u.) per unit cell at ambient conditions [34]–[39]. MgSe and MgTe have a high degree of polymorphism and crystallize in rocksalt (B1), zincblende (B3), wurtzite (B4), and NiAs (B8) forms. At ambient temperature, MgTe crystallizes into the B3 [40] and B8 [41] structures, as determined by X-ray diffraction. The thermodynamic stability of the B3 [42] phase for MgSe, as well as both B3 [42] and B8 [43]–[45] for MgTe, is revealed by first-principles calculations under ambient conditions. In addition, both MgSe and MgTe compounds exhibit dynamic stability (metastability) in the rocksalt-type B1 structure. So, rocksalt-type B1 structure is considered for all sixteen MCh compounds where (M = Mg, Ca, Sr, and Ba and Ch = O, S, Se, and Te) are under investigation.

This enables a direct comparison of the calculated properties of these compounds. The ground-state equilibrium lattice constant for MCh compounds is presented in Table 3.1. This value is compared to previously reported X-ray diffraction measurements [34]–[39][46]–[48] and previous first-principles calculations [5]–[7][49]–[52], and a strong agreement is observed between the two. Furthermore, the electron localization function (ELF) was computed for the compounds BaO and MgTe.

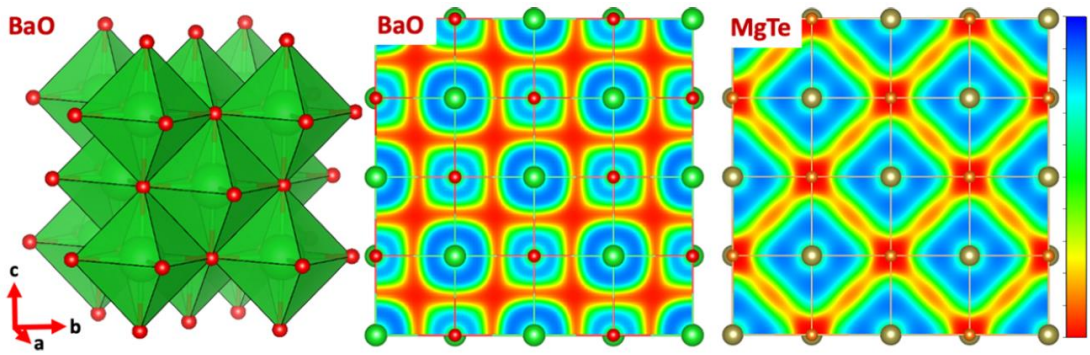

Fig 3.1: Crystal structure of BaO and electron localization function (ELF) of BaO and MgTe along the (001) plane. Light green, red, thick orange and light brown color balls represent Ba, O, Mg and Te atoms, respectively.

Table 3.1: Calculated equilibrium lattice constant (a, in A˚) of MCh (M = Mg, Ca, Sr, Ba and Ch = O, S, Se, Te) compounds at ambient pressure using PBEsol functional and are compared with available X-ray diffraction data and other first principles calculations.

Compound	This work	Expt.	Others
MgO	4.21	4.21 [53]	4.165 [49],4.213 [54]
MgS	5.176	5.203 [55]	5.19 [56],5.234 [42]
MgSe	5.445	5.463 [46]	5.46 [56],5.512 [42]
MgTe	5.901	-	5.98 [56],5.980 [42]
CaO	4.776	4.81 [47]	4.72 [49],4.828 [6]
CaS	5.639	5.689 [39]	5.67 [19],5.712 [6]
CaSe	5.874	5.916 [39]	5.91 [19],5.965 [6]
CaTe	6.298	6.348 [39]	6.33 [19],6.399 [6]
SrO	5.134	5.16 [34]	5.073 [49],5.184 [7]
SrS	5.978	6.024 [35]	6.076[52],6.05 [7]
SrSe	6.205	6.236 [39]	6.323 [52],6.3 [7]
SrTe	6.614	6.66 [57]	6.76 [52],6.718 [7]
BaO	5.533	5.52 [36]	5.562 [58],5.614 [5]
BaS	6.363	6.387 [36]	6.44 [59],6.407 [58]
BaSe	6.578	6.59 [60]	6.593 [61],6.640 [58]
BaTe	6.968	6.99 [60]	7.006 [61],6.989 [58]

Figure 3.1 shows that metal cations (Mg^{2+}, Ba^{2+}) donate electrons while anions (O^{2-}, Te^{2-}) gain electrons, indicating a complete charge transfer and resulting in strong ionic bonding, and this is consistent with the fact that a large electronegativity (on the

Pauling scale) difference (2.55 for BaO) between Ba (0.89) and O (3.44) results in strong ionic character. The low electronegativity difference (0.79 for MgTe) between Mg (1.31) and Te (2.10) atoms implies that MgTe has polar covalent bonding as well as ionic bonding. The distinct type of chemical bonding has a significant impact on the κ_L of these materials.

3.1.2.2 Anharmonic lattice dynamics and thermal conductivity

It is essential to investigate lattice dynamics, including anharmonic effects, in order to comprehend phonon transport in materials. As a preliminary step, the phonon dispersion curves (Figure 3.2) of MCh (M = Mg, Ca, Sr, and Ba ; Ch = O, S, Se, and Te) compounds at 300 K were calculated and carefully analysed. The absence of imaginary frequencies along high symmetry directions of the Brillouin zone (as shown in Figure 3.2) indicates that each material under investigation is dynamically stable. MCh (M = Mg, Ca, Sr, and Ba and Ch = O, S, Se, and Te) compounds contain two atoms per primitive cell, resulting in six vibrational modes, three of which are optical and three of which are acoustic (3N; N = number of atoms per primitive cell). The accurate description of phonon spectra in polar materials is dependent on dipole−dipole interactions.

Calculated Born effective charges (see Table 3.2) and high-frequency dielectric constants integrate these interactions into a dynamic matrix, resulting in a splitting between the longitudinal optic (LO) and transverse optic (TO) phonon modes (Figure 3.2). The three phonon optic modes divide into two degenerate TO (ω_{TO}) and one LO (ω_{LO}) modes along the Γ-direction as a result of this LO-TO splitting. In particular, large LO-TO splitting is found for MO (M = Mg, Ca, Sr, and Ba) compounds; it decreases from MO > MS > MSe > MTe (M = Mg, Ca, Sr, and Ba) compounds and increases from MgO < CaO <SrO < BaO (see Figure 3.2 and Tables 3.2 and 3.3). The compounds MCh (where M = Mg, Ca, Sr, and Ba and Ch = O, S, Se, and Te) exhibit comparable phonon band characteristics and displayed a notable phonon softening as atomic mass increased, from Mg → Ca → Sr → Ba to O → S → Se → Te. These features correlate with earlier first-principles lattice dynamics computations [5]–[7][26].

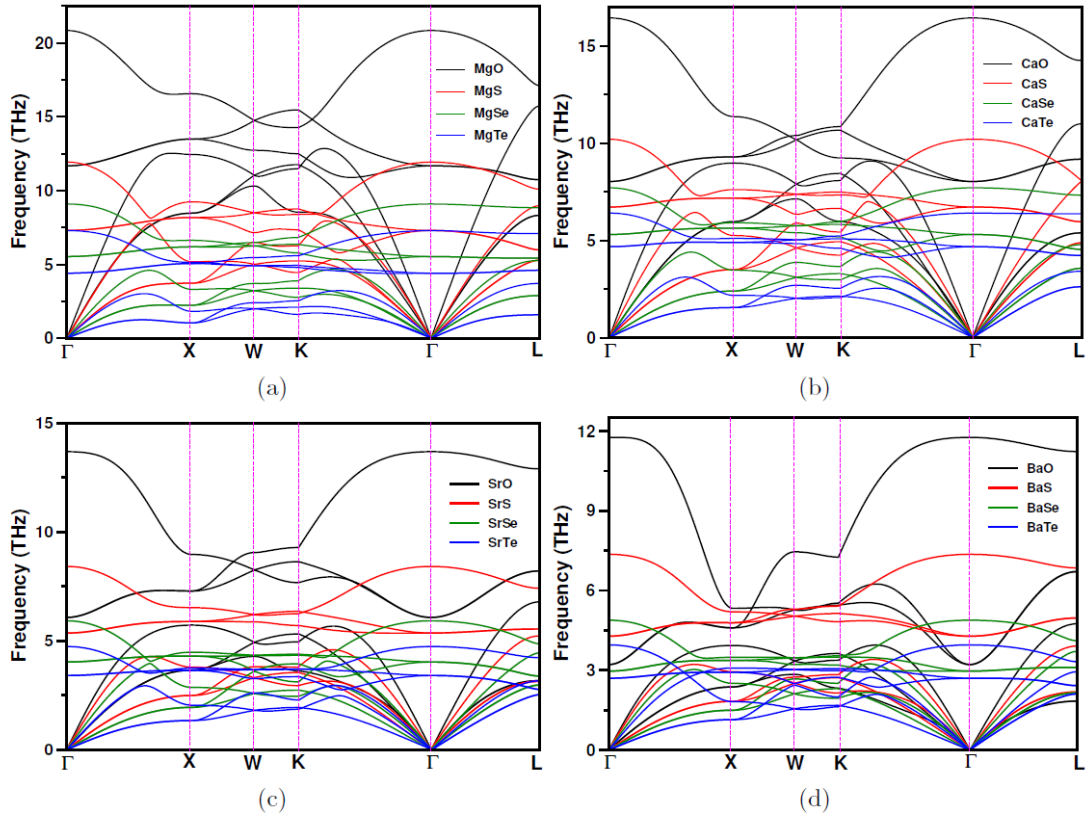

Fig 3.2: Calculated room temperature phonon dispersion curves of (a) MgCh, (b) CaCh, (c) SrCh and (d) BaCh compounds at PBEsol equilibrium volume; where Ch = O, S, Se and Te.

Table 3.2: Calculated Born effective charges (BECs,in electron charge) for MCh (M = Mg, Ca, Sr, Ba and Ch = O, S, Se, Te) compounds. The values given in parenthesis are the difference between LO and TO modes (LO-TO, in THz).

	O	S	Se	Te
Mg	1.98 (9.16)	2.31 (4.63)	2.43 (4.38)	2.67 (2.88)
Ca	2.36 (8.11)	2.35 (3.48)	2.35 (2.4)	2.38 (1.73)
Sr	2.46 (7.62)	2.4 (3.05)	2.39 (1.89)	2.4 (1.33)
Ba	2.77 (8.54)	2.62 (3.08)	2.6 (1.91)	2.59 (1.25)

Table 3.3: Calculated transverse optical (ω_{TO}, in cm^{-1}), longitudinal optical (ω_{LO}, in cm^{-1}) phonon modes and the difference between LO and TO modes (ω_{LO} - ω_{TO}, in cm^{-1}) at 300 K for 16 MCh compounds are compared with the available experimental and previous first-principles calculations. The values given in parenthesis are in THz units.

Compound	**Method**	**ω_{TO}**	**ω_{LO}**	**ω_{LO} - ω_{TO}**
MgO	This work	390.11 (11.68)	696.06 (20.84)	305.94 (9.16)

MgS	This work	243.82 (7.3)	398.46 (11.93)	154.64 (4.63)
	Others	220.64 [50]	385.06 [50]	165.06
MgSe	This work	185.04 (5.54)	331.33 (9.92)	146.29 (4.38)
	Others	171 [62]	296 [62]	123.31
MgTe	This work	147.29 (4.41)	243.49 (7.29)	96.19 (2.88)
	Others	141 [63]	234.1 [63]	99.68
CaO	This work	317.63 (9.51)	588.51 (17.62)	270.87 (8.11)
	Expt	311 [64]	585 [64]	
CaS	This work	224.11 (6.71)	340.35 (10.19)	116.23 (3.48)
	Others	231.42 [65]	336.65 [65]	
	Expt	229[66]	342 [66]	
CaSe	This work	177.02 (5.3)	257.18 (7.7)	80.16 (2.4)
	Others	178.4 [63]	251.4 [63]	
	Expt	168 [66]	220 [66]	
CaTe	This work	155.98 (4.67)	213.76 (6.4)	57.78 (1.73)
	Others	156.2 [63]	209 [63]	
SrO	This work	202.74 (6.07)	457.25 (13.69)	254.51 (7.62)
	Others	217.85 [67]	474.13 [67]	
	Expt	224.15 [68]	484.99 [68]	
SrS	This work	179.02 (5.36)	280.90 (8.41)	101.87 (3.05)
	Others	194.045 [69]	290.577 [69]	
SrSe	This work	136.60 (4.03)	197.73 (5.92)	63.13 (1.89)
	Others	127.496 [69]	193.193 [69]	

SrTe	This work	113.90 (3.41)	158.32 (4.74)	44.42 (1.33)
	Others	110.717 [69]	156.738 [69]	
BaO	This work	107.55 (3.22)	392.78 (11.76)	285.24 (8.54)
	Expt	146 [64]	440 [64]	
BaS	This work	142.95 (4.28)	245.82 (7.36)	102.87 (3.08)
	Expt	150 [66]	246 [66]	
BaSe	This work	99.19 (2.97)	162.99 (4.88)	63.79 (1.91)
	Expt	100 [66]	156 [66]	
BaTe	This work	90.18 (2.7)	131.93 (3.95)	41.75 (1.25)

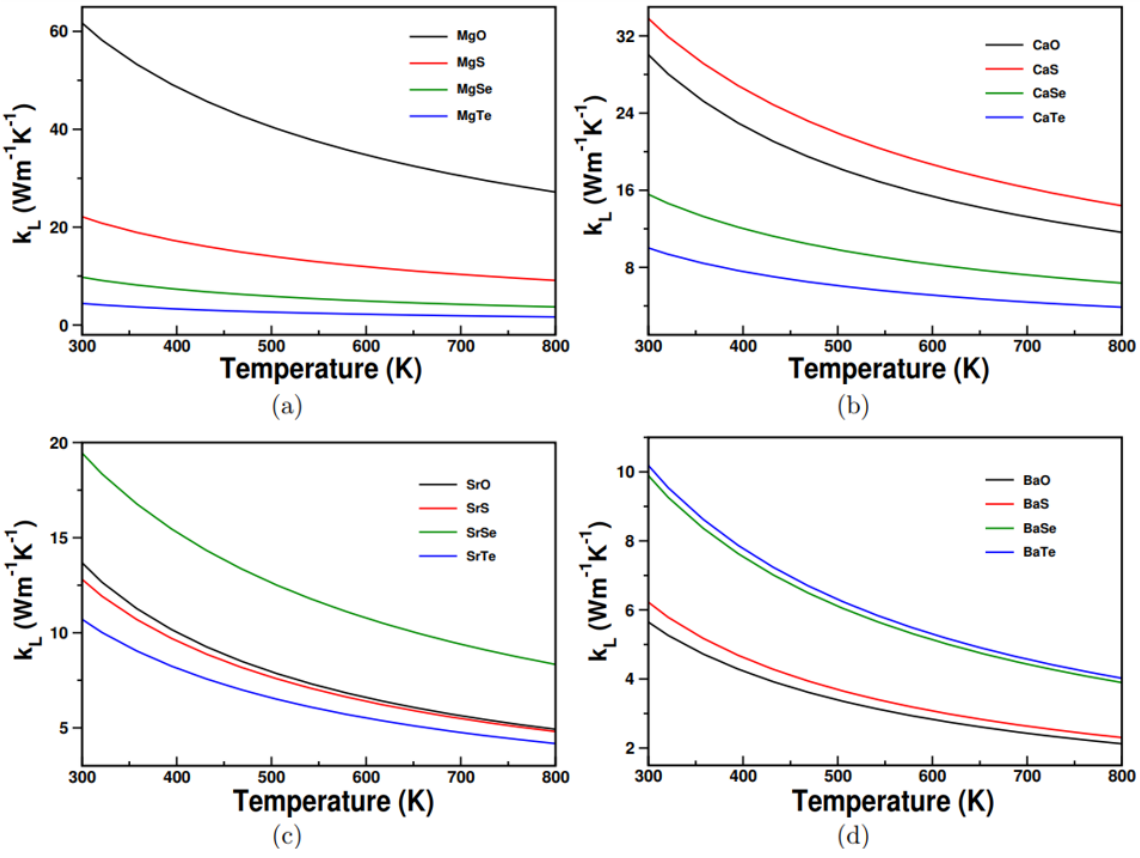

Fig 3.3: Calculated lattice thermal conductivity (κ_L) of (a) MgCh, (b) CaCh, (c) SrCh and (d) BaCh compounds as a function of temperature; Ch = O, S, Se and Te at PBEsol equilibrium volume.

Table 3.4: Calculated lattice thermal conductivity (κ_L, in $Wm^{-1}K^{-1}$) at 300 K for 16 MCh compounds. k_L^a - calculated at the PBESol equilibrium lattice constant; k_L^{Eb}- calculated at the experimental lattice constant.

	This Work		Others				
Compound	k_L^a	k_L^{Eb}	**Expt**	k_{3ph}^{HA}	k_{3ph}^{SCPH}	$k_{3,4ph}^{SCPH}$	**Others**
MgO	61.65	61.65	52 [70]	52.1 [71]	58.7 [71]	50.1 [71]	-
MgS	22.59	18.74	-	-	-	-	-
MgSe	9.8	7.55	-	-	-	-	-
MgTe	4.45	4.45	-	-	-	-	3 [26]
CaO	29.94	24.77	30 [70]	21.3 [71]	25.1 [71]	22.2 [71]	-
CaS	33.66	28.39	-	-	-	-	-
CaSe	15.56	13.21	-	-	-	-	-
CaTe	10.17	8.33	-	-	-	-	8.5 [26]
SrO	13.61	11.65	10 [70]	9.0 [71]	11.0 [71]	9.9 [71]	-
SrS	12.81	11.6	-	-	-	-	-
SrSe	19.36	15.8	-	-	-	-	-
SrTe	10.64	9.66	-	-	-	-	10.5 [26]
BaO	5.63	6.76	3 [70]	2.8 [71]	4.4 [71]	3.3 [71]	-
BaS	6.17	6.28	-	-	-	-	-
BaSe	9.85	10.06	-	-	-	-	-
BaTe	10.14	9.84	-	-	-	-	10.2 [26]

The lattice thermal conductivity (κ_L) as a function of temperature (300-800 K) was then computed, and the results are shown in Figure 3.3. Because of increasing anharmonicity with temperature, the obtained κ_L values decrease with temperature for all 16 compounds under investigation. Because of their large atomic mass, materials with the same crystal structure that include heavy elements often have lower κ_L than those that contain light elements. κ_L decreases with increasing atomic mass of anion, i.e., from MgO → MgS → MgSe → MgTe in MgX compounds, but κ_L shows

anomalous trends for the CaCh (CaS > CaO > CaSe > CaTe), SrCh (SrSe > SrO > SrS > SrTe), and BaCh (BaTe > BaSe > BaS > BaO). The BaCh series, in particular, exhibits an opposite trend for κ_L, which contradicts the predicted trend based on their atomic mass. However, when κ_L is estimated at the experimental lattice constant for SrCh (SrSe > SrO > SrS > SrTe) and BaCh (BaSe >BaTe > BaO > BaS) compounds, the foregoing trends are somewhat changed, but the general trends remain more or less similar in both cases (see Figures 3.3 and Figures 3.4).

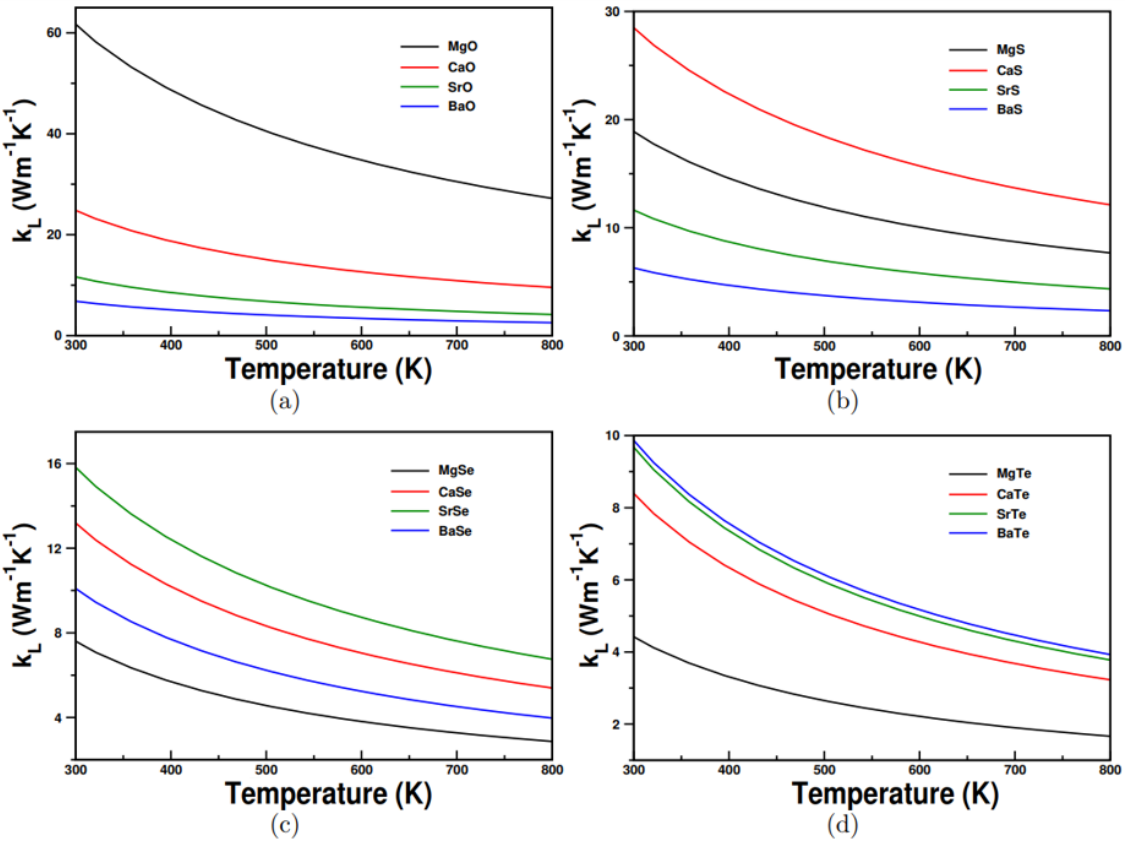

Fig 3.4: Calculated lattice thermal conductivity of (a) MO, (b) MS, (c) MSe and (d) MTe compounds as a function of temperature at the experimental lattice constant; where M = Mg, Ca, Sr and Ba.

To gain insight into the observed anomalous trends, the obtained κ_L values at 300 K were plotted as a function of mass ratio (i.e., metal atom's atomic mass to a nonmetal atom's atomic mass), as shown in Figure 3.6. Low κ_L values are seen in materials with great mass contrast, i.e. with either low or high mass ratios. For example, compared to those with mass ratios close to unity, which are having larger κ_L values, MgTe, BaS, and BaO have comparatively low κ_L values of 4.45, 6.17, and 5.63 W m^{-1} K^{-1} with mass ratios of 0.19, 4.3, and 8.6, respectively. For instance, the mass ratio of BaTe is 1.1, and its κ_L value is 10.14 W m^{-1} K^{-1}, greater than that of the high mass contrast

systems, BaO and MgTe. Furthermore, MgTe and BaTe compounds were considered for the case study to comprehend why materials with significant mass contrast have comparatively low κ_L values compared to materials with mass ratios near to unity [72]. Figure 3.7a illustrates that MgTe exhibits a phonon gap between its acoustic and optic phonon branches, which extend across about ~0−8 THz.

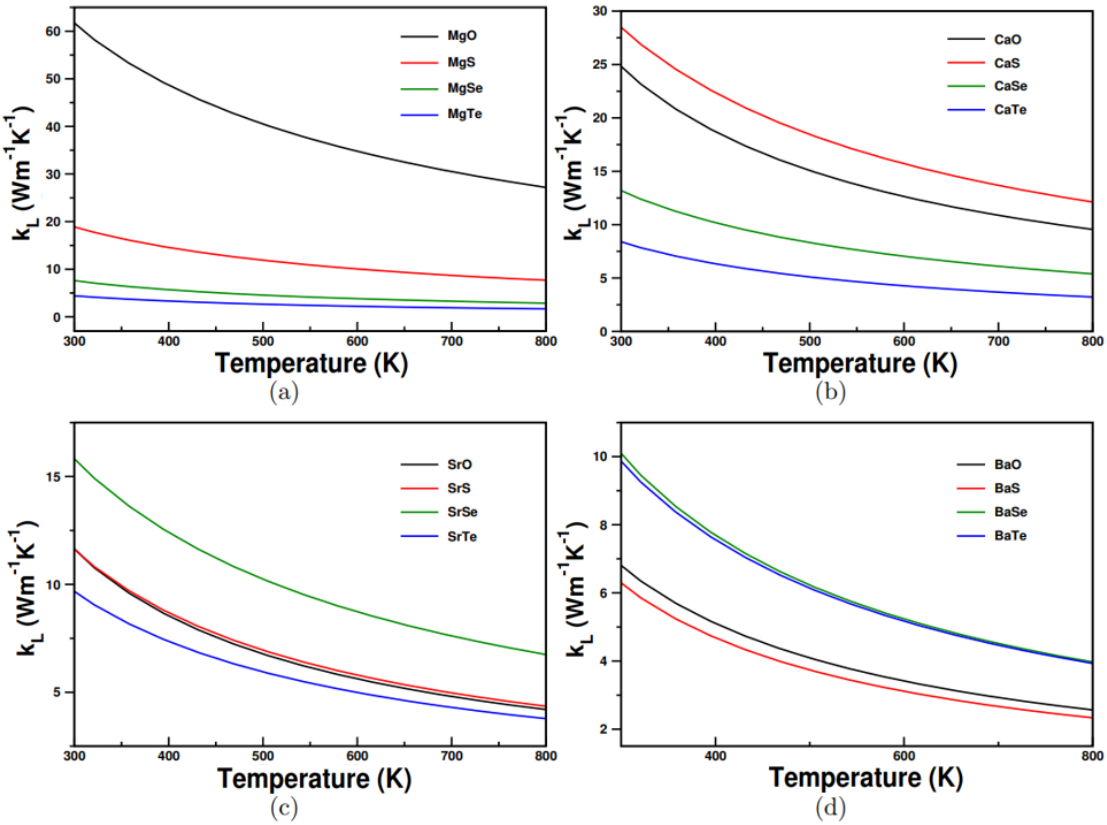

Fig 3.5: Calculated κ_L of (a) MgCh, (b) CaCh, (c) SrCh and (d) BaCh compounds as a function of temperature at the experimental lattice constant; where Ch = O, S, Se and Te.

In contrast, BaTe lacks a phonon gap throughout the whole frequency range of ~0–4 THz due to its mass ratio being close to unity (1.1). According to slack theory,[73] When the optic phonon velocity is high and the distance between the acoustic and optic phonon branches is relatively small, then heat is also carried by optic phonons in crystalline materials. Therefore, the optic phonons in BaTe also facilitate heat conduction (refer to Figure 3.7d), whereas in MgTe, the phonon gap accompanied by low TO optic phonon velocities could potentially hinder phonon transport (refer to Figure 3.7c).

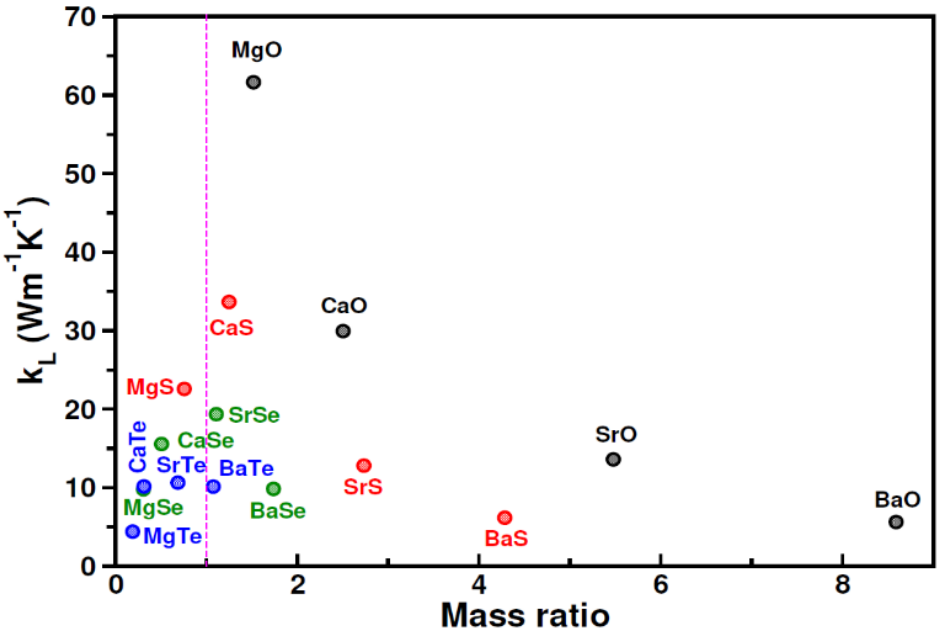

Fig 3.6: Calculated lattice thermal conductivity (κ_L) at 300 K as function of mass ratio for MCh (M = Mg, Ca, Sr, Ba and Ch = O, S, Se, Te) compounds. The vertical line corresponds to mass ratio equal to unity, where metal and non-atoms have equal mass ratio.

Moreover, in the frequency range of 1−4 THz, MgTe exhibits shorter phonon lifetimes than BaTe (refer to Figure 3.7b). As a result of MgTe's reduced phonon propagation and shortened phonon lifetimes in comparison to BaTe, κ_L is decreased. This explanation also holds good for anomalous trends seen in other compounds (Figure 3.8 for CaO and CaS).

This demonstrates conclusively that a finite phonon gap between acoustic-optic branches is essential for achieving (ultra)low κ_L behaviour when designing low kappa materials with a combination of heavy and light elements into materials with high mass contrast.

Phonon dispersion curves (refer to Figures 3.2 and 3.7a) revealed the presence of phonon softening in compounds characterized by a high mass contrast. The TO modes of MO (M = Ca, Sr, and Ba), SrS, and BaS compounds are shown in Figure 2c and d. These modes are low-lying and fall into the acoustic mode region for all compounds, particularly for BaO7 and SrO6 compounds (see Figure 3.2). Furthermore, in contrast to the other compounds in the BaCh series (Ch = S, Se, and Te), BaO exhibits an additional phonon softening of transverse acoustic modes near the L point, despite its relatively low atomic mass.

Among the sixteen systems currently being examined, it is noteworthy that three compounds with high mass contrast demonstrate low κ_L values at 300 K, specifically below ~6 W m^{-1} K^{-1}, these are BaO, BaS, and MgTe.

Furthermore, in comparison to BaTe, MgTe demonstrates phonon softening of the transverse acoustic phonon modes near the X and L points (refer to Figure 7a). This is despite its relatively low atomic mass. The observed trend coincides with findings from a prior study on compressive sensing lattice dynamics (CSLD) [26], but diverges from the phenomenological Debye–Callaway model investigation [74] concerning the lattice thermal transport of MTe compounds (M = Mg, Sr, Ba, and Pb). Furthermore, the Debye-Callaway model significantly underestimates the values (refer to Table 3.4).

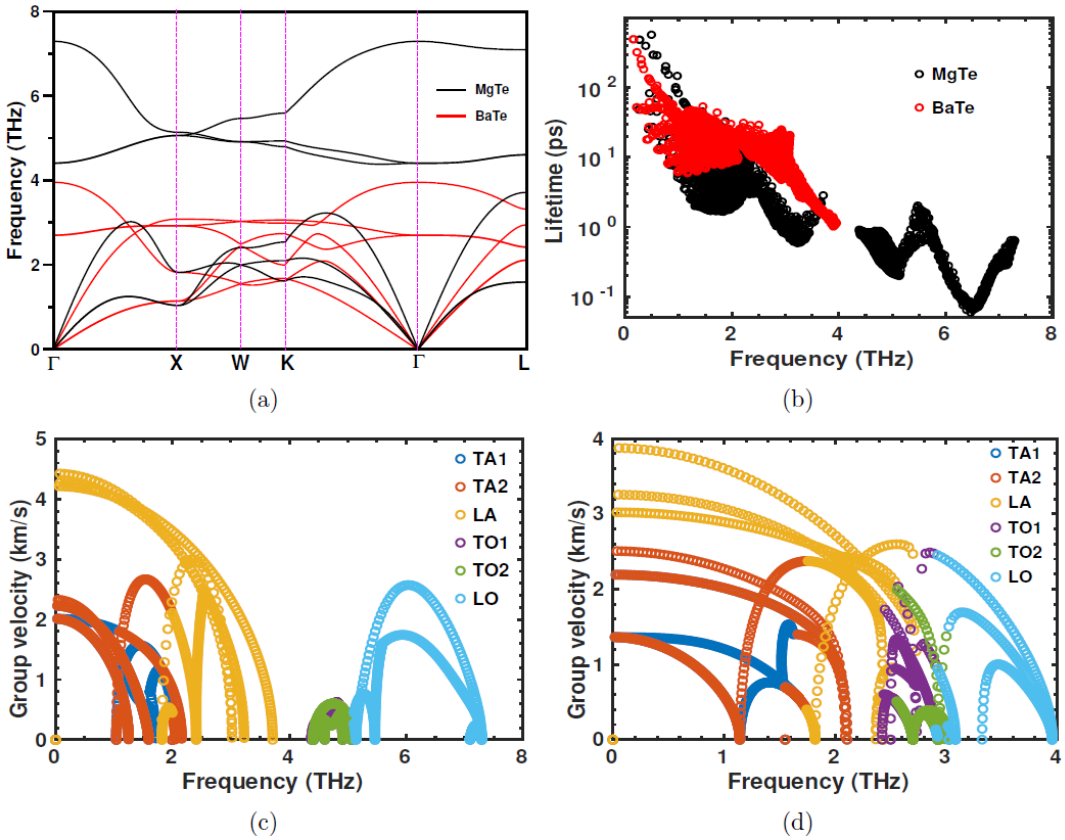

Fig 3.7: Calculated (a) phonon dispersion curves (b) phonon lifetimes of MgTe and BaTe as a function of frequency, (c) group velocity as a function of frequency for MgTe, (d) group velocity as a function of frequency for BaTe.

So far, four significant factors have been identified as having a substantial impact on the κ_L behavior of MgTe, BaO, and BaS compounds: (1) a high mass contrast between metal and nonmetal atoms (see Figure 3.6); (2) low lying TO phonon modes for BaO and BaS transition into the acoustic mode region (see Figure 3.2d); (3) MgTe exhibits

soft transverse acoustic (TA) phonon modes despite having a lower atomic mass than BaTe (see Figure 3.5a); and (4) the phonon lifetimes of MgTe and BaTe are illustrated in Figure 3.7b. In particular, the latter one is crucial in determining trends in κ_L; this is elaborated upon in the following section.

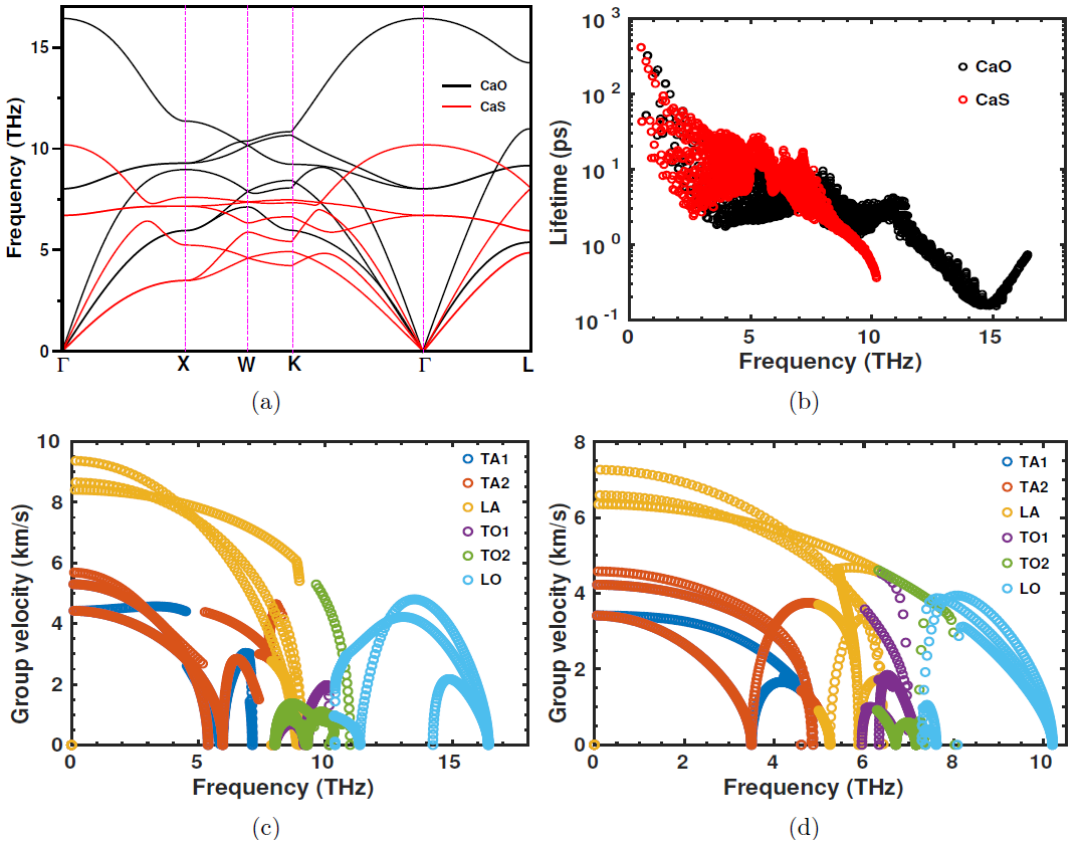

Fig 3.8: Calculated (a) phonon dispersion curves (b) phonon lifetimes of CaO and CaS as a function of frequency, (c) group velocity as a function of frequency for CaO, (d) group velocity as a function of frequency for CaS.

In an effort to gain a more comprehensive understanding of the mechanisms at play behind the peculiar behaviour of κ_L in compounds including MgTe, CaCh (Ch = O and S), SrCh (Ch = O, S, and Se), and BaCh (Ch = O, S, Se, and Te) (refer to Figure 3.3 and Figure 3.6 and 3.7), the scattering rates, phonon mean free paths (MFPs), and group velocities and lifetimes were computed. In Figure 3.9, the calculated phonon MFPs as a function of frequency are displayed. A significant proportion of the phonon MFPs for each MCh compound fall above the minimum interatomic distance, also known as the Ioffe−Regel limit. Consequently, the phonon Boltzmann transport theory adequately describes the thermal transport occurring within MCh compounds. Heat transfer in crystalline materials may be thought of as the propagation of phonons and their scatterings among themselves. Materials with low values of $\tau(\omega)$ and $v(\omega)$ are

anticipated to have low κ_L, as κ_L is constrained by these two variables. The phonon lifetime decreases from MgO > MgS > MgSe > MgTe across the entire frequency range, as shown in Figure 3.10. The corresponding trend is observed for κ_L in MgCh. CaO's phonon lifetimes in the frequency range of ~2−8 THz are comparatively shorter than those of CaS (refer to Figure 3.10b). This discrepancy in κ_L values between CaS and CaO, CaSe, and CaTe, and the subsequent anomalous trend (CaS > CaO > CaSe > CaTe) in the CaCh series, may account for CaO's lower κ_L. This trend aligns with the findings of a prior lattice thermal conductivity investigation [25] utilising ShengBTE on CaCh compounds (where Ch represents O, S, Se, and Te).

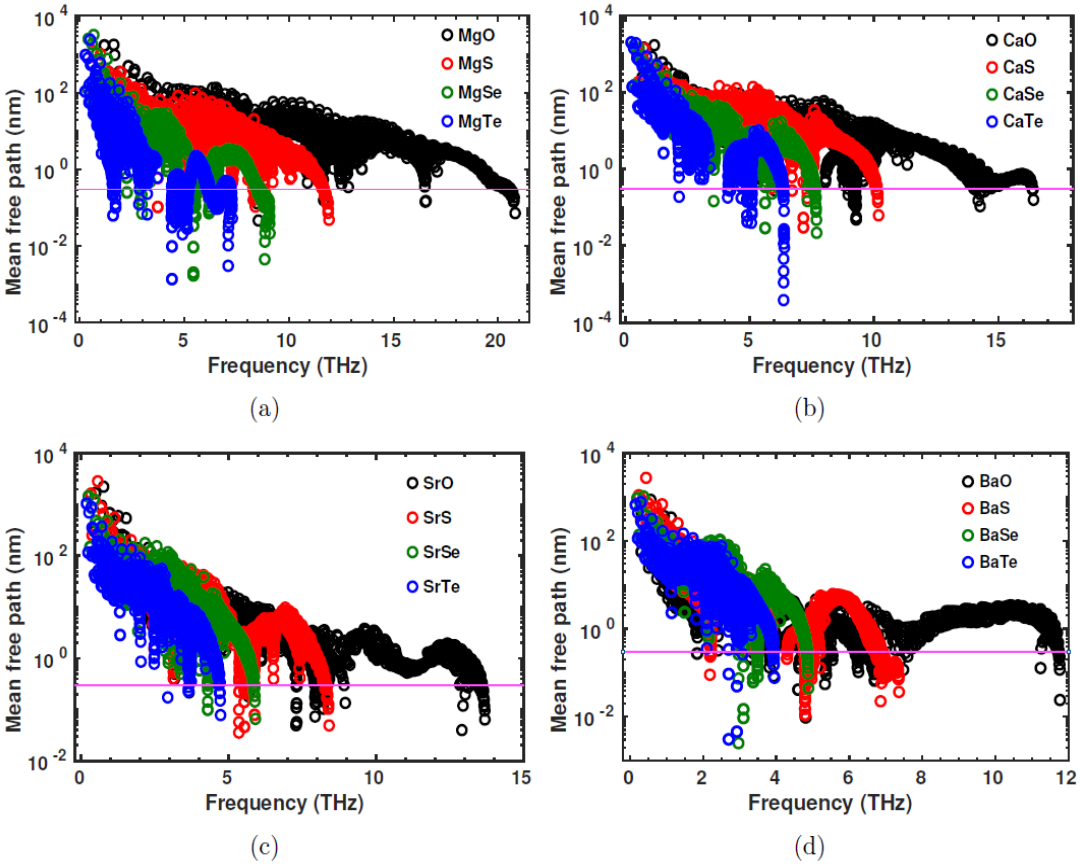

Fig 3.9: Calculated mean free paths of (a) MgCh, (b) CaCh, (c) SrCh and (d) BaCh compounds as a function of frequency; where Ch = O, S, Se and Te. The horizontal solid line (magenta) represents Ioffe-Regel limit for mean free paths.

SrSe and SrO have considerably higher and shorter phonon lifetimes in the ~1-4 THz and ~2- 4 THz frequency ranges, respectively. This might explain the anomalous trend in the SrCh (Ch = O, S, Se, and Te) series for κ_L (SrSe > SrO > SrS > SrTe). Finally, BaO and BaS have shorter phonon lifetimes than BaSe and BaTe, resulting in low κ_L, which is consistent with the anticipated trend of BaTe > BaSe > BaS > BaO for κ_L in BaCh (Ch = O, S, Se, and Te) compounds[27]. Total scattering

rates are obtained by adding absorption, emission, and isotope scattering rates from the three phonon processes for all 16 MCh (M = Mg, Ca, Sr, and Ba and Ch = O, S, Se, and Te) compounds, as illustrated in Figures 3.11 and 3.12.

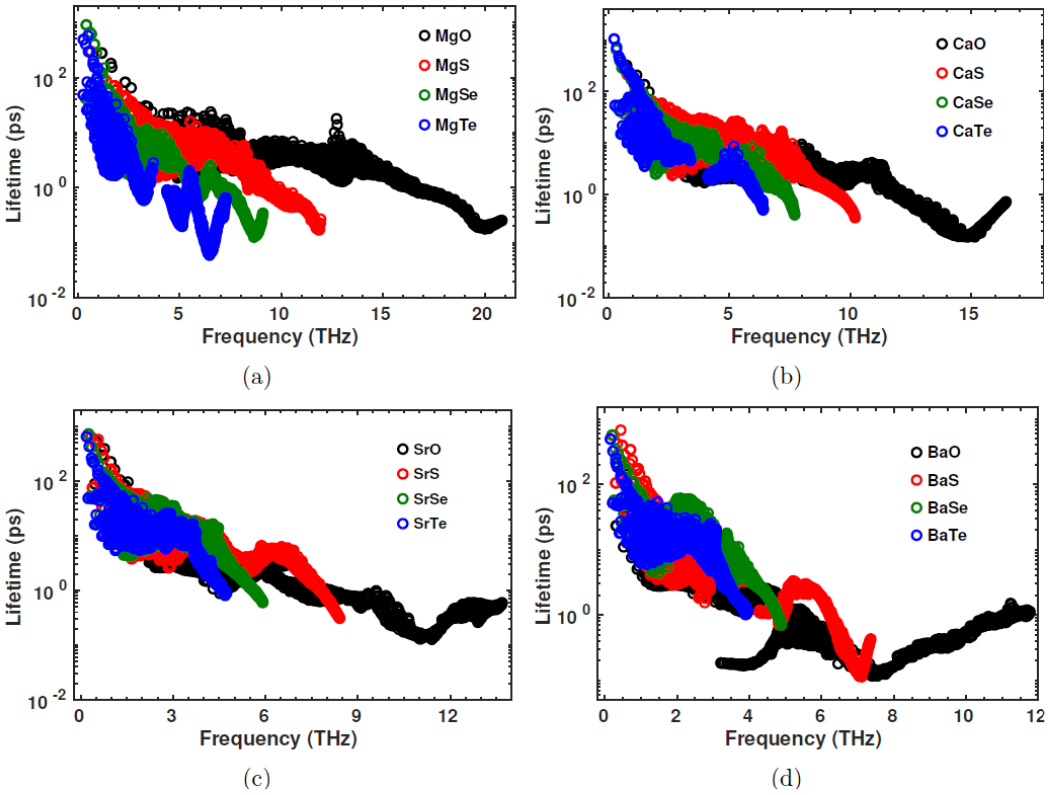

Fig 3.10: Calculated phonon lifetimes of (a) MgCh, (b) CaCh, (c) SrCh and (d) BaCh compounds as a function of frequency; where Ch = O, S, Se and Te.

Absorption scattering rates dominate in the low-frequency domain (for example, below 3 THz for BaO). Phonon scattering processes in the low-frequency range are most likely caused by the conversion of a low-energy phonon to a high-energy phonon via phonon absorption.

The contribution of emission scattering rates increases with frequency and is mainly significant in the high-frequency region, where phonon scattering processes are likely to occur via conversion of a high-energy phonon to a low-energy phonon with phonon emission. Finally, across the whole frequency range, a moderate contribution from isotope scattering rates is observed, for example, in BaCh (Ch = O, S, Se, Te) compounds (see Figure 3.12).

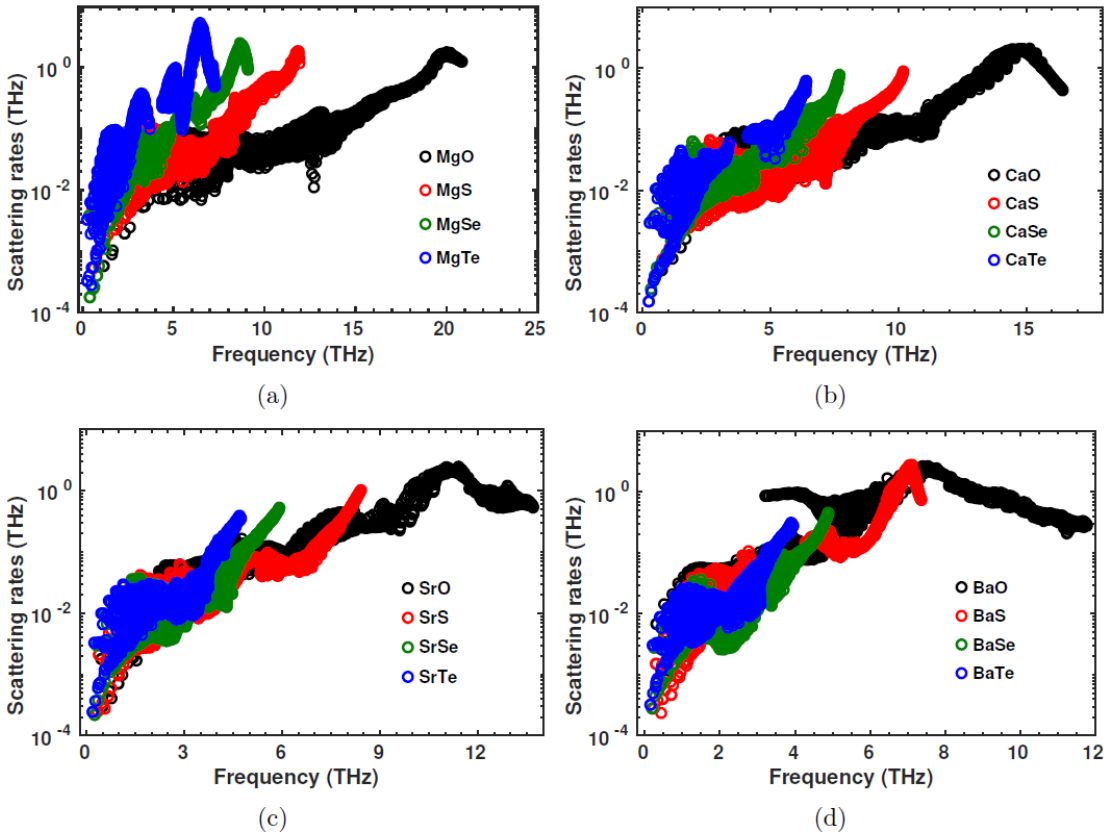

Fig 3.11: Calculated scattering rates of (a) MgCh, (b) CaCh, (c) SrCh and (d) BaCh compounds as a function of frequency; where Ch = O, S, Se and Te.

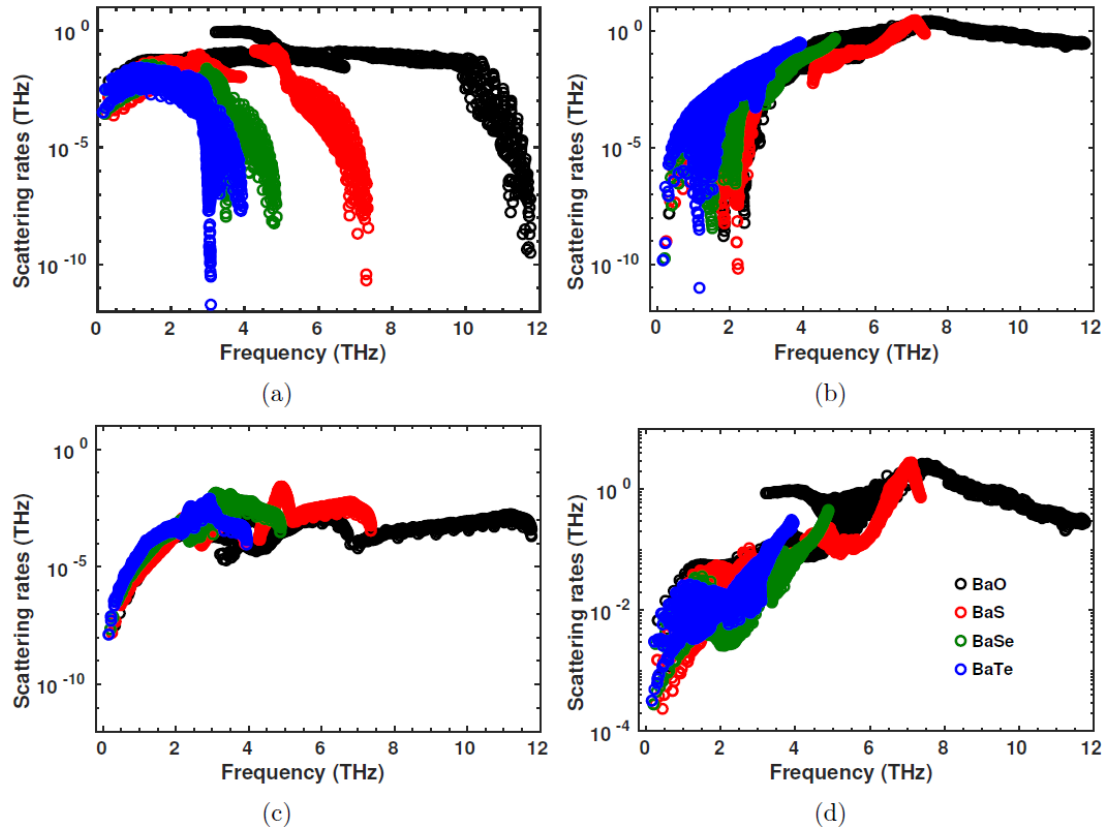

Fig 3.12: Calculated (a) absorption (b) emission (c) isotope and (d) total scattering rates of BaCh (Ch = O, S, Se and Te) compounds as a function of frequency.

3.1.2.3 Effect of Tensile Strain on Lattice Thermal Conductivity

Three (BaO, BaS, and MgTe) of the sixteen MCh compounds (M = Mg, Ca, Sr, and Ba and Ch = O, S, Se, and Te) have been found to have low κ_L values (less than 6 W m^{-1} K^{-1}) over the temperature range of 300−800 K that was investigated. The phonon dispersion curves, phonon lifetimes, scattering rates, and κ_L values of the BaO, BaS, and MgTe compounds were compared, as shown in Figure 3.13. The low κ_L behaviour exhibited by BaO, BaS, and MgTe compounds can be attributed to phonon softening in both the acoustic and optical modes which is caused by phonon gaps and high scattering rates (Figure 3.13a, 3.13b), as well as short phonon lifetimes (Figure 3.13c). The observed κ_L values precisely correspond to the decreasing order of phonon lifetimes as specified below for these three compounds: BaS > BaO > MgTe (see Figure 3.13c, d). Based on that trend and the trends observed for the remaining compounds (refer to Figure 3.10), it was proposed that the phonon lifetime (τ) significantly influences the κ_L behaviour of isostructural compounds possessing identical crystal symmetry.

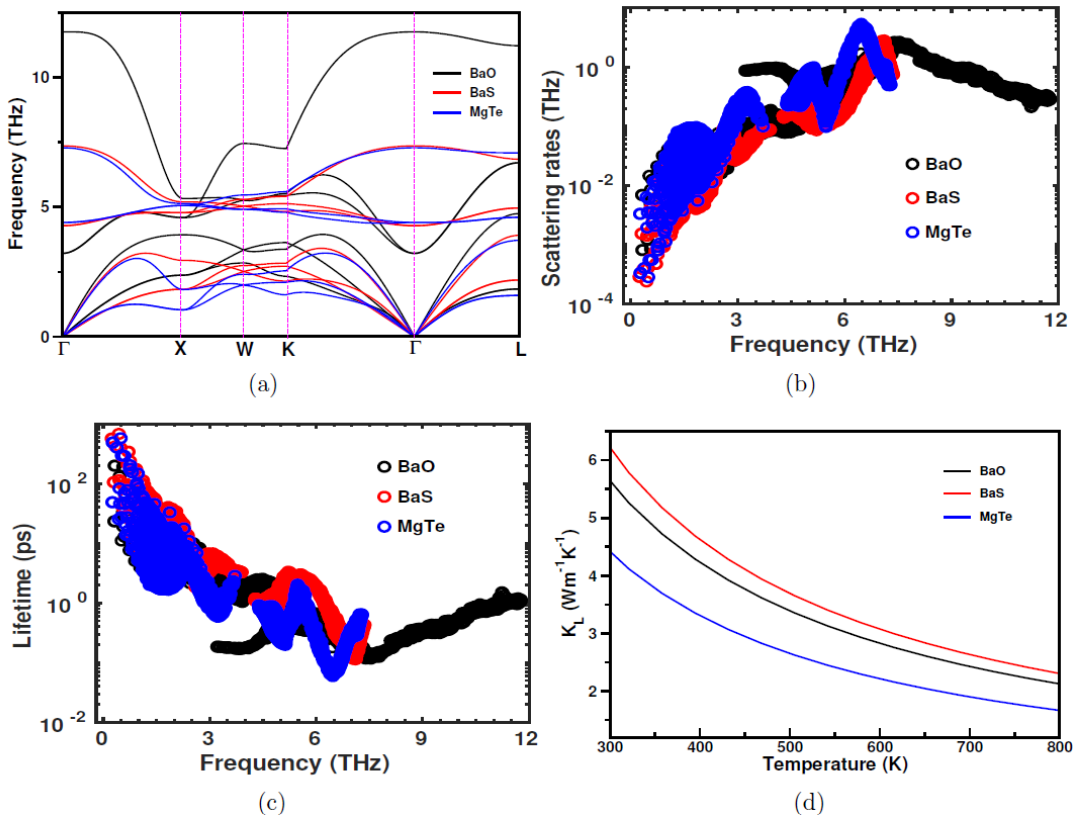

Fig 3.13: Calculated (a) phonon dispersion curves, (b) phonon scattering rates, (c) phonon lifetime, and (d) lattice thermal conductivity (κ_L) of BaO, BaS, MgTe and PbTe compounds at PBEsol equilibrium volume.

Subsequently the impact of tensile strain on lattice dynamics and phonon transport was examined by analysing these three BaO, BaS, and MgTe compounds. In addition, the tensile strain method was utilized, an effective method for achieving a (ultra)low κ_L in materials, to decrease κ_L. A gradual increase in the obtained equilibrium lattice constant upto 6% was done, but soft phonon modes were observed with tensile strains ≥5% of the equilibrium lattice constant for BaO. Consequently, the impact of tensile strains of up to 4% were investigated on the three mentioned compounds. As depicted in Figures 3.14a, 3.15a, and 3.16a, as strain increases, the coupling strength between the acoustic and TO phonon modes is strengthened due to the softening of the acoustic and TO phonon modes. As strain increases, phonon−phonon scattering rates inevitably increase (refer to Figures 3.14b, 3.15b, and 3.16b), resulting in a decrease in κ_L throughout the temperature range under investigation. With an increase in tensile strain, the phonon lifetime decreases substantially (see Figures 3.14c, 3.15c, and 3.16c) due to the high scattering rates for both the acoustic and low-lying TO modes; this further reduces κ_L (see Figures 3.14d, 3.15d, and 3.16d).

The obtained κ_L values for 4% of tensile strain at 300 K are ∼2.06, ∼2.38, and ∼1.05 W m^{-1} K^{-1} for BaO, BaS, and MgTe, respectively. The ultralow κ_L of strained MgTe might be a better candidate for energy conversion applications. From the present and previous studies[25], one can expect a similar behavior for other MCh (M = Mg, Ca, Sr, and Ba and Ch = O, S, Se, and Te) compounds with an application of tensile strain.

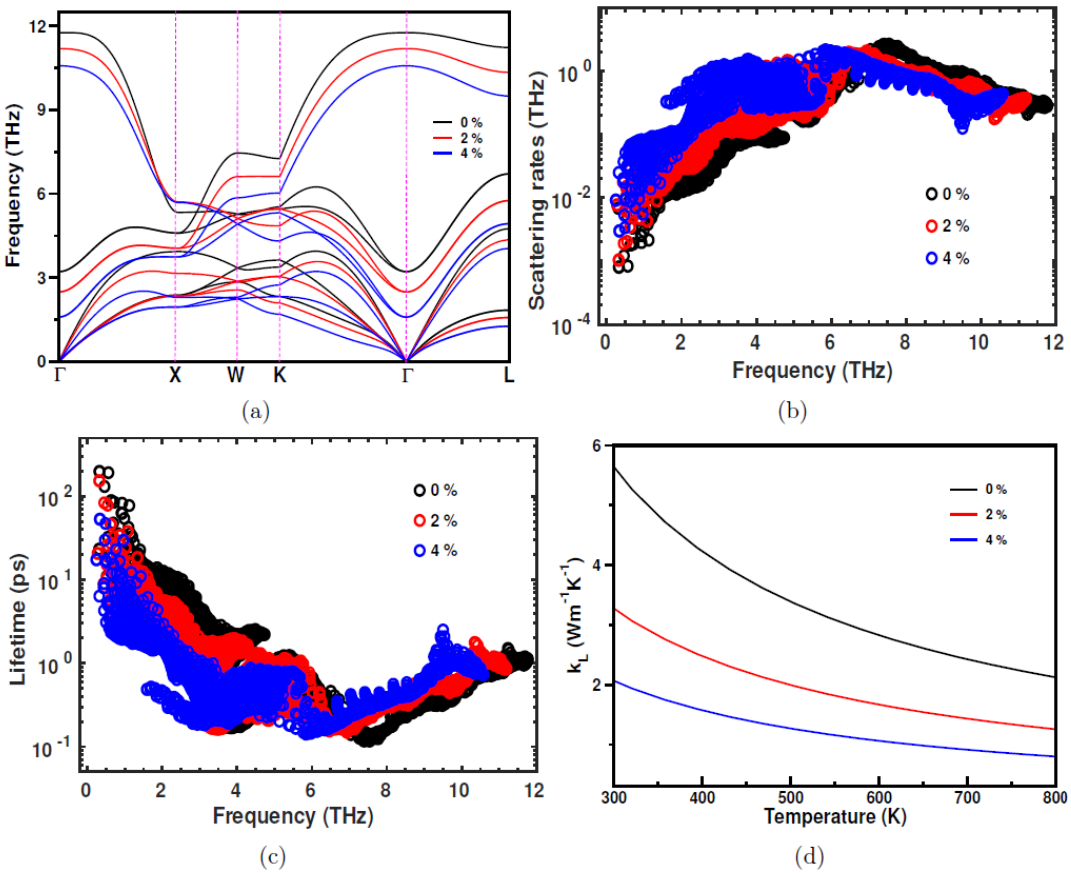

Fig 3.14: Calculated tensile strain dependent (a) phonon dispersion curves, (b) phonon scattering rates, (c) phonon lifetime, and (d) lattice thermal conductivity (κ_L) of BaO.

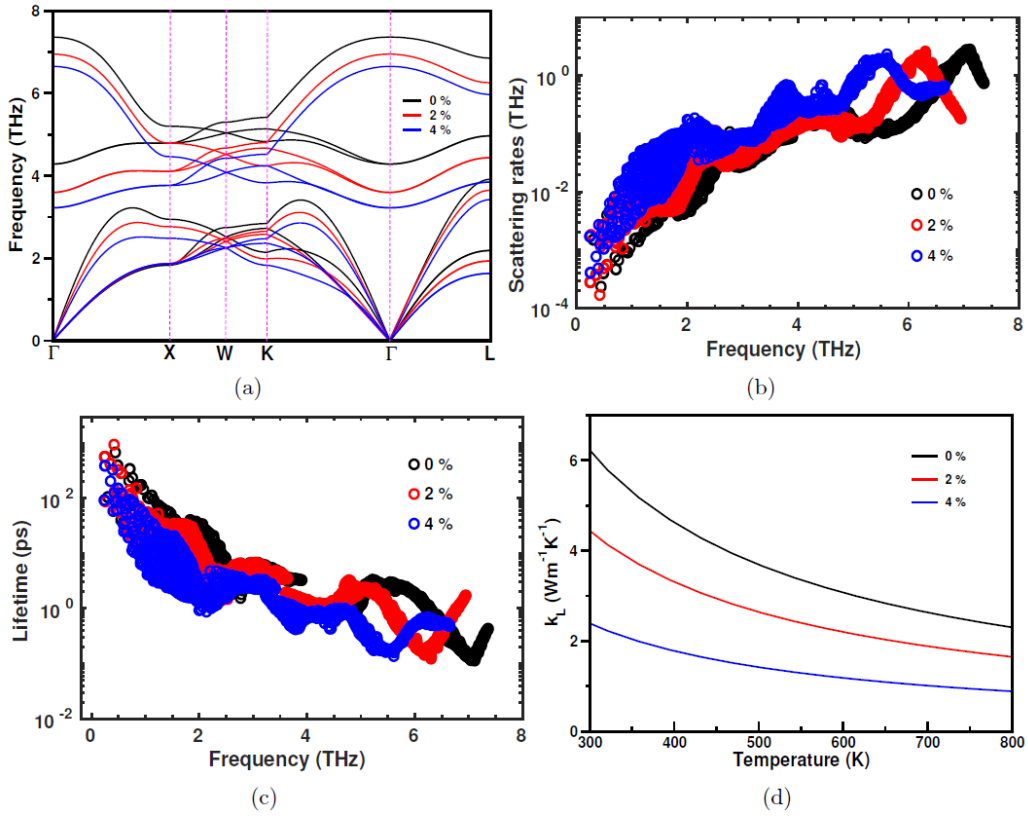

Fig 3.15: Calculated tensile strain dependent (a) phonon dispersion curves, (b) phonon scattering rates, (c) phonon lifetime, and (d) lattice thermal conductivity (κ_L) of BaS.

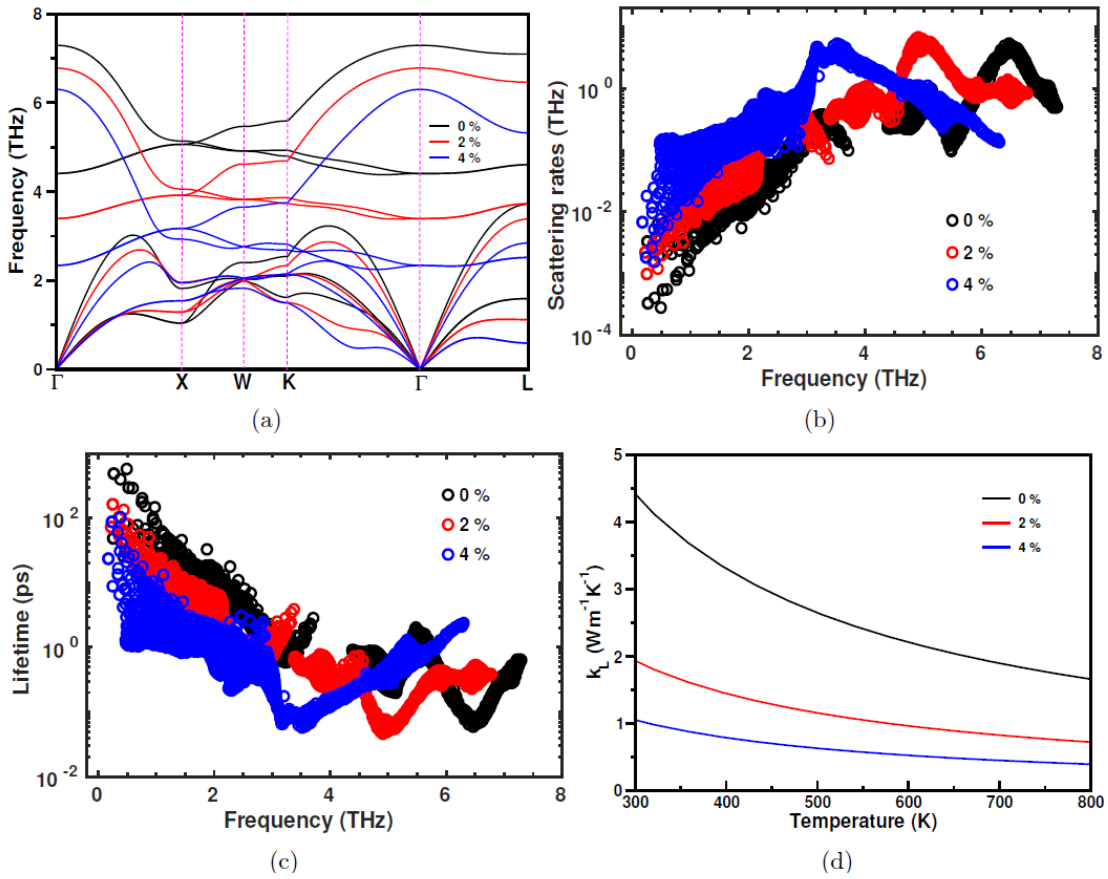

Fig 3.16: Calculated tensile strain dependent (a) phonon dispersion curves, (b) phonon scattering rates, (c) phonon lifetime, and (d) lattice thermal conductivity (κ_L) of MgTe.

3.1.2.4 Elastic constants and mechanical properties

In order to examine the mechanical stability, interatomic bonding strength, and lattice anharmonicity of the compounds under investigation, second-order elastic constants (C_{ij}) were computed. The MCh compounds under investigation (M = Mg, Ca, Sr, and Ba; Ch = O, S, Se, and Te) exhibit a cubic (*Fm3m*) crystal structure. As a result, they possess three distinct elastic constants: longitudinal (C_{11}), transverse (C_{12}), and shear (C_{44}). These constants are determined by symmetry constraints; $C_{11} = C_{22} = C_{33}$, $C_{12} = C_{13} = C_{23}$, $C_{44} = C_{55} = C_{66}$, and $C_{ij} = C_{ji}$. The second-order elastic constants, which have been determined and are presented in Table 3.5, exhibit consistency with the available Brillouin scattering and ultrasonic pulse echo measurements [75]–[77], in addition to previous first-principles calculations[5], [22], [74] ,59−63.

Table 3.5: Calculated second order elastic constants (C_{11}, C_{12}, C_{44}, in GPa) for MCh (M = Mg, Ca, Sr, and Ba and Ch = O, S, Se, and Te) compounds in rock-salt structure type.

	This work			Others		
Compound	**C_{11}**	**C_{12}**	**C_{44}**	**C_{11}**	**C_{12}**	**C_{44}**
MgO	298.03	88.15	143.96	297 [78]	99.6 [78]	151.9 [78]
	-	-	-	296.5 [76]	95.1 [76]	155.9 [76]
	-	-	-	297.9 [79]	95.8 [79]	154.4 [79]
MgS	153.47	39.75	53.58	168.4 [80]	42.2 [80]	55.2 [80]
MgSe	127.78	32.9	42.55	112.66 [62]	33.49 [62]	42.65 [62]
MgTe	100.58	24.88	29.99	94 [74]	24 [74]	29 [74]
CaO	230.72	58.9	77.14	198.8 [16]	57.1 [16]	75.3 [16]
	-	-	-	-	-	81[77]
	-	-	-	220.5 [81]	57.67 [81]	80.03 [81]
CaS	139.88	23.27	34.05	122.1 [16]	23.9 [16]	33.5 [16]
CaSe	119.12	18.97	27.42	104.3 [16]	19.4 [16]	26.6 [16]
CaTe	94.34	13.92	18.7	94.13 [82]	13.76 [82]	17.34 [82]
SrO	186.69	48.25	55.15	159.7 [83]	46.7 [83]	54.3 [83]
SrS	122.77	18.4	26.17	109.7 [83]	19.1 [83]	26.3 [83]
SrSe	106.57	14.63	21.33	93.6 [83]	15.2 [83]	21.1 [83]
SrTe	86.14	10.33	14.75	54.8 [22]	13 [22]	21 [22]
BaO	142.02	44.61	36.04	121.99 [5]	42.12 [5]	36.33 [5]
			-	-	-	34[75]
BaS	104.74	16.6	18.58	91.29 [5]	16.7 [5]	18.74 [5]
BaSe	93.43	12.91	15.53	78.42 [5]	13.14 [5]	15.61 [5]
BaTe	78.04	8.56	11.09	68.36 [5]	9.1 [5]	11.26 [5]

The obtained elastic constants fulfil the Born stability criteria [84], exhibiting that all of these MCh (M = Mg, Ca, Sr, and Ba and Ch = O, S, Se, and Te) compounds are mechanically stable.

$$C_{11} - C_{12} > 0, C_{11} > 0, C_{44} > 0, C_{11} + 2C_{12} > 0 \quad ----3.4$$

Using eq 3.5, the bulk (B) and shear (G) moduli were estimated from the calculated elastic constants using the VoigtReussHill (VRH) approximation. Later, the acquired B and G values are utilised to determine Young's modulus (E). MgO is the stiffest material among the 16 MCh (M = Mg, Ca, Sr, and Ba and Ch = O, S, Se, and Te) compounds because it has the greatest E value.

$$B = \frac{C_{11} + 2C_{12}}{3}$$
$$G = \frac{1}{2}\left[\frac{C_{11} - C_{12} + 3C_{44}}{5} + \frac{5C_{44}(C_{11} - C_{12})}{4C_{44} + 3(C_{11} - C_{12})}\right] \quad ----3.5$$
$$E = \frac{9BG}{3B + G}$$

The observed reduction in the calculated C_{ij} values and E, B, and G moduli (Table 3.6.)from MO to MTe (where M represents Mg, Ca, Sr, and Ba) suggests that weak electrostatic and interatomic interactions occur in the lattice as the atomic size increases, specifically from Mg to Ba and O to Te. As a consequence, materials possessing greater atomic size are susceptible to deformation when subjected to mechanical stress, leading to systems with greater atomic mass exhibiting flexible lattices or low elastic moduli.

$$\nu = \frac{3B - 2G}{2(3B + G)}$$
$$\gamma_\nu = \frac{3}{2}\left(\frac{1 + \nu}{2 - 3\nu}\right) \quad ----3.6$$

The Poisson's ratio (ν) is typically 0.1 and 0.25 for covalent and ionic materials, respectively [83]. The obtained values are in the 0.18-0.28 range, implying a significant ionic contribution to interatomic bonding for these MCh (M = Mg, Ca, Sr, and Ba ; Ch = O, S, Se, and Te) compounds. MgO (0.18) and BaO (0.28), respectively, have the least and biggest values among the 16 MCh (M = Mg, Ca, Sr, and Ba and Ch = O, S, Se, and Te) compounds. Further, the ν values are utilised to computed the Grüneisen parameter (γ_ν). The strength of the lattice anharmonicity of a material is indicated by the Grüneisen parameter (γ_ν), which is commonly determined via phonon.

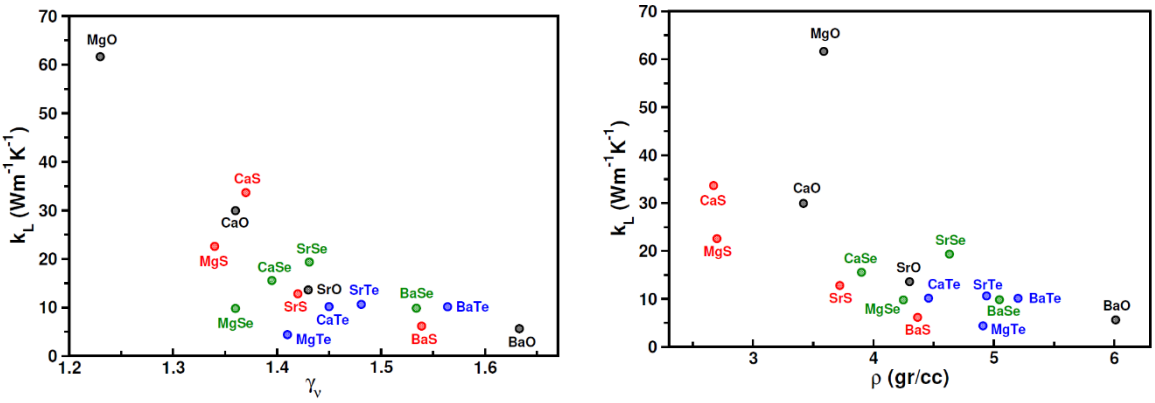

Fig 3.17: Calculated κ_L as a function of (a) Gruneisen parameter (γ_v) and (b) density (ρ) and for 16 MX compounds.

However, computing γ_v includes a sequence of costly phonon computations, which must be repeated for 16 compounds, which is computationally demanding. To prevent this, an efficient procedure was employed to calculate the Poisson's ratio (ν) [85]. The results derived using eq 3.6 for materials with rocksalt structure are in great accord with previous studies [86], [87]. Because the 16 materials under consideration crystallise in the rocksalt structure, eqn. 3.6 was utilized to compute γ_v based on the values of obtained ν . As seen in Figure 3.17, BaO has the highest γ_v, indicating comparatively greater anharmonicity of BaO over the rest of the MCh (M = Mg, Ca, and Sr and Ch = O, S, Se, and Te) compounds, which leads to a low κ_L values.

$$v_{\mathrm{l}} = \sqrt{\frac{B + \frac{4G}{3}}{\rho}}$$

$$v_t = \sqrt{\frac{G}{\rho}} \qquad \text{----3.7}$$

$$v_{\mathrm{m}} = \left[\frac{1}{3}\left(\frac{1}{v_{\mathrm{l}}^3}\right) + \left(\frac{2}{v_{\mathrm{t}}^3}\right)\right]^{-1/3}$$

$$\Theta_{\mathrm{D}} = \frac{h}{k_{\mathrm{B}}}\left[\left(\frac{3N}{4\pi V}\right)\right]^{1/3} v_{\mathrm{m}}$$

Then the sound velocities (v_l, v_t, v_m,) and the Debye temperature (Θ_D) were calculated using the relationships as provided in eq 3.7. Here, ρ, h, k_B, N, and V are the crystal density, Planck constant, Boltzmann constant, and number of atoms and volume of unit cell. The calculated v_l, v_t, v_m, and Θ_D values decrease from MO to MTe (M = Mg, Ca,

Sr, and Ba). Figure 3.18 and Figure 3.19 show the variation of κ_L as a function of Debye temperature (Θ_D) and average (v_m), longitudinal (v_l), and transverse (v_t) sound velocities for the 16 MCh (M = Mg, Ca, Sr, and Ba and Ch = O, S, Se, and Te) compounds. The similar trend can be seen for all four properties, v_l, v_t, v_m, and Θ_D. According to the Slack hypothesis, low Θ_D values in materials indicate low κ_L values. In reality, the presence of LLO phonons softens the acoustic phonon modes, resulting in low group velocities and frequencies for acoustic phonons and hence low Θ_D. In contrast to other MTe (M = Ca, Sr, Ba), BaSe, and SrSe compounds, BaO, BaS, and MgTe exhibit low κ_L values despite possessing higher v_l, v_t, v_m, and Θ_D. Furthermore, estimated phonon group velocities for BaCh (Ch = O, S, and Se) compounds (see Figure 3.20) follow the atomic mass trend, which is in line with sound velocities. Overall, the results of the present study strongly suggest that high mass contrast and phonon lifetimes are the dominant factors that are responsible for the observed anomalous trends in MCh (M = Mg, Ca, Sr, and Ba and Ch = O, S, Se, and Te) compounds.

Table 3.6: Calculated Young's modulus (E, in GPa), Bulk modulus (B, in GPa), Shear modulus (G, in GPa), density (ρ, in gr/cc), sound velocities (v_l, v_t and v_m, in km/s), Debye temperature (Θ_D, in K), Poisson's ratio (σ) and Gruneisen parameter (γ_ν) for MCh compounds.

Compound	**E**	**B**	**G**	**ρ**	**v_l**	**v_t**	**V_m**	**Θ_D**	**σ**	**γ_ν**
MgO	300.23	158.11	126.84	3.59	9.55	5.95	6.55	927.14	0.18	1.23
Others [78]	305	165.5	127.9	3.0	9.83	6.12	6.74	902	0.252	-
MgS	133.23	77.66	54.87	2.7	7.47	4.51	4.98	573.55	0.21	1.24
Others [42]	-	73.1	-	-	-	-	-	-	-	-
Others [88]	-	79.44	-	-	-	-	-	-	-	-
Others [50]	-	72.3	-	-	-	-	-	-	-	-
MgSe	108.43	64.52	44.44	4.25	5.4	3.23	3.58	391.45	0.22	1.36
Others	113.1 [24]	60.2 [42]	46.3 [24]	-	-	-	-	-	0.222 [24]	-
Others	109.2 [62]	67.7 [24]	45.7 [62]	-	-	-	-	-	-	-
	-	65.15 [88]	-	-	-	-	-	-	--	-

MgTe	81.03	50.11	32.92	4.91	4.38	2.59	2.87	289.54	0.23	1.41
Others [74]	77	-	31	-	4.42	2.24	-	251	0.33	-
	-	50.45 [88]	-	-	-	-	-	-	-	-
	-	44.6 [50]	-	-	-	-	-	-	-	-
CaO	196.26	116.17	80.54	3.42	8.09	4.85	5.37	669.61	0.22	1.36
Others	178.5 [16]	104.32 [16]	73.47 [16]	3.2 [78]	8.39 [78]	5.08 [78]	5.61 [78]	691 [78]	0.21	-
	205.6 [78]	118.8 [78]	84.88 [78]	-	-	-	-	-	0.22 [78]	-
CaS	103.43	62.14	42.3	2.67	6.66	3.98	4.4	465.12	0.22	1.37
Others [16]	95.27	56.62	39.06	-	-	-	-	-	0.22	-
	-	62.90 [82]	-	-	-	-	-	-	-	-
	-	64 [39]	-	-	-	-	-	-	-	-
CaSe	85.82	52.35	34.98	3.9	5.04	2.99	3.32	336.21	0.23	1.39
Others [16]	78.69	47.70	32.12	-	-	-	-	-	0.23	-
	-	52.17 [82]	-	-	-	-	-	-	-	-
	-	51 [82]	-	-	-	-	-	-	-	-
CaTe	63.39	40.73	25.55	4.46	4.1	2.4	2.65	251.08	0.24	1.45
Others [74]	6	-	25g	-	4.24	1.99	-	209	-	-
	-	40.45 [82]	-	-	-	-	-	-	-	-
	-	41.8 [82]	-	-	-	-	-	-	-	-
SrO	149.36	94.4	60.41	4.3	6.38	3.75	4.15	481.98	0.24	1.43
Others [83]	135.8	82.4	55.13	-	-	-	-	-	0.23	-
Others [78]	139	87.6	56.28	4.9	5.74	3.38	3.75	430	0.22	-
SrS	85.36	53.19	34.63	3.72	5.17	3.05	3.38	336.8	0.23	1.42
Others [83]	80.48	47.3	32.77	-	-	-	-	-	0.23	-

SrSe	72.04	45.28	29.17	4.63	4.26	2.51	2.78	266.98	0.23	1.43
Others [83]	66.80	40.3	27.14	-	-	-	-	-	0.23	-
SrTe	54.24	35.6	21.77	4.94	3.62	2.1	2.33	209.78	0.25	1.48
Others [89]	64.77	22.12	23.54	-	-	-	-	119.4	0.019	
Others [74]		-	-	-	3.996	1.714	-	172	0.39	-
BaO	103.75	77.08	40.66	6.01	4.67	2.6	2.9	311.79	0.28	1.63
Others [78]	106.2	76.3	41.88	5.7	4.76	2.67	2.97	316	0.255	-
BaS	66.63	45.98	26.47	4.37	4.31	2.46	2.74	256.14	0.26	1.54
Others	88.24 [5]	41.6 [21]	24.935 [21]	-	4.2 [90]	-	2.67 [21]	247.26 [21]	0.18 [5]	-
	-	-	-	-	-	2.37 [90]	2.64 [90]	247 [90]	0.25 [21]	-
BaSe	57.85	39.75	23	5.05	3.73	2.13	2.38	214.81	0.26	1.53
Others	76.21 [5]	34.0 [91]	21.41 [21]	-	3.64 [90]	2.07 [90]	2.3 [21]	205.7 [21]	0.25 [21]	-
	-	36.26 [21]	-	-	-	-	2.31 [90]	208 [90]	0.252 [92]	-
BaTe	45.17	31.72	17.89	5.2	3.27	1.85	2.06	176.28	0.26	1.56
Others	67.15 [5]	27.04 [91]	16.697 [21]	-	3.68 [74]	1.46 [74]	1.99 [21]	171.22 [21]	0.25 [21]	-
	-	28.23 [21]	-	-	-	-	-	139 [74]	0.27 [92]	-

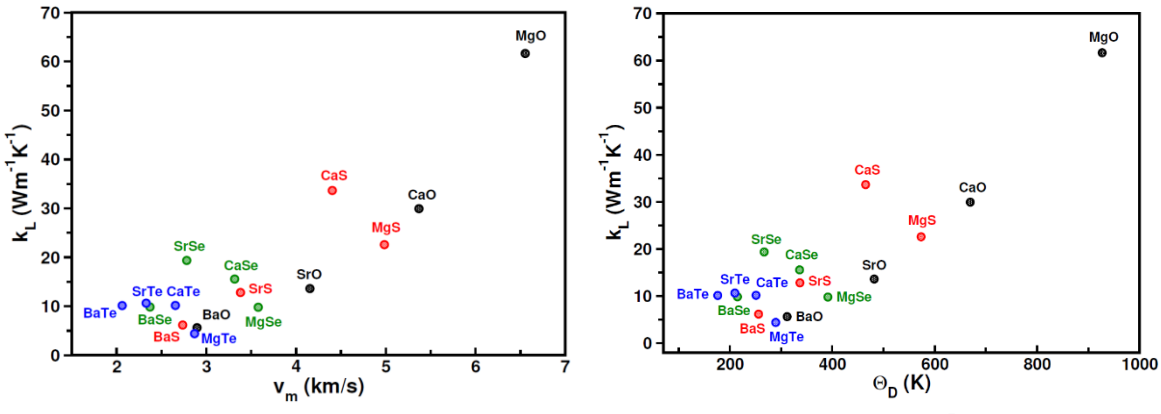

(a) **(b)**

Fig 3.18: Calculated κ_L as a function of (a) average (v_m) sound velocity, (b) Debye temperature (Θ_D) for 16 MCh compounds.

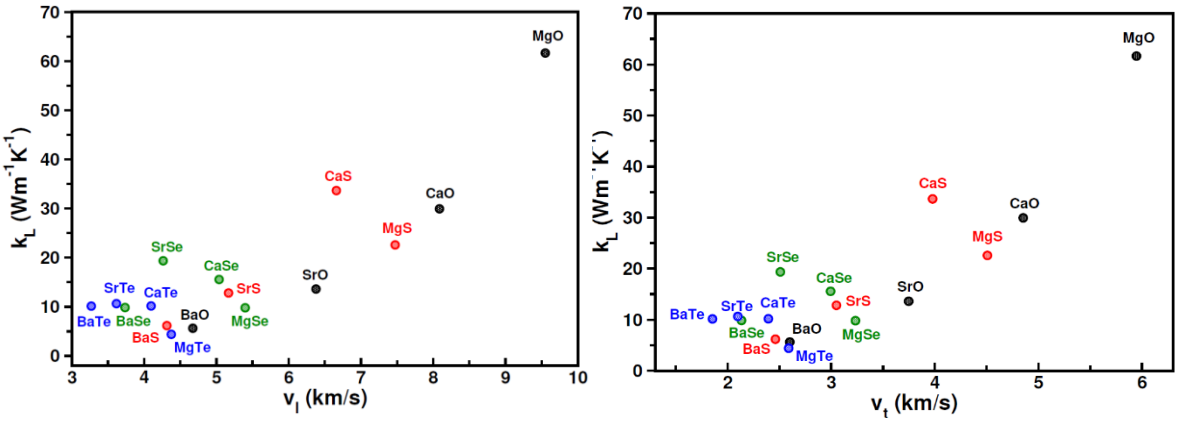

(a) **(b)**

Fig 3.19: Calculated κ_L as a function of (a) longitudinal (v_l) (b) transverse (v_t) sound velocities for 16 MCh compounds.

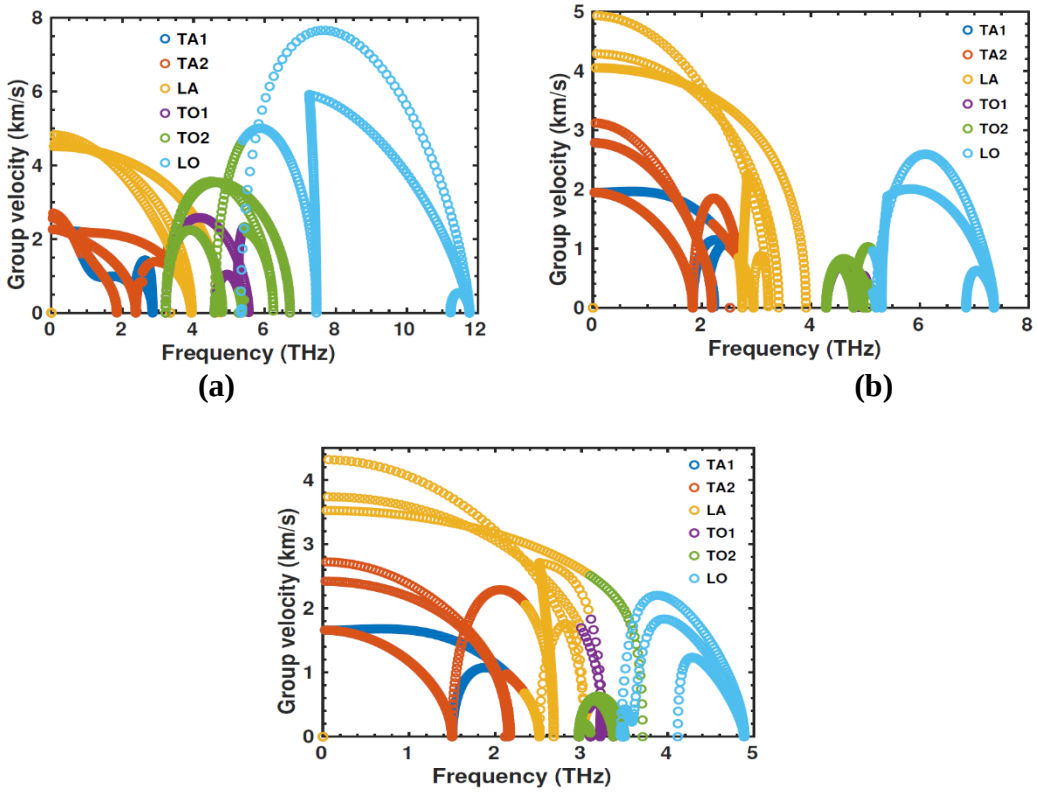

(a) **(b)**

(c)

Fig 3.20: Calculated phonon group velocities of (a) BaO, (b) BaS, (c) BaSe compounds as a function of frequency.

In summary, the lattice dynamics, phonon transport, and mechanical characteristics of 16 binary compounds with rocksalt-type structures were systematically examined. Anomalous trends in κ_L were predicted for the CaCh series of compounds (CaS > CaO > CaSe > CaTe), SrCh series (SrSe > SrO > SrS > SrTe),

and BaCh series (BaTe > BaSe > BaS > BaO) compounds. Specifically, an inverse trend for κ_L in the BaCh series (Ch= O, S, Se, and Te) was noted, which contradicts the trend predicted by their atomic masses. Due to the sensitivity of κ_L to the experimental lattice constant, the aforementioned trends are marginally modified for SrCh (Ch = O, S, and Se) and BaCh (Ch = O, S, Se, and Te) compounds when κ_L is calculated at the experimental lattice constant. A few conclusions regarding the design of (ultra)low κ_L materials are derived from this research: (1) Design a material comprising a blend of light and heavy elements to generate a substantial mass contrast, thereby establishing an acoustic-optic phonon gap; (2) phonon softening of transverse acoustic (TA) modes attributable to the heavy atomic mass element; (3) constituent elements within a substance with a substantial electronegativity difference induce a substantial LO-TO splitting, which results in LLO (TO) phonon modes, some of which may fall into the acoustic mode region; and these are accountable for the phonon softening of a of acoustic phonon modes or enhancing the overlap between the LLO and longitudinal acoustic (LA) phonon modes, thereby increasing scattering rates thus resulting in shorter phonon lifetimes; and (4) selection of a material with a relatively high density (ρ). In BaO, BaS, and MgTe, κ_L is decreased further by tensile strain via phonon softening, which increases scattering rates and consequently shortens phonon lifetimes. In short, the present study offers valuable insights into phonon engineering in simple crystal systems to produce (ultra)low κ_L materials, this is crucial in the advancement of sustainable energy conversion devices intended for future energy applications.

3.2. Alkali Halides, MX (M = Li, Na, K, Rb, Cs and X = F, Cl, Br, I):

Now, in this section, another set of isostructural binary systems, Alkali Halides (AH's), consisting of MX (M = Li, Na, K, Rb, Cs and X = F, Cl, Br, I) compounds are considered and are presented in comparison with the results obtained with AEC's.

The Keye's rule [93] and the Slack theory [73] both state that the lattice thermal conductivity (κ_L) has an inverse relationship to the average atomic mass. In contrast, it is observed that certain materials within a particular series exhibit greater κ_L values than expected trend inspite of their high average atomic mass. This phenomenon is known as anomalous behaviour of κ_L or anomalous phonon transport. Although alkali halides (AHs) and alkaline-earth chalcogenides (AECs) generally have high average

atomic masses, it is seen that RbBr has a greater κ_L value compared to RbCl. Similarly, CsI demonstrates a larger κ_L value when compared to CsCl and CsBr [94].In the same way, it can be observed that CaS exhibits a larger κ_L value in comparison to CaO [25], [95]. Furthermore, SrSe demonstrates a higher κ_L value when compared to both SrO and SrS. In the context of systems with a high average atomic mass, BaTe exhibits a higher κ_L value in contrast to systems with lesser atomic masses, namely BaO, BaS, and BaSe, within the BaCh (Ch = O, S, Se, and Te) series. Additionally, ternary chalcopyrite systems, namely $TlBiCh_2$ (with $TlBiS_2 < TlBiSe_2 > TlBiTe_2$) [96] and $CuAlCh_2$ (with $CuAlS_2 < CuAlSe_2 > CuAlTe_2$) [97] exhibit anomalous trends in lattice thermal conductivity (κ_L). Further, certain mixed-anion compounds, namely Ba_4Sb_2Se, $Ba_4Sb_2Te_4$ [98], as well as transition metal dichalcogenides MoSSe and WSSe [99], demonstrate the anomalous tendency in κ_L within their respective series. This trend has also been detected in the lattice thermal conductivity measurements of several other materials [97] [100]–[103]. Lindsay et al conducted a comprehensive investigation on the anomalous behaviour observed in BAs, BSb, BeSe, and BeTe when subjected to high pressure [104]. Their findings indicate that the anomalous pressure dependence of κ_L originates mainly from unique intrinsic scattering mechanisms affecting acoustic phonons responsible for heat conduction in compounds with significant mass ratios, as opposed to those with smaller mass ratios. This work demonstrates that in addition to mass ratio, the influence of chemical bonding and crystal symmetry on determining κ_L is significant. For instance, the monolayer (ML) BeO [105] has a greater thermal conductivity (κ_L) compared to ML-MgO and ML-CaO. This disparity may be attributed to the presence of strong covalent bonding in BeO. Additionally, zincblend-MgTe[24] shows a higher κ_L value than rocksalt-MgTe5 [24] owing to its distinct bonding characteristics. However, further comprehensive research is required to examine the interplay between mass ratio and chemical bonding. The above-mentioned studies [95], [104], [105] [105] [104]raise many fundamental questions: (1) does atomic mass alone play a key role in determining the magnitude of κ_L? (2) what are the dominant factors (group velocities and/or phonon lifetimes) that determine the low or high κ_L behavior and what is the role of optical phonon modes in phonon transport in small or large mass ratio compounds? (3) is interplay between atomic mass and anharmonicity well understood? and (4) is four-phonon scattering important for small mass ratio systems? The current work focusses on addressing the

first two issues: comprehending the microscopic origins of abnormal trends in κ_L for AHs and AECs, the role of optical phonons in κ_L, and the dominating factors that significantly impact κ_L.

3.2.1 Computational Details

The present study employed the Vienna Ab-initio Simulation Package (VASP) [28] to conduct first-principles calculations. The PBEsol functional was employed to account for electron-electron interactions, while the pseudopotential-based projector-augmented wave (PAW) technique was utilized to account for electron-ion interactions. The applied parameters for the plane wave basis set expansion include a plane wave cutoff energy of 520 eV and a spacing of $2\pi \times 0.024$ A^{-1} for the kmesh in the irreducible Brillouin zone. The initial step involves obtaining crystal structures of various alkali halides (LiF, LiCl, LiBr, LiI, NaF, NaCl, NaBr, NaI, KF, KCl, KBr, KI, RF, RbCl, RbBr, RbI, and CsF) in the rocksalt NaCl-type, CsCl-type (CsCl, CsBr, and CsI), and alkaline-earth chalcogenides (MgO, MgS, MgSe, MgTe, CaO, CaS, CaSe, CaTe, SrO, SrS, SrSe, SrSe, BaO, BaS, BaSe, BaSe, and BaTe) from X-ray diffraction data. These crystal structures are then subjected to full structural optimization at a temperature of 0 K.

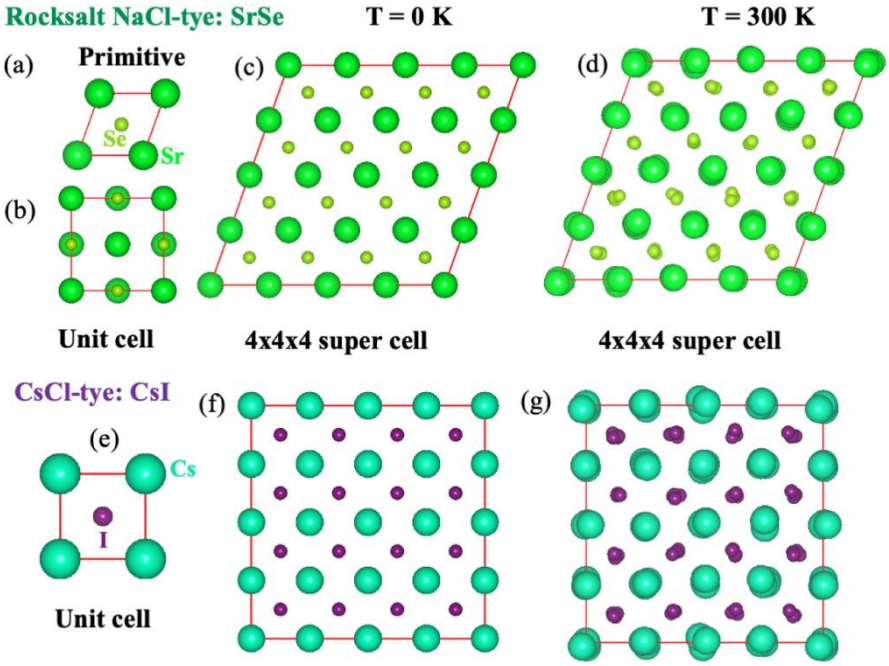

Fig 3.21: Representative crystal structures of (a–d) rocksalt NaCltype SrSe (a) primitive cell, (b) unit cell, 4 × 4 × 4 super cell (128 atoms) at (c) *T* = 0 and (d) 300 K, and (e–g) CsCl-type CsI (e) primitive/unit cell, 4 × 4 × 4 super cell (128 atoms) at (f) *T* = 0 and (g) 300 K.

Figure 3.21 shows the optimised primitive, unit cell, and supercell structures of SrSe with a NaCl-type crystal structure and CsI with a CsCl-type crystal structure. These structures are indicative of the investigated compounds in the current work. Subsequently, ab initio molecular dynamics (AIMD) simulations were performed at a temperature of 300 K, utilising the VASP software, to investigate the ground state structures acquired at T = 0 K. The molecular dynamics (MD) simulations in the canonical ensemble (NVT) were conducted for a total of 5000 MD steps. The time-step used in the simulations was 1 fs, resulting in a simulation duration of 5 ps. The supercell size employed was 4 × 4 × 4, corresponding to a total of 128 atoms. The simulations were performed using a Γ-centered kmesh.

The temperature was regulated using a Nosé−Hoover thermostat [32], [33]. The TDEP (temperature-dependent effective potential) method [29], [106], has been employed for postprocessing purposes. This method enables the extraction of both harmonic (2^{nd} order) and anharmonic (3^{rd} order) interatomic force constants (IFCs). To achieve this, forces obtained from AIMD (ab initio molecular dynamics) simulations conducted with VASP are utilised. Subsequently, lattice dynamical and lattice thermal conductivity calculations are performed at finite temperature using the TDEP code. The lattice thermal conductivity is determined using an iterative solution of the complete Boltzmann transport equation (BTE) using a q-mesh of dimensions 25 × 25 × 25. In the computation of lattice dynamics and phonon transport properties, all permissible interactions inside the supercell were included for second and third order interatomic force constants (IFCs). The detailed methodology can be found in previous studies [95], [107]. In order to conduct a more comprehensive examination of the impact of mass ratio on lattice dynamics and κ_L, an additional calculation was performed to determine the cophonicity. As described in previous studies, [108], [109], this metric provides a quantitative measure of the degree of overlap between the phonon density of states for a specific atomic pair throughout a certain range of phonon energy. To investigate the role of atomic mass and its contribution to both acoustic and optical phonons, cophonicity is determined throughout the whole frequency range for each compound under consideration. Only the absolute value of cophonicity (|Cph|(A-B)) is taken into account.

3.2.2 Results and discussion

3.2.2.1 Role of Mass Contrast on Lattice Dynamics and Thermal Conductivity

To gain a more comprehensive understanding of the phonon transport properties of crystalline solids, a thorough investigation of the lattice dynamics is required. In this work, simple binary systems, AHs and AECs, have been considered for a case study, these crystallize in the face centred cubic (FCC) or NaCl-type structure, with the exception of CsX (X = Cl, Br, and I), which crystallize in the body centred cubic (BCC) structure and exhibit anomalous κ_L behavior [95] [94], [95]. The phonon dispersion curves along high symmetry directions at room temperature for the following series of compounds: LiX, NaX, RbX, CsX (where X represents F, Cl, Br, and I), MSe, MTe, SrCh, and BaCh (where M represents Mg, Ca, Sr, Ba, and Ch represents O, S, Se, and Te), and MO and MS (where M represents Mg and Ca), are presented in Figures 3.22 and 3.23. The colour bar additionally illustrates the atomic contribution to phonon vibration through the projection of eigen displacements. Each of the compounds examined above is composed of two elements per primitive cell (Z = 1), and their phonon dispersion curves illustrate a total of six vibrational modes. Three of the six phonon modes are acoustic, while the other three are optical. The absence of imaginary frequencies suggests that the compounds under investigation are dynamically stable at 300 K. The phonon band profiles exhibit a similarity mostly attributed to the same number of atoms within each primitive cell, with the exception of a distinct distinction between acoustic and optical phonons, commonly referred to as a phonon band gap or a−o band gap. The disparity in atomic mass between alkali/alkaline-earth metals and halogen or chalcogen nonmetals plays a crucial role in determining the a−o gap. This phenomenon is only observable in materials that exhibit a substantial contrast in atomic mass, as indicated in Table 3.7. Examples of such materials include MgSe, MgTe, RbCl, CaTe, BaS, KI, SrO, SrS, LiBr, BaS, LiI, NaBr, NaI, CsF, and RbF, as illustrated in Figures 3.22 and 3.23.

In addition, as the atomic mass of both metal and nonmetal atoms increases, the acoustic and optical phonon frequencies show a red shift for these compounds. The longitudinal optical-transverse optical (LO-TO) splitting strength is significant in metal halides and oxides, but it decreases as metal and nonmetal atom sizes increase because the difference in electronegativity of the constituent elements decreases (Figures 3.22 and 3.23) [95] [94], [95].

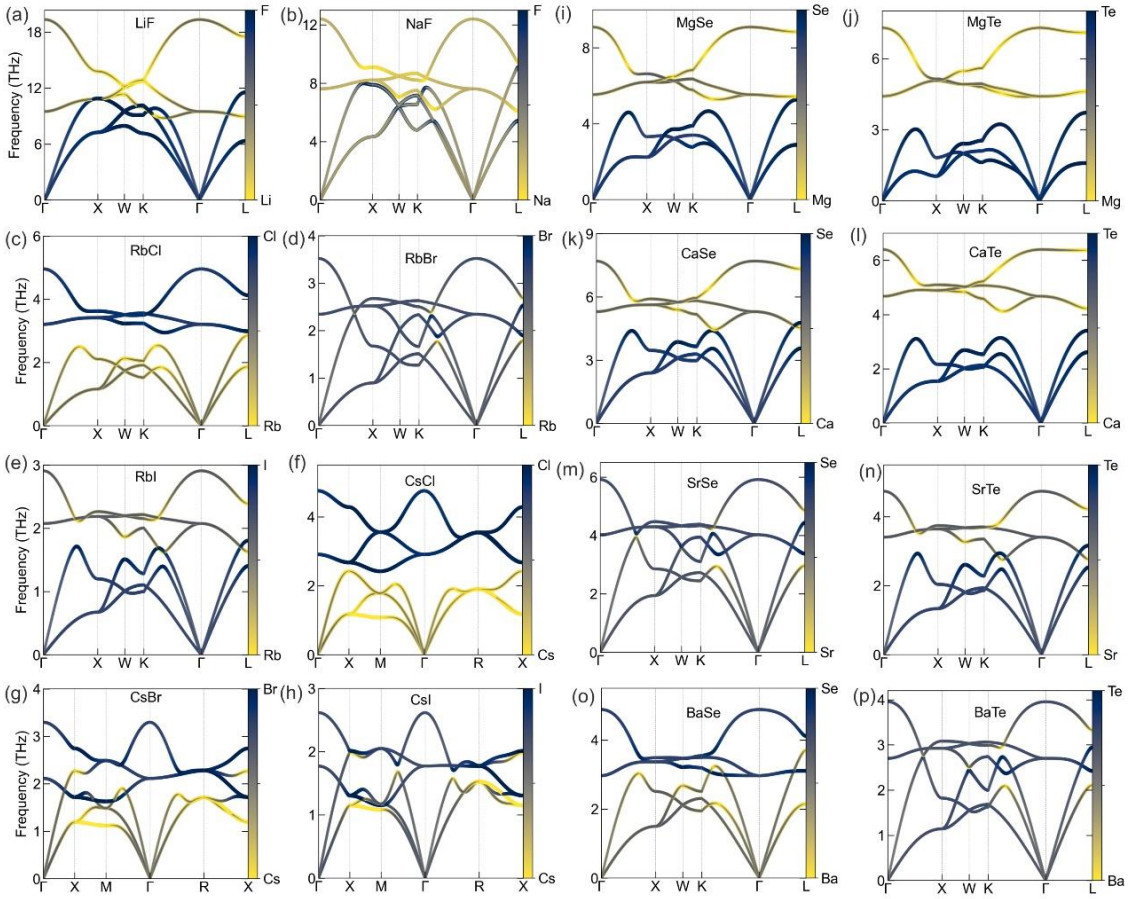

Fig 3.22: Phonon dispersion curves of selected alkali halides (a) LiF, (b) NaF, (c−e) RbX, and (f−h) CsX (where X = Cl, Br, and I) at 300 K. (i−p) Phonon dispersion curves of MSe and MTe (M = Mg, Ca, Sr, and Ba) at 300 K.

In specific, materials with a mass ratio close to unity exhibit a significant overlap in phonon bands between acoustic and optical modes. This is in contrast to systems with a significant contrast in mass, as seen in Figure 3.22. The substantial overlap in the low-lying optical phonon modes greatly enhances the value of κ_L for NaF, KCl, CsI, SrSe, and BaTe in their respective series.

In order to get an in-depth understanding of the significance of mass contrast, the variation of κ_L as a function of mass ratio for AHs and AECs is provided in Figure 3.24a and 3.24b, correspondingly. The data pertaining to alkali halides in Figure 3.24a have been obtained by TDEP calculations carried out in the present study, whilst the data concerning AECs in Figure 3.24b was compiled from previous section. Figure 3.24a includes the prior results of Cheng et al. [94] for AHs, allowing for a comprehensive comparison.

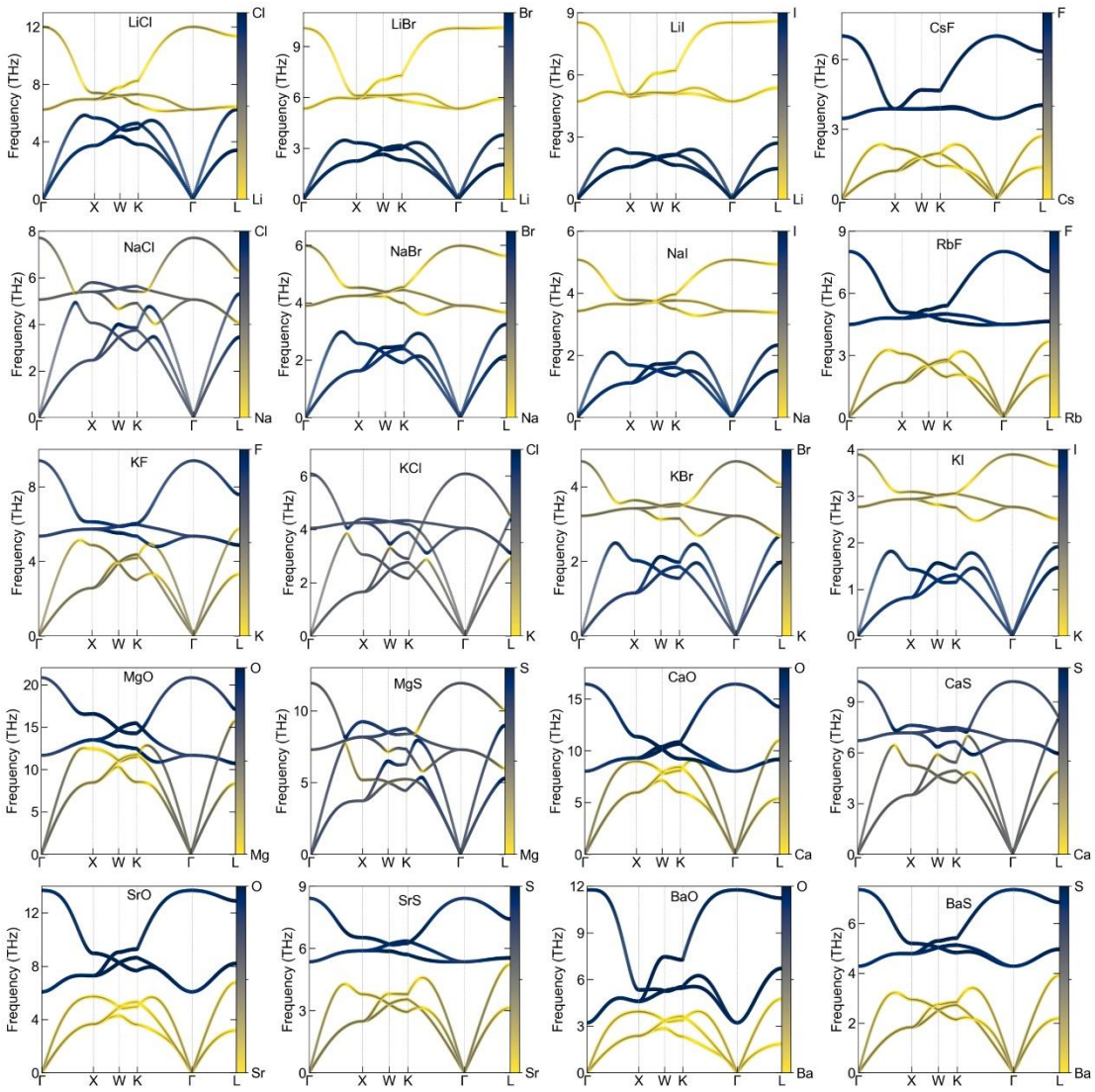

Fig 3.23: Phonon dispersion curves of selected AHs and AECs at 300 K. Mass contrast leads to acoustic-optical phonon gap.

Table 3.7: Calculated Lattice Constant (*a*, in Å), Average Atomic Mass (M_{avg}, in amu), Average Sound Velocity (v_m, in km/s), Debye Temperature (Θ_D, in K), Grüneisen Parameter (γ_v), Specific Heat (C_v, in J/mol K), Mass Ratio, Absolute Value of Cophonicity (|*C*ph|, in THz), and Lattice Thermal Conductivity (κ_L, in W/m K) for Alkali Halides.

Compound	**a**	**M_{avg}**	**v_m**	**Θ_D**	**γ_v**	**C_v**	**mass ratio**	**|Cph|**	**κ_L**
LiF	4.003	12.96	5.05	751.3	1.32	40.27	2.74	3.44	24.2
LiCl	5.061	21.19	3.69	435.2	1.38	45.88	5.11	3.11	6.13

LiBr	5.409	43.42	2.55	250.58	1.39	47.13	11.51	4.06	4.23
LiI	5.902	66.92	2.07	209.13	1.39	47.89	18.28	3.94	3.75
NaF	4.546	20.99	3.92	513.68	1.39	44.89	1.21	0.73	41.25
NaCl	5.557	29.22	2.98	320	1.495	47.81	1.54	0.55	11.1
NaBr	5.892	51.44	2.17	219	1.54	48.61	3.47	1.68	4.42
NaI	6.377	74.95	1.75	163.3	1.595	48.98	5.52	1.94	2.7
KF	5.309	29.04	3.04	340.77	1.595	47.33	2.06	1.46	9.25
KCl	6.249	37.27	2.49	237.17	1.606	48.62	1.1	0.14	10.38
KBr	6.557	59.5	1.9	173.1	1.62	49.1	2.04	0.98	3.49
KI	7.014	83	1.54	130.9	1.683	49.32	3.24	1.27	2.62
RbF	5.599	52.23	2.21	235.67	1.69	48.12	4.5	2.56	4.17
RbCl	6.546	50.46	1.92	174.75	1.67	49.06	2.41	1.15	3.22
RbBr	6.851	82.68	1.59	138.58	1.68	49.434	1.07	0.01	5.2
RbI	7.299	106.19	1.34	109.83	1.74	49.57	1.48	0.36	2.44
CsF	5.949	75.95	1.75	175.12	1.85	48.66	6.99	2.56	2.48
CsCl	4.072	84.18	1.82	168.3	1.52	49.17	3.75	1.56	1.5
CsBr	4.247	106.4	1.59	141	1.49	49.51	1.66	0.5	1.46
CsI	4.512	129.9	1.44	119.6	1.47	49.64	1.05	0.13	2.35

The κ_L values obtained using TDEP exhibit a high degree of similarity to those reported in prior research, with the exception of LiF and NaF, as seen in Figure 3.24a [94][110]. In order to understand the potential factors contributing to the observed

deviation in κ_L, ab initio molecular dynamics (AIMD) simulations were performed for an extended duration of 10 picoseconds (ps). The thermal conductivity (κ_L) value acquired from these simulations, utilizing the temperature-dependent effective potential (TDEP) method at 300 Kelvin, was determined to be 42.93 (W/m K). Notably, this value nearly coincides with the κ_L value of 41.25 W/m K obtained using a 5 ps simulation with TDEP.

In order to provide additional confirmation, the computed κ_L value (34.50 W/m K) for NaF was compared with the one obtained using ShengBTE [111]at the same lattice constant. The κ_L values obtained exhibit a greater magnitude compared to those obtained through the (ShengBTE).

The validity of the result is pending, awaiting further measurements of lattice thermal conductivity on single crystals of pure NaF and LiF. Binary systems that have a mass ratio near to unity have a relatively high κ_L. Examples of such systems are NaF, NaCl, KCl, MgO, and CaS. Additionally, these systems may exhibit anomalous behaviour in their series of MCh compounds, where M represents Mg, Ca, Sr, and Ba, and Ch represents O, S, Se, and Te. Furthermore, the compounds RbX and CsX, where X represents Cl, Br, and I, also display similar anomalous behaviour.

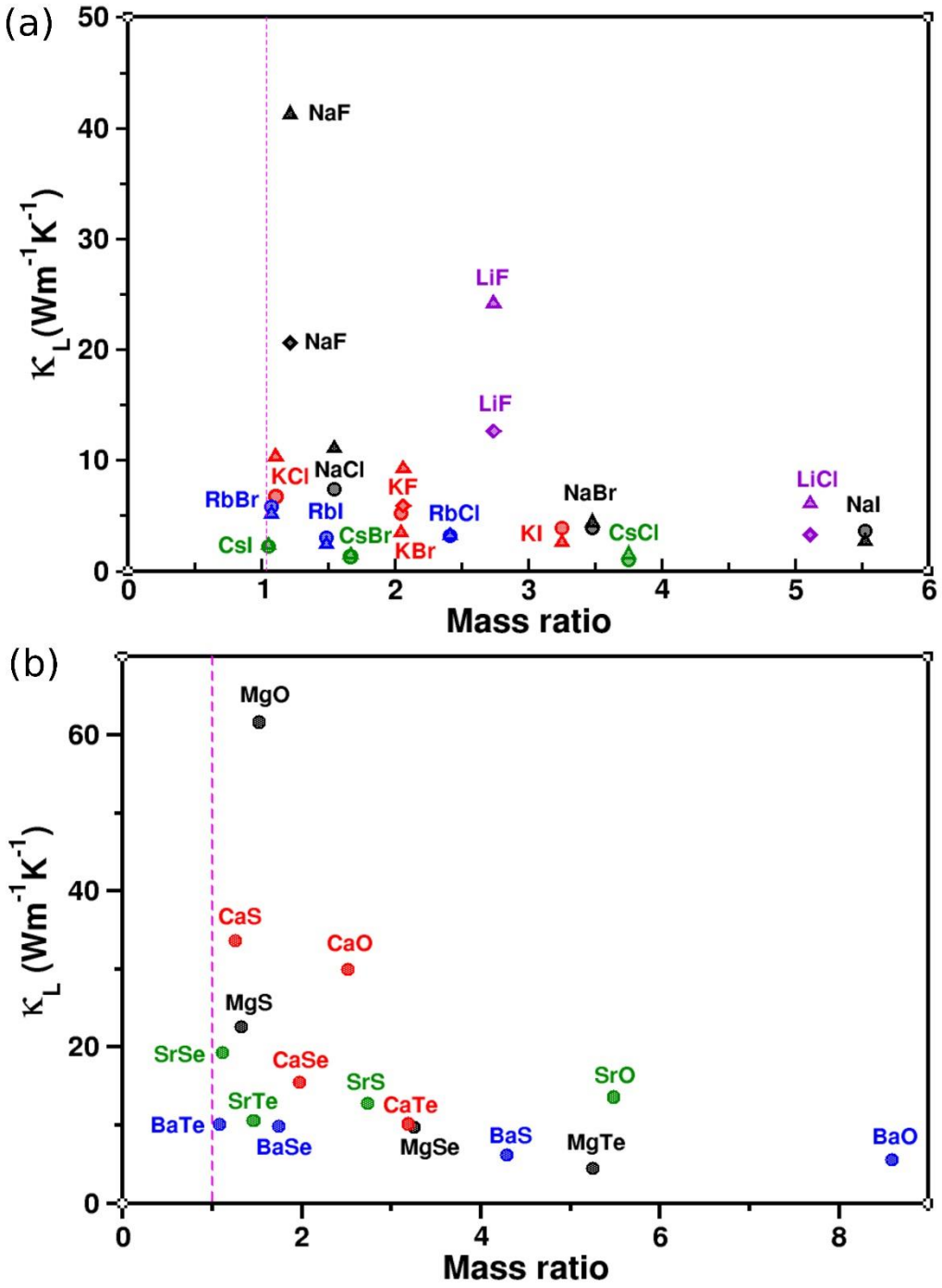

Fig 3.24: (a,b) Lattice thermal conductivity as a function of atomic mass ratio for alkali halides and alkaline-earth chalcogenides. The lattice thermal conductivity values are taken from the present work and previous literature.[94] [95]In panel (a) △ refer to values obtained from the present work, ○ refer to values considered from [94], and ◊ refers to values taken from [110].

To gain insight into the anomalous trends, the calculated spectral and cumulative L of LiF, NaF, RbX, and CsX (X = Cl, Br, and I), MSe, MTe, SrCh, and BaCh (M = Mg, Ca, Sr, and Ba and Ch = O, S, Se, and Te) compounds have been plotted, as shown in Figures 3.25a-c and 3.26a-d.

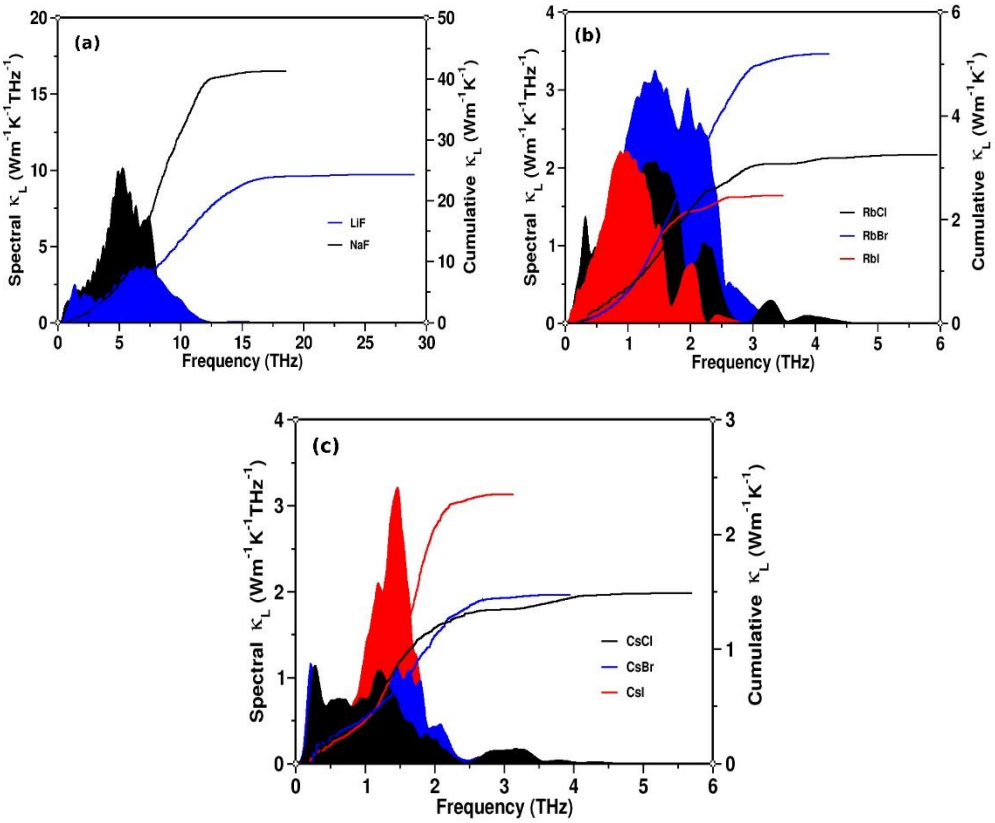

Fig 3.25: (a−c) Calculated spectral and cumulative lattice thermal conductivity of LiF,NaF, RbX, and CsX (X = Cl, Br, and I) compounds as a function of frequency.

Although they possess a greater average atomic mass, they have a greater κ_L value, as seen in Table 3.7. In the instances of AHs [94] [94], [110][112], it is evident that despite the much greater average atomic mass of NaF in comparison to LiF, NaF exhibits a considerably higher κ_L [110] over LiF [112]. This may be attributed to the mass ratio of NaF being near to unity (1.21) as depicted in Figures 3.24a and 3.25a. In the same way, the mass ratio is nearly equal to one for KCl (1.10), RbBr (1.07), and CsI (1.05). These compounds exhibit greater κ_L values in the KX (X = F, Cl, Br, and I), RbX [94], and CsX (X = Cl, Br, and I) [94] series. This information is depicted in Figure 3.25b and 3.25c for RbX and CsX, respectively. Similiarly, CaS exhibits a greater average atomic mass compared to both CaO and MgS.

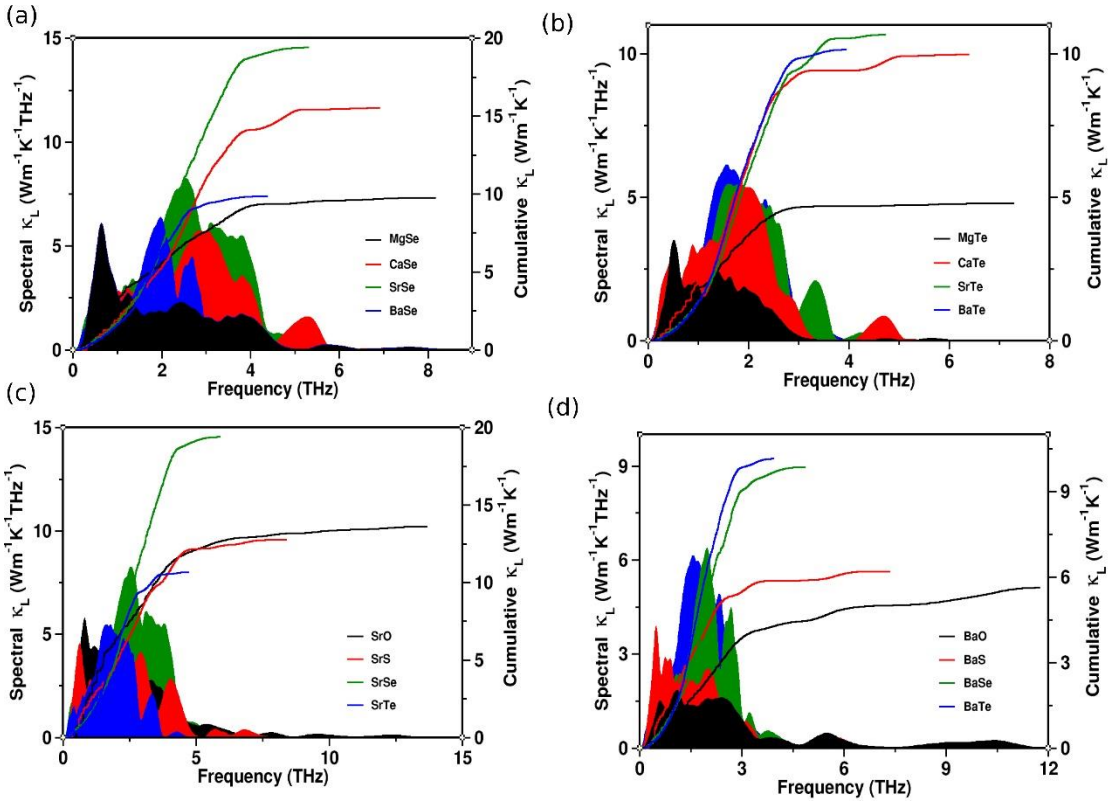

Fig 3.26: (a−d) Calculated spectral and cumulative lattice thermal conductivity of MSe, MTe, SrCh, and BaCh (M = Mg, Ca, Sr, and Ba; Ch = O, S, Se, and Te) series of compounds as a function of frequency.

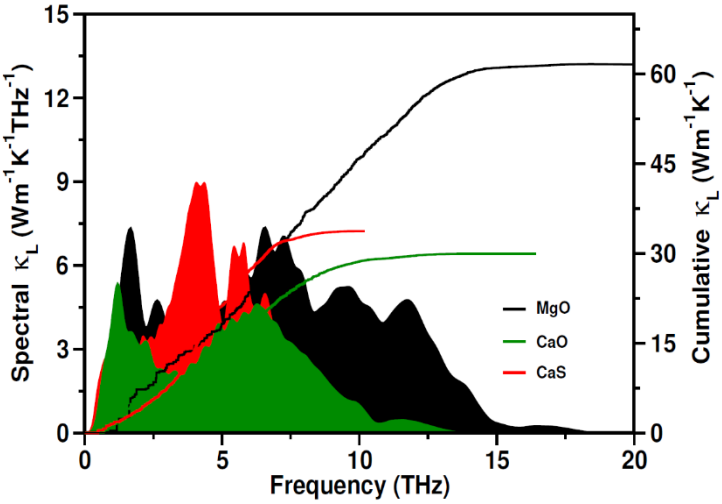

Fig 3.27: Spectral and cumulative lattice thermal conductivity of MgO, CaO, and CaS as a function of frequency.

However, it is worth noting that CaS also has a larger κ_L value in comparison to CaO (as depicted in Figure 3.27) and MgS (as depicted in Figure 3.28). The optical phonons associated with MgO and CaS exhibit a notable contribution to the thermal

conductivity (κ_L) when compared to CaO and MgS, as demonstrated by Figures 3.26 and 3.28.

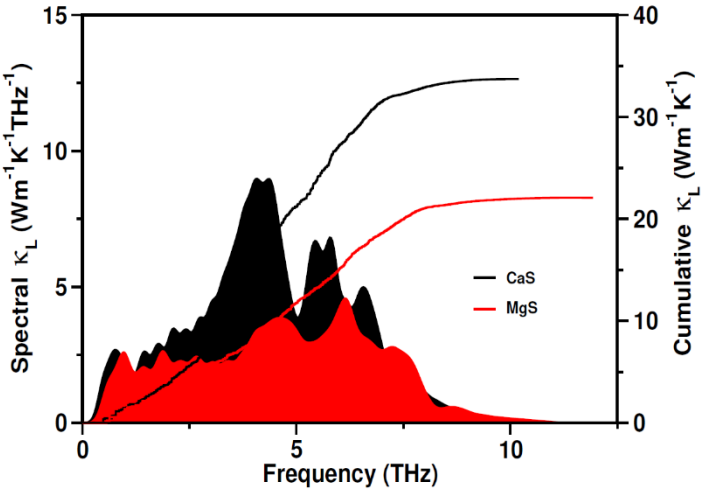

Fig 3.28: Spectral and cumulative lattice thermal conductivity of CaS and MgS as a function of frequency.

While the dispersion of optical phonons in MgS and CaO is significant, their impact on the thermal conductivity (κ_L) is comparatively minimal when compared to the contribution of optical phonons to κ_L in CaS. The mass ratio of CaS is almost equal to unity, compared to the mass ratios of CaO (2.51) and MgS (1.32). SrSe and CaSe exhibit larger κ_L values compared to BaSe, whereas MgSe has a lower κ_L value in comparison to MSe (where M represents Ca, Sr, and Ba). Among the compounds MgSe, CaSe, SrSe, and BaSe, it is seen that the mass ratio of SrSe (1.11) is about equal to unity. Notably, in SrSe, the optical phonons play a substantial role in determining the thermal conductivity κ_L, as depicted in Figure 3.24b. Hence, it can be shown from Figure 3.26c that SrSe exhibits a greater thermal conductivity (κ_L) compared to SrO and SrS, despite the fact that these materials possess highly dispersive optical phonon bands. The whole BaCh (Ch = O, S, Se, and Te) series exhibits an anomalous behaviour, as seen in Figure 3.26d. This trend can be attributed to the significant influence of optical phonons on the thermal conductivity (κ_L), which is comparable to the behaviour reported in CaS and SrSe. The compounds MgSe and MgTe exhibit lower κ_L values compared to MSe and MTe (where M represents Ca, Sr, and Ba), as seen in Figure 3.24.

Typically, the dominant factor in phonon transport is the contribution of acoustic phonons to κ_L. Nevertheless, it is evident Figures 3.25 and 3.26 that the primary factor influencing κ_L in these AHs and AECs is the contribution of optical

phonons. This effect is particularly pronounced in systems where the mass ratio approaches unity, as depicted in Figure 3.24. Chang et al. [94] postulated that a smaller difference in atomic mass result in an increased dispersive optical phonon. Consequently, this phenomenon contributes to an increased group velocity of optical phonons, ultimately increasing κ_L. As seen in Figure 3.22, the optical phonon bands exhibit a greater degree of dispersion in LiF as compared to NaF. However, it is noteworthy that the lower-frequency optical phonon considerably contributes to the thermal conductivity (κ_L) in NaF as compared to LiF, as evidenced by Figure 3.25a. This may be attributed to the fact that the mass ratio of NaF is close to unity. Similiarly, it can be shown from Figure 3.24b that BaO exhibits optical phonons that are extremely dispersive, characterised by a substantial mass ratio of 8.59. However, in comparison to the other compounds in the BaCh series (where Ch represents S, Se, or Te), the contribution of optical phonons to κ_L in BaO is very little. Hence, it is proposed that materials exhibiting a mass ratio approaching unity or possessing a small atomic mass difference have a reduced presence of dispersive optical phonons. However, despite their low energy levels, these optical phonons make a substantial contribution to phonon transport, hence increasing the thermal conductivity (κ_L). Materials that exhibit a high difference in mass have relatively low κ_L values in the corresponding series. This is primarily attributed to the limited or negligible involvement of optical phonons in κ_L, which can be attributed to the distinct separation between acoustic and optical phonons. Additionally, the presence of a small phonon band gap may further facilitate the suppression of κ_L through Umklapp scattering.

As previously mentioned, the Slack model [73] suggests that various parameters are influential in determining lattice thermal conductivity. Average atomic mass, interatomic bonding, crystal structure, and anharmonicity are among those factors. Table 3.7 shows a variety of material parameters, including average atomic mass, mass ratio, average sound velocity, Gruneisen parameter and specific heat at constant volume in order to establish correlations between these properties and the lattice thermal conductivity of AHs and AECs. Harmonic parameters such as phonon group velocity and specific heat capacity can explain the observed trends in κ_L in certain cases when a fixed alkali/alkaline-earth metal atom is considered, as illustrated in Table 3.7. One example of this is the increased phonon group velocities of LiF, NaF, and MgO in

comparison to the compounds LiX, NaF, and NaX that were examined in this study, which account for their high κ_L values.

Nevertheless, the calculated κ_L for the remaining compounds fails to correspond with the trends observed in the harmonic properties. For example, despite the fact that the

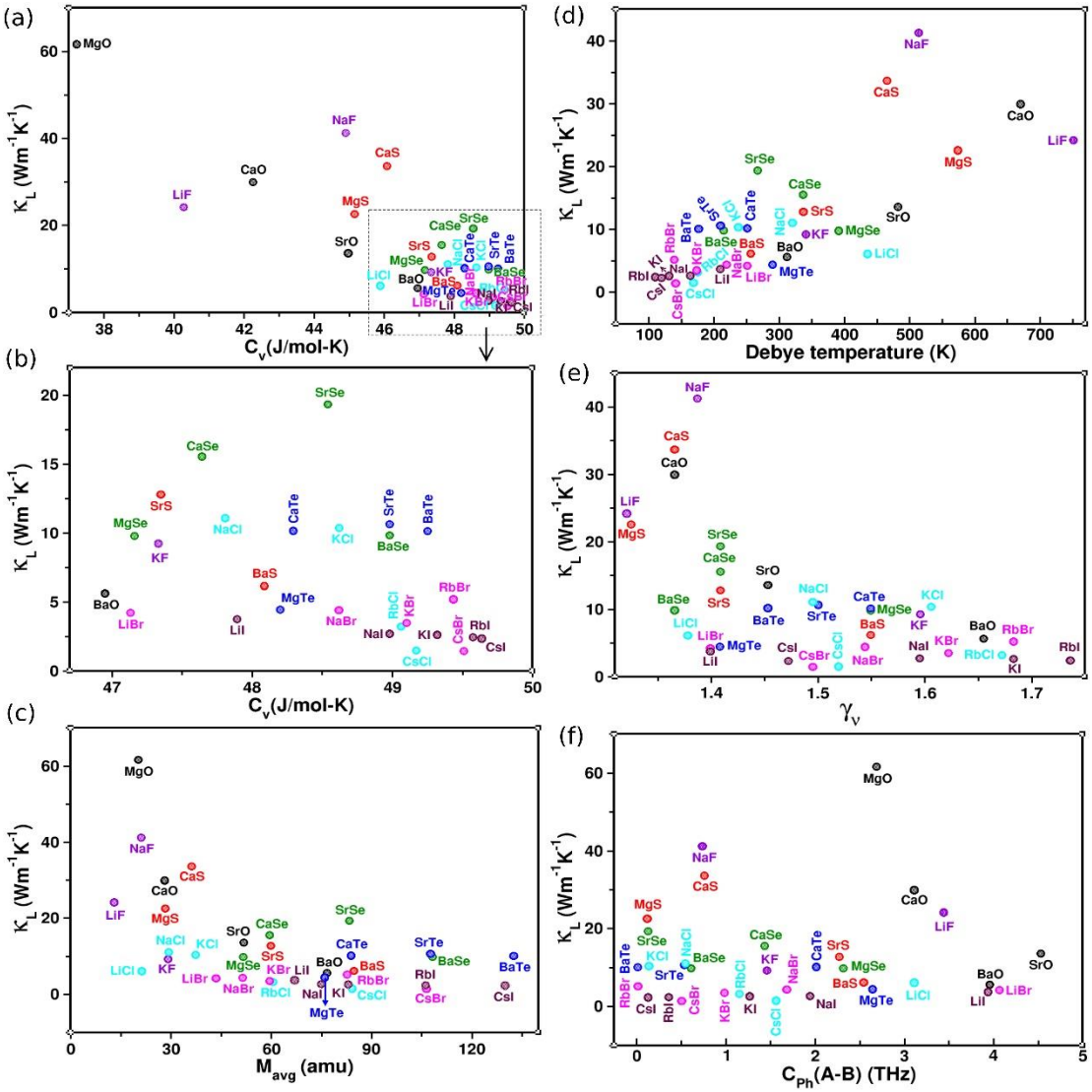

Fig 3.29: Calculated lattice thermal conductivity κ_L (in W/m K) at 300 K is plotted as a function of (a,b) specific heat at constant volume (C_v, in J/mol K), (b) zoomed-in image of the bottom right portion of panel (a), (c) average atomic mass (M_{avg}, in amu), (d) Debye temperature (Θ_D, in K),(e) Grüneisen parameter (γ_v), and (f) absolute value of cophonicity (|*C*ph|, in THz) for AHs and AECs.

group velocity (v_g) and Debye temperature (Θ_D) of BaO are considerably higher than those of BaTe, BaTe demonstrates a much greater κ_L. Therefore, it is critical to take into account the anharmonic nature of compounds in order to comprehend the trends in

κ_L, whether they pertain to a fixed group (e.g., BaCh, where Ch represents O, S, Se, and Te) or across different compounds.

In order to illustrate the influence of atomic masses on vibrational properties, additionally cophonicity was computed, this is a metric utilised to quantify the overlap in atomic contributions within a designated range of vibrational frequencies. The cophonicity values for all the compounds under investigation are displayed in Table 3.7. The relationship between cophonicity and the evolution of lattice thermal conductivity is visually depicted in Figure 3.29f. Compounds with comparable atomic masses (mass ratios close to 1) ought to demonstrate cophonicity close to zero. This value close to zero represents atomic displacements, in which the average velocity of motion for both atoms is identical. As illustrated in Table 3.7, the mass ratios of RbBr and BaTe are 1.07 and 1.08, respectively, and these elements exhibit a cophonicity of 0.01. This is consistent with the atomic contributions of projected phonons, in which the vibrational spectrum is uniformly influenced by both atomic pairs throughout the entire frequency range. In addition, although cophonicity tends to follow the trend of κ_L in certain series (Ch = O, S, Se, and Te) including BaCh, SrCh, and CaCh (where Te is present), a direct correlation between κ_L and cophonicity is typically not observed. This discovery emphasizes the fact that κ_L is determined by a complex interplay of harmonic and anharmonic properties. A comprehensive examination of these properties is essential in order to understand the trend in lattice thermal conductivity. Further investigation reveals that anharmonicity, as reflected by phonon lifetime, is critical in determining the trend of lattice thermal conductivity in the AHs and AECs studied in this work. In order to figure out the microscopic origins of the anomalous trends observed in κ_L, the lifetimes (τ) and phonon group velocities (g_v) are represented in Figures 3.30 and 3.31.

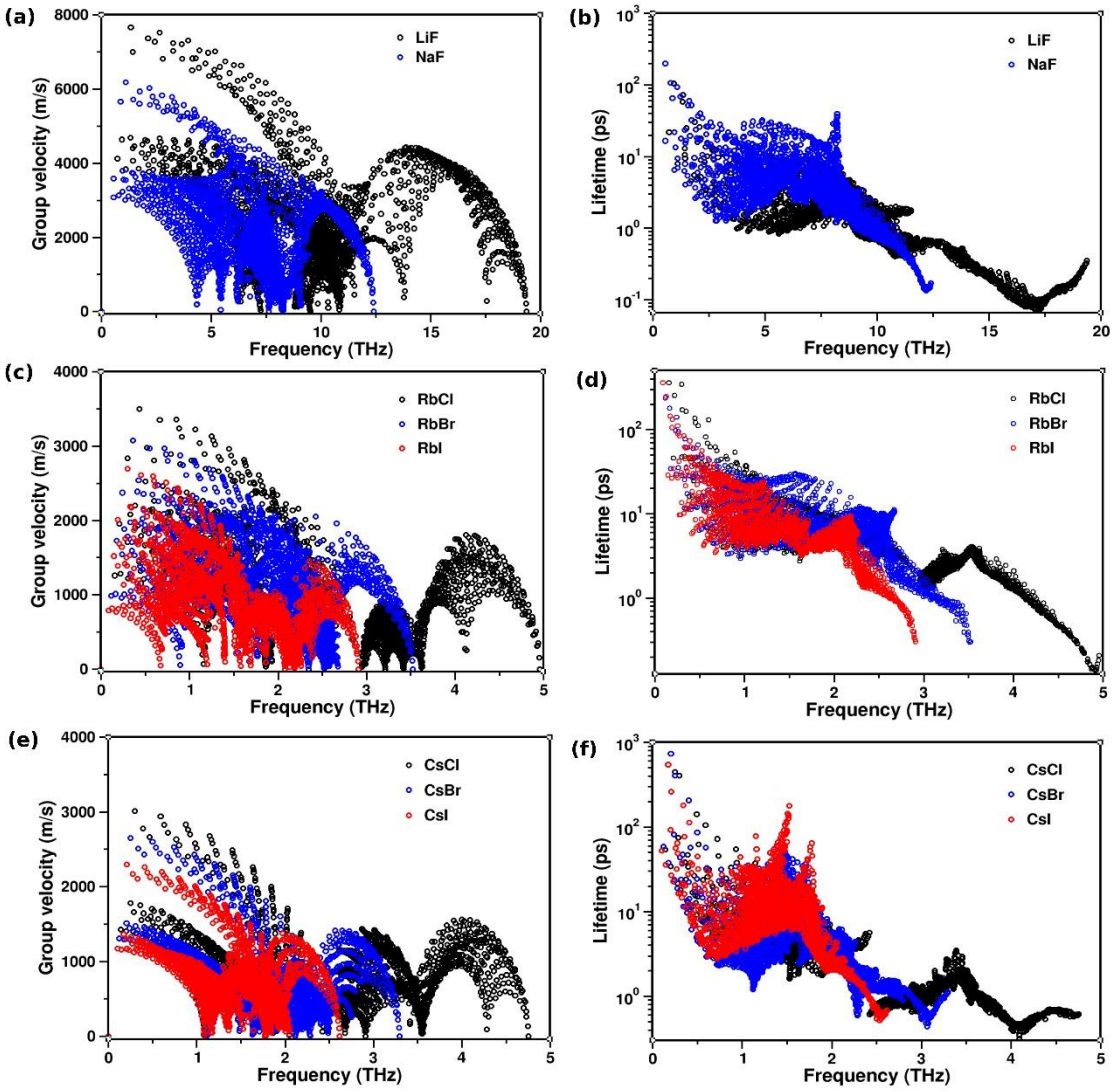

Fig. 3.30: Phonon (a,c,e) group velocities (b,d,f) lifetimes of (a,b) LiF and NaF and (c,d) RbX and (e,f) CsX (X = Cl, Br, I).

The phonon group velocities of alkali/alkaline-earth metals decrease as their atomic mass increases, whereas nonmetal halogens/chalcogens exhibit no anomalous behaviour (Figures 3.31a,c, 3.32a, and Figure 3.33a). The significance of the trend of κ_L in materials with a mass ratio approaching unity is largely determined by the lifetimes of optical phonon modes, as illustrated in Figures 3.30b,d,f, 3.31c,d. To illustrate, the phonon lifetimes of CsI, NaF, RbBr, and SrSe are comparatively higher in the frequency ranges of ~1−3, ~0.5−2, and ~4−7.5 THz, respectively, while those of BaTe are notably smaller at 2−4 THz.

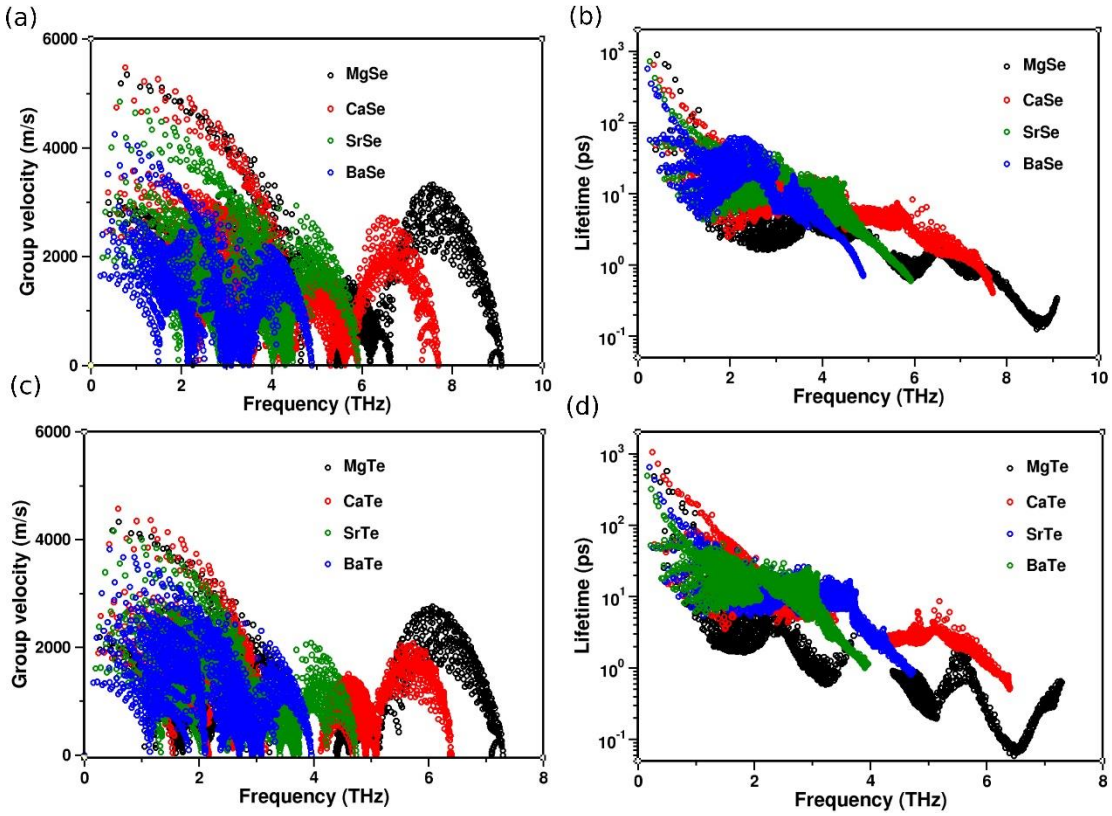

Fig. 3.31: Phonon (a,c) group velocities and (b,d) lifetimes of (a,b) MSe and (c,d) MTe series of compounds, where M = Mg, Ca, Sr, and Ba.

In addition, the characteristics of the absorption and emission scattering rates of the compounds that belong to the BaCh series are illustrated in Figure 3.34. The graphs show that absorption dominates in the low-frequency zone of scattering rates, whereas emission dominates in the high-frequency zone. In addition, materials having a narrow acoustic-optical gap have comparatively higher scattering rates in the acoustic-optical gap region. In general, materials with a mass ratio close to unity have relatively modest scattering rates. As a result, these materials have longer phonon lifetimes (τ) and so abnormally high κ_L relative to materials with mass contrast.

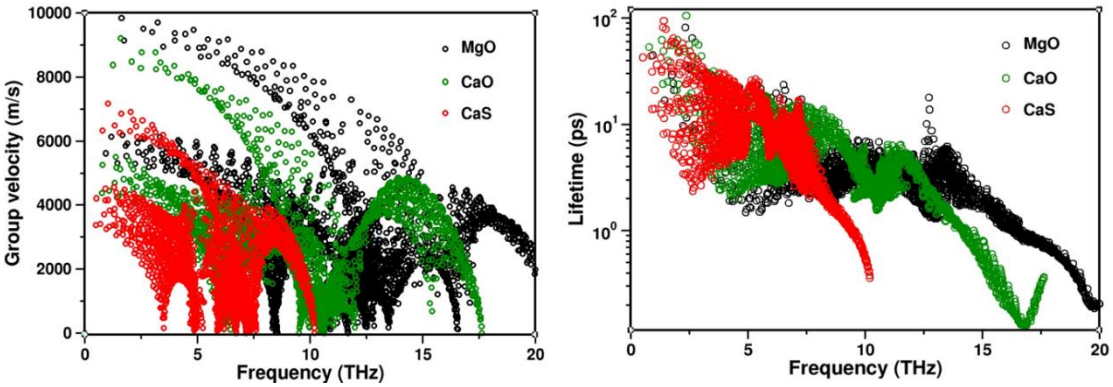

(a) **(b)**

Fig. 3.32: Phonon (a) group velocities (b) lifetimes of MgO, CaO and CaS.

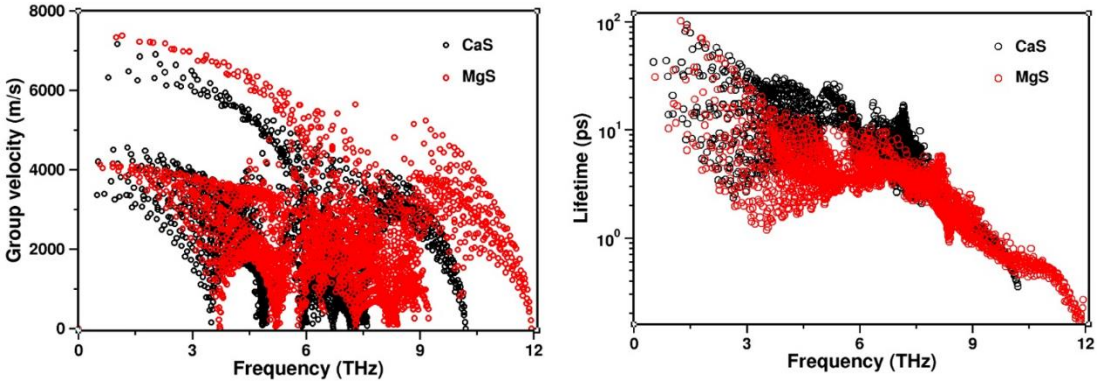

(a) **(b)**

Fig. 3.33: Phonon (a) group velocities (b) lifetimes of MgS and CaS.

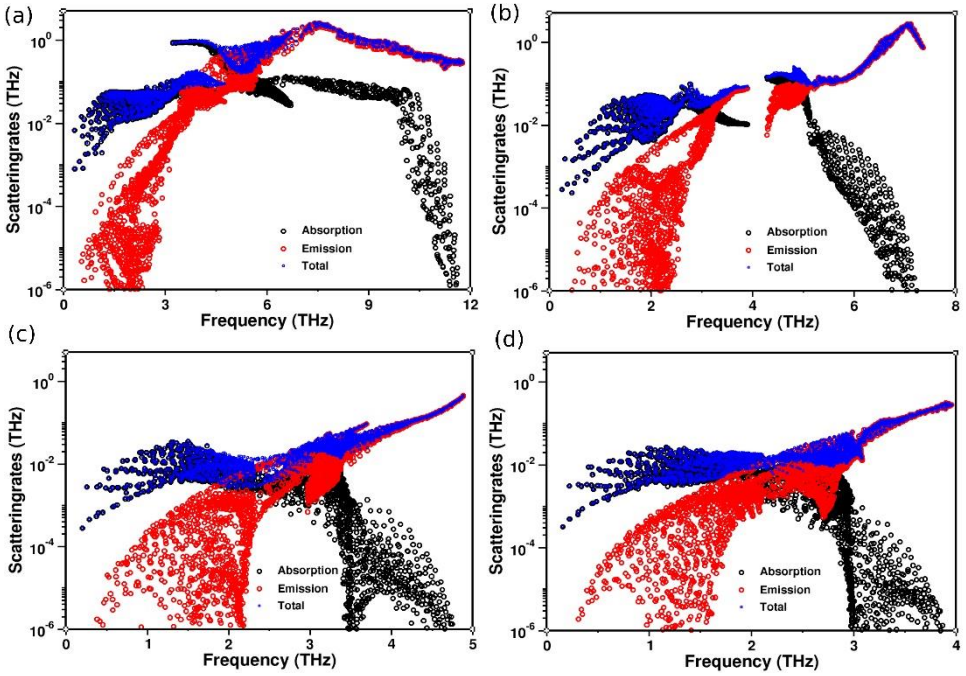

Fig. 3.34: Phonon scattering rates of (a) BaO, (b) BaS, (c) BaSe, and (d) BaTe

3.2.2.2 Effect of Tensile Lattice Strain on Lattice Thermal Conductivity

To conduct a more comprehensive examination of the impact of atomic mass variation on κ_L, the influence of tensile lattice strain has been explored in relation to lattice dynamics and phonon transport. This investigation focuses on two specific materials, namely MgTe with a significant mass contrast of 5.25 and BaTe with a mass ratio close to unity of 1.08. These materials have been selected as case studies from a pool of 36 compounds that are currently under scrutiny. The equilibrium lattice constant is then incremented in a systematic manner, resulting in the observation of soft phonon modes for MgTe when subjected to a lattice strain of 6% (Figure 3.35a). Consequently, the impact of lattice strain has also been investigated for BaTe, with the study extending up to 6%. The phonon dispersion curves of BaTe, calculated for various lattice strains, are depicted in Figure 3.35b.

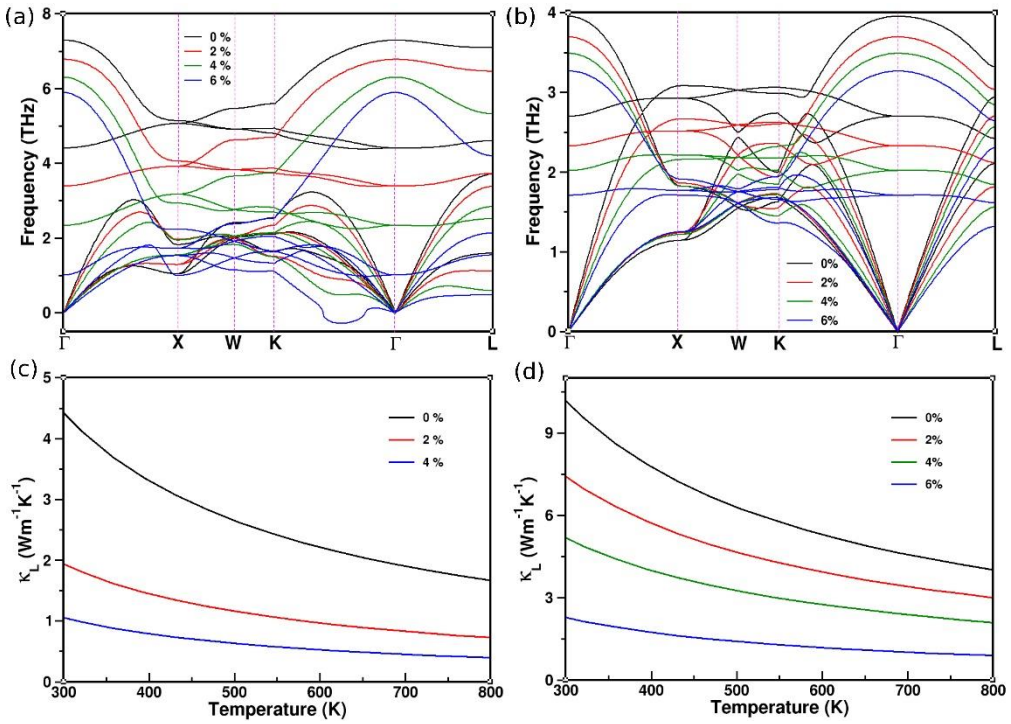

Fig. 3.35: Tensile lattice strain dependent (a, b) Phonon dispersion curves (c, d) lattice thermal conductivity of (a, c) MgTe and (b, d) BaTe.

It is noteworthy that no imaginary frequencies are detected for BaTe throughout a range of 6% lattice strain. This observation suggests that BaTe remains dynamically stable when subjected to the applied tensile strain. The dispersion of optical phonon modes in both MgTe and BaTe materials is shown to increase under the influence of tensile strain, as depicted in Figure 3.35a and Figure 3.35b. Furthermore, it has been observed that

the acoustic and optical phonon modes of both MgTe and BaTe undergo softening under the influence of tensile strain (Figure 3.35a,b). This phenomenon leads to an increase in the coupling strength between the acoustic and optical phonon modes,

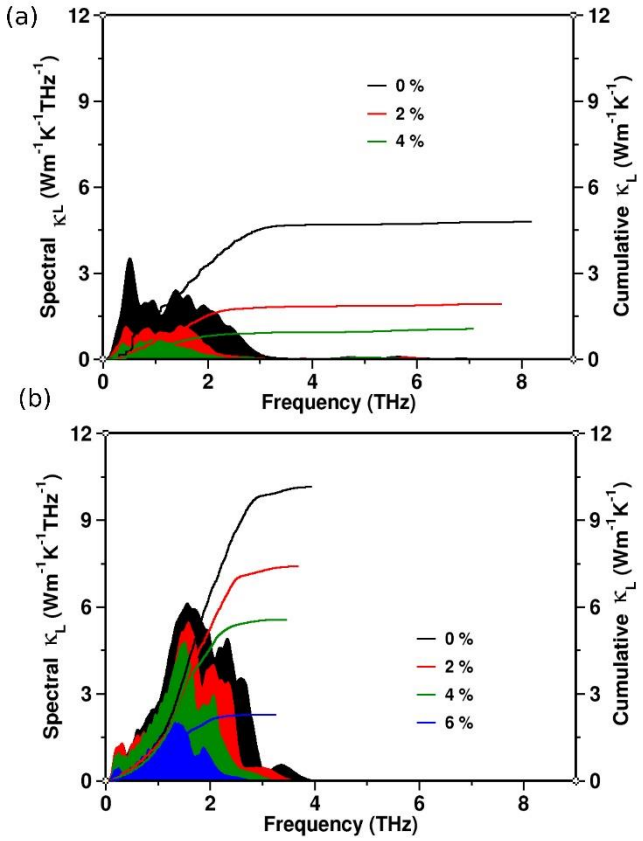

Fig 3.36: Tensile strain-dependent spectral and cumulative lattice thermal conductivities of (a) MgTe and (b) BaTe as a function of frequency.

particularly the transverse optical (TO) mode. The observed phenomenon implies a rise in phonon-phonon scattering rates, leading to a related reduction in the thermal conductivity (κ_L) as the tensile lattice strain increases. This relationship is illustrated in Figure 3.35c and Figure 3.35d for MgTe and BaTe, respectively. The measured thermal conductivity values exhibit a decline from 10.1 W/m K (4.78) to 2.22 W/m K (1.04) at a temperature of 300 K when subjected to an applied tensile lattice strain ranging from 0 to 6 (4) percent for the materials BaTe and MgTe, respectively. The calculated κ_L values exhibit a monotonic decline with increasing temperature.

Subsequently, spectral and cumulative κ_L values were computed as a function of frequency for BaTe and MgTe. The significance of the contribution of optical phonons to the lattice thermal conductivity (κ_L) in BaTe, compared to MgTe, is evident from the data shown in Figure 3.36 as tensile strain is increased. Furthermore, as tensile

lattice strain increases, the contribution of optical phonons to κ_L decreases progressively as a result of substantial phonon softening. The study of the effect of tensile lattice strain on BaTe and MgTe makes it evident that optical phonons contribute significantly to determining phonon transport in materials, particularly in those where the atomic mass ratio is almost unity.

To gain a better understanding of how κ_L decreases with tensile strain, phonon group velocities (g_v) and lifetimes (τ) were estimated as a function of tensile lattice strain, because κ_L is proportional to g_v and (τ). The tensile strain-dependent group velocities are shown in Figure 3.37a,b; the gv's of acoustic modes decrease with strain due to phonon softening, whereas the gv's of optical modes increase with strain due to a rise in the dispersive nature of MgTe as a function of strain. In the case of BaTe, it can be shown that both the group velocities (g_v) of the acoustic and optical modes decrease with strain.

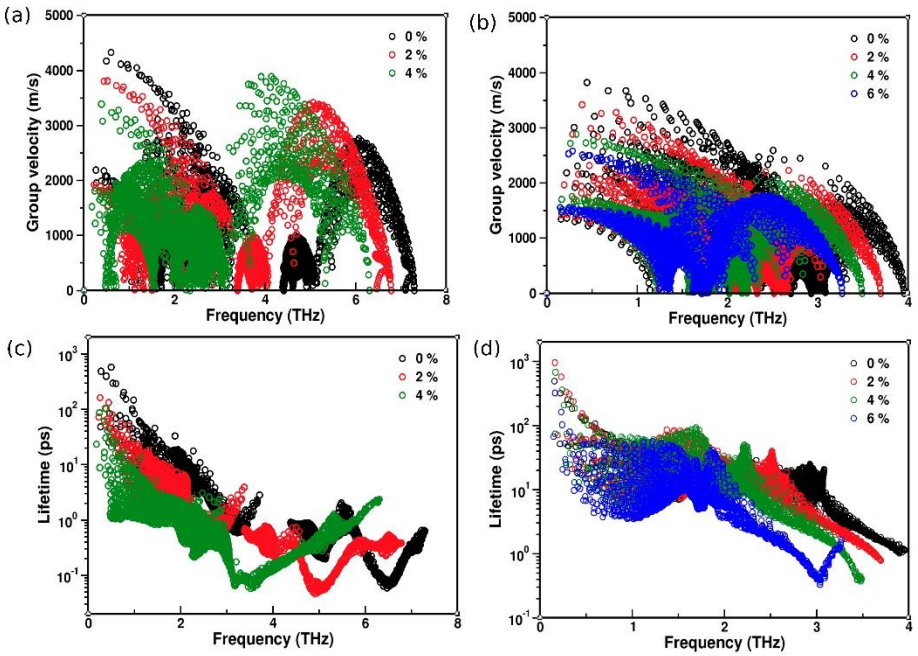

Fig 3.37: Tensile strain-dependent phonon (a,b) group velocities and (c,d) lifetimes of (a,c) MgTe and (b,d) BaTe.

This phenomenon may be attributed to the relatively low dispersive character of the optical phonons in BaTe compared to MgTe. Hence, the (g_v's) do not serve as the dominant factor for the observed trends in κ_L. Phonon lifetimes are calculated and depicted in Figure 3.37c,d, illustrating their dependence on strain. It is evident from Figure 3.37c that the τ values for MgTe decrease in accordance with strain. Conversely, the decline in phonon lifetimes for optical phonons may significantly affect the trends

observed for κ_L in BaTe. As the applied tensile lattice strain increases, the associated phonon lifetimes decrease (Figure 3.37) due to the increased scattering rates. Overall, when tensile lattice strain is applied to MgTe and BaTe, κ_L is suppressed due to the dominant role of τ and the modest contribution of g_v's due to increased phonon−phonon scattering. This clearly shows the dominance of phonon scattering rates/lifetimes and the contribution of optical phonon modes to κ_L even when tensile strain is applied.

The complete study described above gives some crucial insights into the relationship between mass ratio and κ_L: (a) When there is a minimum variation in atomic mass between elements in a material, it leads to a large enhancement of the contribution of optical phonons to the thermal conductivity (κ_L), ultimately leading in an overall rise in κ_L. (b) Materials with a mass ratio near to unity and low atomic masses in a binary system, such as NaF, NaCl, KCl, MgO, CaO, and MgS, have a higher presence of dispersive optical phonons. The optical phonons have a significant role in the thermal conductivity, κ_L. (c) On the other hand, in a binary system where the mass ratio is close to unity but the atomic masses are heavier, such as RbBr, CsI, SrSe, SrTe, and BaTe, there is a reduced presence of dispersion optical phonons. These optical phonons exhibit sharp peaks within a narrow frequency range, leading to a relatively more minor contribution to κ_L compared to acoustic phonons. (d) In general, materials with a mass ratio near to unity have longer phonon lifetimes, which continue to be a dominant factor for attaining high values of κ_L. Materials comprised of elements with similar atomic masses have, on average, relatively high values of κ_L; conversely, materials comprising elements with dissimilar atomic masses have lower values of κ_L.

This study carefully investigates the microscopic origins of anomalous trends observed in the thermal conductivity (κ_L) of alkali halides (AHs) and alkaline-earth chalcogenides (AECs). Given that AHs and AECs are binary systems characterised by a diverse range of κ_L values, they present an opportunity to investigate the underlying factors contributing to their anomalous behaviour, particularly in relation to various mass ratios. It has been shown that the presence of low-lying optical phonons has a substantial role in enhancing the thermal conductivity (κ_L) in some materials (namely NaF, NaCl, KCl, MgO, CaO, MgS, SrSe, SrTe, and BaTe) that have a mass ratio near to unity, in addition to their average atomic mass. Materials that have a mass ratio near

to unity have very low scattering rates, leading to longer lifetimes of phonons. As a consequence, these materials demonstrate an unusually high thermal conductivity (κ_L) within a certain series. The phonon transport characteristics of BaTe and MgTe are influenced by the tensile lattice strain-dependent strain, which in turn affects the phonon lifetimes. These phonon lifetimes have a significant impact on the observed trends in κ_L. In general, the dominant factor influencing the anomalous trends in κ_L for AHs and AECs with a mass ratio close to one is the phonon scattering rates, which are inversely proportional to the phonon lifetimes. Phonon group velocities, on the other hand, have little effect in this regard. The present work offers a comprehensive analysis of the relationship between atomic mass and the phonon transport characteristics of AHs and AECs. Furthermore, this study reveals that by manipulating the atomic masses, materials could be engineered with high and low κ_L values, providing exciting possibilities for tailored thermal conductivity in various applications.

References:

[1] J. Ding *et al.*, "Soft anharmonic phonons and ultralow thermal conductivity in $Mg_3(Sb, Bi)_2$ thermoelectrics," *Sci Adv*, vol. 7, no. 21, May 2021, doi: 10.1126/sciadv.abg1449.

[2] M. Dutta, D. Sarkar, and K. Biswas, "Intrinsically ultralow thermal conductive inorganic solids for high thermoelectric performance," *Chemical Communications*, vol. 57, no. 39, pp. 4751–4767, 2021, doi: 10.1039/D1CC00830G.

[3] B. Liu *et al.*, "Advances on strategies for searching for next generation thermal barrier coating materials," *J Mater Sci Technol*, vol. 35, no. 5, pp. 833–851, May 2019, doi: 10.1016/j.jmst.2018.11.016.

[4] E. Bsaibess, F. Delorme, I. Monot-Laffez, and F. Giovannelli, "Ultra-low thermal conductivity in scheelite and A-deficient scheelite ceramics," *Scr Mater*, vol. 201, p. 113950, Aug. 2021, doi: 10.1016/j.scriptamat.2021.113950.

[5] P. Kumar, K. Rajput, and D. R. Roy, "Structural, electronic, vibrational, mechanical and thermoelectric properties of 2D and bulk BaX (X=O, S, Se and Te) series under DFT and BTE framework," *Physica E Low Dimens Syst Nanostruct*, vol. 127, p. 114523, Mar. 2021, doi: 10.1016/j.physe.2020.114523.

[6] K. Rajput and D. R. Roy, "h-CaS and h-CaSe nanosheets in CaX (X = O, S, Se and Te) series: promising thermoelectric materials under DFT investigation," *Appl Nanosci*, vol. 9, no. 8, pp. 1845–1856, Nov. 2019, doi: 10.1007/s13204-019-00997-4.

[7] K. Rajput and D. R. Roy, "Structure, stability, electronic and thermoelectric properties of strontium chalcogenides," *Physica E Low Dimens Syst Nanostruct*, vol. 119, p. 113965, May 2020, doi: 10.1016/j.physe.2020.113965.

[8] H. Zheng *et al.*, "Monolayer II-VI semiconductors: A first-principles prediction," *Phys Rev B*, vol. 92, no. 11, p. 115307, Sep. 2015, doi: 10.1103/PhysRevB.92.115307.

[9] K. Biswas *et al.*, "High thermoelectric figure of merit in nanostructured p-type PbTe–MTe (M = Ca, Ba)," *Energy Environ Sci*, vol. 4, no. 11, p. 4675, 2011, doi: 10.1039/c1ee02297k.

[10] R. Al Rahal Al Orabi *et al.*, “Band Degeneracy, Low Thermal Conductivity, and High Thermoelectric Figure of Merit in SnTe–CaTe Alloys,” *Chemistry of Materials*, vol. 28, no. 1, pp. 376–384, Jan. 2016, doi: 10.1021/acs.chemmater.5b04365.

[11] Y.-J. Kim, L.-D. Zhao, M. G. Kanatzidis, and D. N. Seidman, “Analysis of Nanoprecipitates in a Na-Doped PbTe–SrTe Thermoelectric Material with a High Figure of Merit,” *ACS Appl Mater Interfaces*, vol. 9, no. 26, pp. 21791–21797, Jul. 2017, doi: 10.1021/acsami.7b04098.

[12] G. Tan *et al.*, “Non-equilibrium processing leads to record high thermoelectric figure of merit in PbTe–SrTe,” *Nat Commun*, vol. 7, no. 1, p. 12167, Jul. 2016, doi: 10.1038/ncomms12167.

[13] S. Lo, J. He, K. Biswas, M. G. Kanatzidis, and V. P. Dravid, “Phonon Scattering and Thermal Conductivity in p-Type Nanostructured PbTe-BaTe Bulk Thermoelectric Materials,” *Adv Funct Mater*, vol. 22, no. 24, pp. 5175–5184, Dec. 2012, doi: 10.1002/adfm.201201221.

[14] T. Fan and A. R. Oganov, “Discovery of high performance thermoelectric chalcogenides through first-principles high-throughput screening,” *J Mater Chem C Mater*, vol. 9, no. 38, pp. 13226–13235, 2021, doi: 10.1039/D1TC03146E.

[15] A. M. Hao, X. C. Yang, Z. M. Gao, X. Liu, Y. Zhu, and R. P. Liu, “First-principles investigations on structural and elastic properties of CaX (X=S, Se and Te) under high pressure,” *High Press Res*, vol. 30, no. 2, pp. 310–317, Jun. 2010, doi: 10.1080/08957951003774254.

[16] M. M. Abdus Salam, “Theoretical study of CaO, CaS and CaSe via first-principles calculations,” *Results Phys*, vol. 10, pp. 934–945, Sep. 2018, doi: 10.1016/j.rinp.2018.07.042.

[17] X.-D. Zhang, Z.-J. Li, and G.-M. Shi, “Lattice Dynamics Study of Magnesium Chalcogenides,” *Commun Theor Phys*, vol. 57, no. 2, pp. 295–300, Feb. 2012, doi: 10.1088/0253-6102/57/2/22.

[18] S. C. Rakesh Roshan, L. Kunduru, N. Yedukondalu, and M. Sainath, “Structure and Lattice Dynamics of Calcium Chalcogenides under High Pressure,” *Mater Today Proc*, vol. 5, no. 9, pp. 18874–18878, 2018, doi: 10.1016/j.matpr.2018.06.235.

[19] M. Bayrakci, K. Colakoglu, E. Deligoz, and Y. O. Ciftci, “A first-principle study of the structural and lattice dynamical properties of CaX (X=S, Se, and Te),” *High Press Res*, vol. 29, no. 2, pp. 187–203, Jun. 2009, doi: 10.1080/08957950802526436.

[20] Ş. Uğur, “Theoretical study of the phonon properties of SrS,” *Materials Science and Engineering: B*, vol. 162, no. 2, pp. 116–119, May 2009, doi: 10.1016/j.mseb.2009.03.013.

[21] A. A. Musari and S. A. Orukombo, “Theoretical study of phonon dispersion, elastic, mechanical and thermodynamic properties of barium chalcogenides,” *Int J Mod Phys B*, vol. 32, no. 08, p. 1850092, Mar. 2018, doi: 10.1142/S0217979218500923.

[22] D. Varshney, S. Jain, S. Shriya, and R. Khenata, “High-pressure and temperature-induced structural, elastic, and thermodynamical properties of strontium chalcogenides,” *Journal of Theoretical and Applied Physics*, vol. 10, no. 3, pp. 163–193, Sep. 2016, doi: 10.1007/s40094-016-0214-z.

[23] R. Muthaiah and J. Garg, “Thermal conductivity of magnesium selenide (MgSe)–A first principles study,” *Comput Mater Sci*, vol. 198, p. 110679, Oct. 2021, doi: 10.1016/j.commatsci.2021.110679.

[24] R. Muthaiah and J. Garg, “Thermal conductivity of magnesium telluride (MgTe) - A first principles study,” *Solid State Commun*, vol. 337, p. 114414, Oct. 2021, doi: 10.1016/j.ssc.2021.114414.

[25] Z. Yang, K. Yuan, J. Meng, X. Zhang, D. Tang, and M. Hu, “Why thermal conductivity of CaO is lower than that of CaS: a study from the perspective of phonon splitting of optical mode,” *Nanotechnology*, vol. 32, no. 2, p. 025709, Jan. 2021, doi: 10.1088/1361-6528/abbb4c.

[26] Y. Xia, J. M. Hodges, M. G. Kanatzidis, and M. K. Y. Chan, “Lattice thermal transport in group II-alloyed PbTe,” *Appl Phys Lett*, vol. 112, no. 18, Apr. 2018, doi: 10.1063/1.5002587.

[27] A. Seko, A. Togo, H. Hayashi, K. Tsuda, L. Chaput, and I. Tanaka, “Prediction of Low-Thermal-Conductivity Compounds with First-Principles Anharmonic Lattice-Dynamics Calculations and Bayesian Optimization,” *Phys Rev Lett*, vol. 115, no. 20, p. 205901, Nov. 2015, doi: 10.1103/PhysRevLett.115.205901.

[28] G. Kresse and J. Furthmüller, “Efficient iterative schemes for *ab initio* total-energy calculations using a plane-wave basis set,” *Phys Rev B*, vol. 54, no. 16, pp. 11169–11186, Oct. 1996, doi: 10.1103/PhysRevB.54.11169.

[29] O. Hellman and I. A. Abrikosov, “Temperature-dependent effective third-order interatomic force constants from first principles,” *Phys Rev B*, vol. 88, no. 14, p. 144301, Oct. 2013, doi: 10.1103/PhysRevB.88.144301.

[30] O. Hellman, I. A. Abrikosov, and S. I. Simak, “Lattice dynamics of anharmonic solids from first principles,” *Phys Rev B*, vol. 84, no. 18, p. 180301, Nov. 2011, doi: 10.1103/PhysRevB.84.180301.

[31] O. Hellman, P. Steneteg, I. A. Abrikosov, and S. I. Simak, “Temperature dependent effective potential method for accurate free energy calculations of solids,” *Phys Rev B*, vol. 87, no. 10, p. 104111, Mar. 2013, doi: 10.1103/PhysRevB.87.104111.

[32] W. G. Hoover, “Constant-pressure equations of motion,” *Phys Rev A (Coll Park)*, vol. 34, no. 3, pp. 2499–2500, Sep. 1986, doi: 10.1103/PhysRevA.34.2499.

[33] W. G. Hoover, “Canonical dynamics: Equilibrium phase-space distributions,” *Phys Rev A (Coll Park)*, vol. 31, no. 3, pp. 1695–1697, Mar. 1985, doi: 10.1103/PhysRevA.31.1695.

[34] L. Liu and W. A. Bassett, “Effect of pressure on the crystal structure and the lattice parameters of BaO,” *J Geophys Res*, vol. 77, no. 26, pp. 4934–4937, Sep. 1972, doi: 10.1029/JB077i026p04934.

[35] K. Syassen, N. E. Christensen, H. Winzen, K. Fischer, and J. Evers, “Optical response and band-structure calculations of alkaline-earth tellurides under pressure,” *Phys Rev B*, vol. 35, no. 8, pp. 4052–4059, Mar. 1987, doi: 10.1103/PhysRevB.35.4052.

[36] S. Yamaoka, O. Shimomura, H. Nakazawa, and O. Fukunaga, “Pressure-induced phase transformation in BaS,” *Solid State Commun*, vol. 33, no. 1, pp. 87–89, Jan. 1980, doi: 10.1016/0038-1098(80)90702-4.

[37] H. G. Zimmer, H. Winzen, and K. Syassen, “High-pressure phase transitions in CaTe and SrTe,” *Phys Rev B*, vol. 32, no. 6, pp. 4066–4070, Sep. 1985, doi: 10.1103/PhysRevB.32.4066.

[38] S. Yamaoka, O. Shimomura, H. Nakazawa, and O. Fukunaga, “Pressure-induced phase transformation in BaS,” *Solid State Commun*, vol. 33, no. 1, pp. 87–89, Jan. 1980, doi: 10.1016/0038-1098(80)90702-4.

[39] H. Luo, R. G. Greene, K. Ghandehari, T. Li, and A. L. Ruoff, “Structural phase transformations and the equations of state of calcium chalcogenides at high pressure,” *Phys Rev B*, vol. 50, no. 22, pp. 16232–16237, Dec. 1994, doi: 10.1103/PhysRevB.50.16232.

[40] A. Waag, H. Heinke, S. Scholl, C. R. Becker, and G. Landwehr, “Growth of MgTe and Cd1−xMgxTe thin films by molecular beam epitaxy,” *J Cryst Growth*, vol. 131, no. 3–4, pp. 607–611, Aug. 1993, doi: 10.1016/0022-0248(93)90213-G.

[41] T. Li, H. Luo, R. G. Greene, A. L. Ruoff, S. S. Trail, and Jr. , F. J. DiSalvo, “High Pressure Phase of MgTe: Stable Structure at STP?,” *Phys Rev Lett*, vol. 74, no. 26, pp. 5232–5235, Jun. 1995, doi: 10.1103/PhysRevLett.74.5232.

[42] L. Tairi *et al.*, “Phase stability and electronic behavior of MgS, MgSe and MgTe compounds,” *Phase Transitions*, vol. 90, no. 10, pp. 929–941, Oct. 2017, doi: 10.1080/01411594.2017.1302085.

[43] S. Duman, S. Bağcı, H. M. Tütüncü, and G. P. Srivastava, “First-principles studies of ground-state and dynamical properties of MgS, MgSe, and MgTe in the rocksalt, zinc blende, wurtzite, and nickel arsenide phases,” *Phys Rev B*, vol. 73, no. 20, p. 205201, May 2006, doi: 10.1103/PhysRevB.73.205201.

[44] A. Chakrabarti, “Role of NiAs phase in pressure-induced structural phase transitions in IIA-VI chalcogenides,” *Phys Rev B*, vol. 62, no. 3, pp. 1806–1814, Jul. 2000, doi: 10.1103/PhysRevB.62.1806.

[45] P. E. Van Camp, V. E. Van Doren, and J. L. Martins, “High-pressure phases of magnesium selenide and magnesium telluride,” *Phys Rev B*, vol. 55, no. 2, pp. 775–779, Jan. 1997, doi: 10.1103/PhysRevB.55.775.

[46] R. Pandey and A. Sutjianto, “Study of structural phase transition in MgSe,” *Solid State Commun*, vol. 91, no. 4, pp. 269–271, Jul. 1994, doi: 10.1016/0038-1098(94)90300-X.

[47] P. Richet, H. Mao, and P. M. Bell, “Static compression and equation of state of CaO to 1.35 Mbar,” *J Geophys Res Solid Earth*, vol. 93, no. B12, pp. 15279–15288, Dec. 1988, doi: 10.1029/JB093iB12p15279.

[48] Y. Fei, “Effects of temperature and composition on the bulk modulus of (Mg,Fe)O,” *American Mineralogist*, vol. 84, no. 3, pp. 272–276, Mar. 1999, doi: 10.2138/am-1999-0308.

[49] H. Baltache, R. Khenata, M. Sahnoun, M. Driz, B. Abbar, and B. Bouhafs, “Full potential calculation of structural, electronic and elastic properties of alkaline earth oxides MgO, CaO and SrO,” *Physica B Condens Matter*, vol. 344, no. 1–4, pp. 334–342, Feb. 2004, doi: 10.1016/j.physb.2003.09.274.

[50] S. H. Mir, P. C. Jha, S. Dabhi, and P. K. Jha, “Ab initio study of phase stability, lattice dynamics and thermodynamic properties of magnesium chalcogenides,” *Mater Chem Phys*, vol. 175, pp. 54–61, Jun. 2016, doi: 10.1016/j.matchemphys.2016.02.066.

[51] Cihan Kürkçü, “An Ab-initio Study of Structural and Electronic Properties of CaTe under High Pressure,” *Russian Journal of Physical Chemistry A*, vol. 93, no. 11, pp. 2226–2232, Nov. 2019, doi: 10.1134/S0036024419110165.

[52] R. Khenata *et al.*, “First-principle study of structural, electronic and elastic properties of SrS, SrSe and SrTe under pressure,” *Physica B Condens Matter*, vol. 339, no. 4, pp. 208–215, Dec. 2003, doi: 10.1016/j.physb.2003.07.003.

[53] Y. Fei, “Effects of temperature and composition on the bulk modulus of (Mg,Fe)O,” *American Mineralogist*, vol. 84, no. 3, pp. 272–276, Mar. 1999, doi: 10.2138/am-1999-0308.

[54] J. Fu, F. Bernard, and S. Kamali-Bernard, “First-principles calculations of typical anisotropic cubic and hexagonal structures and homogenized moduli estimation based on the Y-parameter: Application to CaO, MgO, CH and Calcite CaCO3,” *Journal of Physics and Chemistry of Solids*, vol. 101, pp. 74–89, Feb. 2017, doi: 10.1016/j.jpcs.2016.10.010.

[55] J. Zemann, “*Crystal structures*, 2 *nd edition. Vol. 1* by R. W. G. Wyckoff,” *Acta Crystallogr*, vol. 18, no. 1, pp. 139–139, Jan. 1965, doi: 10.1107/S0365110X65000361.

[56] I. Khan, A. Afaq, H. A. Rahnamaye Aliabad, and I. Ahmad, “Transition from optically inactive to active Mg-chalcogenides: A first principle study,” *Comput Mater Sci*, vol. 61, pp. 278–282, Aug. 2012, doi: 10.1016/j.commatsci.2012.04.036.

[57] K. Syassen, “Ionic monochalcogenides under pressure,” *Physica B+C*, vol. 139–140, pp. 277–283, May 1986, doi: 10.1016/0378-4363(86)90577-2.

[58] G. Q. Lin, H. Gong, and P. Wu, “Electronic properties of barium chalcogenides from first-principles calculations: Tailoring wide-band-gap II-VI semiconductors,” *Phys Rev B*, vol. 71, no. 8, p. 085203, Feb. 2005, doi: 10.1103/PhysRevB.71.085203.

[59] D. Zagorac, K. Doll, J. Zagorac, D. Jordanov, and B. Matović, “Barium Sulfide under Pressure: Discovery of Metastable Polymorphs and Investigation of Electronic Properties on ab Initio Level,” *Inorg Chem*, vol. 56, no. 17, pp. 10644–10654, Sep. 2017, doi: 10.1021/acs.inorgchem.7b01617.

[60] J. Wang, S. Yip, S. R. Phillpot, and D. Wolf, “Crystal instabilities at finite strain,” *Phys Rev Lett*, vol. 71, no. 25, pp. 4182–4185, Dec. 1993, doi: 10.1103/PhysRevLett.71.4182.

[61] K. Kholiya and S. Verma, “Pressure-induced phase transition and elastic properties of barium chalcogenides,” *Phase Transitions*, vol. 84, no. 1, pp. 67–76, Jan. 2011, doi: 10.1080/01411594.2010.519967.

[62] H. Y. Wu, Y. H. Chen, C. R. Deng, X. Y. Han, and P. F. Yin, “Electronic, elastic and dynamical properties of MgSe under pressure: rocksalt and iron silicide phase,” *Philosophical Magazine*, vol. 95, no. 21, pp. 2240–2256, Jul. 2015, doi: 10.1080/14786435.2015.1047427.

[63] M. A. Ghebouli, H. Choutri, N. Bouarissa, B. Ghebouli, M. Fatmi, and E. Uçgun, “Ab initio calculation of fundamental properties of CaxMg1−xA (A=Se and Te) alloys in the rock-salt structure,” *Physica E Low Dimens Syst Nanostruct*, vol. 49, pp. 83–91, Mar. 2013, doi: 10.1016/j.physe.2013.01.022.

[64] M. Galtier, A. Montaner, and G. Vidal, “Phonons Optiques de CaO, SrO, BaO Au Centre de la Zone de Brillouin à 300 et 17K,” *Journal of Physics and Chemistry of Solids*, vol. 33, no. 12, pp. 2295–2302, Jan. 1972, doi: 10.1016/S0022-3697(72)80304-4.

[65] M. A. Ghebouli, H. Choutri, and N. Bouarissa, “Electronic structure and lattice dynamics of $Ca_xMg_{1-x}S$ in the rock-salt phase,” *Mater Sci Semicond Process*, vol. 18, pp. 71–79, Feb. 2014, doi: 10.1016/j.mssp.2013.10.029.

[66] Y. Kaneko, K. Morimoto, and T. Koda, “Optical Properties of Alkaline-Earth Chalcogenides. I. Single Crystal Growth and Infrared Reflection Spectra Due to Optical Phonons,” *J Physical Soc Japan*, vol. 51, no. 7, pp. 2247–2254, Jul. 1982, doi: 10.1143/JPSJ.51.2247.

[67] M. Souadkia, B. Bennecer, and F. Kalarasse, “Ab initio lattice dynamics and thermodynamic properties of SrO under pressure,” *Journal of Physics and Chemistry of Solids*, vol. 73, no. 1, pp. 129–135, Jan. 2012, doi: 10.1016/j.jpcs.2011.10.023.

[68] K. H. Rieder, R. Migoni, and B. Renker, “Lattice dynamics of strontium oxide,” *Phys Rev B*, vol. 12, no. 8, pp. 3374–3379, Oct. 1975, doi: 10.1103/PhysRevB.12.3374.

[69] M. Souadkia, B. Bennecer, and F. Kalarasse, “Elastic and lattice dynamical properties of ternary strontium chalcogenide alloys,” *Mater Sci Semicond Process*, vol. 26, pp. 267–275, Oct. 2014, doi: 10.1016/j.mssp.2014.05.009.

[70] U. R. M. S. O. Madelung, Ed., “II-VI and I-VII Compounds; Semimagnetic Compounds,” 1st ed., vol. XXVI, 721, Springer Berlin, Heidelberg.

[71] Y. Xia *et al.*, “High-Throughput Study of Lattice Thermal Conductivity in Binary Rocksalt and Zinc Blende Compounds Including Higher-Order Anharmonicity,” *Phys Rev X*, vol. 10, no. 4, p. 041029, Nov. 2020, doi: 10.1103/PhysRevX.10.041029.

[72] E. S. Toberer, A. Zevalkink, and G. J. Snyder, “Phonon engineering through crystal chemistry,” *J Mater Chem*, vol. 21, no. 40, p. 15843, 2011, doi: 10.1039/c1jm11754h.

[73] G. A. Slack, “Nonmetallic crystals with high thermal conductivity,” *Journal of Physics and Chemistry of Solids*, vol. 34, no. 2, pp. 321–335, Jan. 1973, doi: 10.1016/0022-3697(73)90092-9.

[74] Y. Ren, “First principles study of electronic, phonon and elastic properties of rock-salt-phase MTe (M = Mg, Ca, Sr, Ba),” *Computational Condensed Matter*, vol. 11, pp. 69–76, Jun. 2017, doi: 10.1016/j.cocom.2017.05.004.

[75] V. H. Vetter and R. A. Bartels, “BaO single crystal elastic constants and their temperature dependence,” *Journal of Physics and Chemistry of Solids*, vol. 34, no. 8, pp. 1448–1449, Aug. 1973, doi: 10.1016/S0022-3697(73)80046-0.

[76] O. L. ANDERSON and P. ANDREATCH, “Pressure Derivatives of Elastic Constants of Single-Crystal MgO at 23o and -195.8oC,” *Journal of the American Ceramic Society*, vol. 49, no. 8, pp. 404–409, Aug. 1966, doi: 10.1111/j.1151-2916.1966.tb15405.x.

[77] P. R. Son and R. A. Bartels, “CaO and SrO single crystal elastic constants and their pressure derivatives,” *Journal of Physics and Chemistry of Solids*, vol. 33, no. 4, pp. 819–828, Jan. 1972, doi: 10.1016/S0022-3697(72)80098-2.

[78] A. J. Cinthia, G. S. Priyanga, R. Rajeswarapalanichamy, and K. Iyakutti, “Structural, electronic and mechanical properties of alkaline earth metal oxides MO (M=Be, Mg, Ca, Sr, Ba),” *Journal of Physics and Chemistry of Solids*, vol. 79, pp. 23–42, Apr. 2015, doi: 10.1016/j.jpcs.2014.10.021.

[79] S. V. Sinogeikin and J. D. Bass, “Single-crystal elasticity of MgO at high pressure,” *Phys Rev B*, vol. 59, no. 22, pp. R14141–R14144, Jun. 1999, doi: 10.1103/PhysRevB.59.R14141.

[80] S. Saib, N. Bouarissa, P. Rodríguez-Hernández, and A. Muñoz, “Ab initio lattice dynamics and piezoelectric properties of MgS and MgSe alkaline earth chalcogenides,” *Eur Phys J B*, vol. 73, no. 2, pp. 185–193, Jan. 2010, doi: 10.1140/epjb/e2009-00426-6.

[81] H. Oda, OrsonL. Anderson, DonaldG. Isaak, and I. Suzuki, “Measurement of elastic properties of single-crystal CaO up to 1200 K,” *Phys Chem Miner*, vol. 19, no. 2, Aug. 1992, doi: 10.1007/BF00198607.

[82] Rafik Maizi, A.-G. Boudjahem, and M. Boulbazine, “First-Principles Investigations on Structural, Elastic, and Thermodynamic Properties of CaX (X = S, Se, and Te) under Pressure,” *Russian Journal of Physical Chemistry A*, vol. 93, no. 13, pp. 2726–2734, Dec. 2019, doi: 10.1134/S0036024419130181.

[83] M. M. Abdus Salam, “First principles study of structural, elastic and electronic structural properties of strontium chalcogenides,” *Chinese Journal of Physics*, vol. 57, pp. 418–434, Feb. 2019, doi: 10.1016/j.cjph.2018.10.027.

[84] M. Born, “On the stability of crystal lattices. I,” *Mathematical Proceedings of the Cambridge Philosophical Society*, vol. 36, no. 2, pp. 160–172, Apr. 1940, doi: 10.1017/S0305004100017138.

[85] D. S. Sanditov and V. N. Belomestnykh, “Relation between the parameters of the elasticity theory and averaged bulk modulus of solids,” *Technical Physics*, vol. 56, no. 11, pp. 1619–1623, Nov. 2011, doi: 10.1134/S106378421111020X.

[86] T. Jia, G. Chen, and Y. Zhang, “Lattice thermal conductivity evaluated using elastic properties,” *Phys Rev B*, vol. 95, no. 15, p. 155206, Apr. 2017, doi: 10.1103/PhysRevB.95.155206.

[87] Y. Xiao *et al.*, “Origin of low thermal conductivity in SnSe,” *Phys Rev B*, vol. 94, no. 12, p. 125203, Sep. 2016, doi: 10.1103/PhysRevB.94.125203.

[88] B. Debnath, U. Sarkar, M. Debbarma, R. Bhattacharjee, and S. Chattopadhyaya, “Modification of band gaps and optoelectronic properties of binary calcium chalcogenides by means of doping of magnesium atom(s) in rock-salt phase- a first principle based theoretical initiative,” *J Solid State Chem*, vol. 258, pp. 358–375, Feb. 2018, doi: 10.1016/j.jssc.2017.10.028.

[89] F. Saad Saoud, J. Claude Plenet, and M. Henini, “Structural, electronic and vibrational properties of InN under high pressure,” *Physica B Condens Matter*, vol. 407, no. 6, pp. 1008–1013, Mar. 2012, doi: 10.1016/j.physb.2011.12.129.

[90] G. Gökoğlu, “First principles study of barium chalcogenides,” *Journal of Physics and Chemistry of Solids*, vol. 69, no. 11, pp. 2924–2927, Nov. 2008, doi: 10.1016/j.jpcs.2008.08.012.

[91] S. Drablia *et al.*, “*Ab initio* calculations of the structural, electronic, thermodynamic and thermal properties of $BaSe_{1-x}Te_x$ alloys,” *Phys Scr*, vol. 92, no. 10, p. 105701, Oct. 2017, doi: 10.1088/1402-4896/aa842e.

[92] B. Khalfallah *et al.*, “A first-principles study of the structural, elastic, electronic, vibrational, and optical properties of $BaSe_{1-x}Te_x$,” *J Comput Electron*, vol. 17, no. 4, pp. 1478–1491, Dec. 2018, doi: 10.1007/s10825-018-1249-y.

[93] R. W. Keyes, “High-Temperature Thermal Conductivity of Insulating Crystals: Relationship to the Melting Point,” *Physical Review*, vol. 115, no. 3, pp. 564–567, Aug. 1959, doi: 10.1103/PhysRev.115.564.

[94] Z. Chang *et al.*, “Anomalous Thermal Conductivity Induced by High Dispersive Optical Phonons in Rubidium and Cesium Halides,” *ES Energy & Environment*, 2022, doi: 10.30919/esee8c653.

[95] S. C. Rakesh Roshan *et al.*, “Anomalous Lattice Thermal Conductivity in Rocksalt IIA–VIA Compounds,” *ACS Appl Energy Mater*, vol. 5, no. 1, pp. 882–896, Jan. 2022, doi: 10.1021/acsaem.1c03310.

[96] M. Al-Fahdi, X. Zhang, and M. Hu, “Phonon transport anomaly in metavalent bonded materials: contradictory to the conventional theory,” *J Mater Sci*, vol. 56, no. 33, pp. 18534–18549, Nov. 2021, doi: 10.1007/s10853-021-06540-7.

[97] M. L. Valeri-Gil and C. Rincón, “Thermal conductivity of ternary chalcopyrite compounds,” *Mater Lett*, vol. 17, no. 1–2, pp. 59–62, Jul. 1993, doi: 10.1016/0167-577X(93)90148-Q.

[98] E. Al Dawood, A. Shafique, and U. Schwingenschlögl, “Anomalous Ultralow Lattice Thermal Conductivity in Mixed-Anion Ba_4Sb_2Se and Ba_4Sb_2Te,” *ACS Appl Electron Mater*, vol. 5, no. 8, pp. 4268–4274, Aug. 2023, doi: 10.1021/acsaelm.3c00542.

[99] J. Sun, G. Chen, S. Li, and X. Liu, “Light Atomic Mass Induces Low Lattice Thermal Conductivity in Janus Transition-Metal Dichalcogenides MSSe (M═Mo, W),” *The Journal of Physical Chemistry C*, vol. 127, no. 35, pp. 17567–17574, Sep. 2023, doi: 10.1021/acs.jpcc.3c03201.

[100] L. Tairi *et al.*, “Phase stability and electronic behavior of MgS, MgSe and MgTe compounds,” *Phase Transitions*, vol. 90, no. 10, pp. 929–941, Oct. 2017, doi: 10.1080/01411594.2017.1302085.

[101] S. N. Rashkeev and W. R. L. Lambrecht, “Second-harmonic generation of I-III- VI2 chalcopyrite semiconductors: Effects of chemical substitutions,” *Phys Rev B*, vol. 63, no. 16, p. 165212, Apr. 2001, doi: 10.1103/PhysRevB.63.165212.

[102] S. Pan *et al.*, “A $_2$ Cu $_3$ In $_3$ Te $_8$ (A = Cd, Zn, Mn, Mg): A Type of Thermoelectric Material with Complex Diamond-like Structure and Low Lattice Thermal Conductivities,” *ACS Appl Energy Mater*, vol. 2, no. 12, pp. 8956–8965, Dec. 2019, doi: 10.1021/acsaem.9b02004.

[103] J. Yao *et al.*, “Thermoelectric properties of p-type CuInSe2 chalcopyrites enhanced by introduction of manganese,” *Phys Rev B*, vol. 84, no. 7, p. 075203, Aug. 2011, doi: 10.1103/PhysRevB.84.075203.

[104] L. Lindsay, D. A. Broido, J. Carrete, N. Mingo, and T. L. Reinecke, “Anomalous pressure dependence of thermal conductivities of large mass ratio compounds,” *Phys Rev B*, vol. 91, no. 12, p. 121202, Mar. 2015, doi: 10.1103/PhysRevB.91.121202.

[105] B. Mortazavi, F. Shojaei, T. Rabczuk, and X. Zhuang, “High tensile strength and thermal conductivity in BeO monolayer: A first-principles study,” *FlatChem*, vol. 28, p. 100257, Jul. 2021, doi: 10.1016/j.flatc.2021.100257.

[106] N. Shulumba, O. Hellman, and A. J. Minnich, “Intrinsic localized mode and low thermal conductivity of PbSe,” *Phys Rev B*, vol. 95, no. 1, p. 014302, Jan. 2017, doi: 10.1103/PhysRevB.95.014302.

[107] N. Yedukondalu, T. Pandey, and S. C. Rakesh Roshan, “Effect of Hydrostatic Pressure on Lone Pair Activity and Phonon Transport in Bi $_2$ O $_2$ S,” *ACS Appl Energy Mater*, vol. 6, no. 4, pp. 2401–2411, Feb. 2023, doi: 10.1021/acsaem.2c03725.

[108] A. Cammarata and T. Polcar, “Fine control of lattice thermal conductivity in low-dimensional materials,” *Phys Rev B*, vol. 103, no. 3, p. 035406, Jan. 2021, doi: 10.1103/PhysRevB.103.035406.

[109] A. Cammarata and T. Polcar, “Layering effects on low frequency modes in n-layered MX $_2$ transition metal dichalcogenides,” *Physical Chemistry Chemical Physics*, vol. 18, no. 6, pp. 4807–4813, 2016, doi: 10.1039/C5CP06788J.

[110] Y. Xia *et al.*, “High-Throughput Study of Lattice Thermal Conductivity in Binary Rocksalt and Zinc Blende Compounds Including Higher-Order Anharmonicity,” *Phys Rev X*, vol. 10, no. 4, p. 041029, Nov. 2020, doi: 10.1103/PhysRevX.10.041029.

[111] W. Li, J. Carrete, N. A. Katcho, and N. Mingo, “ShengBTE: A solver of the Boltzmann transport equation for phonons,” *Comput Phys Commun*, vol. 185, no. 6, pp. 1747–1758, Jun. 2014, doi: 10.1016/j.cpc.2014.02.015.

[112] T. Liang, W.-Q. Chen, C.-E. Hu, X.-R. Chen, and Q.-F. Chen, “Lattice dynamics and thermal conductivity of lithium fluoride via first-principles calculations,” *Solid State Commun*, vol. 272, pp. 28–32, Apr. 2018, doi: 10.1016/j.ssc.2018.01.004.

CHAPTER-4

Highly Anisotropic to Isotropic and Ultralow out-of-plane Lattice Thermal Conductivity of Layered PbClF-type Materials (Alkaline Earth halo fluorides)

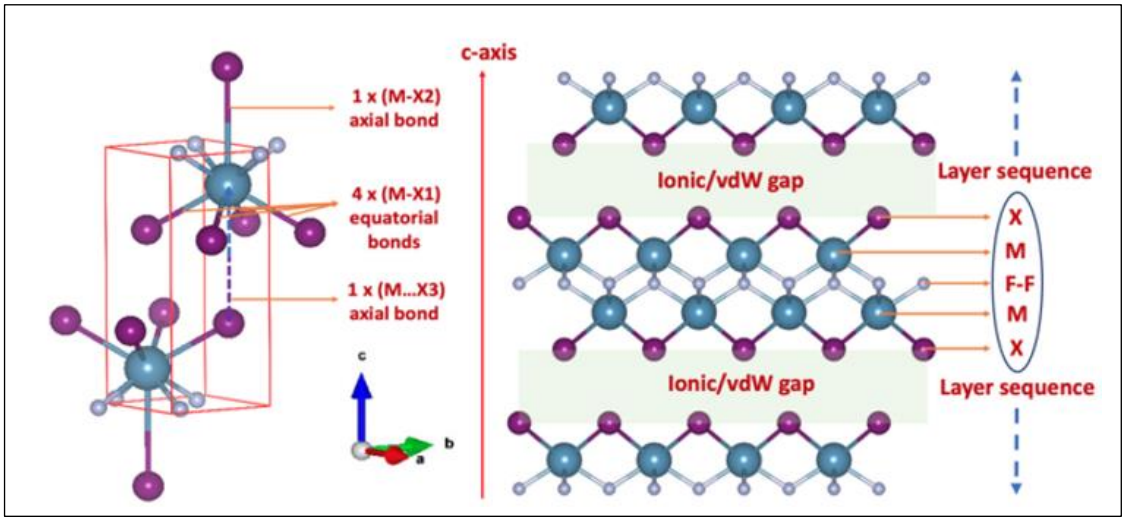

Publication from this chapter: (Accepted for Publication)

Highly Anisotropic to Isotropic nature and Ultralow Out-of-plane Lattice Thermal Conductivity of Layered PbClF-type Materials**, Rakesh Roshan, S. Chand;** Yedukondalu, Neelam.; Rajaboina, Rakesh Kumar; Huang, Haw-Tyng; T., E,Lars; Parise, J.B., ***ACS inorganic Chemistry*** **(2024) .**

Discovery and design of functional quasi two dimensional (2D) layered materials with extremely low or high lattice thermal conductivity (κ_L) are crucial for thermal energy management applications [1], [2]. Ultralow κ_L materials find potential applications in thermoelectrics [3], [4], thermal insulation [5], [6], thermal storage [7], [8] , thermal barrier coatings [9]–[12], while high κ_L materials find applications in power electronics and solid state lighting [13], [14].

A plethora of mechanisms [15]–[21] were proposed to achieve low κ_L. Among them, bonding heterogeneity is an essential mechanism and it is an intrinsic property of layered materials. The layered materials are bonded through strong covalent/ionic bonds in the in-plane and coupled by weak van der Waals (vdWs)/strong electrostatic interactions in the out-of-plane direction i:e:, bonding heterogeneity thus resulting in a strong/weak structural anisotropy [1], [22]. Therefore, through bonding heterogeneity, these layered materials provide an avenue for tailoring phonon transport properties. Investigation of iso-structural layered materials with varying average atomic mass is intriguing because they allow to make structure-property correlations by exploring the interplay between bonding heterogeneity and atomic mass and also their implications on lattice dynamics thereby fine tuning the phonon transport properties [1], [2].

Exploring mechanisms to achieve low κ_L is essential for discovering functional materials through chemical intuition in layered materials by fine tuning the phonon group velocities and scattering rates/lifetimes.

4.1. Alkali halo fluorides

MXF (M = Ca, Sr, Ba and X = Cl, Br, I) compounds are quasi-2D materials crystallizing in the tetragonal crystal structure with space group *P4/nmm* (Fig. 4.1a). The structure is obtained from ionically bonded X-M-F-F-M-X layers that are stacked along the c-axis and bound to each other by weak vdW forces (Fig. 4.1b). These materials attracted tremendous attention because of their unique electronic properties and promising applications such as energy storage, photo-detectors, optoelectronic devices [23]–[25]. Barhoumi et al. [26] investigated the vibrational and electronic properties of monolayers of BaFBr, CaFBr, and BaFCl. According to the findings of Tan et al. [27], lead dihalides with bandgaps ranging from 2.3 eV (PbI_2) to 5.8 eV (PbF_2)

are optimal wide bandgap semiconductors for the fabrication of UV photodetectors. In numerous applications, including power electronics and solid-state lightings, ultra-wide bandgap (UWBG) semiconductors have been utilized extensively [13], [14]. Recently, materials with UWBG and ultralow κ_L have gained lot of attention as these materials find promising applications in thermal barrier coatings and turbine industries [9]–[12]. As the MXF materials are layered with bonding heterogeneity and the variation of alkaline-earth metal (M) and halogen (X) atomic mass provides an opportunity to explore the interplay between bonding heterogeneity and atomic mass on the phonon transport. Although MXF materials have been investigated extensively, only a few studies were focused to comprehend the phonon transport properties and anharmonic lattice dynamics under ambient conditions [28], [29]. Therefore, in the present study, a detailed investigation has been carried out to explore chemical bonding, anharmonic lattice dynamics and phonon transport properties of these layered PbClF-type materials.

4.2 Computational Details

The Vienna Ab-initio Simulation Package (VASP) [30] was employed to perform the first-principles calculations. The Perdew-Burke-Ernzerhof revised for solids (PBEsol) functional within the generalized gradient approximation (GGA) was utilized to treat the exchange-correlation interactions. The electron-ion interactions were treated employing the projector augmented wave (PAW) pseudopotential approach. The plane wave basis orbitals listed below were regarded as valence electrons. **F:** $2s^2$,$2p^5$; **Cl:** $3s^2$,$3p^5$; **Br:** $4s^2$,$4p^5$; **I:** $5s^2$,$5p^5$; **Ca:** $4s^2$, **Sr:** $5s^2$, **Ba:** $6s^2$. A plane wave energy cutoff of 560 eV was used for plane wave basis set expansion and a spacing of $2\pi\times$ 0.025 A^{-1} for k-mesh in the irreducible Brillouin zone for the structural optimization, as well as the calculation of elastic constants using the stress-strain approach, born effective charges, and dielectric constants using density functional perturbation theory (DFPT). Later, ab-initio molecular dynamics (AIMD) simulations have been carried out using VASP at 300 K by considering the optimized structures at 0 K within DFT. The AIMD simulations at high temperature (Fig. 1c,d) were run for 5000 MD steps with a time-step of 1 fs (i.e., 5 ps) with a supercell sizes as summarized in Table 4.1 at Γ centred k-mesh for the MXF compounds. The temperature was controlled with a Nose-Hoover thermostat [31], [32]. The AIMD output obtained using VASP was post-processed using temperature dependent effective potential

(TDEP) [33] method to compute lattice dynamics and phonon transport properties of MXF compounds including harmonic (2^{nd}) and anharmonic (3^{rd}) interatomic force constants (IFCs). Up to 9^{th} nearest neighbours were considered for both 2^{nd} and 3^{rd} order IFCs to calculate phonon dispersion curves and phonon transport properties. The lattice thermal conductivity is determined by repeatedly solving the full Boltzmann transport equation (BTE) using a q-mesh specified in Table 4.1 for the explored MXF compounds.

4.3 Results and discussion

4.3.1 Crystal structure, chemical bonding and Raman spectra

Matlockite-type, MXF (Ca, Sr, Ba, Pb and X = Cl, Br and I) compounds crystallize in the primitive tetragonal *P4/nmm* symmetry with Z = 2 (f.u./cell) at ambient conditions [34]. The metal M (Ca, Sr, Ba, Pb), non-metal X (Cl, Br, and I) and F atoms are located at Wyckoff 5 sites 2c:(0.25, 0.25, v), 2c: (0.25, 0.25, u), and 2a:(0.75, 0.25, 0), respectively, where u and v are the internal variable coordinates of X and M atoms, respectively. By considering the crystal structures determined from X-ray diffraction (XRD) measurements [34] full structural optimization has been performed to obtain the equilibrium or ground state structures for all the MXF compounds under investigation and are compared with the XRD data and there is a good agreement between them as presented in Tables 4.2 – 4.4. In total, there are 4 inequivalent bonds, one M-F, three M-X (M-X1, M-X2 and M...X3) bonds in these MXF compounds, in which M-F bond lengths are shorter than M-X bond lengths (Table 4.5), M-X1 and M-X2, M...X3 are equatorial and axial bonds, respectively, M-X2 is bond between M and halogen (X2) within the layer whereas M...X3 is bond between M and halogen (X3) in the adjacent layer (Fig. 4.1a). As shown in Fig. 4.1a, the optimized crystal structure consists of two metal (M) cations per primitive cell based on the multiplicity of their Wyckoff site (2c), each M cation is surrounded by a 4-fold coordination of F anions in the form of square planar and a 5-fold coordination of X (Cl, Br, I) anions. M with four X's lying in the same plane forms 4 equatorial (M-X1) bonds whereas with X2 and X3, M forms M-X2/M...X3 bond within the (mono)layer/adjacent layer (see Fig. 4.1a), thus resulting in a total coordination number of 9 with a structural motif of MX_5F_4 (Fig. 4.1a). Bond length of M...X3 is lower than

M-X2 bond in CaClF, SrClF, SrBrF, BaXF (X = Cl, Br, I) compounds while the bond length of M...X3 is greater than M-X2 bond in CaBrF, CaIF and SrIF, which differentiates the later three compounds from the former 6 iso-structural compounds. The inequivalent M-X1, M-X2 and M...X3 bonds play a critical role in determining the layered nature of these materials. M-X1 and M...X3 bond lengths are closely comparable in CaClF, SrClF and BaClF (Table 1). (Table 4.5). In contrast, with increasing size of X (Cl → Br → I), the axial M-X2/M...X3 bond length is higher than equatorial M-X1 bond length for MXF (M = Ca, Sr, Ba and X = Br, I). With increasing size of X (Cl → Br → I), the packing of halide sublattice becomes largely constrained, therefore, this stress is relieved by stretching of the lattice

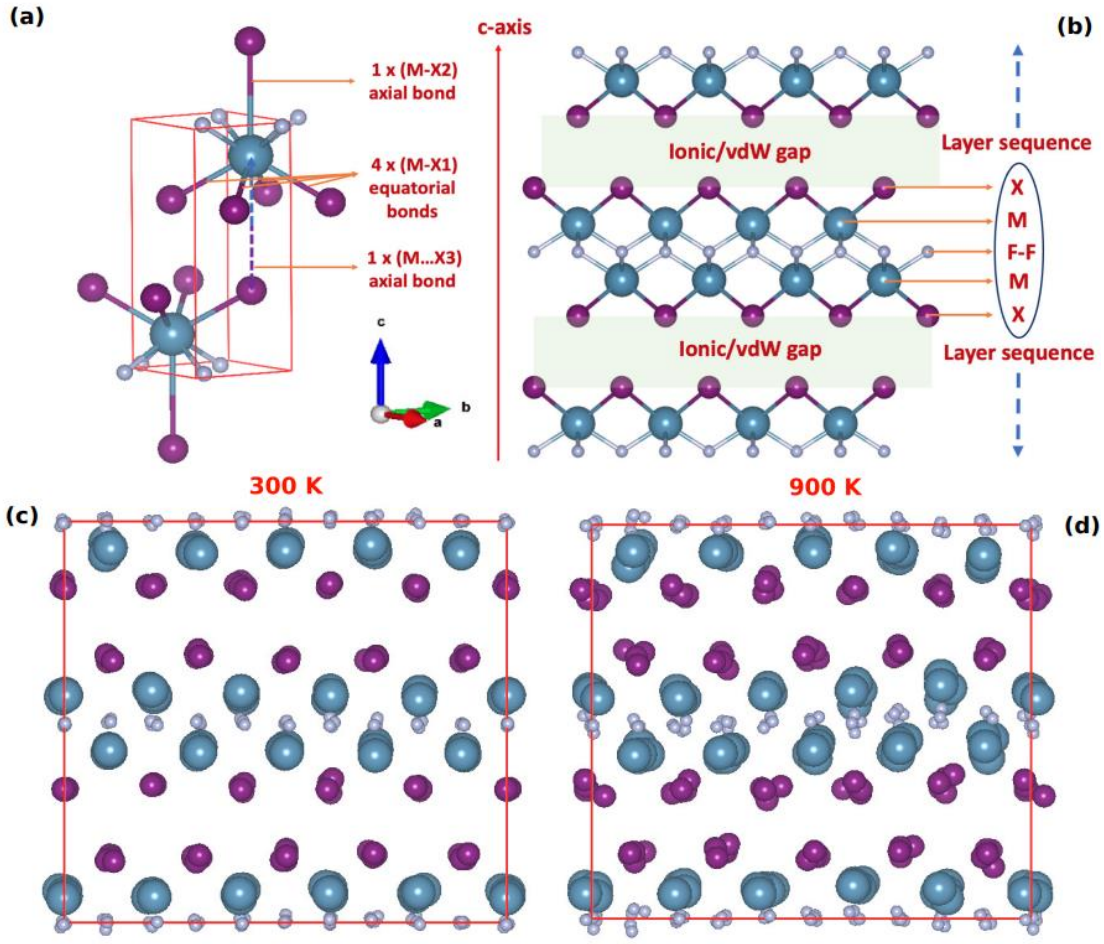

Fig 4.1: (a) Primitive/unit cell of MXF compounds with one axial (M-X2) and four equatorial (M-X1) bonds (b) Side view of layered structure with a layer sequence X-M-F-F-M-X (M = Ca, Sr, Ba and X = Cl, Br, I), and these layers are stacked along the c-axis with vdW gaps between X...X layers. Snapshot of heated CaIF supercell viewed along bc-plane (c) 300 K and (d) 900 K using AIMD simulations and visualized using VESTA software.

along the c-axis [35]. This results in increasing the axial M-X2/M...X3 bond length, which is manifested by the axial (c/a) ratio as given in Table 4.6. The bonding in CaBrF, CaIF, and SrIF is different compared to the other 6 compounds in the MXF series. The intralayer M-X1 and M-F bonds compare well with the ones calculated from the effective ionic radii (for Ca, Sr, Ba and Cl, Br, I, are 1.18, 1.31, 1.47 and 1.31, 1.81, 1.96, 2.20 in A˚, respectively), suggesting strong ionic bonding within the layers. However, the interlayer M...X3 bond is significantly longer in CaBrF, CaIF, and SrIF by 0.908 A˚, 1.506 A˚, and 1.048 A˚, respectively. This points to a change in the interlayer bonding character from ionic to vdWs bonding. The increase of axial M-X2/M...X3 bond length strongly determines the quasi two dimensional layered nature of the MXF compounds by stretching the X...X layer distance (Table 4.5). The c/a ratio is mirroring the effect observed in the bond distances, showing a decrease from CaIF to SrIF to BaIF due to a decrease of axial M-X2/M...X3 and increase of equatorial M-X1 bond lengths and the same is observed in iso-structural MHI (M = Ca, Sr, Ba) compounds [34]. The increase of axial M-X1 bond length strongly determines the quasi two-dimensional layered nature of the MXF compounds by stretching the X...X layer distance (Table 4.5), in particular, the c/a ratio is greater than 2 for CaBrF, CaIF and SrIF, enhancing the layered character in these three compounds (Fig. 4.1b). The c/a ratio increases with size of the X, while it decreases with increase in size of M (see Table 4.6). The bond angle between opposite F's (F-M-F) increases with increasing size of X, which causes the lattice to flatten out equatorially by stretching the M-F bond length while the bond angle X1-M-X3 decreases with increasing the size of X, squeezes the halide sublattice thus enhancing the electron density in the equatorial M-X1 bonds [35].

Table 4.1: Supercell and K-mesh details of MXF (M = Ca, Sr, Ba and X =Cl, Br, I) compounds considered for computations in current study.

Compound	**Supercell (No. of atoms)**	**q-mesh**
CaClF	4*4*2 (192)	19*19*19
CaBrF	4*4*2 (192)	22*22*10
CaIF	5*5*2 (300)	21*21*9
SrClF	3*3*2 (108)	20*20*12

SrBrF	4*4*2 (192)	20*20*11
SrIF	4*4*2 (192)	20*20*9
BaClF	4*4*2 (192)	19*19*12
BaBrF	4*4*2 (192)	19*19*11
BaIF	4*4*2 (192)	18*18*11

Table 4.2: Calculated structural properties i.e. lattice constants (a,c) (in A^o), Volume V (in $(A^o)^3$), internal coordinates (v,u) of CaXF (X = Cl, Br and I) compounds using PBEsol are compared with available X-ray diffraction data and other theoretical calculations.

Compound	**Method**	**a**	**c**	**V**	**v**	**u**
CaClF	This Work	3.854	6.742	100.14	0.196	0.642
	Expt.[36]	3.894	6.818	103.38	0.1962	0.6432
	Others	3.939 [37], 3.894 [38]	6.898 [37], 6.811 [38]	-	0.194902 [37]	0.642250 [37]
CaBrF	This Work	3.84	8.043	118.6	0.164	0.667
	Expt.[39]	3.883	8.05	121.38	0.17	0.67
	Others	3.926 [37], 3.829 [38]	8.139 [37], 7.926 [38]	-	0.165145 [37]	0.665408 [37]
CaIF	This Work	3.965	9.046	142.21	0.139	0.679
	Others [37]	4.029	9.669	-	0.132683	0.691725

Table 4.3: Calculated structural properties i.e. lattice constants (a,c) (in A^o), Volume V (in $(A^o)^3$), internal coordinates (v,u) of SrXF (X = Cl, Br and I) compounds using PBEsol are compared with available X-ray diffraction data and other theoretical calculations.

Compound	**Method**	**a**	**c**	**V**	**v**	**u**
SrClF	This Work	4.092	6.915	115.79	0.202	0.643
	Expt.[40]	4.126	6.958	118.452	0.2015	0.6429

	Others	4.185 [41], 4.129 [38]	7.057 [41], 6.966 [38]	-	0.20152 [41]	0.642900 [41]
		4.163 [42]	6.827 [42]	-	0.189 [42]	0.664 [42]
SrBrF	This Work	4.184	7.284	127.51	0.187	0.646
	Expt.[43]	4.218	7.337	130.536	0.1859	0.6479
	Others	4.261 [44], 4.084 [45]	7.482 [44], 7.105 [45]	-	0.187089 [44]	0.645628 [44]
		4.212 [38]	6.985 [38]	-	0.184 [38]	0.668 [38]
SrIF	This Work	4.211	8.834	156.65	0.151	0.667
	Expt.[44]	4.253	8.833	159.77	0.167	0.657
	Others	4.305 [44] 4.173 [45]	8.916 [44] 8.667 [45]	143.96 [46]	0.152826 [44]	0.664 [44]
		4.4469 [46]	7.2801 [46]			

Table 4.4: Calculated structural properties i.e. lattice constants (a,c) (in A^o), Volume V (in $(A^o)^3$), internal coordinates (v,u) of BaXF (X = Cl, Br and I) compounds using PBEsol are compared with available X-ray diffraction data and other theoretical calculations.

Compound	**Method**	**a**	**c**	**V**	**v**	**u**
BaClF	This Work	4.368	7.201	137.39	0.206	0.648
	Expt.[40]	4.394	7.225	139.49	0.2049	0.6472
	Others	4.450 [37], 4.391 [25]	7.317 [37], 7.22 [25]	139.48[47]	0.204436 [37]	0.647142 [37]
		4.427 [42], 4.3934[25]	7.126 [42], 7.2264 [25]	139.48 [25]	0.191 [42]	0.660 [42]
BaBrF	This Work	4.482	7.419	149.04	0.193	0.648

	Expt.[36]	4.508	7.441	151.22	0.1911	0.6497
	Others [42]	4.536	7.639	-	0.192544	0.648100
	Others	4.479 [47]	7.229 [47]	-	0.1911 [47]	0.662 [47]
BaIF	This Work	4.625	7.896	168.9	0.172	0.648
	Expt.[36]	4.654	7.962	172.45	0.1704	0.6522
	Others	4.634 [42], 4.709 [47]	7.752 [42], 8.085 [47]	-	0.173 [42], 0.170359 [47]	0.6522 [42] 0.649649 [47]

Table 4.5: Calculated bond lengths (in A^o) and angles (in ^{0}) of MXF (M = Ca, Sr, Ba and X = Cl, Br, I) compounds.

Compound	**Method**	**M-F**	**∠F-M-F**	**M…X3**	**M-X1**	**M-X2**	**∠X1-M-X3**
CaClF	This Work	2.338	111	3.007	2.934	3.735	68.2
	Others[36]	2.32	111	3.048	2.963	-	68.3
CaBrF	This Work	2.328	111.1	4.048	3.037	3.994	63.4
CaFI	This Work	2.349	115.1	4.886	3.248	4.16	59.7
SrClF	This Work	2.477	111.4	3.054	3.085	3.862	69.7
	Others [40]	2.494	111.6	3.072	3.112	-	69.6
SrBrF	This Work	2.495	113.9	3.346	3.201	3.938	67.6
	Others [44]	2.511	-	-	3.222	-	-
SrIF	This Work	2.494	115.2	4.558	3.382	4.276	61.7
BaClF	This Work	2.641	111.6	3.179	3.263	4.022	71.2
	Others[36]	2.649	112.1	3.196	3.286	-	71
BaBrF	This Work	2.659	114.9	3.375	3.382	4.044	69.6
	Others[36]	2.665	115.5	3.412	3.401	-	69.6
BaIF	This Work	2.682	119.1	3.762	3.564	4.134	66.6

	Others[36]	2.694	119.5	3.836	3.581	-	66.8

Table 4.6: Calculated (c/a) ratio compared with other theory and experiments.

Compound	**This Work**	**Theory**	**Experiment**
CaClF	1.749	1.751 [41], 1.749[38]	1.751 [36]
CaBrF	2.095	2.073 [41], 2.070[45]	2.073 [44]
CaIF	2.281	2.399 [41]	-
SrClF	1.689	1.686 [41],1.687 [38],1.639 [42]	1.686 [40]
SrBrF	1.741	1.765 [41],1.74 [38],1.658 [42]	1.739 [44]
SrIF	2.098	2.071 [41],2.07 [38]	2.071 [44]
BaClF	1.648	1.644 [41],1.644 [38],1.609 [42]	1.644 [40],1.64[48], 1.646[49]
BaBrF	1.655	1.684 [41],1.651 [38],1.614 [42]	1.651 [36],1.65 [48]
BaIF	1.707	1.728 [41],1.711 [38],1.673 [42]	1.711 [36],1.71 [48]

Overall, the crystal structure is formed by a sequence of ionically (as evidenced from the calculated Bader charges presented in Table 4.7) bonded X-M-F-F-M-X layers [22], [50], which are stacked perpendicular to c-axis and these layers are bonded through weak van der Waals (vdW) interactions along the c-axis (Fig. 4.1b), thus, resulting in a bonding heterogeneity [15] i:e:, intralayer ionic and weak interlayer vdW bonding in these class of PbClF-type or matlockite-type materials.

Table 4.7: Calculated Bader Charges for MXF (M = Ca, Sr, Ba and X = Cl, Br,I) compounds.

Compound	**M**	**F**	**X**
CaClF	1.616	-0.827	-0.789
CaBrF	1.596	-0.831	-0.764
CaFI	1.572	-0.846	-0.728
SrClF	1.632	-0.838	-0.793
SrBrF	1.617	-0.848	-0.77

SrIF	1.596	-0.855	-0.741
BaClF	1.626	-0.834	-0.792
BaBrF	1.604	-0.843	-0.762
BaIF	1.57	-0.853	-0.717

To further reveal the bonding nature of MXF compounds, the potential energy curves are calculated by off-centering M, X, F atoms from their equilibrium position. As shown in Fig. 4.2, the potential energy curves show deep potential wells for M and X atoms, when they are displaced along the out-of-plane direction. While the shallow potential well is observed along in-plane direction for X atoms, this indicates rattling motion of X atoms originating from the bonding heterogeneity, especially for materials with axial ratio (c/a) > 2, such as CaBrF, CaIF and SrIF, which would be highly anistropic and expected to have low κ_L along the out-of-plane direction.

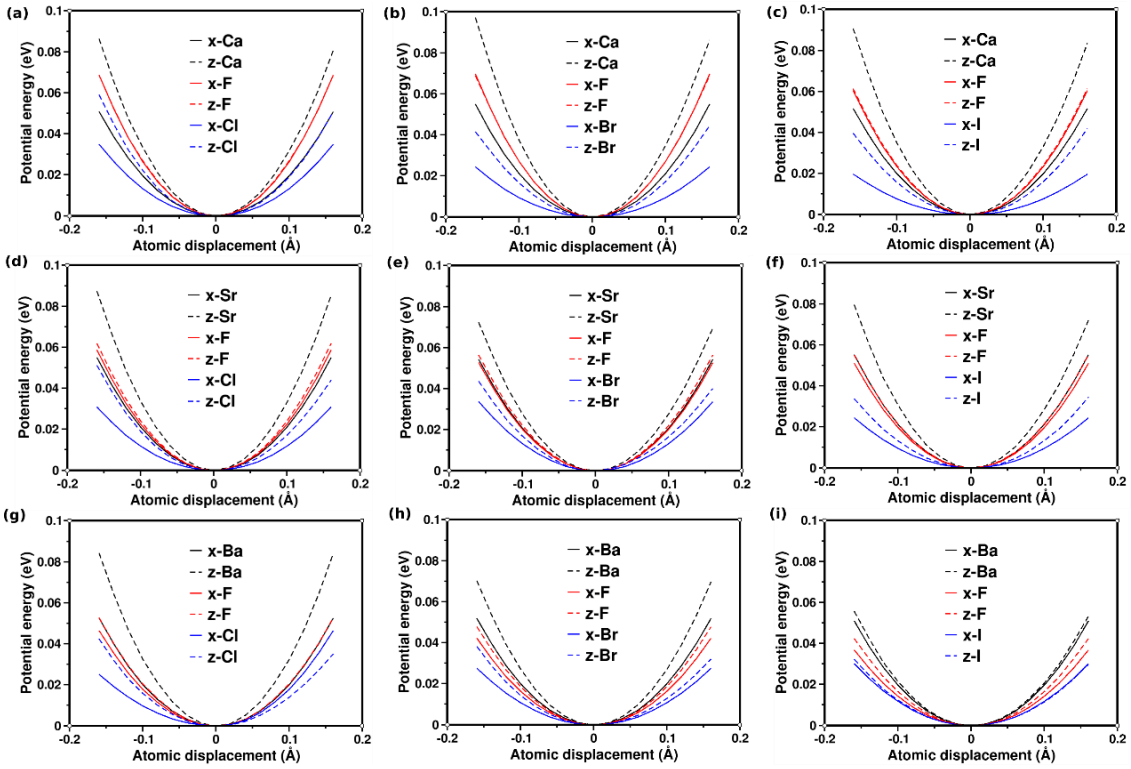

Fig 4.2: Potential energy curves for (a) CaClF, (b) CaBrF, (c) CaIF, (d) SrClF, (e) SrBrF, (f) SrIF, (g) BaClF, (h) BaBrF and (i) BaIF by off-centering M (Ca, Sr, Ba), X (Cl, Br, I), F atoms from their equilibrium positions.

Zone center Raman and/or IR spectra are used to further explore the chemical bonding and lattice dynamics of materials. The zone center phonon frequencies are extensively studied for PbClF-type materials [15], [28] [51]–[54]. The PbClF-type

materials consist of six atoms per primitive cell resulting in total of 18 (3 acoustic and 15 optic) phonon modes. Group theory predicts the symmetry decomposition of phonon modes at Γ-point for *P4/nmm* space group is given as follows:

$$\Gamma_{18} = 2A_{1g} \oplus B_{1g} \oplus 3E_g \oplus 3E_u \oplus 3A_{2u},$$

in which six are Raman active (A_{1g}, B_{1g}, E_g) and four are IR active (A_{2u}, E_u) modes. Here, "E" denotes the doubly degenerate vibrational modes in xy-plane, whereas "A" and "B" modes represent vibrations along c-axis or out-of-plane direction (Table 4.8). The detailed phonon vibrational mode analysis can be found elsewhere [15], [28] [51]–[54]. In this study, Raman spectra and Raman-shift for MXF (Ca, Sr Ba and X = Cl, Br and I) compounds have been calculated and are presented in Figure 4.3 and Tables 4.9 – 4.11, respectively.

As it can be clearly seen from Fig. 4.3, all the 9 compounds under investigation have 6 Raman active modes due to their iso-structure. However, these compounds show significant differences in the Raman spectra owing to difference in atomic mass as well as nature of layered structure in Ca, Sr and Ba series. As lighter atoms can vibrate with higher frequency compared to heavier ones, the Raman-shift shows a red-shift with increase in atomic mass of alkaline-earth metal (M) and halogen (X). In addition, this red-shift is much more pronounced in CaXF and SrXF series over BaXF series. The red-shift observed in the low-frequency optic phonon modes is greater than in the high-frequency optic phonon modes. A strong A_{1g} mode is observed for layered materials (CaBrF, CaIF and SrIF) especially with axial ratio greater than 2, which might serve as an indication from Raman spectra to distinguish between strongly anisotropic materials from the isotropic ones.

Table 4.8 : Factor group analysis for the crystal structure of tetragonal MFX unit cell.

Ion	**Wyckoff site**	**Site symmetry**	**Irreducible Representation**
M	2c	4mm (C_{4v})	$A_{1g} \oplus A_{2u} \oplus E_g \oplus E_u$
F	2a	-4m2 (D_{2d})	$A_{2u} \oplus B_{1g} \oplus E_g \oplus E_u$
X	2c	4mm (C_{4v})	$A_{1g} \oplus A_{2u} \oplus E_g \oplus E_u$

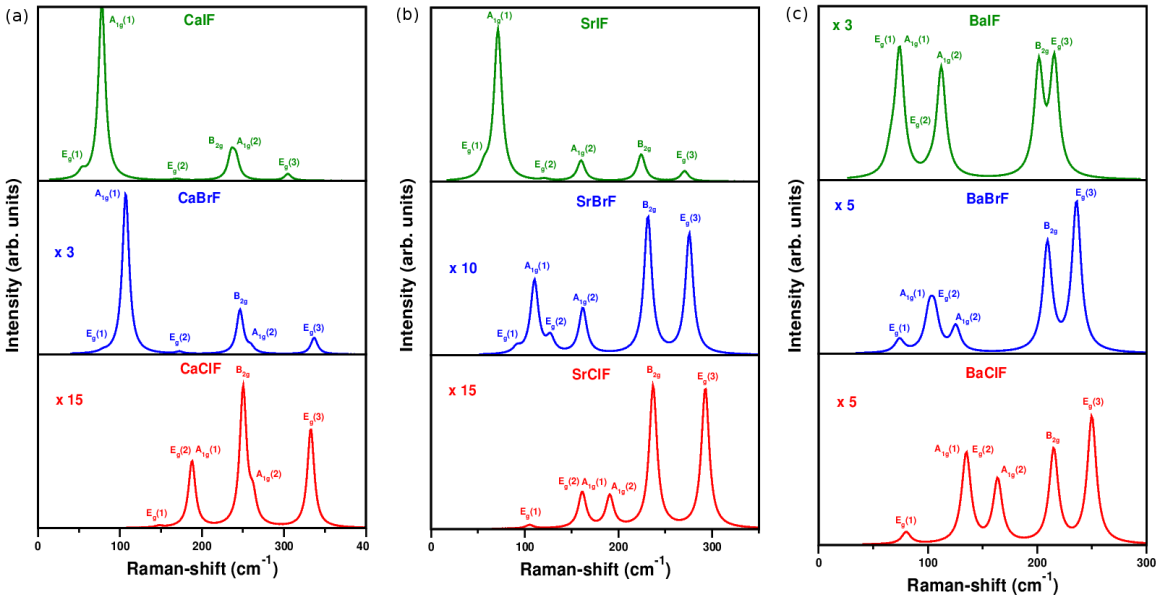

Fig 4.3: Raman Spectra for MXF (M = Ca, Sr, Ba and X = Cl, Br, I) at ambient conditions. The Raman intensities are scaled for CaClF (×15), CaBrF (×3), SrClF (×15) and SrBrF (×10), BaClF (×5), BaBrF (×5) and BaIF (×3).

Table 4.9: Calculated Raman active modes for CaXF (X = Cl, Br, I) compounds compared with available experimental and other previous studies.

Compound	Raman Mode	Frequency		
		(This work)	Experiment	Others
CaClF	$E_g(1)$	147.6	156[55]	168[56]
	$E_g(2)$	184.37	209 [55]	204 [56]
	$A_{1g}(1)$	187.86	192 [55]	202 [56]
	B_{2g}	250.24	252 [55]	262 [56]
	$A_{1g}(2)$	262.21	265 [55]	278 [56]
	$E_g(3)$	332.72	336 [55]	347 [56]
CaBrF	$E_g(1)$	79.36	-	-
	$A_{1g}(1)$	107	-	-
	Eg(2)	172.53	-	-
	B_{2g}	246.36	-	-
	$A_{1g}(2)$	259.59	-	-
	$E_g(3)$	336.84	-	-

CaIF	$E_g(1)$	53.64	-	-
	$A_{1g}(1)$	77.88	-	-
	$E_g(2)$	169.56	-	-
	B_{2g}	235.67	-	-
	$A_{1g}(2)$	241.4	-	-
	$E_g(3)$	304.82	-	-

Table 4.10: Calculated Raman active modes for SrXF (X = Cl, Br, I) compounds compared with available experimental and other previous studies.

Compound	**Raman Mode**	**Frequency**		
		This work	**Experiment**	**Others**
SrClF	$E_g(1)$	105.17	107[57]	105.45 [58], 107 [59], 115 [56]
	$E_g(2)$	161.18	167 [57],164[55]	160.99 [58],168 [59],180 [56]
	$A_{1g}(1)$	162.05	159 [57]	161.76 [58],170 [59],173 [56]
	$A_{1g}(2)$	190.76	196 [57], 194 [55]	190.74 [58], 201 [59] ,214 [56]
	B_{2g}	231.5	243 [57], 241 [55]	242.72 [58], 230 [59], 251 [56]
	$E_g(3)$	292.72	298 [57], 296 [55]	296.28 [58], 289 [59], 312 [56]
SrBrF	$E_g(1)$	91.7	-	97[42]
	$A_{1g}(1)$	110.41	-	114 [42]
	$E_g(2)$	127.4	-	138 [42]
	$A_{1g}(2)$	162.01	-	186 [42]
	B_{2g}	237.02	-	235 [42]
	$E_g(3)$	275.63	-	241 [42]
SrIF	$E_g(1)$	56.83	-	-

	$A_{1g(}1)$	71.42	-	-
	$E_{g(}2)$	121.12	-	-
	$A_{1g}(2)$	160.15	-	-
	B_{2g}	224.35	-	-
	$E_g(3)$	270.58	-	-

Table 4.11: Calculated Raman active modes for BaXF (X = Cl, Br, I) compounds compared with available experimental and other previous studies.

Compound	**Raman Mode**	**Frequency**		
		This work	**Experiment**	**Others**
BaClF	$E_g(1)$	80.15	89 [57],82 [55]	81.34 [51], 83[60], 79[56]
	$A_{1g(}1)$	132.79	125 [57], 132 [55]	128.36 [51],145 [60], 131 [56]
	$E_{g(}2)$	135.27	142 [57], 143 [55]	135.54 [51],147 [60], 141 [56]
	$A_{1g}(2)$	163.9	162 [57], 165 [55]	161.64 [51],169 [60], 165 [56]
	B_{2g}	215.17	212 [57], 216 [55]	216.73 [51], 237 [60],215 [56]
	$E_{g(}3)$	250.02	247 [57], 251 [55]	308.72 [51], 277 [60],253 [56]
BaBrF	$E_g(1)$	74.09	76 [57], 76 [55]	74.46 [51], 70 [56],76[61]
	$A_{1g}(1)$	101.29	105 [57], 103 [55]	99.85 [51], 95 [56],105 [61]
	$E_g(2)$	106.21	109 [57], 109 [55]	104.71 [51], 98 [56],109 [61]

	$A_{1g}(2)$	125.58	119 [57], 123 [55]	122.94 [51], 123 [56],119 [61]
	B_{2g}	209.4	215 [57], 211 [55]	208.85 [51], 211 [56],215 [61]
	$E_g(3)$	235.99	240 [57], 238 [55]	315.90 [51], 234 [56],240 [61]
BaIF	$E_g(1)$	66.35	40[48],67 [55]	70[62],64 [56]
	$A_{1g}(1)$	74.15	81 [48], 78 [55]	79 [62],76 [56]
	$E_g(2)$	101.41	74 [48], 111 [55]	105 [62],101 [56]
	$A_{1g(}2)$	112.27	113 [48], 102 [55]	113 [62],118 [56]
	B_{2g}	201.52	205 [48], 203 [55]	203 [62],205 [56]
	$E_g(3)$	215.75	221 [48], 219 [55]	218 [62],227 [56]

4.3.2 Elastic constants and poly-crystalline properties

To furthermore investigate the bonding heterogeneity, elastic constants are calculated for the nine MXF compounds and are presented in the Table 4.12. Since the PbClF-type materials crystallize in the primitive tetragonal symmetry (*P4/nmm*), they possess six independent elastic constants C_{11}, C_{33}, C_{12}, C_{13}, C_{44} and C_{66}. The computed elastic constants obey Born's stability criteria [63], [64], which clearly indicates that the investigated MXF materials are mechanically stable at ambient pressure. The out-of-plane elastic constant C_{33} is less than the in-plane elastic constant C_{11} indicating that the lattice is weaker along the c- axis compared to a-axis for all these MXF systems, and it is due to weakly bonded vdW interactions between the X-M-F-F-M-X layers stacked along the c-axis.

Table 4.12: Calculated second order elastic constants (in GPa) at PBEsol equilibrium volume for MXF (M = Ca, Sr, Ba and X = Cl, Br, I) compounds.

Compound	**Method**	**C_{11}**	**C_{33}**	**C_{44}**	**C_{66}**	**C_{12}**	**C_{13}**
CaClF	This Work	106.8	72.5	33.9	36.4	36	46.6

	Others [50]	98.9	69.7	24.4	32.9	38.1	52.9
	Others [65]	110.8	93.2	34.8	38.2	35.7	50.5
CaBrF	This Work	93.7	15.3	18.3	29.2	21.1	17.7
	Others [50]	93	24.3	10	27.2	18.7	15.6
CaIF	This Work	79.3	16.6	8.9	22.3	12	9.1
SrClF	This Work	92.4	78	27.8	30.3	28.8	42.2
	Expt-1 [66]	91.2	77	29.5	30.9	29	40.2
	Expt-2 [67]	93.8	76.8	28.7	31.5	29.6	-
	Others [68]	93	76.1	29.8	31.2	29.2	42.2
	Others [50]	81	65.3	28.3	27.8	26.3	38.9
SrBrF	This Work	83.3	50.9	27.9	30.8	28.4	35.8
	Expt. [43]	88.7	53.3	27.4	-	-	35
	Others [50]	73.6	57.7	29.4	28.9	27.6	37.6
	Others [65]	80.9	68.2	26.1	27.9	26.1	36.9
SrIF	This Work	66.1	13.7	13.7	23.5	12.8	14
	Others [46]	80.87	30.65	23.42	26.69	19.05	23.37
	Others [50]	71.3	24.3	31.5	30.2	27.2	29.8
	Others [65]	65.5	55.2	20.6	22.6	21	30
BaClF	This Work	76.8	66.9	19.8	23.8	26.3	39.7
	Others [69]	73.1	67.3	19.8	26.1	29.3	34
	Expt. [65]	74.3	65.7	21	24.1	25.2	33
	Expt. [65]	74.3	65.9	21.3	23.5	24.9	36
BaBrF	This Work	70	54.8	19.6	24.9	25.9	34.4
	Others [69]	71.9	56.1	21.1	27.2	26.7	33.2
	Others [65]	65.3	55	20.5	22.5	21	29.8
BaIF	This Work	60.4	35.7	21.2	25.3	24.5	27.4
	Others [69]	59.2	33.8	20.4	26.69	24.3	27.3

	Others [65]	55.5	46.8	17.5	19.1	17.9	25.3

The bulk (B), shear (G), and Young's (E) moduli have been derived from the obtained elastic constants using the relationships as given in the ref. [70]. CaClF has the highest E value among the MXF (M = Ca, Sr, Ba and X = Cl, Br, I) compounds, indicating that CaClF is the stiffest compound. The derived elastic moduli (E, B, G) decrease with increasing size of halogen (X) in a series (Tables 4.13 & 4.14). For instance, in CaXF (X = Cl, Br, I) series, this indicates weak electrostatic/interatomic interactions in the lattice as atomic size increases, i:e: from Cl to I and the same is true for SrXF and BaXF series, where X = Cl, Br, I. As a result, materials with larger anionic sizes are more easily deformed under mechanical stress. In contrast, anomalous trends are observed with increasing size of the alkaline-earth metal (M) in these MXF (X = Br, I) compounds. For example, the elastic moduli (E, B, G) values are lower for CaBrF over SrBrF and BaBrF, similarly, lower elastic moduli are observed for CaIF and SrIF compared to BaIF, which will be reflected in lowering κ_L for the CaBrF, CaIF and SrIF. For covalent and ionic materials, typical Poisson's ratio (σ) values are 0.1 and 0.25, respectively [71]. The MXF compounds investigated here have σ values from 0.21 to 0.32, implying a significant ionic contribution to the interatomic bonding. B/G ratio aid to differentiate the material's brittleness from ductility. According to Pugh's criteria [72], the material is brittle, if B/G ratio is less than 1.75, and is ductile, if it is greater than 1.75. As can be seen from Table 4.14, CaBrF, CaIF and SrIF are brittle while the remaining six compounds are ductile in nature.

Table 4.13: Calculated average atomic mass (M_{avg}, in amu), Bulk and Shear moduli (B,G, in GPa), average sound velocity (v_m, in km/s), Debye temperature (Θ_D, in K), specific Heat (C_v, in J/mol-K), and lattice thermal conductivity (κ_L, in W/m-K) for alkaline halofluorides. Cv values are given at 300 K and κ_L are given at 300 K and 900 K.

Compound	**Method**	**M_{avg}**	**B**	**G**	**G/B**	**v_m**	**Θ_D**	**C_v**	**κ_L at 300 K**	**κ_L at 900 K**
CaClF	This Work	31.51	60	29.9	0.498	3.44	401.4	45.61	4.22	1.44
CaBrF	This Work	46.33	25.17	18.44	0.732	2.4	264.86	46.19	2.51	0.85

CaIF	This Work	61.99	20.76	14.86	0.716	2.04	211.96	46.74	2.98	0.99
SrClF	This Work	47.36	54.45	26.6	0.488	2.85	316.53	46.54	3.34	1.13
	Others	54.3 [68]	27.4 [68]	-	-	-	320.3 [68], 305[73]	-	-	-
	Expt	61 [74]	-	-	-	-	-	-	-	-
SrBrF	This Work	62.17	45.49	23.45	0.515	2.45	263.24	47.25	2.91	0.97
	Others	-	-	-	-	-	260 [73], 255[65]	-	-	-
SrIF	This Work	77.84	19.53	14.19	0.726	1.87	187.8	47.56	1.93	0.64
	Others	32.54 [46]	21.01 [46]	-	-	-	170 [73], 212 [65]	-	-	-
BaClF	This Work	63.93	48	19.79	0.412	2.3	242.69	47.32	3.46	1.15
	Others	51.04 [69]	42.1 [60]	21.21 [69]	-	-	241 [65]		-	-
	Expt	45 [75], 62 [74]		-	-	-	-	-	-	-
BaBrF	This Work	78.74	42.9	18.78	0.438	2.11	215.62	47.81	3.35	1.12
	Others	-	49.85 [69]	21.2 [69]	-	-	212 [65]	-	-	-
	Expt	-	42 [75], 44 [74]	-	-	-	-	-	-	-
BaIF	This Work	94.41	34.13	16.98	0.497	1.95	192.63	48.12	2.37	0.78

	Others	-	41.88 [69]	17.21 [69]	-	-	180 [65]	-	-	-
	Expt	-	36 [75]	-	-	-	-	-	-	-

Table 4.14: Calculated Young's modulus (E, in GPa), (B/G), density (ρ, in gr/cc), sound velocities (v_l and v_t in km/s) and Poisson's ratio (σ) for MXF compounds.

Compound	**Method**	**E**	**B/G**	**ρ**	**v_l**	**v_t**	**σ**
CaClF	This Work	76.96	2	3.14	5.64	3.09	0.286
CaBrF	This Work	44.47	1.37	3.89	3.58	2.18	0.206
CaIF	This Work	35.99	1.4	4.34	3.06	1.85	0.211
SrClF	This Work	68.64	2.05	4.07	4.7	2.56	0.289
SrBrF	This Work	60.04	1.94	4.86	3.98	2.2	0.28
SrIF	This Work	34.27	1.38	4.95	2.79	1.69	0.207
	Others [46]	51.87	1.55	-	-	-	0.234
BaClF	This Work	52.22	2.42	4.63	4.01	2.07	0.319
	Others [49]	55.88	-	-	-	-	0.3175
BaBrF	This Work	49.17	2.28	5.26	3.59	1.89	0.309
	Others [49]	55.70	-	-	-	-	0.3153
BaIF	This Work	43.69	2.01	5.57	3.19	1.75	0.287
	Others [49]	45.40	-	-	-	-	0.3193

Later, longitudinal (v_l), transverse (v_t), and average (v_m) sound velocities are calculated from the derived elastic moduli (B, G) and crystal density with the formulae given in our previous study [70]. The v_l, v_t, and v_m are decreasing owing to low elastic moduli (B, G) and high crystal density with increasing size of both metal (M) and halogen (X). According to the Slack theory, low Debye temperature (Θ_D) is an indicative of low κ_L in materials. SrIF has the lowest v_m and Θ_D, which might have the lowest κ_L among the nine investigated MXF compounds in the present study.

4.3.3 Anharmonic lattice dynamics and lattice thermal conductivity

To compute κ_L, phonon dispersion curves and phonon density of states have been calculated and thoroughly analyzed for the nine investigated MXF compounds including anharmonic (3rd order IFCs) effects at 300 K and plotted them along high symmetry points of the Brillouin zone as well as in-plane (Γ-X) and out-of-plane (Γ-Z) directions (Fig. 4.4 & Figs. 4.2 – 4.4). As illustrated in Fig. 4.4, the phonon bands along Γ-X (a-axis) are more dispersive while they are at along Γ-Z (c-axis) especially for materials with c/a ratio > 2, which is due to bonding heterogeneity.

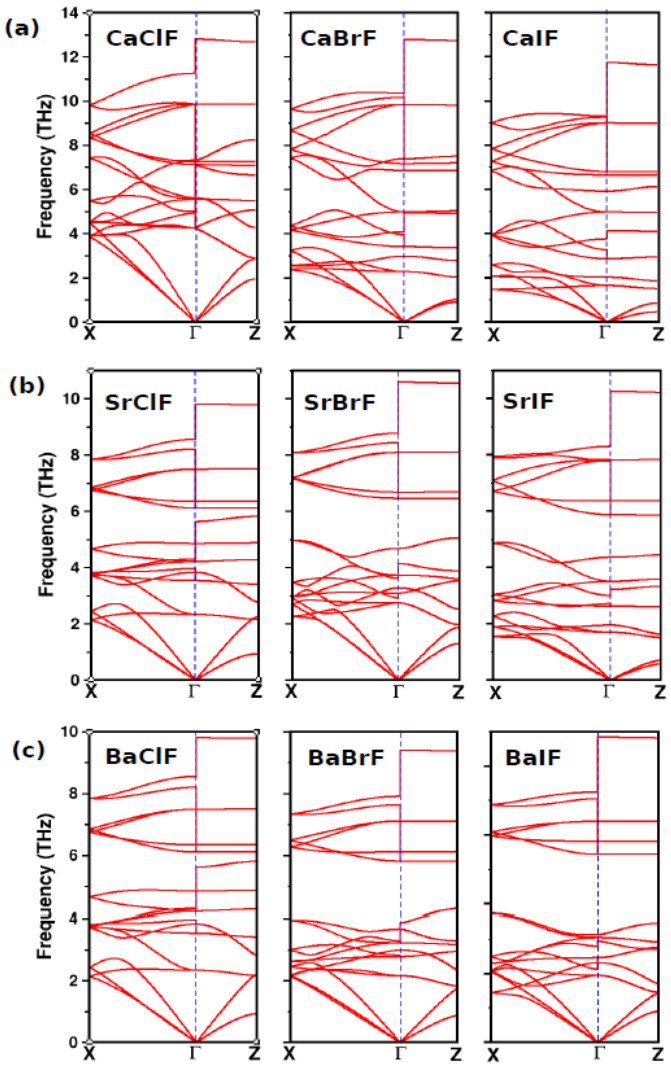

Fig 4.4: Phonon dispersion curves of MXF (M = Ca, Sr, Ba and X = Cl, Br, I) compounds along X-Γ-Z high symmetry directions of the Brillouin zone at 300 K.

The phonon bands show red-shift with increasing size of both M and X as shown in Figs. 4.5 – 4.7. The low frequency phonon bands mainly arise from M and X, whereas the high frequency bands are mainly dominated by the F atoms. They show significant differences in their phonon dispersion curves due to variation of alkaline-earth metal (M) and halogen (X) despite the same crystal symmetry.

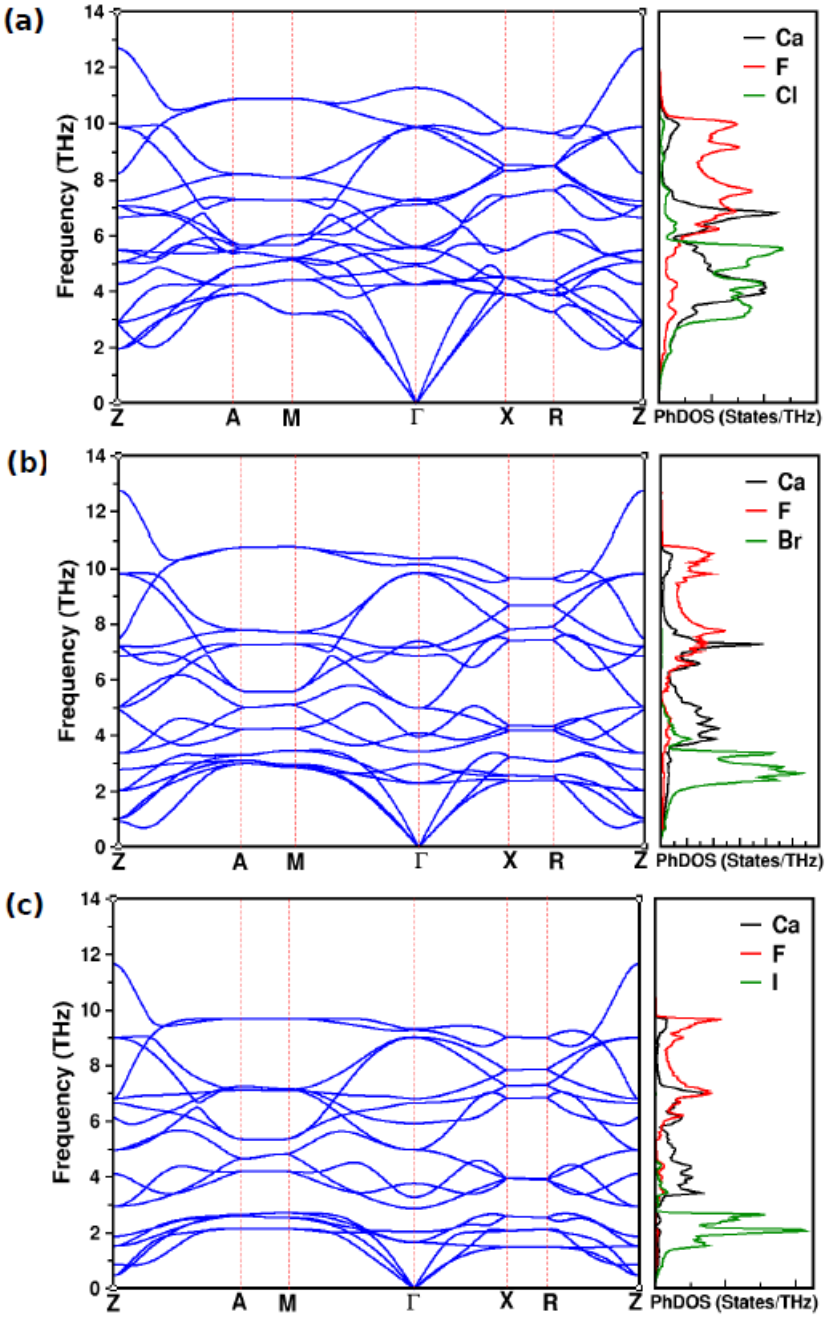

Fig 4.5: Phonon dispersion curves and atom projected phonon density of states for CaXF (X = Cl, Br, I) compounds.

In CaClF, the phonon bands are highly dispersive and overlap with low frequency phonon bands of Ca and Cl with high frequency F phonon bands as shown in Fig. 4.5a.

However, with increase in size of X, phonon bands of Br and I are well separated from F bands in CaBrF and CaIF except for a very small contribution of Ca around 4 THz. In case of SrXF and BaXF (X = Cl, Br, I), a gap between phonon bands of M, X and F has been observed, which is due to atomic mass difference between Sr/Ba, X and F atoms. Moreover, the overlapping nature of M and X phonon bands increase with increasing size of X (Cl →Br→ I). The c/a ratio, a measure of the anisotropy of the structure , is large for CaXF and SrXF compared to the BaXF compounds. CaXF and SrXF possess large c/a ratio over BaXF compounds.

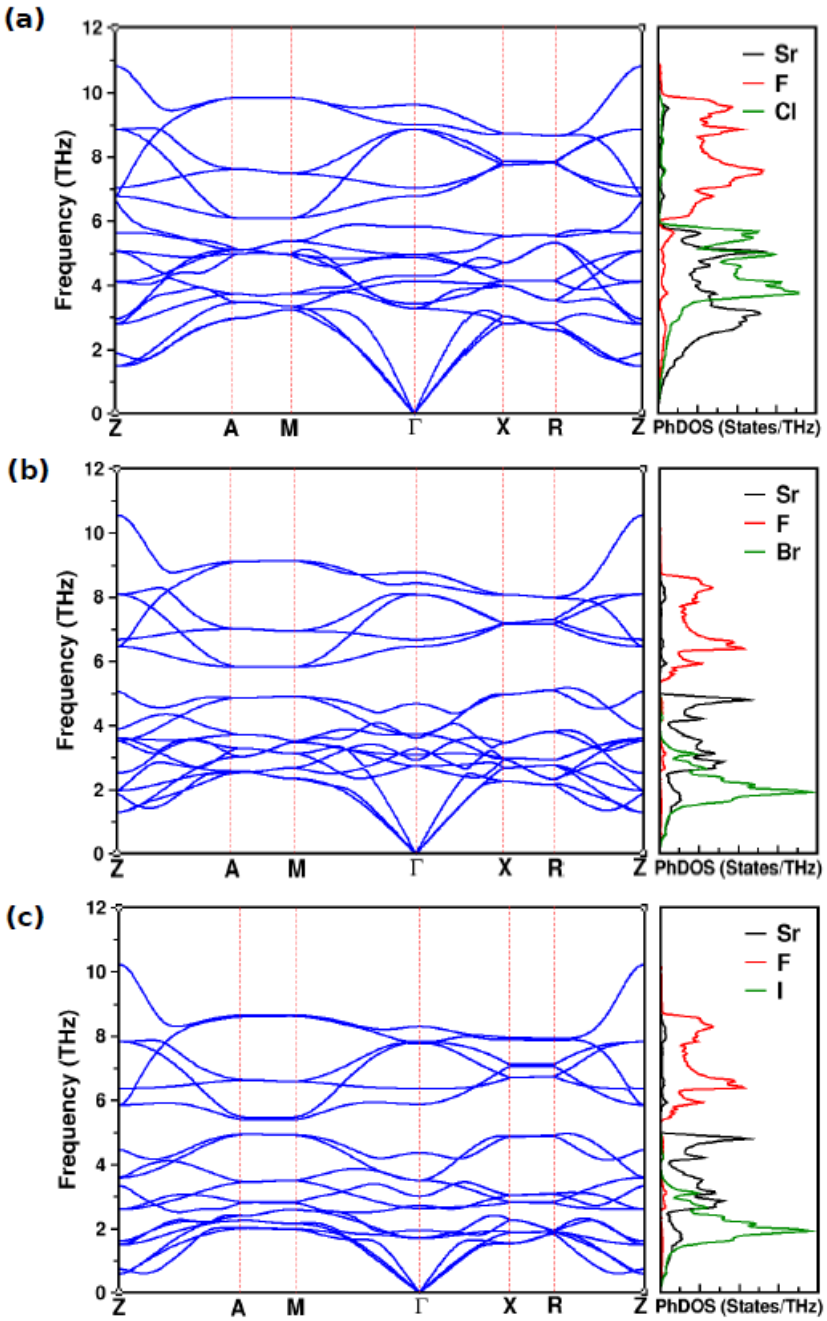

Fig 4.6: Phonon dispersion curves and atom projected phonon density of states for SrXF (X = Cl, Br, I) compounds.

Therefore, highly at and soft (along Γ-Z and A-Z/R-Z directions) phonon bands are expected for the CaXF and SrXF series of compounds, especially with heavy X over BaXF series of compounds as illustrated in Fig. 4.5 – 4.7. Significant phonon softening is observed along Γ-Z and A-Z/R-Z directions for CaBrF, CaIF and SrIF compounds, which have axial (c/a) ratio > 2.

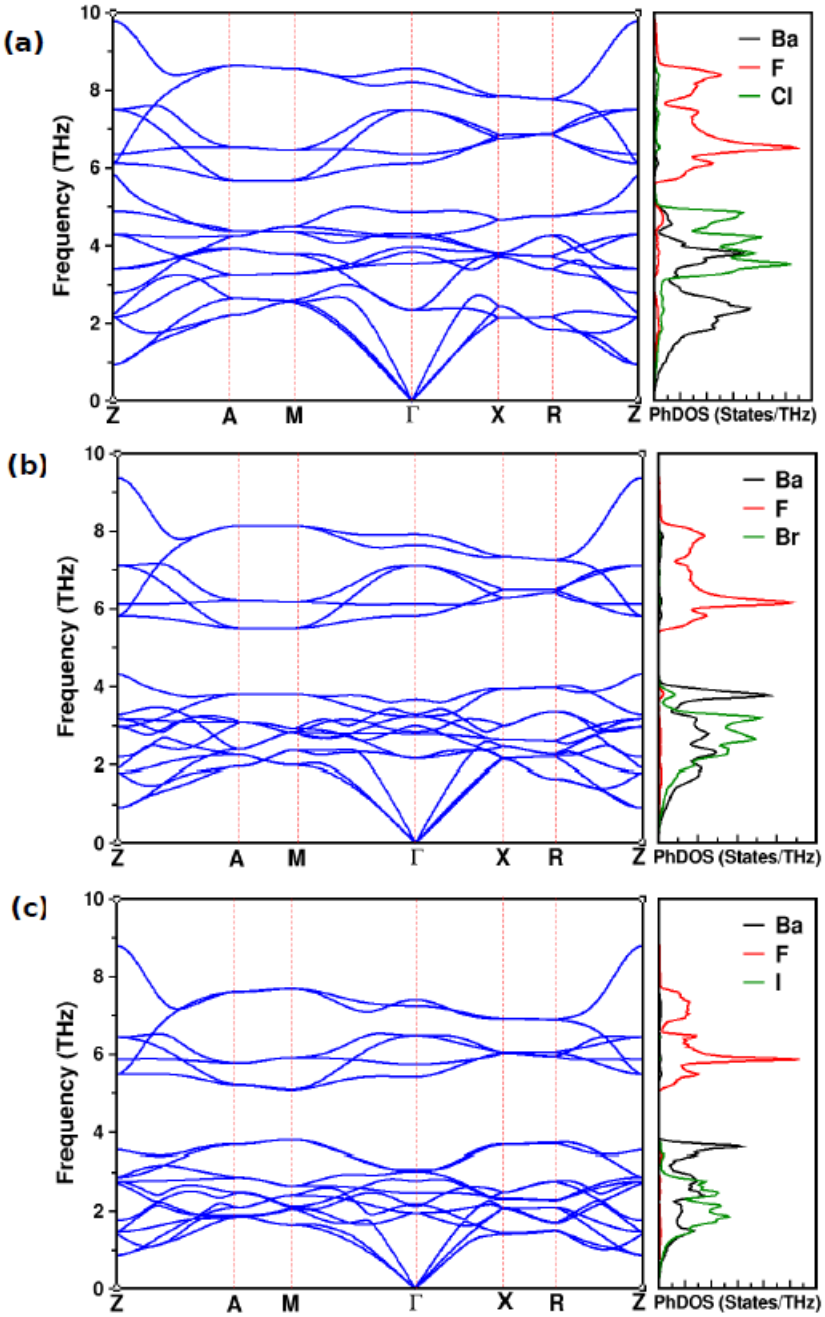

Fig 4.7: Phonon dispersion curves and atom projected phonon density of states for BaXF (X = Cl, Br, I) compounds.

The flat bands results in sharp peaks in the phonon density of states (PhDOS) in the low frequency region for CaBrF (Fig. 4.5b), CaIF (Fig. 4.5c) and SrIF (Fig. 4.5c) indicating

that the heavy X can serve as a rattler in these highly anisotropic compounds, especially along the a-axis as clearly seen from the calculated potential energy curves (Fig. 4.2).

As shown in Fig. 4.8, the obtained κ_L values are decreasing monotonically with temperature. As expected for the layered materials due to bonding heterogeneity, the κ_L values along out of- plane direction are lower than the in-plane direction for all these MXF compounds over the studied temperature range. However, there are some anomalous behavior observed for in plane or out-of-plane κ_L values in these compounds, despite their high average atomic mass.

The contribution of low-lying optical phonons to κ_L along in-plane direction are responsible for higher κ_L in CaIF over CaBrF. Similarly, SrBrF (BaBrF) has higher κ_L over SrClF (BaClF) along the out-of-plane direction due to relatively more contribution of low-lying optical phonons to κ_L in this direction as previously reported for few binary alkali halides and alkaline-earth chalcogenides [76]. CaIF possesses ultralow κ_L (0.39 W/m-K) along the out-of plane direction due to extremely low contribution of acoustic and optical phonons to κ_L. In addition, CaIF has the highest phonon transport anisotropy ratio (in-plane κ_L to out-of plane κ_L) of 10.95 at 300 K (Table 4.13) due to highly anisotropic crystal structure with the highest axial ratio (c/a) of 2.281.

The phonon transport anisotropy ratio values slightly increase for all the compounds at 900 K (Table 4.13) except for SrClF. Similarly, ultralow κ_L values are predicted for CaBrF (0.79 W/m-K) and SrIF (0.70 W/m-K) along the out of- plane direction. Moreover, the out-of-plane κ_L values of CaXF (X = Br, I) and SrXF (X = Br, I) are significantly lower than the BaXF (X = Br, I) due to strong quasi two-dimensional nature. This is clearly seen from the very soft acoustic and at phonon bands along Γ-Z direction (Fig. 4.4) for CaXF and SrXF series of compounds (Figs. 4.5-4.6), while relatively high acoustic and dispersive optical phonon bands for BaXF (Fig. 4.6).

Relatively higher κ_L of CaIF along in-plane direction results in high average κ_L of CaIF over CaBrF. All these layered MXF compounds are found to have low κ_L (< 5 W/m-K). SrIF is found have the lowest κ_L of 1.93 W/m-K at 300 K among all these materials. Overall, CaBrF, CaIF and SrIF materials exhibit quite intriguing anisotropic phonon transport properties among the nine investigated MXF compounds, which might be helpful to find their possible applications in opto-electronics. With UWBG

nature[22], [50], As presented in Table 4.15, high temperature κ_L values at 900 K (~ 1-1.5 W/mK) and G/B ratio less than 0.571 (except CaBrF, CaIF and SrIF) suggest their possible applications in TBCs [77].

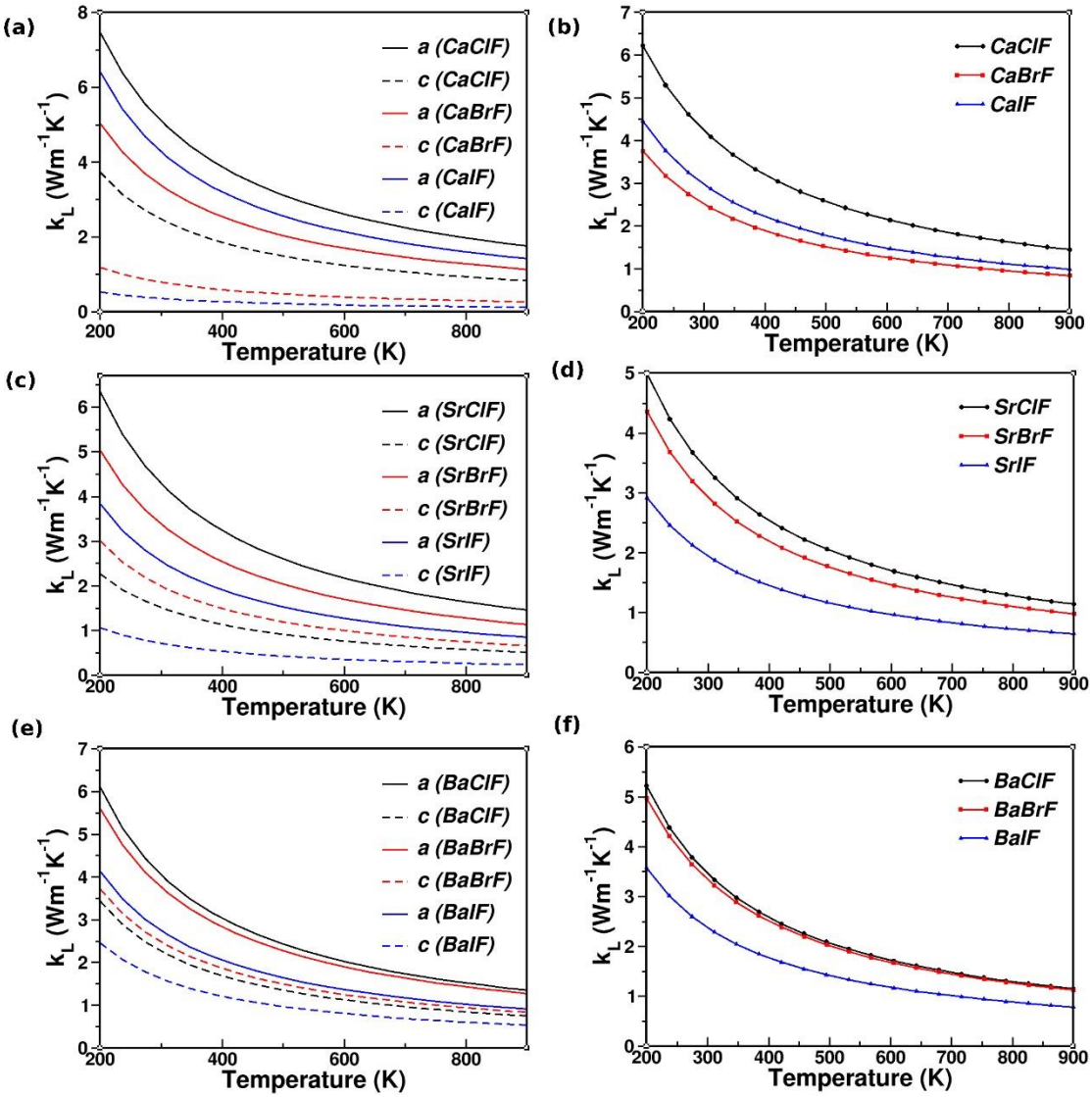

Fig 4.8: (a, c, e) Anisotropic and (b, d, f) average lattice thermal conductivities (κ_L) of (a b) CaXF, (c, d) SrXF and (e,f) BaXF compounds, where X = Cl, Br, I.

Table 4.15: Anisotropic κ_L values (in W/m-K) and anisotropic phonon transport ratio for MXF (M = Ca, Sr, Ba and X = Cl, Br, I) compounds at 300 K and 900 K. (along 'a' axis- κ_L^{xx} and along 'c' axis-κ_L^{zz})

	300K			**900K**		
Compound	$\boldsymbol{\kappa_L^{xx}}$	$\boldsymbol{\kappa_L^{zz}}$	$\boldsymbol{\kappa_L^{xx}/\kappa_L^{zz}}$	$\boldsymbol{\kappa_L^{xx}}$	$\boldsymbol{\kappa_L^{zz}}$	$\boldsymbol{\kappa_L^{xx}/\kappa_L^{zz}}$
CaClF	5.1	2.47	2.06	1.75	0.83	2.11
CaBrF	3.37	0.79	4.27	1.14	0.26	4.38

CaIF	4.27	0.39	10.95	1.42	0.12	11.83
SrClF	4.28	1.47	2.91	1.45	0.5	2.9
SrBrF	3.37	2	1.68	1.13	0.66	1.71
SrIF	2.54	0.7	3.63	0.84	0.23	3.65
BaClF	4.05	2.27	1.78	1.35	0.75	1.8
BaBrF	3.76	2.52	1.49	1.27	0.83	1.53
BaIF	2.74	1.62	1.69	0.91	0.53	1.72

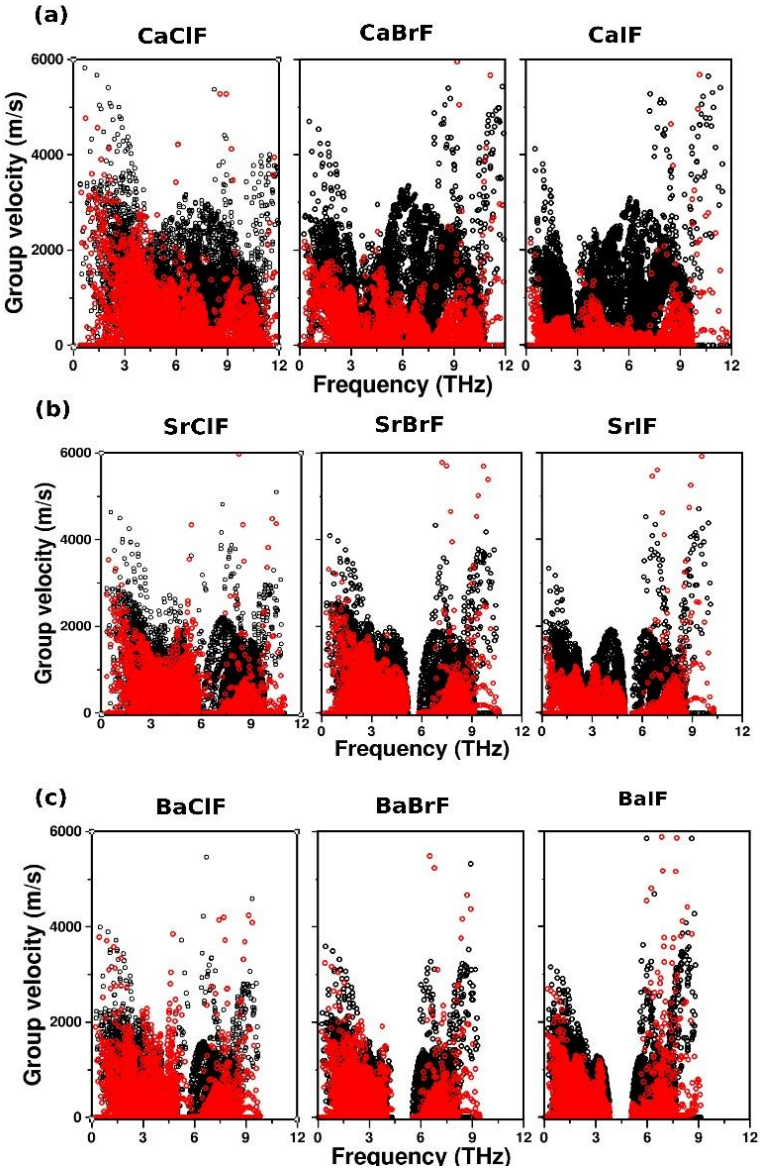

Fig 4.9: Anisotropic group velocities of (a) CaXF, (b) SrXF and (c) BaXF compounds, where X = (Cl, Br, I).

However, their low elastic moduli, high temperature phase stability and low melting temperatures (for instance, melting temperature of SrIF is 1073K [73]) are the major disadvantages to limit their possible applications in TBCs.Further enhancing the aforementioned properties might be a good scope for the future investigations on these MXF compounds. To get further insights on κ_L and the factors that strongly influence its trends in these MXF compounds, phonon group velocities and phonon lifetimes

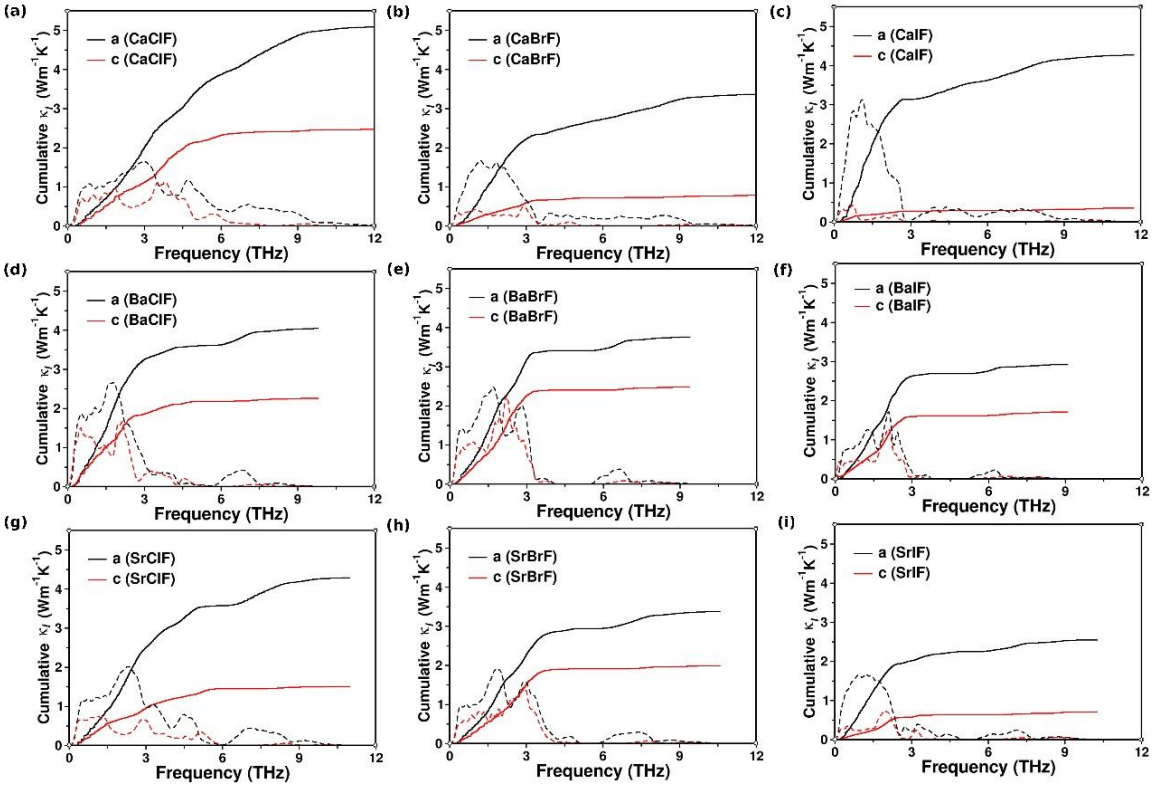

Fig 4.10: Cumulative and spectral lattice thermal conductivity of MXF (M = Ca, Sr, Ba and X = Cl, Br, I) compounds along 'a' (κ^{xx}_L) and 'c' (κ^{zz}_L) axes. Here, dotted lines represent the spectral thermal conductivity.

are calculated and presented along with cumulative and spectral thermal conductivities in Fig. 4.10 – 4.12. The calculated phonon group velocities are higher along in-plane direction over out-of-plane direction as depicted in Fig. 4.9 due to relatively high dispersive nature of phonons along Γ-X over Γ-Z direction. This behavior is clearly seen from group velocities of CaBrF, CaIF and SrIF, thus indicating highly anistropic κ_L in these materials (Fig. 4.9) similar to the iso-structural PbXF (X = Cl, Br, I) compounds due to bonding hierarchy.

The phonon scattering rates are relatively low for CaClF compared to CaBrF and CaIF, (Fig. 4.12) therefore, CaClF has relatively high phonon lifetimes, which in turn results in high κ_L in CaXF series. CaBrF has high scattering rates in the frequency range of 0-3.5 and 5-10 THz, which results in relatively low phonon lifetimes (Fig. 4.11) along

with low in-plane phonon group velocities in CaBrF resulting in relatively low κ_L for CaBrF over CaIF despite very low phonon group velocities along the out-of-plane direction for CaIF.

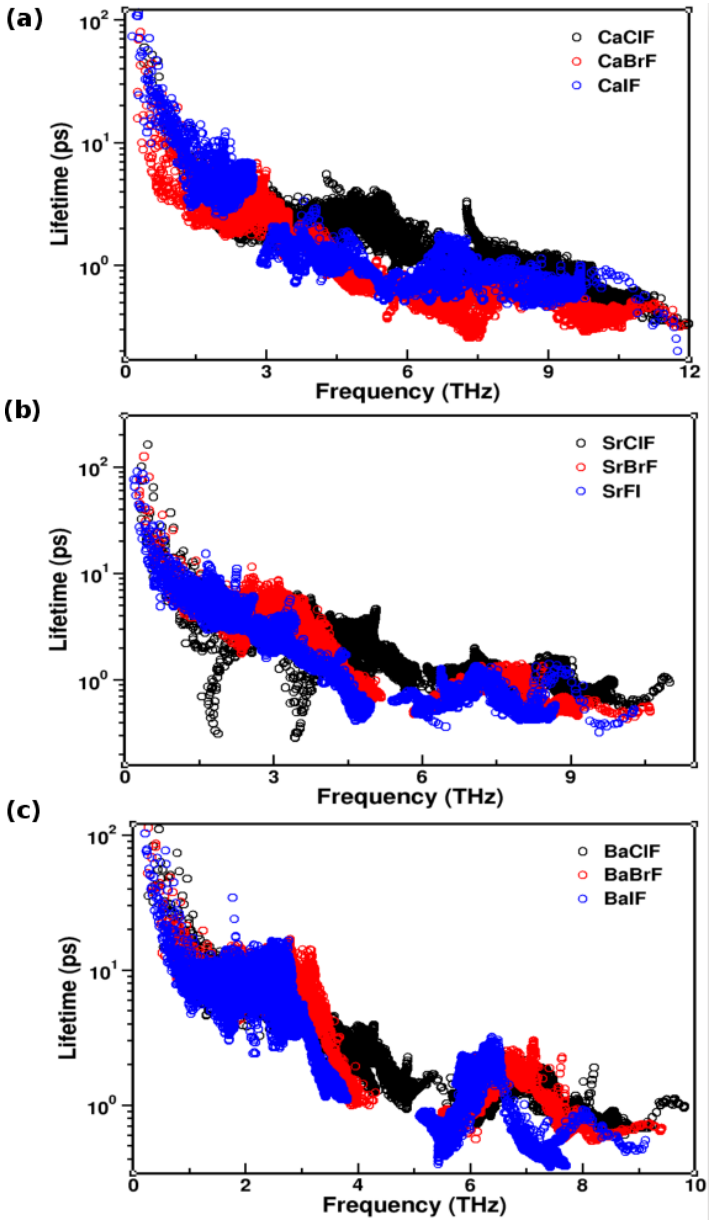

Fig 4.11: Phonon lifetimes of (a) CaXF, (b) SrXF and (c) BaXF compounds, where X =(Cl, Br, I).

However, no anomalous trends are observed for scattering rates or phonon lifetimes in MXF (M = Sr, Ba and X = Cl, Br, I) (Fig. 4.13 & 4.14). To get further insights on anomalous trends of κ_L, it is plotted as a function of elastic moduli (B, G) (Fig. 4.15), sound velocities (v_l, v_t and v_m) and Θ_D (Fig. 4.16) . This clearly demonstrates that the convolutionary effect of B, G moduli and crystal density (ρ) to lower the κ_L. The average phonon group velocities also follow the same trend (Fig. 4.17).

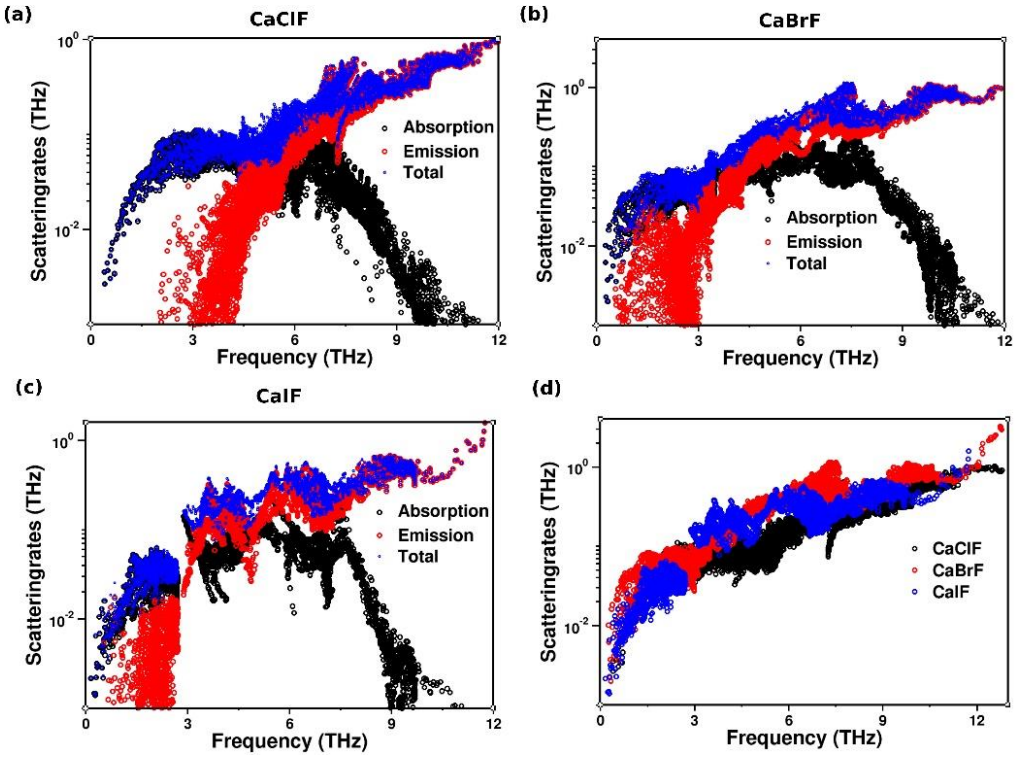

Fig 4.12: Absorption, emission and total scattering rates for (a) CaClF, (b) CaBrF, (c) CaIF and (d) CaXF (X = Cl, Br, I) compounds.

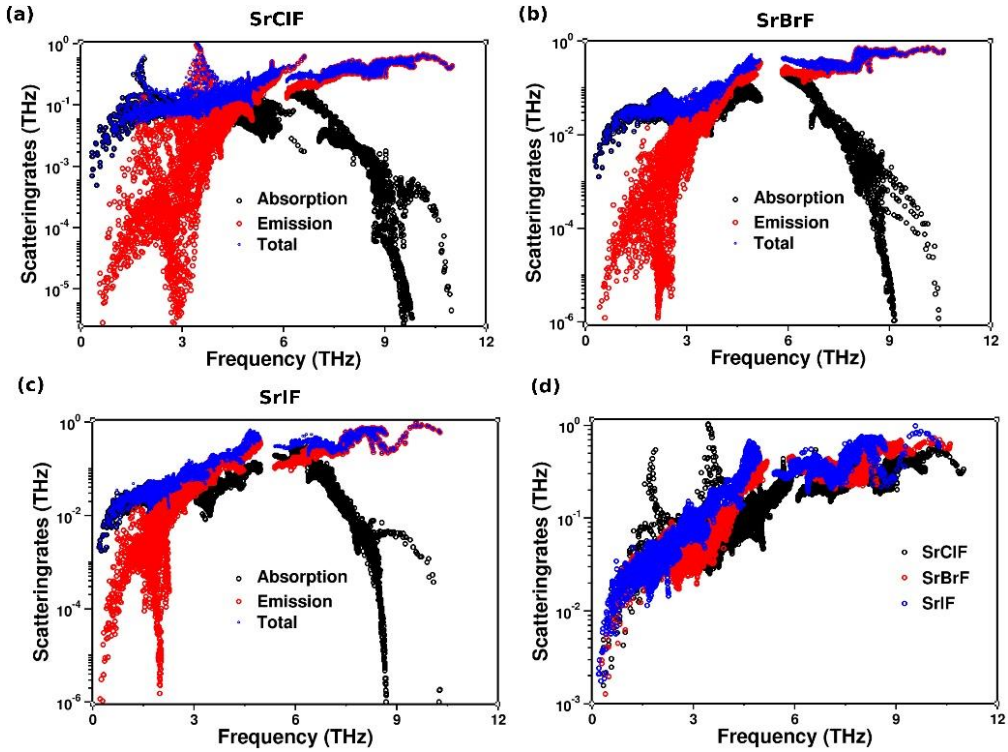

Fig 4.13: Absorption, emission and total scattering rates for (a) SrClF, (b) SrBrF, (c) SrIF and (d) SrXF (X = Cl, Br, I) compounds.

For instance, bulk modulus of BaIF is higher than CaBrF but the shear modulus value of CaBrF is higher than BaIF, but the highest ρ of BaIF to have relatively low v_m (due to inverse proportionality) and Θ_D in turn resulting in relatively low κ_L for BaIF compared to CaBrF and CaIF. Overall, CaBrF, CaIF, and SrIF are found to have ultralow κ_L (< 1 W/m-K) along the out-of-plane direction and these κ_L values are much lower than BaXF compounds (despite their high average atomic mass) due to large axial ratio (c/a) or (M-X1) bond length thereby strong bonding hierarchy.

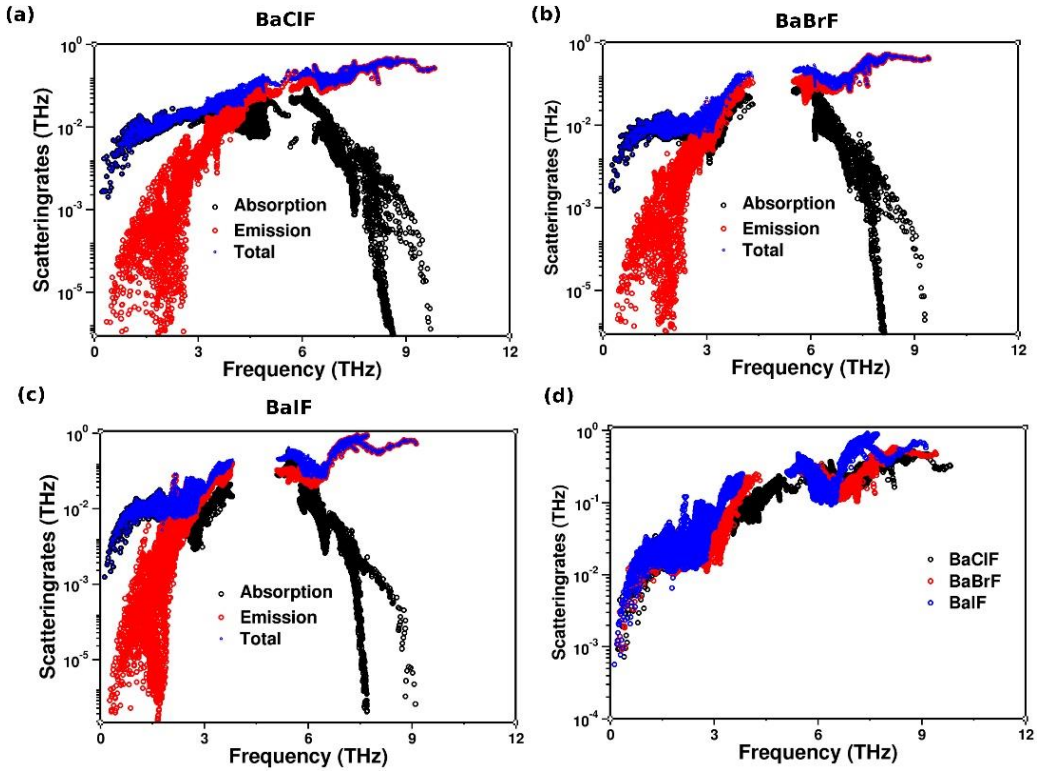

Fig 4.14: Absorption, emission and total scattering rates for (a) BaClF, (b) BaBrF, (c) BaIF and (d) BaXF (X = Cl, Br, I) compounds.

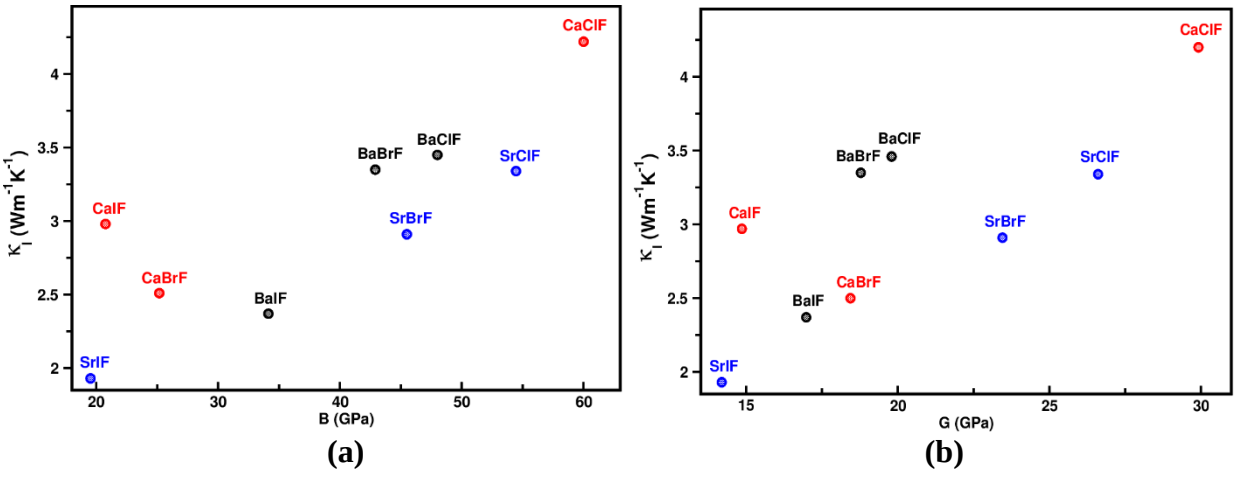

Fig 4.15: Calculated κ_L as a function of (a) bulk (B) modulus (b) shear (G) modulus for MXF (M = Ca, Sr, Ba and X = Cl, Br, I) compounds.

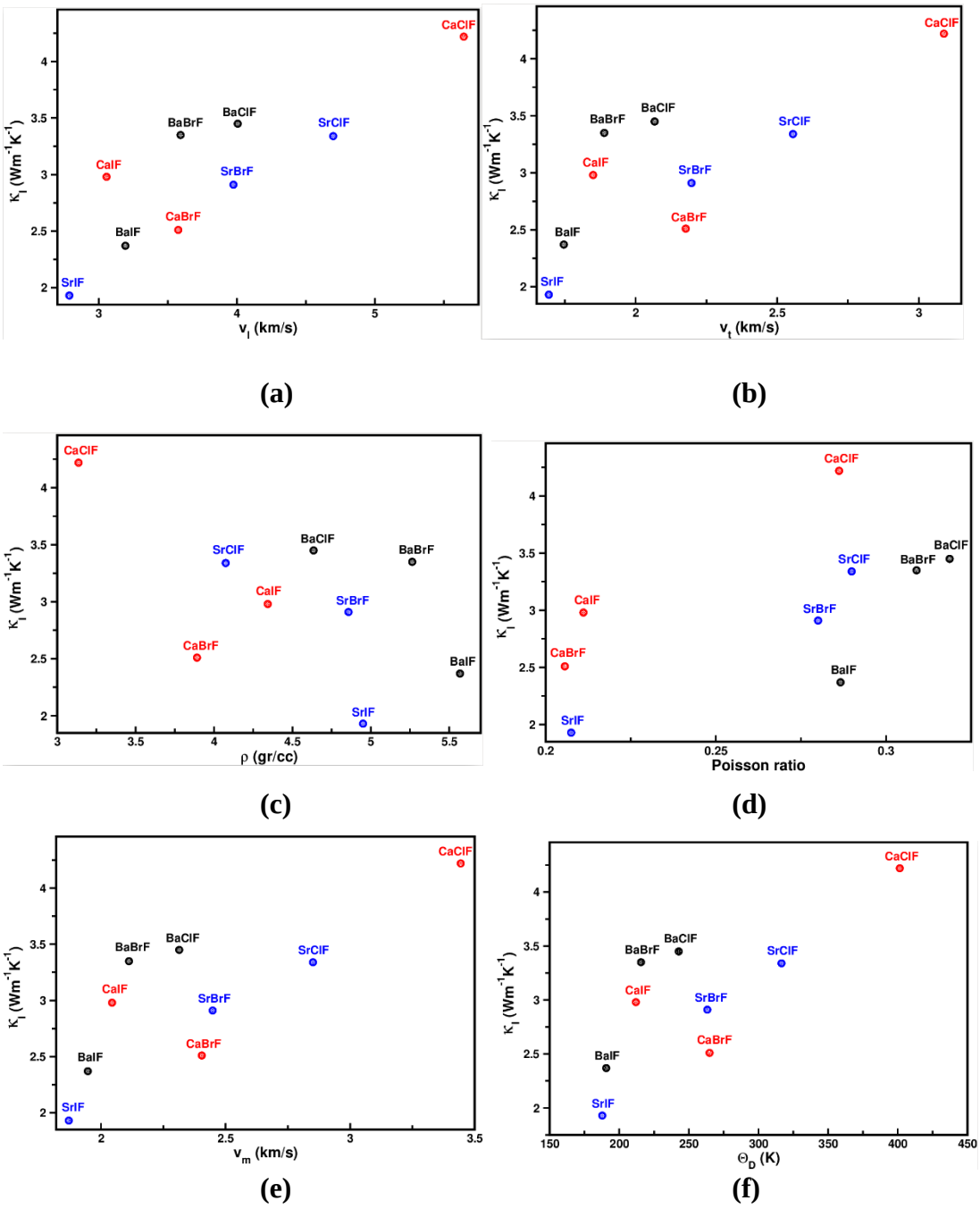

Fig 4.16: Calculated κ_L as a function of (a) longitudinal (v_l) sound velocities (b) transverse (v_t) sound velocities (c) density and (d) Poisson ratio (e) average sound velocities (f) Debye temperature for MXF (M = Ca, Sr, Ba and X = Cl, Br, I) compounds

This comprehensive study on MXF compounds not only provides insights on role of layered structure and bonding on phonon transport properties but also aid in designing low κ_L materials by exploiting them through chemical intuition in quasi-2D layered materials.

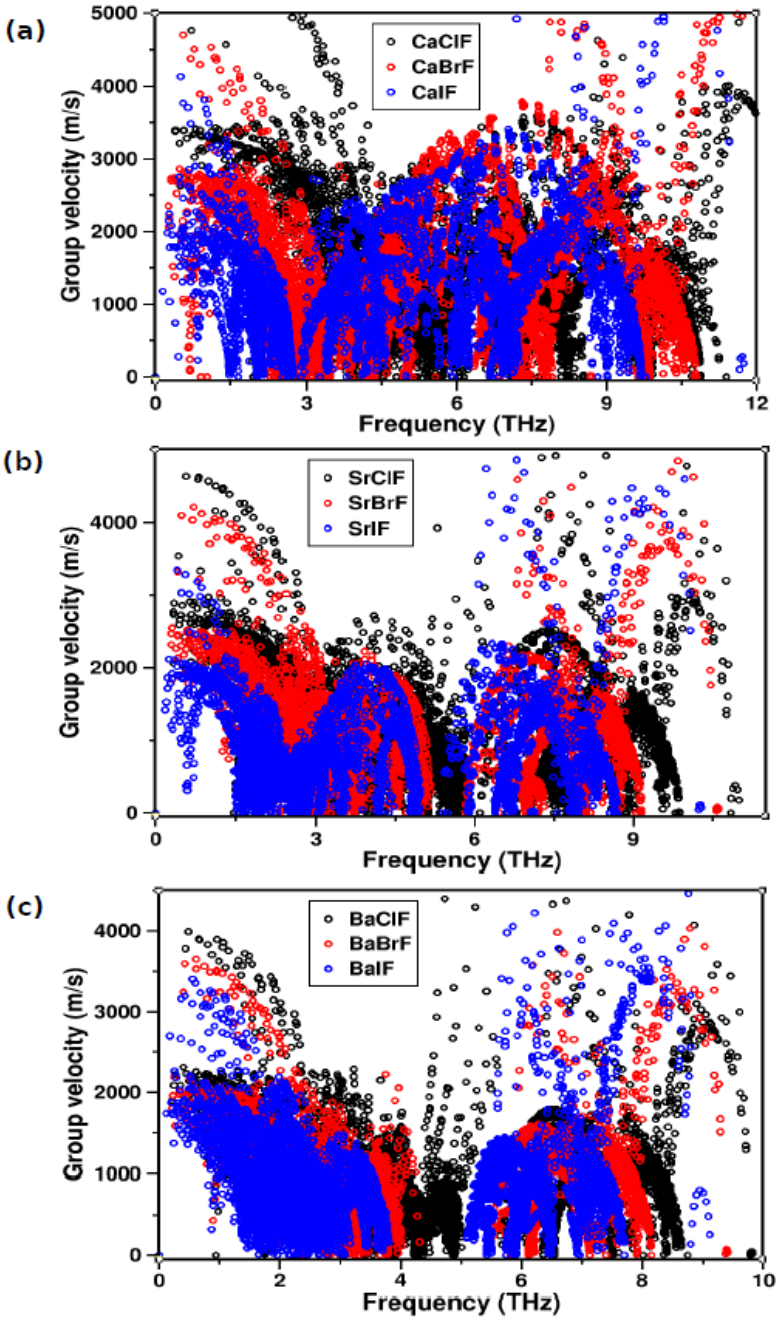

Fig 4.17: Average phonon group velocities of MXF (M = Ca, Sr, Ba and X = Cl, Br, I) compounds

In summary, a systematic investigation has been carried out to explore the structure, bonding, lattice dynamics and phonon transport properties of PbClF-type alkaline-earth halo fluorides, MXF (M = Ca, Sr, Ba and X = Cl, Br, I) in combination with first principles calculations and Boltzmann transport theory. MXF compounds exhibit anisotropy from both crystal structure and elastic properties. The axial bond (M-X1) strongly determines its structural anisotropy, which is attributed to the large axial

ratio (c/a > 2) especially for CaBrF, CaIF and SrIF compared to the rest of the six investigated MXF compounds. Interestingly, Br/I acts as a rattler in CaBrF, CaIF and SrIF compounds as showed from potential energy curves and phonon density of states. BaXF (X = Cl, Br, I) compounds possess relatively isotropic κ_L over CaXF and SrXF series of compounds. The large phonon transport anisotropy ratio 10.95 of CaIF reveals that highly anisotropic phonon transport in CaIF while a small phonon transport anisotropy ratio 1.49 of BaBrF indicating the isotropic phonon transport in BaBrF at 300 K. Moreover, ultralow out-of-plane κ_L (< 1 W/m-K) has been predicted for CaBrF, CaIF and SrIF due to weak vdW bonding along the out-of-plane direction. This detailed study on MXF compounds provides an in-depth understanding on interplay among crystal structure, atomic mass and bonding heterogeneity, which would aid in designing extreme κ_L materials by manipulating in-plane and out-of-plane bonding for future thermal energy management applications.

References:

[1] Y. Cai *et al.*, "Anisotropic phonon thermal transport in two-dimensional layered materials," *Front Phys (Beijing)*, vol. 18, no. 4, p. 43303, Aug. 2023, doi: 10.1007/s11467-023-1276-4.

[2] R. McKinney, P. Gorai, E. S. Toberer, and V. Stevanovic̀, "Rapid Prediction of Anisotropic Lattice Thermal Conductivity: Application to Layered Materials," *Chemistry of Materials*, vol. 31, no. 6, pp. 2048–2057, Mar. 2019, doi: 10.1021/acs.chemmater.8b05084.

[3] L. Hu *et al.*, "High thermoelectric performance enabled by convergence of nested conduction bands in $Pb_7Bi_4Se_{13}$ with low thermal conductivity," *Nat Commun*, vol. 12, no. 1, p. 4793, Aug. 2021, doi: 10.1038/s41467-021-25119-z.

[4] M. Dutta, D. Sarkar, and K. Biswas, "Intrinsically ultralow thermal conductive inorganic solids for high thermoelectric performance," *Chemical Communications*, vol. 57, no. 39, pp. 4751–4767, 2021, doi: 10.1039/D1CC00830G.

[5] Y. Li, Y. Luo, Z. Tian, J. Wang, and J. Wang, "Theoretical exploration of the abnormal trend in lattice thermal conductivity for monosilicates RE_2SiO_5 (RE = Dy, Ho, Er, Tm, Yb and Lu)," *J Eur Ceram Soc*, vol. 38, no. 10, pp. 3539–3546, Aug. 2018, doi: 10.1016/j.jeurceramsoc.2018.04.014.

[6] E. Bsaibess, F. Delorme, I. Monot-Laffez, and F. Giovannelli, "Ultra-low thermal conductivity in scheelite and A-deficient scheelite ceramics," *Scr Mater*, vol. 201, p. 113950, Aug. 2021, doi: 10.1016/j.scriptamat.2021.113950.

[7] M. T. Agne, T. Böger, T. Bernges, and W. G. Zeier, "Importance of Thermal Transport for the Design of Solid-State Battery Materials," *PRX Energy*, vol. 1, no. 3, p. 031002, Dec. 2022, doi: 10.1103/PRXEnergy.1.031002.

[8] Q. D. Gibson *et al.*, "Low thermal conductivity in a modular inorganic material with bonding anisotropy and mismatch," *Science (1979)*, vol. 373, no. 6558, pp. 1017–1022, Aug. 2021, doi: 10.1126/science.abh1619.

[9] B. Liu *et al.*, "Advances on strategies for searching for next generation thermal barrier coating materials," *J Mater Sci Technol*, vol. 35, no. 5, pp. 833–851, May 2019, doi: 10.1016/j.jmst.2018.11.016.

[10] B. Liu *et al.*, “Application of high-throughput first-principles calculations in ceramic innovation,” *J Mater Sci Technol*, vol. 88, pp. 143–157, Oct. 2021, doi: 10.1016/j.jmst.2021.01.071.

[11] Z.-Y. Wei *et al.*, “Progress in ceramic materials and structure design toward advanced thermal barrier coatings,” *Journal of Advanced Ceramics*, vol. 11, no. 7, pp. 985–1068, Jul. 2022, doi: 10.1007/s40145-022-0581-7.

[12] X. Shao *et al.*, “Contributions of bonding heterogeneity to mechanical and thermal properties of rare earth molybdates for thermal barrier coatings,” *Journal of Physics and Chemistry of Solids*, vol. 173, p. 111087, Feb. 2023, doi: 10.1016/j.jpcs.2022.111087.

[13] H. Mashiko, K. Oguri, T. Yamaguchi, A. Suda, and H. Gotoh, “Petahertz optical drive with wide-bandgap semiconductor,” *Nat Phys*, vol. 12, no. 8, pp. 741–745, Aug. 2016, doi: 10.1038/nphys3711.

[14] F. Odobel and Y. Pellegrin, “Recent Advances in the Sensitization of Wide-Band-Gap Nanostructured p-Type Semiconductors. Photovoltaic and Photocatalytic Applications,” *J Phys Chem Lett*, vol. 4, no. 15, pp. 2551–2564, Aug. 2013, doi: 10.1021/jz400861v.

[15] N. Yedukondalu *et al.*, “Lattice Instability and Ultralow Lattice Thermal Conductivity of Layered PbIF,” *ACS Appl Mater Interfaces*, vol. 14, no. 36, pp. 40738–40748, Sep. 2022, doi: 10.1021/acsami.2c01135.

[16] B. Qin, D. Wang, and L. Zhao, “Slowing down the heat in thermoelectrics,” *InfoMat*, vol. 3, no. 7, pp. 755–789, Jul. 2021, doi: 10.1002/inf2.12217.

[17] M. Dutta, D. Sarkar, and K. Biswas, “Intrinsically ultralow thermal conductive inorganic solids for high thermoelectric performance,” *Chemical Communications*, vol. 57, no. 39, pp. 4751–4767, 2021, doi: 10.1039/D1CC00830G.

[18] M. K. Jana and K. Biswas, “Crystalline Solids with Intrinsically Low Lattice Thermal Conductivity for Thermoelectric Energy Conversion,” *ACS Energy Lett*, vol. 3, no. 6, pp. 1315–1324, Jun. 2018, doi: 10.1021/acsenergylett.8b00435.

[19] J. He *et al.*, “Accelerated Discovery and Design of Ultralow Lattice Thermal Conductivity Materials Using Chemical Bonding Principles,” *Adv Funct Mater*, vol. 32, no. 14, Apr. 2022, doi: 10.1002/adfm.202108532.

[20] H. Kim, G. Park, S. Park, and W. Kim, “Strategies for Manipulating Phonon Transport in Solids,” *ACS Nano*, vol. 15, no. 2, pp. 2182–2196, Feb. 2021, doi: 10.1021/acsnano.0c10411.

[21] T. Ghosh, M. Dutta, D. Sarkar, and K. Biswas, “Insights into Low Thermal Conductivity in Inorganic Materials for Thermoelectrics,” *J Am Chem Soc*, vol. 144, no. 23, pp. 10099–10118, Jun. 2022, doi: 10.1021/jacs.2c02017.

[22] N. Yedukondalu, K. R. Babu, Ch. Bheemalingam, D. J. Singh, G. Vaitheeswaran, and V. Kanchana, “Electronic structure, optical properties, and bonding in alkaline-earth halofluoride scintillators: BaClF, BaBrF, and BaIF,” *Phys Rev B*, vol. 83, no. 16, p. 165117, Apr. 2011, doi: 10.1103/PhysRevB.83.165117.

[23] X.-J. Ye, Z.-X. Zhu, L. Meng, and C.-S. Liu, “Two-dimensional CaFCl: ultra-wide bandgap, strong interlayer quantum confinement, and n-type doping,” *Physical Chemistry Chemical Physics*, vol. 22, no. 30, pp. 17213–17220, 2020, doi: 10.1039/D0CP02804E.

[24] M. Barhoumi and M. Said, “Electronic and optical properties of PbFCl and PbFI monolayers using density functional theory and beyond,” *Mater Chem Phys*, vol. 252, p. 123233, Sep. 2020, doi: 10.1016/j.matchemphys.2020.123233.

[25] K. Manjunath, S. Servottam, A. Soni, and C. N. R. Rao, “A study of two-dimensional PbFCl and BaFCl,” *Bulletin of Materials Science*, vol. 43, no. 1, p. 312, Dec. 2020, doi: 10.1007/s12034-020-02117-3.

[26] M. Barhoumi *et al.*, “Electronic properties of several two dimensional halides from ab initio calculations,” *Beilstein Journal of Nanotechnology*, vol. 10, pp. 823–832, Apr. 2019, doi: 10.3762/bjnano.10.82.

[27] M. Tan *et al.*, “2D Lead Dihalides for High-Performance Ultraviolet Photodetectors and their Detection Mechanism Investigation,” *Small*, vol. 13, no. 47, Dec. 2017, doi: 10.1002/smll.201702024.

[28] Z.-L. Lv, H.-L. Cui, X.-H. Li, H. Wang, and G.-F. Ji, “First principles study of the vibrational, dielectric and thermal properties of SrClF,” *Eur Phys J B*, vol. 90, no. 3, p. 57, Mar. 2017, doi: 10.1140/epjb/e2017-70487-y.

[29] L. Kunduru *et al.*, “Pressure-Induced Martensitic Phase Transition and Low Lattice Thermal Conductivity of SrClF,” *Journal of Physical Chemistry C*, vol. 125, no. 31, 2021, doi: 10.1021/acs.jpcc.1c00800.

[30] G. Kresse and J. Furthmüller, “Efficient iterative schemes for *ab initio* total-energy calculations using a plane-wave basis set,” *Phys Rev B*, vol. 54, no. 16, pp. 11169–11186, Oct. 1996, doi: 10.1103/PhysRevB.54.11169.

[31] W. G. Hoover, “Canonical dynamics: Equilibrium phase-space distributions,” *Phys Rev A (Coll Park)*, vol. 31, no. 3, pp. 1695–1697, Mar. 1985, doi: 10.1103/PhysRevA.31.1695.

[32] W. G. Hoover, “Constant-pressure equations of motion,” *Phys Rev A (Coll Park)*, vol. 34, no. 3, pp. 2499–2500, Sep. 1986, doi: 10.1103/PhysRevA.34.2499.

[33] O. Hellman, I. A. Abrikosov, and S. I. Simak, “Lattice dynamics of anharmonic solids from first principles,” *Phys Rev B*, vol. 84, no. 18, p. 180301, Nov. 2011, doi: 10.1103/PhysRevB.84.180301.

[34] J. Flahaut, “Les structures type PbFCl (EOI) et type anti-Fe2As (C38) des composés ternaires à deux anions MXY,” *J Solid State Chem*, vol. 9, no. 2, pp. 124–131, Feb. 1974, doi: 10.1016/0022-4596(74)90063-2.

[35] D. Tuschel, “Raman Spectroscopy and Chemical Bonding of BaFCl, BaFBr, and BaFl,” *Spectroscopy*, pp. 7–10, Dec. 2021, doi: 10.56530/spectroscopy.ec5681h6.

[36] B. W. Liebich and D. Nicollin, “Refinement of the PbFCl types BaFI, BaFBr and CaFCl,” *Acta Crystallogr B*, vol. 33, no. 9, pp. 2790–2794, Sep. 1977, doi: 10.1107/S0567740877009480.

[37] F. E. H. Hassan, H. Akbarzadeh, and S. J. Hashemifar, “Theoretical study of structural and electronic properties of CaFI,” *Journal of Physics: Condensed Matter*, vol. 16, no. 20, pp. 3329–3337, May 2004, doi: 10.1088/0953-8984/16/20/004.

[38] G. Kalpana, B. Palanivel, I. B. Shameem Banu, and M. Rajagopalan, “Structural and electronic properties of alkaline-earth fluorohalides under pressure,” *Phys Rev B*, vol. 56, no. 7, pp. 3532–3535, Aug. 1997, doi: 10.1103/PhysRevB.56.3532.

[39] H. P. Beck, “New mixed halide compounds MFX of divalent rare earths (M = Sm, Eu, Tm, and Yb; X = Cl, Br, and I),” *J Solid State Chem*, vol. 23, no. 1–2, pp. 213–217, Jan. 1978, doi: 10.1016/0022-4596(78)90067-1.

[40] M. Sauvage, “Refinement of the structures of SrFCl and BaFCl,” *Acta Crystallogr B*, vol. 30, no. 11, pp. 2786–2787, Nov. 1974, doi: 10.1107/S0567740874008132.

[41] F. El haj Hassan, H. Akbarzadeh, S. J. Hashemifar, and A. Mokhtari, “Structural and electronic properties of matlockite MFX (MSr, Ba, Pb; XCl, Br, I) compounds,” *Journal of Physics and Chemistry of Solids*, vol. 65, no. 11, pp. 1871–1878, Nov. 2004, doi: 10.1016/j.jpcs.2004.07.002.

[42] R. Mittal, S. L. Chaplot, A. Sen, S. N. Achary, and A. K. Tyagi, “Lattice dynamics and inelastic neutron scattering studies of MFX (M=Sr,Pb & X= Cl,Br,I), *Phys Rev B*, vol. 67, no. 13, p. 134303, Apr. 2003, doi: 10.1103/PhysRevB.67.134303.

[43] F. Decremps, M. Fischer, A. Polian, and M. Sieskind, “Sound velocity measurement by ultrasonic and Brillouin scattering techniques in compounds with matlockite structure,” *High Temperatures-High Pressures*, vol. 30, no. 2, pp. 235–240, 1998, doi: 10.1068/htec152.

[44] H. P. Beck, “A study on mixed halide compounds MFX (M = Ca, Sr, Eu, Ba; X = Cl, Br, I),” *J Solid State Chem*, vol. 17, no. 3, pp. 275–282, Mar. 1976, doi: 10.1016/0022-4596(76)90132-8.

[45] V. Kanchana, G. Vaitheeswaran, and M. Rajagopalan, “Electronic structure of ionic PbFCl-type compounds under pressure,” *Journal of Physics: Condensed Matter*, vol. 15, no. 10, pp. 1677–1683, Mar. 2003, doi: 10.1088/0953-8984/15/10/315.

[46] H. Öztürk, Y. Güzel, and C. Kürkçü, “Investigation of structural, electronic and elastic properties of matlockite-type SrFI under high pressure: An Ab-initio study,” *Solid State Commun*, vol. 336, p. 114399, Oct. 2021, doi: 10.1016/j.ssc.2021.114399.

[47] A. H. Reshak, Z. Charifi, and H. Baaziz, “Optical properties of alkaline-earth fluorohalides BaFX (X=Cl, Br, I) compounds,” *Solid State Electron*, vol. 51, no. 8, pp. 1133–1138, Aug. 2007, doi: 10.1016/j.sse.2007.06.003.

[48] F. Decremps, M. Gauthier, J.-C. Chervin, M. Fischer, and A. Polian, “Unexpected value of transition pressure in the ionic layered BaFI compound observed by Raman scattering,” *Phys Rev B*, vol. 66, no. 2, p. 024115, Jul. 2002, doi: 10.1103/PhysRevB.66.024115.

[49] H. P. Beck, A. Limmer, W. Denner, and H. Schulz, “Influence of high hydrostatic pressure on the crystal structure of BaFCl in the pressure range up to 6.5 GPa,” *Acta Crystallogr B*, vol. 39, no. 4, pp. 401–404, Aug. 1983, doi: 10.1107/S0108768183002633.

[50] V. Kanchana, N. Yedukondalu, and G. Vaitheeswaran, “Structural, elastic, electronic and optical properties of layered alkaline-earth halofluoride scintillators,” *Philosophical Magazine*, vol. 93, no. 26, pp. 3563–3575, Sep. 2013, doi: 10.1080/14786435.2013.815817.

[51] N. Yedukondalu and G. Vaitheeswaran, “Vibrational properties of BaClF, BaBrF and BaIF under high pressure,” *J Phys Conf Ser*, vol. 377, p. 012070, Jul. 2012, doi: 10.1088/1742-6596/377/1/012070.

[52] V. Kanchana, N. Yedukondalu, and G. Vaitheeswaran, “Lattice dynamics and electronic structure of mixed halofluoride scintillators under high pressure,” 2015, p. 090009. doi: 10.1063/1.4917989.

[53] Y. A. Sorb, N. Subramanian, and T. R. Ravindran, “High pressure Raman spectroscopy of layered matlockite, PbFCl,” *Journal of Physics: Condensed Matter*, vol. 25, no. 15, p. 155401, Apr. 2013, doi: 10.1088/0953-8984/25/15/155401.

[54] B. Sundarakannan, T. R. Ravindran, R. Kesavamoorthy, and S. V. M. Satyanarayana, “High pressure Raman spectroscopic study of BaFCl,” *Solid State Commun*, vol. 124, no. 10–11, pp. 385–389, Dec. 2002, doi: 10.1016/S0038-1098(02)00604-X.

[55] D. Nicollin and H. Bill, “Experimental contribution to the study of S-state ions in ionic single crystals,” *Journal of Physics C: Solid State Physics*, vol. 11, no. 23, pp. 4803–4814, Dec. 1978, doi: 10.1088/0022-3719/11/23/022.

[56] D. Sethio, J. B. L. Martins, L. M. Lawson Daku, H. Hagemann, and E. Kraka, "Modified Density Functional Dispersion Correction for Inorganic Layered MFX Compounds (M = Ca, Sr, Ba, Pb and X = Cl, Br, I)," *J Phys Chem A*, vol. 124, no. 8, pp. 1619–1633, Feb. 2020, doi: 10.1021/acs.jpca.9b10357.

[57] J. F. Scott, "Raman Spectra of BaClF, BaBrF, and SrClF," *J Chem Phys*, vol. 49, no. 6, pp. 2766–2769, Sep. 1968, doi: 10.1063/1.1670481.

[58] Z.-L. Lv, H.-L. Cui, X.-H. Li, H. Wang, and G.-F. Ji, "First principles study of the vibrational, dielectric and thermal properties of SrClF," *Eur Phys J B*, vol. 90, no. 3, p. 57, Mar. 2017, doi: 10.1140/epjb/e2017-70487-y.

[59] P. Labguerie, F. Pascale, M. Mrawa, C. Zicovich-Wilson, N. Makhouki, and R. Dovesi, "Phonon vibrational frequencies and elastic properties of solid SrFCl. An ab initio study," *Eur Phys J B*, vol. 43, no. 4, pp. 453–461, Feb. 2005, doi: 10.1140/epjb/e2005-00078-6.

[60] V. D'Anna, L. M. L. Daku, H. Hagemann, and F. Kubel, "Ionic layered BaFCl and $BaSr_xFCl$compounds: Physical- and chemical-pressure effects," *Phys Rev B*, vol. 82, no. 2, p. 024108, Jul. 2010, doi: 10.1103/PhysRevB.82.024108.

[61] H. Haeuseler, "Lattice dynamics of BaFBr," *Phys Chem Miner*, vol. 7, no. 3, pp. 135–137, Jun. 1981, doi: 10.1007/BF00308230.

[62] M. Sieskind, D. Ayachour, J. -C. Merle, and J. -C. Boulou, "Crystal Growth, Raman and Infrared Spectra of BaFI Single Crystals," *physica status solidi (b)*, vol. 158, no. 1, pp. 103–112, Mar. 1990, doi: 10.1002/pssb.2221580109.

[63] M. Born, "On the stability of crystal lattices. I," *Mathematical Proceedings of the Cambridge Philosophical Society*, vol. 36, no. 2, pp. 160–172, Apr. 1940, doi: 10.1017/S0305004100017138.

[64] I. Waller, "*Dynamical Theory of Crystal Lattices* by M. Born and K. Huang," *Acta Crystallogr*, vol. 9, no. 10, pp. 837–838, Oct. 1956, doi: 10.1107/S0365110X56002370.

[65] M. Sieskind, A. Polian, M. Fischer, and F. Decremps, "Some scaling factors of physical properties dependent on phonons in the case of the families of the fluorite and of the matlockite," *Journal of Physics and Chemistry of Solids*, vol. 59, no. 1, pp. 75–82, Jan. 1998, doi: 10.1016/S0022-3697(97)00106-6.

[66] K. R. Balasubramanian, T. M. Haridasan, and N. Krishnamurthy, “Elastic constants of SrClF and BaClF crystals,” *Chem Phys Lett*, vol. 67, no. 2–3, pp. 530–532, Nov. 1979, doi: 10.1016/0009-2614(79)85221-5.

[67] M. Fischer, A. Polian, and M. Sieskind, “Ultrasonic and Brillouin scattering measurements of the elastic constants of SrFCl,” *Journal of Physics: Condensed Matter*, vol. 6, no. 47, pp. 10407–10413, Nov. 1994, doi: 10.1088/0953-8984/6/47/023.

[68] Z.-L. Lv, H.-L. Cui, H. Wang, X.-H. Li, and G.-F. Ji, “*Ab initio* study of the structural, electronic, elastic and thermal conductivity properties of SrClF with pressure effects,” *Philosophical Magazine*, vol. 97, no. 10, pp. 743–758, Apr. 2017, doi: 10.1080/14786435.2017.1280195.

[69] A. K. Kushwaha, S. Akbudak, A. C. Yadav, Ş. Uğur, and G. Uğur, “Lattice dynamical and elastic properties of BaF *X* (*X* = Cl, Br and I): Matlockite structure compounds,” *Int J Mod Phys B*, vol. 33, no. 20, p. 1950221, Aug. 2019, doi: 10.1142/S0217979219502217.

[70] S. C. Rakesh Roshan *et al.*, “Anomalous Lattice Thermal Conductivity in Rocksalt IIA–VIA Compounds,” *ACS Appl Energy Mater*, vol. 5, no. 1, pp. 882–896, Jan. 2022, doi: 10.1021/acsaem.1c03310.

[71] J. Haines, J. Léger, and G. Bocquillon, “Synthesis and Design of Superhard Materials,” *Annu Rev Mater Res*, vol. 31, no. 1, pp. 1–23, Aug. 2001, doi: 10.1146/annurev.matsci.31.1.1.

[72] S. F. Pugh, “XCII. Relations between the elastic moduli and the plastic properties of polycrystalline pure metals,” *The London, Edinburgh, and Dublin Philosophical Magazine and Journal of Science*, vol. 45, no. 367, pp. 823–843, Aug. 1954, doi: 10.1080/14786440808520496.

[73] M. Sieskind, Y. Dossmann, R. Kuentzler, and J. P. Lambour, “Low temperature specific heat of SrFCl, SrFBr, and SrFI,” *Physica Status Solidi (a)*, vol. 148, no. 1, pp. 153–157, Mar. 1995, doi: 10.1002/pssa.2211480112.

[74] Y. R. Shen *et al.*, “A structural study on the PbFCl-type compounds MFCl (M=Ba, Sr and Ca) and BaFBr under high pressure,” *Journal of Physics: Condensed Matter*, vol. 6, no. 17, pp. 3197–3206, Apr. 1994, doi: 10.1088/0953-8984/6/17/009.

[75] F. Decremps, M. Fischer, A. Polian, J. P. Itié, and M. Sieskind, “Ionic layered PbFCl-type compounds under high pressure,” *Phys Rev B*, vol. 59, no. 6, pp. 4011–4022, Feb. 1999, doi: 10.1103/PhysRevB.59.4011.

[76] S. C. Rakesh Roshan *et al.*, “Effect of Atomic Mass Contrast on Lattice Thermal Conductivity: A Case Study for Alkali Halides and Alkaline-Earth Chalcogenides,” *ACS Appl Electron Mater*, Oct. 2023, doi: 10.1021/acsaelm.3c00759.

[77] Y. Liu, K. Chu, Y. Zhou, Y. Li, W. Li, and B. Liu, “Discovery of orthorhombic perovskite oxides with low thermal conductivity by first-principles calculations,” *Journal of Advanced Ceramics*, vol. 11, no. 10, pp. 1596–1603, Oct. 2022, doi: 10.1007/s40145-022-0632-0.

CHAPTER-5

Phonon Transport in Layered Bismuth halooxides, BiXO (X= Cl, Br, I)

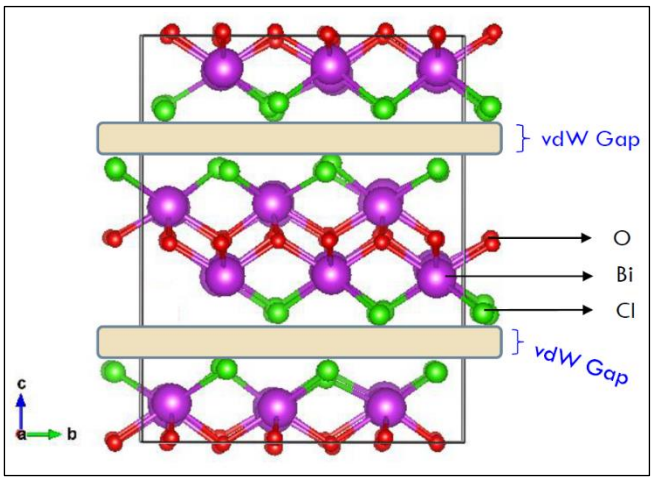

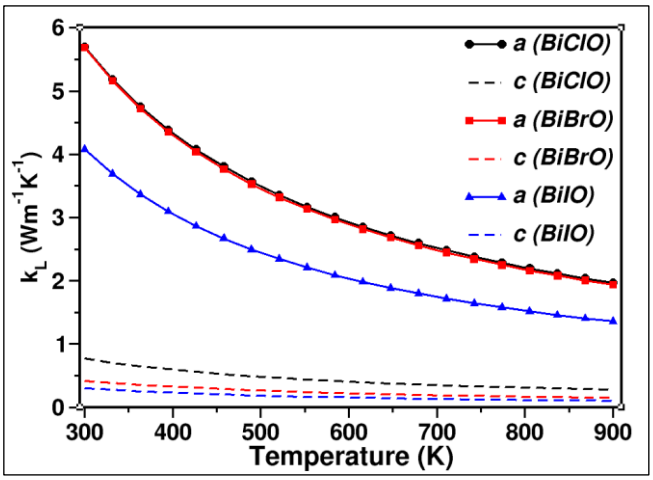

Materials with low or ultralow lattice thermal conductivity (κ_L) are indispensable for designing efficient energy harvesting devices. These functional low or ultralow κ_L materials are crucial for various thermal energy management applications such as thermoelectrics [1]–[3], thermal barrier coatings [4]–[7], and thermal insulation [8], [9]. Intensive research has been done and being progressed to explore various mechanisms to achieve ultralow κ_L materials. For instance, weakly bound atoms or atomic clusters can serve as rattler and these rattlers can scatter phonons to enhance phonon scattering rates and thereby lowering phonon lifetimes to suppress κ_L [10]–[13][14]. Materials having stereochemically active lone pair of electrons (ns^2, n= 4, 5, 6) (i.e. presence of one or more post-transition elements in a material with specific oxidation states) induce strong anharmonicity, which increases phonon scattering channels to reduce κ_L [15]–[18]. Usually materials consisting of heavy atomic mass elements result in less dispersive phonon dispersion curves, thus resulting in lowering phonon group velocities to reduce κ_L [19]–[23]. However, some exceptional cases exist where lighter atomic mass elements in a material possess relatively lower κ_L [24]. Moreover, materials with layered crystal structure possess distinct bonding nature along in-plane and cross-plane directions [19], [25]–[27], i.e. bonding heterogeneity. Understanding the interplay among the aforementioned mechanisms or convolutionary effect on phonon transport would be quite intriguing to aid in selecting or designing materials with ultralow κ_L.

5.1. Bismuth halooxides, BiXO (X= Cl, Br, I)

Layered materials with post-transition element(s) have intrinsic bonding heterogeneity, lone pair electrons induced anharmonicity, and heavy atomic mass elements [28]. We have considered Bismuth halooxides, which are promising materials for photocatalysis [29]–[31] and thermoelectric applications [32]–[37]. These materials received tremendous research interest due to their chemical and thermal stability. The family of materials containing Bismuth are being researched intensively for thermoelectric applications [36], [38], [39] because of their potential applications in energy storage and conversion devices [40]–[42]. The electronic and phonon transport properties of layered bismuth oxysulfide [18] [43], [44] and oxyselenide [45]–[47] materials have been theoretically investigated. Moreover, Bi_2Te_3 and its derivatives [48] find potential applications in thermoelectrics [49], [50]. In particular, Bismuth

halooxides, BiXO (X = Cl, Br, I) belong to the class of layered materials, in which Bi^{3+} consists of $6s^2$ lone pair electrons and strong bonding heterogeneity from their layered crystal structure. The BiXO series provide an opportunity to explore interplay among heavy atomic mass of Bi and I, lone pair $6s^2$ electrons of Bi^{3+} cation induced anharmonicity and bonding heterogeneity to achieve ultralow κ_L.

5.2. Computational details

All the first principles calculations have been carried out using Vienna Ab-initio Simulation Package (VASP) [51]. The exchange-correlation interactions were treated with PBE parameterization for solids (PBEsol) functional within the generalized gradient approximation (GGA), whereas the electron-ion interactions were treated with projector augmented wave (PAW) pseudopotential approach. The following plane wave basis orbitals were considered as valence electrons **O**: $2s^2,2p^4$; **Cl**: $3s^2,3p^5$; **Br**: $4s^2,4p^5$; **I**: $5s^2,5p^5$; **Bi**: $5d^{10}\ 6s^2\ 6p^3$. A plane wave energy cutoff of 560 eV was used for plane wave basis set expansion and a spacing of $2\pi \times 0.025\ ^{\circ}A^{-1}$ for k-mesh in the irreducible Brillouin zone for the structural optimization. Elastic constants were computed using stress-strain method as implemented in VASP.

By considering the obtained ground state structure at 0 K, ab-initio molecular dynamics (AIMD) simulations have been carried out using VASP at 300 K. The AIMD simulations were run for 5000 MD steps with a time-step of 1 fs (i.e., 5 ps) with a supercell size of 4×4×2 and 5×5×2 at Γ-centred k-mesh for the BiClO, BiBrO and BiIO, respectively. The temperature was controlled with a Nose Hoover thermostat [52], [53]. Lattice dynamics and phonon transport properties of BiXO (X = Cl, Br, I) compounds were computed using temperature dependent effective potential (TDEP) [54] method including harmonic (2^{nd}) and anharmonic (3^{rd}) interatomic force constants (IFCs). 9^{th} and 7^{th} nearest neighbours were considered for 2^{nd} and 3^{rd} order IFCs, respectively to calculate phonon dispersion curves, phonon density of states and phonon transport properties. The lattice thermal conductivity is calculated by iteratively solving the full Boltzmann transport equation (BTE) with a q-mesh of 25×25×11.

5.3 Results and discussion

5.3.1 Crystal structure, bonding and mechanical properties

Multifunctional behavior of Bismuth halooxides, BiXO (X = Cl, Br, I) arose tremendous research interest from both experimental and theoretical perspective. BiXO crystallizes in the primitive tetragonal (*P4/nmm*) crystal structure (PbClF-type) with Z = 2 f.u./cell at ambient conditions [55]. The metal Bi, non-metal X (Cl, Br, and I) and O atoms are located at Wyckoff positions 2c: (0.25, 0.25, v), 2c: (0.25,0.25, u), and 2a: (0.75,0.25,0), respectively, where u and v are the internal variable coordinates of X and Bi atoms, respectively. Full structural optimization was performed (i.e. both lattice constants and fractional coordinates) to obtain ground state crystal structure with an initial crystal structure determined from X-ray diffraction (XRD) measurements [55]. Table 5.1 shows the calculated ground state structural properties, which agree with the XRD [55] and earlier studies employing first principles calculations.

Table 5.1: Calculated ground state lattice parameters (a, c in A˚), bond lengths (in A˚) and bond angles (in ^{o}) of BiXO (X = Cl, Br, I) compounds.

Compound	**Work**	**a**	**c**	**Bi-O**	**∠O1-Bi-O2**	**Bi-X1**	**Bi-X2**	**∠X1-Bi-X2**
BiClO	This Work	3.887	7.354	2.326	113.36	3.467	3.054	64.15
	Others	3.8743 [56]	7.3997 [56]	2.237 [57]	114.22 [57]	3.462 [57]	2.961 [57]	-
		3.89 [58]	7.38 [58]	-	-	-	-	-
		3.894 [59]	7.369 [59]	-	-	-	-	-
BiBrO	This Work	3.923	8.105	2.336	114.22	4.023	3.175	60.88
	Others	3.924 [59]	8.101 [59]	2.245 [57], 2.325 [60]	115.316 [57]	4.033 [57]	3.086 [57]	-
		3.93 [35]	8.06 [35]	-	-	-	-	-

BiIO	This Work	3.995	9.151	2.352	116.25	4.829	3.369	56.96
	Others	3.992 [59]	9.15 [59]	2.262 [57]	117.39 [57]	4.826 [57]	3.275 [57]	-
		4.02 [34]	9.04 [34]	-	-	-	-	-

Each Bi atom is surrounded by four O atoms, four X's, and one X from the adjacent layer, as illustrated in Figure 5.1(a). This arrangement results in a BiO_4X_5 structural motif with a coordination number of 9. As seen in Figure 5.1(a), the crystal structure of BiXO has three non-equivalent bonds: one Bi-O bond and two Bi-X bonds (Bi-X1 and Bi-X2). The strength of the Bi-O, Bi-X1, and Bi-X2 bonds in BiXO increases as the size of X (Cl → Br → I) increases. As the size of X increases from Cl to Br and then to I in BiXO, the packing of the halide sublattice becomes significantly restricted. To relieve this stress, the lattice stretches along the c-axis by increasing the axial Bi-X1 bond length. This behaviour is similar to that observed in the iso-structural BaXF (X = Cl, Br, I). As the size of X increases, the axial ratio (c/a) of BiOCl, BiOBr, and BiOI increases from 1.892 to 2.066 to 2.291, respectively.

Hence, the increase of the axial Bi-X1 bond accounts for the quasi-two-dimensional layered structure in the PbClF-type materials.

The crystal structure of BiXO consists of a series of X-Bi-O-O-Bi-X layers that are bonded together through weak van der Waals (vdW) interactions. These layers are stacked perpendicular to the c-axis, resulting in a bonding heterogeneity [28]. Specifically, there is an in-plane ionic bonding and cross-plane weak vdW bonding in these BiXO compounds.

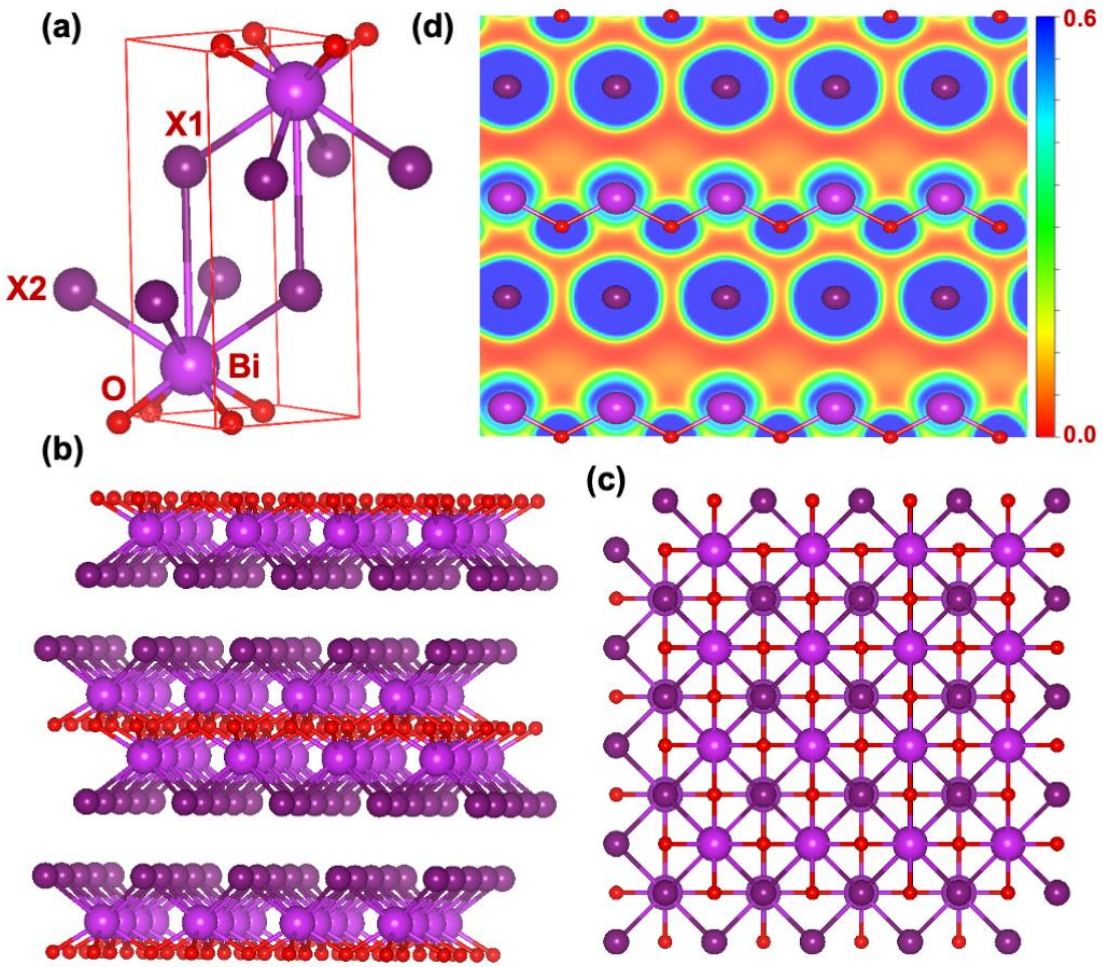

Fig. 5.1: Crystal structure of layered Bismuth halooxides, BiXO (X = Cl, Br, I) (a) Primitive/unit cell of BiXO compounds with one axial (Bi-X1) and equatorial (Bi-X2) bonds (b) Side view of layered structure (c) Top view (d) Electron localization function (ELF) of BiXO along the (001) plane.

In order to have a deeper comprehension of chemical bonding, the potential energy is determined by off-centering the Bi, O, and X atoms from their equilibrium position. A deep potential well appears for all atoms when they are displaced in the cross-plane direction, whereas a shallow potential well is observed in the in-plane direction for all atoms (Figure 5.2). This suggests that the Bi and X atoms exhibit a rattling motion, which arises from the bonding heterogeneity.

In order to examine the mechanical stability and bonding heterogeneity of BiXO, as well as to determine any potential relationship between mechanical and phonon transport properties, computed elastic constants for BiXO compounds are presented in table 5.2. PbClF-type materials have a primitive tetragonal symmetry (*P4/nmm*) and feature six distinct elastic constants: C_{11}, C_{33}, C_{12}, C_{13}, C_{44}, and C_{66}.

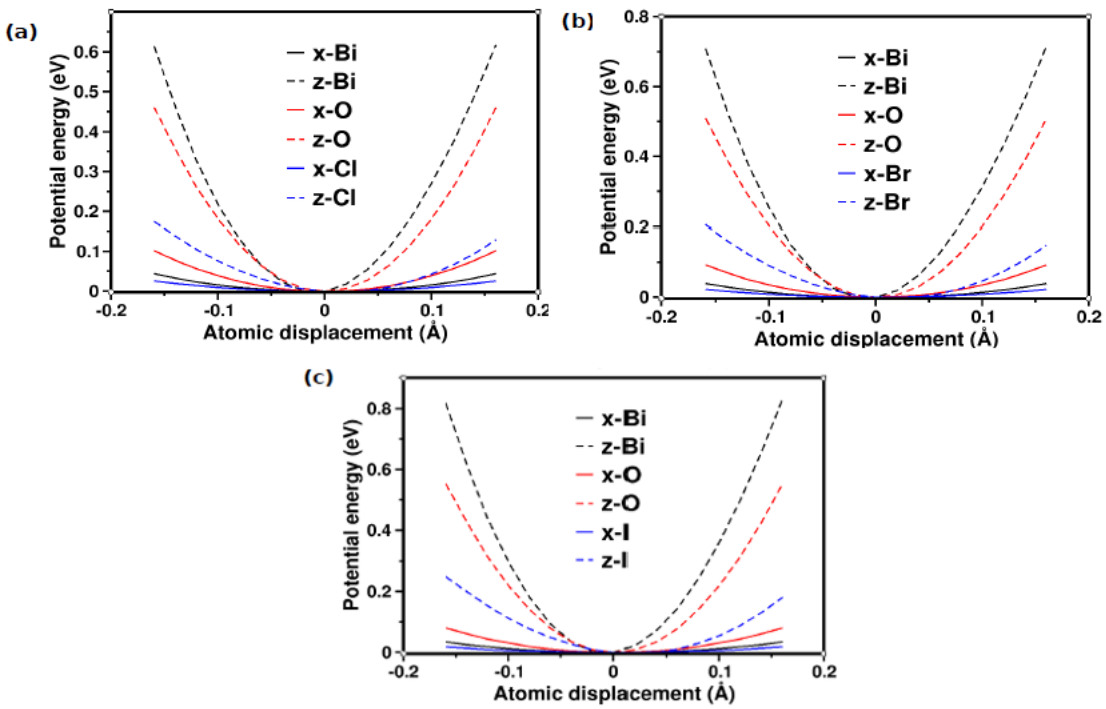

Fig. 5.2: Potential energy curves for (a) BiClO (b) BiBrO and (c) BiIO compounds by off-centering each atom from its equilibrium position.

The calculated elastic constants adhere to Born's stability requirements, indicating that all the examined BiXO materials are mechanically stable under normal pressure conditions. For the three BiXO compounds, the cross-plane elastic constant C_{33} is lower than the in-plane elastic constant C_{11}, indicating that the lattice is weaker along the 'c' axis than along the 'a' axis. This is due to the presence of weakly bonded van der Waals (vdW) interactions between the stacked X-Bi-O-O-Bi-X layers along the c-axis. C_{12} has a much greater value than C_{13}, suggesting that when a typical stress is applied along the 'a' axis, a larger strain will result along the 'c' axis. The elastic constant C_{44} has the smallest value, thus applying shear force will result in the highest strain. Consequently, this crystal is more prone to cracking along the 'c' axis.

The findings indicate the robust bonding within the ab-plane of BiXO and the weak bonding along the c-axis.

Table 5.2: Calculated second order elastic constants (in GPa) for BiXO (X = Cl, Br, I) compounds

Compound	**Method**	**C_{11}**	**C_{33}**	**C_{44}**	**C_{66}**	**C_{12}**	**C_{13}**
BiClO	This work	135.98	46.67	60.8	25.05	71.11	35.09

BiBrO	This work	118.24	22.75	53.87	19.19	59.29	22.06
BiIO	This work	101.68	24.37	43.64	12.24	41.88	14.23
	Others [61]	99	17.1	43.7	9.5	39.9	10.8

The calculated bulk modulus of BiXO (refer to table 5.3) is greater than its shear modulus, suggesting that BiXO is more resistant to changes in volume than to shape deformation (table 5.3). BiOI possesses the lowest Young's modulus value compared to other BiXO compounds. This suggests that BiOI has a high degree of flexibility, allowing it to be readily stretched or compressed. The calculated Poisson's ratio (σ) values for BiXO are in close proximity to 0.25, suggesting that the ionic contribution to interatomic bonding might be substantial. The formulas provided in our earlier work [23] are used to compute the longitudinal (v_l), transverse (v_t), and average (v_m) sound velocities based on the elastic moduli (B, G) and crystal density. The decrease in v_l, v_t, and v_m can be attributed to the low elastic moduli (B, G) that occur when both the metal (M) and halogen (X) increase in size. According to the Slack hypothesis, materials with a low Debye temperature (Θ_D) have a correspondingly low thermal conductivity (κ_L). BiOI has the lowest (v_m) and Debye temperature (Θ_D) compared to other BiXO compounds. Consequently, it is probable that BiOI possesses the lowest thermal conductivity (κ_L) among these compounds.

Table 5.3 : Computed polycrystalline aggregate properties, bulk moduli (B_V , B_R, B_{VRH} in GPa), shear moduli (G_V , G_R, G_{VRH} in GPa), Young's modulus (E in GPa), density (ρ in gr/cc), sound velocities (v_l, v_t and v_m, in km/s) and Debye temperature (in K) for BiXO (X = Cl, Br, I) compounds.

Parameter	**BiClO**	**BiOBr**	**BiIO**
ρ	7.81	8.12	8
B_V	66.8	51.78	40.93
G_V	41.15	35.75	30.38
B_R	45.01	22.88	22.91
G_R	31.39	22.27	20.8
B_{VRH}	55.91	37.33	31.92

G_{VRH}	36.27	29	25.59
E	89.46	69.12	60.59
σ	0.23	0.19	0.18
v_l	3.65	3.06	2.87
v_t	2.15	1.89	1.79
v_m	2.39	2.08	1.97
Θ_D	268.73	225.84	202.55

5.3.2 Born effective charges and chemical bonding

Born effective charges (BEC's) are critical parameters that quantify the relationship between atomic displacement and the evolution of lattice polarisation. Materials comprised of lone pair cations, wherein the outermost ns^2 (n = 4, 5, 6) electrons are completely occupied, exhibit improved BEC's as a consequence of mixed ionic-covalent bonding. Consequently, these materials exhibit increased static dielectric constants as a consequence of their strong lattice polarisation, which enhances BEC's [18], [28], [61], [62]. The substantial separation between longitudinal optic (LO) and transverse optic (TO) modes caused by the increased BEC's results in soft TO modes and brings the lattice to the verge of ferroelectric instability or lattice instability. This is an exceptionally advantageous method for attaining ultralow κ_L [28]. Figure 5.1(d) demonstrates that BiXO, analogous to PbXF (X = Cl, Br, I) materials, possesses a lone pair at the Bi^{3+} cation that is stereochemically active. This is demonstrated by the polar semiconductor properties of the $6s^2$ lone pair Bi^{3+} cation and the tetragonal symmetry (*P4/nmm*) structure of BiXO [28]. In the in-plane direction, the BEC's obtained are nearly double or greater than double their formal ionic charges Bi (+3), O (-2), and X (-1) ions, particularly for halogens (refer to Table 5.4).

The fact that the magnitude of BEC's increases from Cl to Br to I is consistent with the Bader charge (Table 5.5) and ELF analysis (Figure 5.1d) and suggests that the covalent character of these compounds is intensifying.

Table 5.4: Born effective charge (Z*), electronic dielectric constant (ϵ^{∞}), and ionic dielectric constant (ϵ^{0}) of BiXO (X = Cl, Br, I). The symbols 'a' and 'c' represent the in-plane and cross-plane directions, respectively.

Compound	**Atom**	$\mathbf{Z}_a^*$	$\mathbf{Z}_c^*$	$\boldsymbol{\epsilon}_a^{\infty}$ $(\boldsymbol{\epsilon}_c^{\infty})$	$\boldsymbol{\epsilon}_a^{\mathbf{0}}$ $(\boldsymbol{\epsilon}_c^{\mathbf{0}})$
BiClO	Bi	5.34	3.63	6.57 (5.23)	41.59 (7.89)
	O	-3.24	-2.15	-	-
	Cl	-2.09	-1.48	-	-
BiBrO	Bi	5.62	3.43	7.37 (5.48)	43.87 (4.80)
	O	-3.47	-2.23	-	-
	Br	-2.15	-1.2	-	-
BiIO	Bi	5.93	3.42	8.72 (6.23)	50.15 (3.39)
	O	-2.13	-1.02	-	-
	I	-3.8	-2.4	-	-

Table 5.5: Calculated Bader Charges for BiXO (X = Cl, Br, I) compounds.

Compound	**BiClO**	**BiBrO**	**BiIO**
Bi	1.796	1.719	1.631
O	-1.143	-1.146	-1.154
Cl/Br/I	-0.654	-0.573	-0.478

5.3.3 Raman spectra, lattice dynamics and thermal conductivity

Due to the fact that BiXO is composed of six elements per primitive cell, the zone centre exhibits a total of eighteen vibrational modes, of which fifteen are optical modes and three are acoustic modes.

The following is a classification of the phonon modes of the *P4/nmm* space group in accordance with group theory:

$$\Gamma_{18} = 2A_{1g} \oplus B_{1g} \oplus 3E_g \oplus 3E_u \oplus 3A_{2u}$$

where six are Raman active (A_{1g}, B_{1g}, E_g) and four are IR active (A_{2u}, E_u) modes (table 5.6). Here, "A" and "B" modes correspond to vibrations in the c-axis or cross-plane direction, whereas the "E" mode represents doubly degenerate vibrational modes on the

a-axis or in-plane direction. Figure 5.3 shows that the Raman-shift undergoes a red-shift as the atomic mass of the halogen (X) grows. This phenomenon occurs because lighter atoms possess the ability to vibrate at greater frequencies when compared to heavier atoms.

The red-shift in the low-lying optical phonon modes becomes more pronounced with an increase in the size of X , this is in contrast to the shift in the high frequency optical phonon modes. The low-frequency optical phonon modes play a crucial role in phonon transport as they may either enhance or reduce the lattice component of thermal conductivity, depending on whether they have a dispersive or flat band character in the phonon branches. The high dispersive and flat-band nature of optical phonons exhibit relatively low and high κ_L in BiClO and BiIO, respectively.

In order to gain a deeper comprehension of lattice dynamics, the phonon dispersion curves and phonon density of states were calculated and plotted, taking into account the effects of anharmonic (3^{rd} order force constants) at a temperature of 300 K.

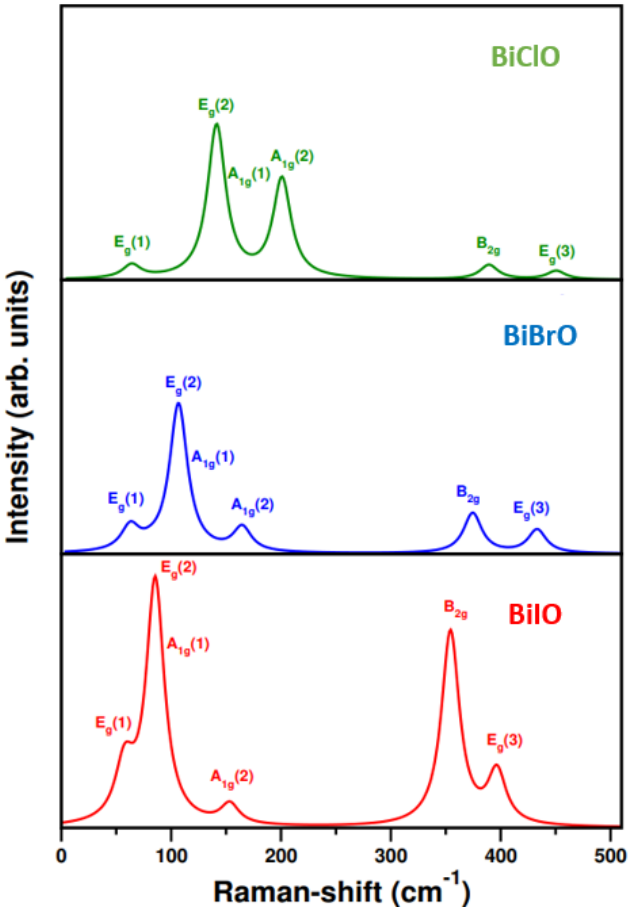

Fig. 5.3: Raman Spectra for BiXO (X = Cl, Br, I) compounds.

Table 5.6: Calculated Raman active modes for BiXO (X = Cl, Br, I) compounds compared with available experimental and previous first principles calculations.

Compound	Raman mode	Frequency		
		This work	**Experiment**	**Others**
BiClO	$E_g(1)$	64.08	59.5 [63]	87.7 [64]
	$E_g(2)$	138.69	150 [63]	161.1 [64]
	$A_{1g}(1)$	141.56	144.5 [63], 146 [65]	153.3 [64]
	$A_{1g}(2)$	200.91	201.5 [63]	200 [64]
	B_{2g}	389.37	400 [65]	451.9 [64]
	$E_g(3)$	450.58	-	499.9 [64]
BiBrO	$E_g(1)$	62.83	59 [60]	70 [60]
	$E_g(2)$	81.56	93 [60] , 92 [65]	98 [60]
	$A_{1g}(1)$	106.71	113 [60], 113 [65]	115 [60]
	$A_{1g}(2)$	164.69	162 [60]	167 [60]
	B_{2g}	374.54	384 [60], 385 [65]	382 [60]
	$E_g(3)$	433.18	425 [60], 410 [65]	429 [60]
BiIO	$E_g(1)$	31.61	-	-
	$E_g(2)$	139.08	-	-
	$A_{1g}(1)$	165.97	-	-
	$A_{1g}(2)$	243.2	-	-
	B_{2g}	420.21	-	-
	$E_g(3)$	516.92	-	-

These computations were carried out along the Brillouin zone's high symmetry points (Figure 5.4), in addition to the in-plane (Γ-X) and cross-plane (Γ-Z) directions (Figure 5.5). The phonon bands exhibit a red-shift as the size of X increases, as seen in figure 5.4.

The low frequency phonon bands mostly originate from the Bi and X elements, whereas O atoms predominantly influence the high frequency phonon bands. These O atoms are highly isolated from the Bi and X phonon bands, as seen in Figure 5.4. The phonon bands of chlorine (Cl), bromine (Br), and iodine (I) in BiXO compounds exhibit a noticeable red-shift as the size of X increases. Furthermore, the degree of overlap between Bi and X phonon bands intensifies as the size of X increases (from Cl to Br to I).

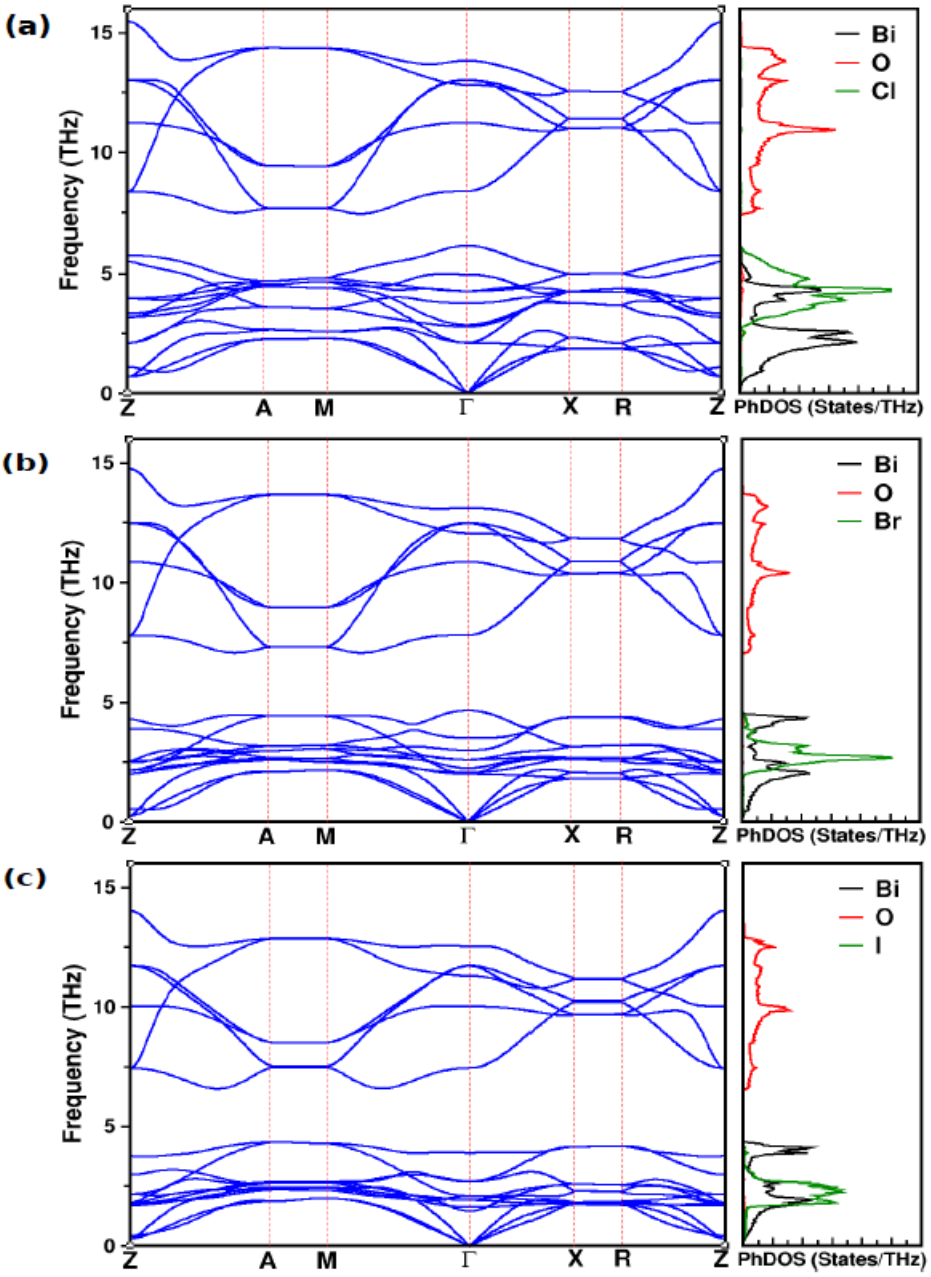

Fig. 5.4: Phonon dispersion curves for BiXO (X=Cl,Br and I) compounds.

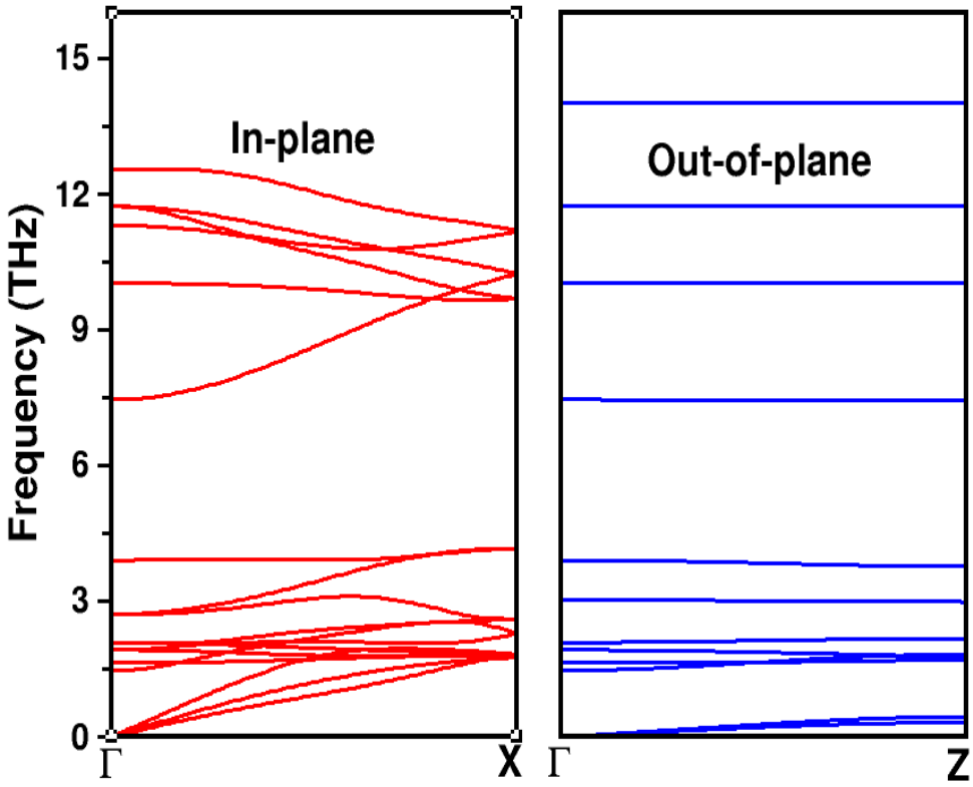

Fig. 5.5: Phonon dispersion curves for BiIO compound along in-plane and cross-plane directions.

As seen in Figure 5.6, the κ_L values obtained exhibit a consistent reduction as temperature increases. The κ_L values obtained at a temperature of 300 K are as follows: 5.69, 5.89, and 4.08 W/m-K for the in-plane direction of BiClO, BiBrO, and BiIO, respectively. For the cross-plane direction, the κ_L values are 0.77, 0.42, and 0.30 W/m-K for BiClO, BiBrO, and BiIO, respectively. Consistent with the nature of layered materials, the κ_L values in the cross-plane direction are lower than those in the in-plane direction for all three BiXO compounds over the temperature range. This is attributed to the presence of substantial bonding heterogeneity. The computed anisotropic and average cumulative and spectral κ_L clearly indicate that optical phonons make a significant contribution to κ_L, in addition to the contribution from acoustic phonons, along the in-plane direction. However, the contribution from acoustic phonons to κ_L along the cross-plane direction is almost negligible for BiBrO and BiIO. Relatively large contribution of acoustic and optical phonons to κ_L (3.93 w/m-K) for BiBrO increase its κ_L value (4.05 w/m-K) approximately close to BiClO, as shown in Figure 5.7 and Figure 5.8.

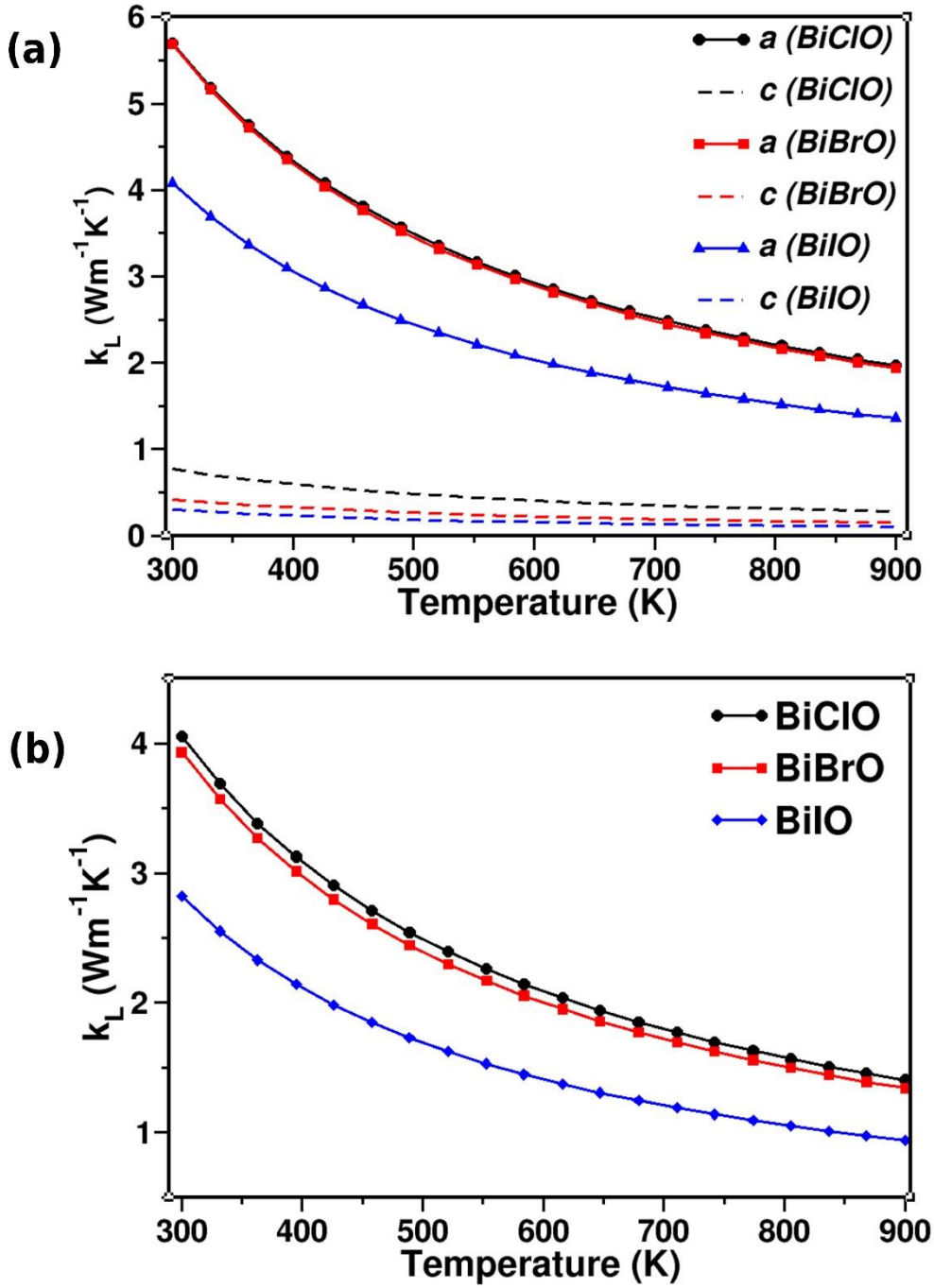

Fig. 5.6: Variation of (a) lattice thermal conductivity (κ_L) along in-plane and cross-plane directions and (b) average (κ_L) as a function of temperature for BiXO (X = Cl, Br and I) compounds.

This is noteworthy considering the relatively high average atomic mass of BiBrO. The three compounds have extremely low κ_L values in the cross-plane direction. Overall, the typical κ_L values exhibited by them are quite low, measuring below 5 W/m-K as seen in Table 5.7.

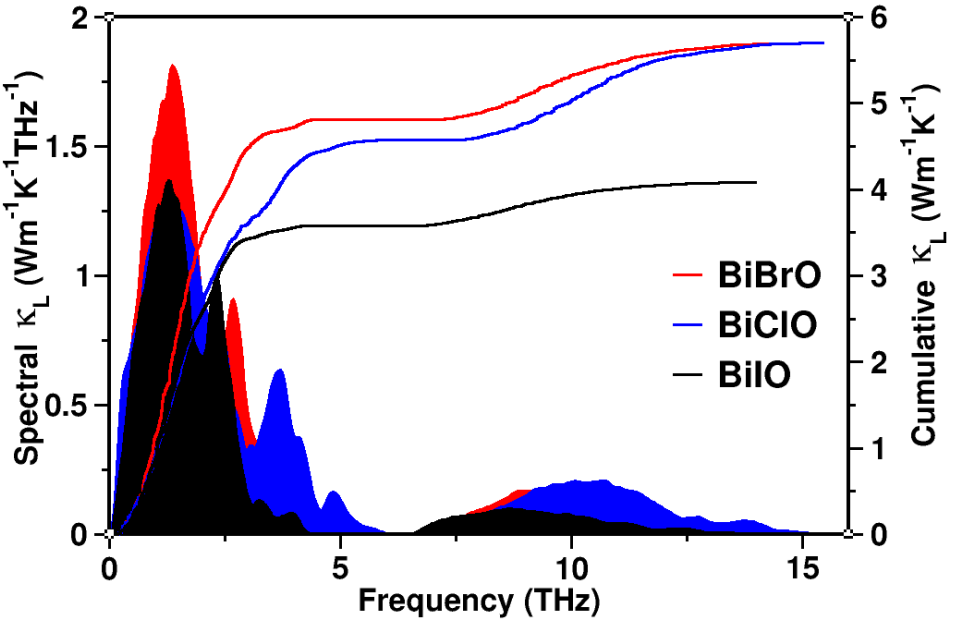

Fig. 5.7: Average cumulative and spectral lattice thermal conductivity for BiXO (X = Cl, Br and I) compounds.

To obtain a better understanding of κ_L and the factors that greatly impact its trends in these BiXO compounds, phonon lifetimes and phonon group velocities are computed and shown in Figs. 5.9 and 5.11, respectively. Phonons that are highly dispersive have a greater slope of $d\omega/dk$, which determines the magnitude of phonon group velocities (v_g).

Table 5.7: Anisotropic and average κ_L values (in W/m-K) for BiXO (X = Cl, Br, I) compounds at 300 K.

Compound	**Method**	$\boldsymbol{\kappa_L^{xx}}$	$\boldsymbol{\kappa_L^{zz}}$	$\boldsymbol{\kappa_L^{xx}/\kappa_L^{zz}}$	$\boldsymbol{\kappa_{LAvg}}$
BiClO	This work	5.69	0.77	7.4	4.049
BiBrO	This work	5.68	0.42	13.5	3.926
BiIO	This work	4.08	0.3	15.6	2.82
	Others [34]	4	0.5	-	-

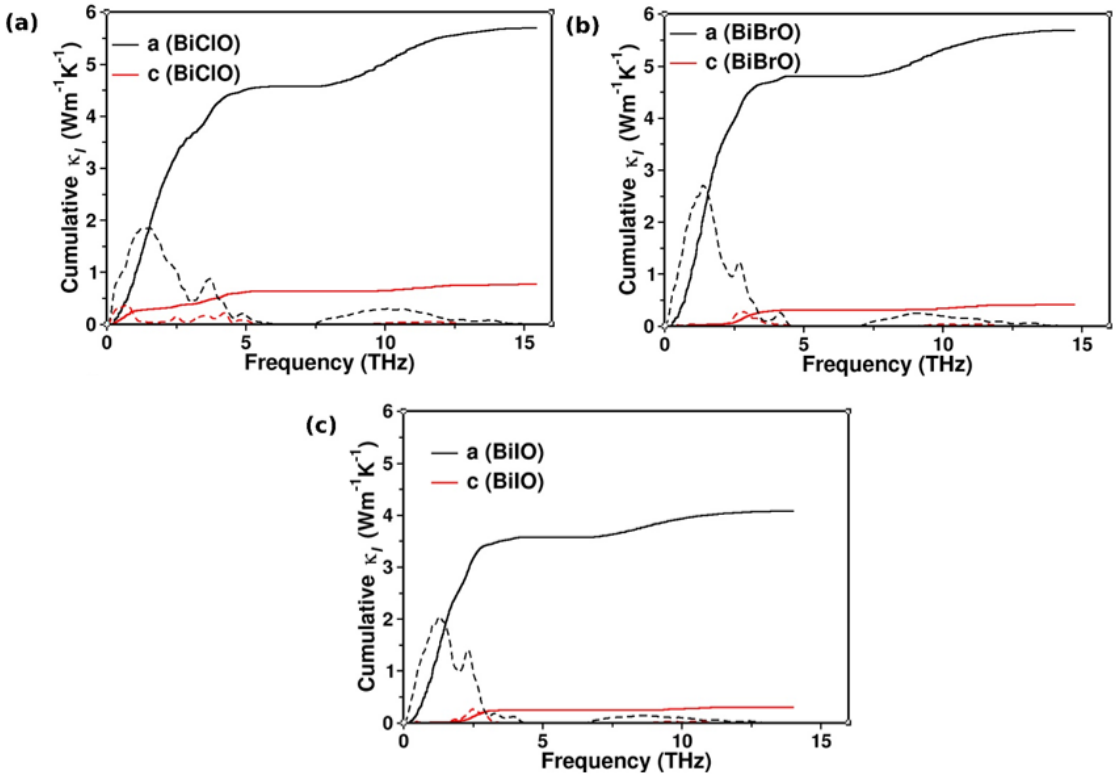

Fig. 5.8: Cumulative (solid lines) and spectral (dotted lines) lattice thermal conductivity for BiXO (X = Cl, Br and I) compounds along in-plane and cross-plane directions.

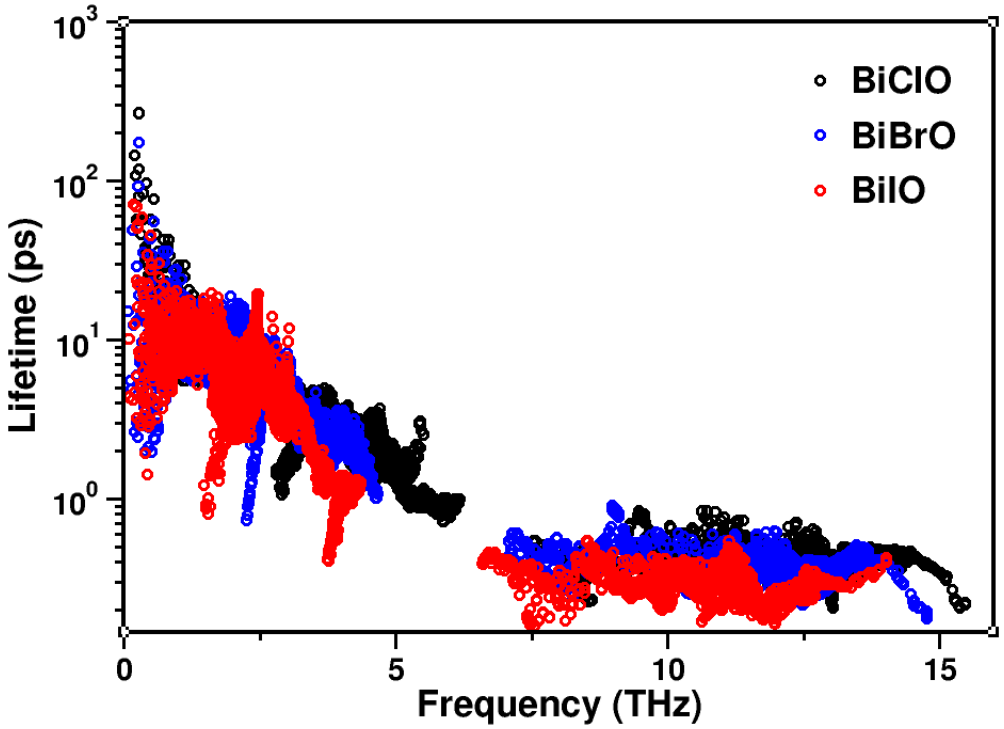

Fig. 5.9: Phonon lifetimes for BiXO (X = Cl, Br and I) compounds. The observed troughs originated from flat bands observed in the computed phonon dispersion curves.

Figure 5.11 demonstrates that the calculated phonon group velocities are greater in the in-plane direction than in the cross-plane direction. This is explained by the fact that phonons are more dispersive in the Γ-X direction than they are along the Γ-Z direction. Furthermore, the phonon group velocities of BiIO are somewhat lower in comparison to those of BiClO and BiBrO. The phonon lifetimes are found to decrease in the following order: BiClO > BiBrO > BiIO across all frequencies. As a result, BiOI exhibits a lower κ_L compared to BiClO and BiBrO. The phonon dispersion curves (Fig. 5.4) reveal flat bands that correspond to severe troughs in the phonon lifetimes, as seen in Figure 5.9. These troughs are caused by an increase in three-phonon scattering, leading to reduced phonon lifetimes. The phonon scattering rates of BiOI are comparatively higher than those of BiOBr and BiOCl, as shown in Figure 5.10.

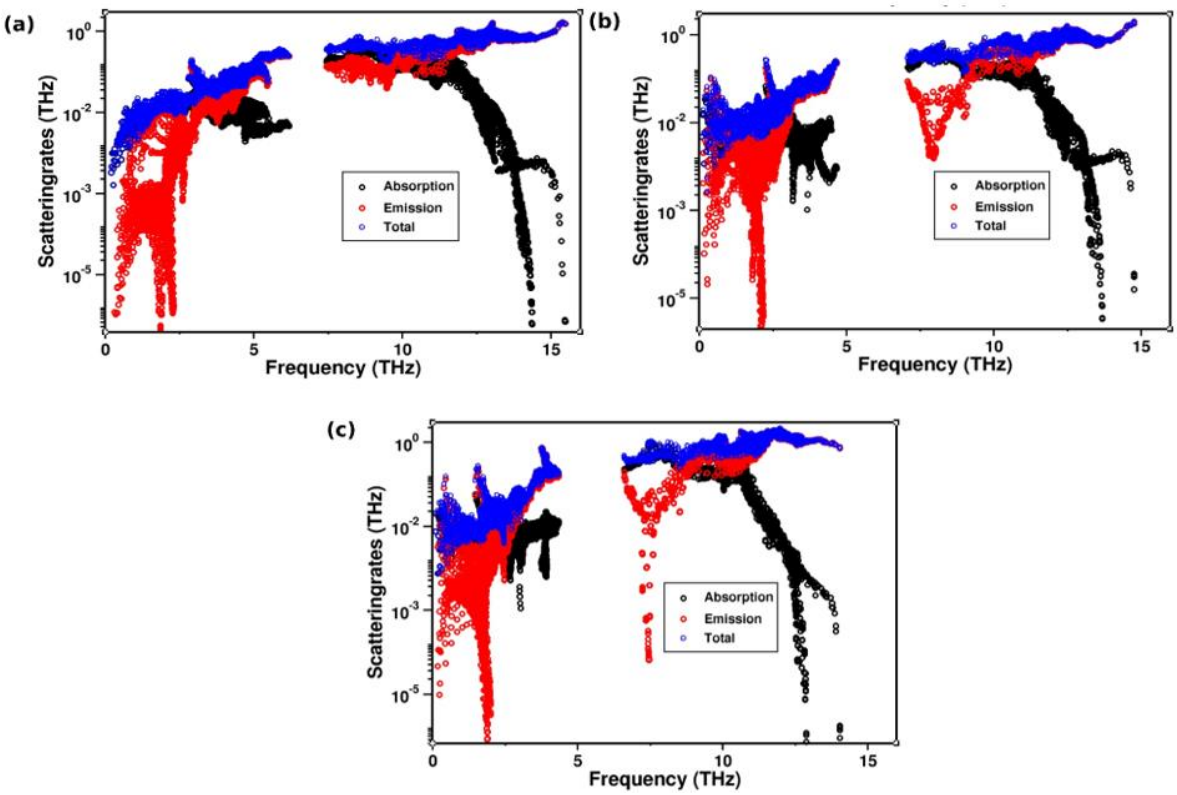

Fig. 5.10: Scattering rates for (a) BiClO (b) BiBrO (c) BiIO compounds.

Consequently, BiOI exhibits very short phonon lifetimes and low phonon group velocities (Figure 5.12), leading to a low κ_L in BiIO compared to BiClO and BiBrO.

The significant reduction in phonon frequencies is attributed to the large atomic mass of Bi and I atoms, whereas the low phonon group velocities are a consequence of the strong bonding heterogeneity.

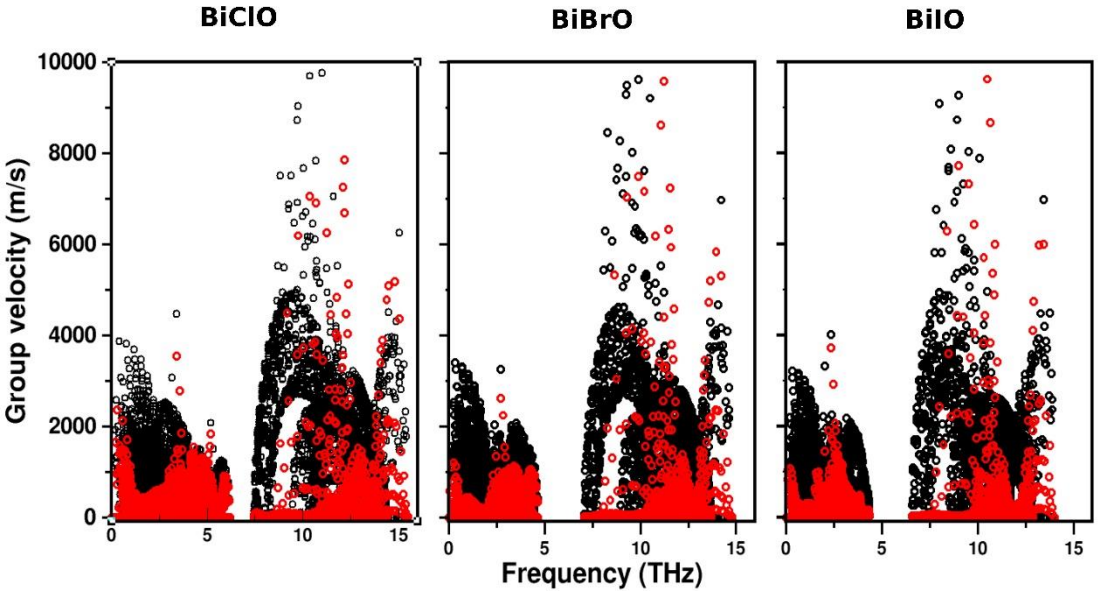

Fig. 5.11: Group velocities along in-plane (open black circles) and cross-plane (open red circles) for BiXO (X = Cl, Br and I) compounds

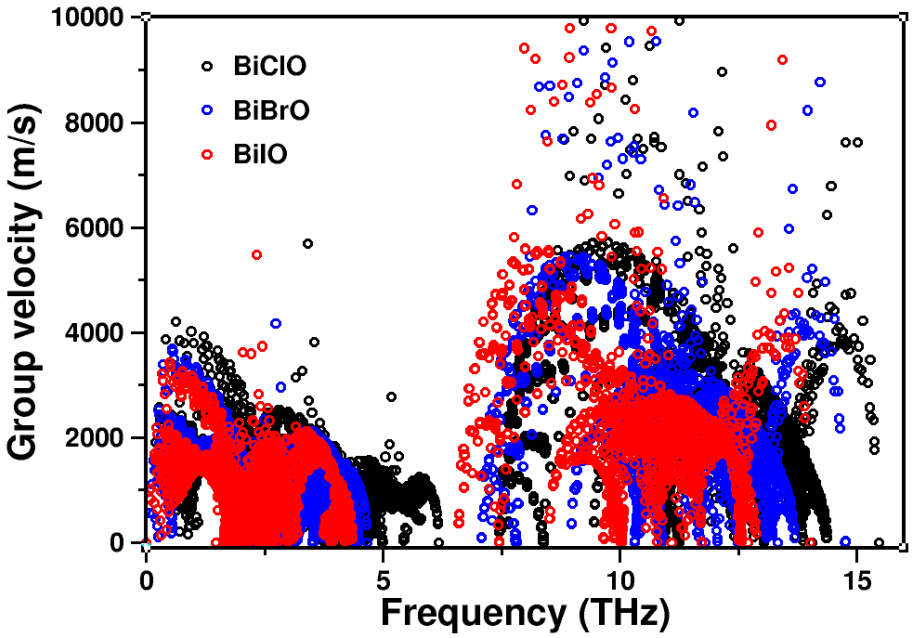

Fig. 5.12: Average Velocity plots for BiXO (X=Cl,Br and I).

Additionally, the flat phonon bands and the influence of lone pairs create anharmonicity, leading to shorter phonon lifetimes and ultimately resulting in poor thermal conductivity (κ_L) in BiIO.

In summary, the current study employed a comprehensive methodology that involved static first principles computations, first principles molecular dynamics simulations, and Boltzmann transport theory. The objective was to examine the chemical bonding, lattice dynamics, and phonon transport features of layered matlockite PbClF-type

Bismuth halooxides. For BiBrO and BiIO, the large axial ratio (c/a > 2) is attributable to the large axial Bi-X1 bond, which determines the structural (c > a) and elastic (C_{11} > C_{33}) anisotropy in BiXO compounds. This property is similar to BaXF compounds, which have weak van der Waals bonds in the cross-plane direction. The three compounds under investigation have been predicted to have an ultralow cross-plane κ_L (< 1 W/m-K). Furthermore, the presence of structural and elastic anisotropy leads to a significant phonon transport anisotropy ratio of 13.5 for BiBrO and 15.6 for BiIO at a temperature of 300 K. This indicates a highly anisotropic phonon transport in these two compounds. The computed potential energy curves demonstrate that Bi and Br/I atoms function as rattlers within the compounds BiBrO and BiIO. The presence of $6s^2$ lone pair electrons causes enhanced Born effective charges are observed along in-plane directions.

An in-depth understanding of the interplay between the atomic mass, lone pair induced anharmonicity, and bonding heterogeneity is provided by the comprehensive understanding of crystal structure, chemical bonding, mechanical properties, lattice dynamics, and phonon transport properties. This is crucial for the selection of elements or the discovery of extremely low κ_L materials for future thermal energy management applications.

References:

[1] J. Mao, G. Chen, and Z. Ren, "Thermoelectric cooling materials," *Nat Mater*, vol. 20, no. 4, pp. 454–461, Apr. 2021, doi: 10.1038/s41563-020-00852-w.

[2] L. Hu *et al.*, "High thermoelectric performance enabled by convergence of nested conduction bands in $Pb_7Bi_4Se_{13}$ with low thermal conductivity," *Nat Commun*, vol. 12, no. 1, p. 4793, Aug. 2021, doi: 10.1038/s41467-021-25119-z.

[3] M. Dutta, D. Sarkar, and K. Biswas, "Intrinsically ultralow thermal conductive inorganic solids for high thermoelectric performance," *Chemical Communications*, vol. 57, no. 39, pp. 4751–4767, 2021, doi: 10.1039/D1CC00830G.

[4] B. Liu *et al.*, "Advances on strategies for searching for next generation thermal barrier coating materials," *J Mater Sci Technol*, vol. 35, no. 5, pp. 833–851, May 2019, doi: 10.1016/j.jmst.2018.11.016.

[5] B. Liu *et al.*, "Application of high-throughput first-principles calculations in ceramic innovation," *J Mater Sci Technol*, vol. 88, pp. 143–157, Oct. 2021, doi: 10.1016/j.jmst.2021.01.071.

[6] Z.-Y. Wei *et al.*, "Progress in ceramic materials and structure design toward advanced thermal barrier coatings," *Journal of Advanced Ceramics*, vol. 11, no. 7, pp. 985–1068, Jul. 2022, doi: 10.1007/s40145-022-0581-7.

[7] X. Shao *et al.*, "Contributions of bonding heterogeneity to mechanical and thermal properties of rare earth molybdates for thermal barrier coatings," *Journal of Physics and Chemistry of Solids*, vol. 173, p. 111087, Feb. 2023, doi: 10.1016/j.jpcs.2022.111087.

[8] Y. Li, Y. Luo, Z. Tian, J. Wang, and J. Wang, "Theoretical exploration of the abnormal trend in lattice thermal conductivity for monosilicates RE_2SiO_5 (RE = Dy, Ho, Er, Tm, Yb and Lu)," *J Eur Ceram Soc*, vol. 38, no. 10, pp. 3539–3546, Aug. 2018, doi: 10.1016/j.jeurceramsoc.2018.04.014.

[9] E. Bsaibess, F. Delorme, I. Monot-Laffez, and F. Giovannelli, "Ultra-low thermal conductivity in scheelite and A-deficient scheelite ceramics," *Scr Mater*, vol. 201, p. 113950, Aug. 2021, doi: 10.1016/j.scriptamat.2021.113950.

[10] M. K. Jana, K. Pal, A. Warankar, P. Mandal, U. V. Waghmare, and K. Biswas, "Intrinsic Rattler-Induced Low Thermal Conductivity in Zintl Type TlInTe $_2$," *J Am Chem Soc*, vol. 139, no. 12, pp. 4350–4353, Mar. 2017, doi: 10.1021/jacs.7b01434.

[11] J. Li, W. Hu, and J. Yang, "High-Throughput Screening of Rattling-Induced Ultralow Lattice Thermal Conductivity in Semiconductors," *J Am Chem Soc*, vol. 144, no. 10, pp. 4448–4456, Mar. 2022, doi: 10.1021/jacs.1c11887.

[12] T. Jia, X. Liu, Y. Zhang, and S.-H. Wei, "Origin of the variation in lattice thermal conductivities in pyrite-type dichalcogenides," *Phys Rev B*, vol. 107, no. 11, p. 115204, Mar. 2023, doi: 10.1103/PhysRevB.107.115204.

[13] Y. Wang, Q. Gan, M. Hu, J. Li, L. Xie, and J. He, "Anharmonic lattice dynamics and the origin of intrinsic ultralow thermal conductivity in AgI materials," *Phys Rev B*, vol. 107, no. 6, p. 064308, Feb. 2023, doi: 10.1103/PhysRevB.107.064308.

[14] M. Dutta, M. Samanta, T. Ghosh, D. J. Voneshen, and K. Biswas, "Evidence of Highly Anharmonic Soft Lattice Vibrations in a Zintl Rattler," *Angewandte Chemie*, vol. 133, no. 8, pp. 4305–4311, Feb. 2021, doi: 10.1002/ange.202013923.

[15] Y. Zhu *et al.*, "Giant phonon anharmonicity driven by the asymmetric lone pairs in Mg3Bi2," *Materials Today Physics*, vol. 27, p. 100791, Oct. 2022, doi: 10.1016/j.mtphys.2022.100791.

[16] V. Carnevali *et al.*, "Lone Pair Rotation and Bond Heterogeneity Leading to Ultralow Thermal Conductivity in Aikinite," *J Am Chem Soc*, vol. 145, no. 16, pp. 9313–9325, Apr. 2023, doi: 10.1021/jacs.3c02536.

[17] I. Maria, R. Arora, M. Dutta, S. Roychowdhury, U. V. Waghmare, and K. Biswas, "Metavalent Bonding-Mediated Dual $6s^2$ Lone Pair Expression Leads to Intrinsic Lattice Shearing in n-Type $TlBiSe_2$," *J Am Chem Soc*, vol. 145, no. 16, pp. 9292–9303, Apr. 2023, doi: 10.1021/jacs.3c02146.

[18] N. Yedukondalu, T. Pandey, and S. C. Rakesh Roshan, "Effect of Hydrostatic Pressure on Lone Pair Activity and Phonon Transport in Bi $_2$ O $_2$ S," *ACS Appl Energy Mater*, vol. 6, no. 4, pp. 2401–2411, Feb. 2023, doi: 10.1021/acsaem.2c03725.

[19] X. Yu, H. Shao, X. Wang, Y. Zhu, D. Fang, and J. Hong, “Anomalous lattice thermal conductivity in layered MNCl (M = Zr, Hf) materials driven by lanthanide contraction,” *J Mater Chem A Mater*, vol. 8, no. 6, pp. 3128–3134, 2020, doi: 10.1039/C9TA12600G.

[20] K. Guo *et al.*, “Unveiling the origins of low lattice thermal conductivity in 122-phase Zintl compounds,” *Materials Today Physics*, vol. 21, p. 100480, Nov. 2021, doi: 10.1016/j.mtphys.2021.100480.

[21] L. Lindsay, D. A. Broido, J. Carrete, N. Mingo, and T. L. Reinecke, “Anomalous pressure dependence of thermal conductivities of large mass ratio compounds,” *Phys Rev B*, vol. 91, no. 12, p. 121202, Mar. 2015, doi: 10.1103/PhysRevB.91.121202.

[22] Z. Chang *et al.*, “Anomalous Thermal Conductivity Induced by High Dispersive Optical Phonons in Rubidium and Cesium Halides,” *ES Energy & Environment*, 2022, doi: 10.30919/esee8c653.

[23] S. C. Rakesh Roshan *et al.*, “Anomalous Lattice Thermal Conductivity in Rocksalt IIA–VIA Compounds,” *ACS Appl Energy Mater*, vol. 5, no. 1, pp. 882–896, Jan. 2022, doi: 10.1021/acsaem.1c03310.

[24] S. C. Rakesh Roshan *et al.*, “Effect of Atomic Mass Contrast on Lattice Thermal Conductivity: A Case Study for Alkali Halides and Alkaline-Earth Chalcogenides,” *ACS Appl Electron Mater*, Oct. 2023, doi: 10.1021/acsaelm.3c00759.

[25] Y. Grin, “Inhomogeneity and anisotropy of chemical bonding and thermoelectric properties of materials,” *J Solid State Chem*, vol. 274, pp. 329–336, Jun. 2019, doi: 10.1016/j.jssc.2018.12.055.

[26] N. Sato *et al.*, “Bonding heterogeneity in mixed-anion compounds realizes ultralow lattice thermal conductivity,” *J Mater Chem A Mater*, vol. 9, no. 39, pp. 22660–22669, 2021, doi: 10.1039/D1TA04958E.

[27] X. Jin *et al.*, “Bonding Heterogeneity Leads to Hierarchical and Ultralow Lattice Thermal Conductivity in Sodium Metavanadate,” *J Phys Chem Lett*, vol. 13, no. 48, pp. 11160–11168, Dec. 2022, doi: 10.1021/acs.jpclett.2c03061.

[28] N. Yedukondalu *et al.*, “Lattice Instability and Ultralow Lattice Thermal Conductivity of Layered PbIF,” *ACS Appl Mater Interfaces*, vol. 14, no. 36, pp. 40738–40748, Sep. 2022, doi: 10.1021/acsami.2c01135.

[29] L. Xu, J. C. Yu, and Y. Wang, “Recent advances on bismuth oxyhalides for photocatalytic CO_2 reduction,” *Journal of Environmental Sciences*, Jul. 2023, doi: 10.1016/j.jes.2023.07.002.

[30] X. Wei, M. U. Akbar, A. Raza, and G. Li, “A review on bismuth oxyhalide based materials for photocatalysis,” *Nanoscale Adv*, vol. 3, no. 12, pp. 3353–3372, 2021, doi: 10.1039/D1NA00223F.

[31] A. Zulkiflee, M. M. Khan, and M. H. Harunsani, “Bismuth oxyhalides: Recent progress and its applications in photocatalysis, hydrogen production, antibacterial studies, and sensors,” *Mater Sci Semicond Process*, vol. 163, p. 107547, Aug. 2023, doi: 10.1016/j.mssp.2023.107547.

[32] Y. He and J. Zhou, “First-principles study on the ultralow lattice thermal conductivity of BiSeI,” *Physica B Condens Matter*, vol. 646, p. 414278, Dec. 2022, doi: 10.1016/j.physb.2022.414278.

[33] C.-W. Wu, X. Ren, G. Xie, W.-X. Zhou, G. Zhang, and K.-Q. Chen, “Enhanced High-Temperature Thermoelectric Performance by Strain Engineering in BiOCl,” *Phys Rev Appl*, vol. 18, no. 1, p. 014053, Jul. 2022, doi: 10.1103/PhysRevApplied.18.014053.

[34] M. Sajjad, N. Singh, and J. A. Larsson, “Bulk and monolayer bismuth oxyiodide (BiOI): Excellent high temperature *p* -type thermoelectric materials,” *AIP Adv*, vol. 10, no. 7, Jul. 2020, doi: 10.1063/1.5133711.

[35] D. Singh, M. Sajjad, J. Andreas Larsson, and R. Ahuja, “Promising high-temperature thermoelectric response of bismuth oxybromide,” *Results Phys*, vol. 19, p. 103584, Dec. 2020, doi: 10.1016/j.rinp.2020.103584.

[36] J. Yu, T. Li, and Q. Sun, “Single-layer BiOBr: An effective *p* -type 2D thermoelectric material,” *J Appl Phys*, vol. 125, no. 20, May 2019, doi: 10.1063/1.5098826.

[37] Y. Gan *et al.*, “Excellent Medium-Temperature Thermoelectric Performance of Monolayer BiOCl,” *Langmuir*, vol. 38, no. 25, pp. 7733–7739, Jun. 2022, doi: 10.1021/acs.langmuir.2c00741.

[38] S. Tippireddy, P. K. D S, S. Das, and R. C. Mallik, “Oxychalcogenides as Thermoelectric Materials: An Overview,” *ACS Appl Energy Mater*, vol. 4, no. 3, pp. 2022–2040, Mar. 2021, doi: 10.1021/acsaem.0c02770.

[39] M. C *et al.*, “Insights into structural features and thermoelectric properties of layered oxychalcogenides, *BiCuOCh* (*Ch = S, Se, Te*): promising green materials for energy conversion,” *Materials Research Innovations*, vol. 27, no. 4, pp. 267–280, Jun. 2023, doi: 10.1080/14328917.2022.2140784.

[40] S. Adhikari, S. Mandal, and D. Kim, “Recent Development Strategies for Bismuth-Driven Materials in Sustainable Energy Systems and Environmental Restoration,” *Small*, vol. 19, no. 10, Mar. 2023, doi: 10.1002/smll.202206003.

[41] Z. Mengting, T. A. Kurniawan, L. Duan, Y. Song, S. W. Hermanowicz, and M. H. D. Othman, “Advances in BiOX-based ternary photocatalysts for water technology and energy storage applications: Research trends, challenges, solutions, and ways forward,” *Rev Environ Sci Biotechnol*, vol. 21, no. 2, pp. 331–370, Jun. 2022, doi: 10.1007/s11157-022-09617-0.

[42] J. Sharma *et al.*, “Advances in photocatalytic environmental and clean energy applications of bismuth-rich oxy halides-based heterojunctions: a review,” *Materials Today Sustainability*, vol. 21, p. 100327, Mar. 2023, doi: 10.1016/j.mtsust.2023.100327.

[43] C. Kim, D. H. Kim, H. Kim, and J. S. Chung, “Significant Enhancement in the Thermoelectric Performance of a Bismuth Telluride Nanocompound through Brief Fabrication Procedures,” *ACS Appl Mater Interfaces*, vol. 4, no. 6, pp. 2949–2954, Jun. 2012, doi: 10.1021/am3002764.

[44] H.-Y. Song, X.-J. Ge, M.-Y. Shang, J. Zhang, and J.-T. Lü, “Intrinsically low thermal conductivity of bismuth oxychalcogenides originating from interlayer coupling,” *Physical Chemistry Chemical Physics*, vol. 21, no. 33, pp. 18259–18264, 2019, doi: 10.1039/C9CP03394G.

[45] A. Parida, S. Senapati, and R. Naik, “Recent developments on Bi-based oxychalcogenide materials with thermoelectric and optoelectronic applications: an overview,” *Mater Today Chem*, vol. 26, p. 101149, Dec. 2022, doi: 10.1016/j.mtchem.2022.101149.

[46] J. Sun, M. Hu, C. Zhang, L. Bai, C. Zhang, and Q. Wang, “Ultralow Thermal Conductivity of Layered Bi_2O_2Se Induced by Twisting,” *Adv Funct Mater*, vol. 32, no. 47, Nov. 2022, doi: 10.1002/adfm.202209000.

[47] J. Wang *et al.*, "Thermoelectric properties of Bi_2O_2Se single crystals," *Appl Phys Lett*, vol. 119, no. 8, Aug. 2021, doi: 10.1063/5.0063091.

[48] L. Lou *et al.*, "Tunable Electrical Conductivity and Simultaneously Enhanced Thermoelectric and Mechanical Properties in n-type Bi_2Te_3," *Advanced Science*, vol. 9, no. 27, Sep. 2022, doi: 10.1002/advs.202203250.

[49] D. Singh and R. Ahuja, "Dimensionality effects in high-performance thermoelectric materials: Computational and experimental progress in energy harvesting applications," *WIREs Computational Molecular Science*, vol. 12, no. 1, Jan. 2022, doi: 10.1002/wcms.1547.

[50] T. Cao *et al.*, "Advances in bismuth-telluride-based thermoelectric devices: Progress and challenges," *eScience*, vol. 3, no. 3, p. 100122, Jun. 2023, doi: 10.1016/j.esci.2023.100122.

[51] G. Kresse and J. Furthmüller, "Efficient iterative schemes for *ab initio* total-energy calculations using a plane-wave basis set," *Phys Rev B*, vol. 54, no. 16, pp. 11169–11186, Oct. 1996, doi: 10.1103/PhysRevB.54.11169.

[52] W. G. Hoover, "Constant-pressure equations of motion," *Phys Rev A (Coll Park)*, vol. 34, no. 3, pp. 2499–2500, Sep. 1986, doi: 10.1103/PhysRevA.34.2499.

[53] W. G. Hoover, "Canonical dynamics: Equilibrium phase-space distributions," *Phys Rev A (Coll Park)*, vol. 31, no. 3, pp. 1695–1697, Mar. 1985, doi: 10.1103/PhysRevA.31.1695.

[54] O. Hellman and I. A. Abrikosov, "Temperature-dependent effective third-order interatomic force constants from first principles," *Phys Rev B*, vol. 88, no. 14, p. 144301, Oct. 2013, doi: 10.1103/PhysRevB.88.144301.

[55] F. A. Bannister, "The crystal-structure of the bismuth oxyhalides," *Mineralogical Magazine and Journal of the Mineralogical Society*, vol. 24, no. 149, pp. 49–58, Jun. 1935, doi: 10.1180/minmag.1935.024.149.01.

[56] J. Yi and Z.-Y. Zhao, "The electronic structure and photoluminescence properties of $BiOCl:Eu^{3+}$ from first-principles calculations," *J Lumin*, vol. 156, pp. 205–211, Dec. 2014, doi: 10.1016/j.jlumin.2014.08.023.

[57] J. Ketterer and V. Krämer, “Structure refinement of bismuth oxide bromide, BiOBr,” *Acta Crystallogr C*, vol. 42, no. 8, pp. 1098–1099, Aug. 1986, doi: 10.1107/S0108270186093307.

[58] N. Kijima *et al.*, “Oxidative catalytic cracking of n-butane to lower alkenes over layered BiOCl catalyst,” *Appl Catal A Gen*, vol. 206, no. 2, pp. 237–244, Jan. 2001, doi: 10.1016/S0926-860X(00)00598-6.

[59] H. AN, Y. DU, T. WANG, C. WANG, W. HAO, and J. ZHANG, “Photocatalytic properties of BiOX (X = Cl, Br, and I),” *Rare Metals*, vol. 27, no. 3, pp. 243–250, Jun. 2008, doi: 10.1016/S1001-0521(08)60123-0.

[60] M. M. Ferrer *et al.*, “Theoretical methods for calculations of optical phonons in BiOBr: Analysis and correction of propagated errors,” *Journal of Raman Spectroscopy*, vol. 49, no. 8, pp. 1356–1363, Aug. 2018, doi: 10.1002/jrs.5377.

[61] M.-H. Du and D. J. Singh, “Enhanced Born charges in III-VII, IV-VII_2,V-VII_3 compounds,” *Phys Rev B*, vol. 82, no. 4, p. 045203, Jul. 2010, doi: 10.1103/PhysRevB.82.045203.

[62] H. Shi, W. Ming, and M.-H. Du, “Bismuth chalcohalides and oxyhalides as optoelectronic materials,” *Phys Rev B*, vol. 93, no. 10, p. 104108, Mar. 2016, doi: 10.1103/PhysRevB.93.104108.

[63] A. Rulmont, “Raman spectra of a single crystal of BiOCl,” *Spectrochim Acta A*, vol. 30, no. 1, pp. 311–313, Jan. 1974, doi: 10.1016/0584-8539(74)80235-7.

[64] J. Lu, W. Zhou, X. Zhang, and G. Xiang, “Electronic Structures and Lattice Dynamics of Layered BiOCl Single Crystals,” *J Phys Chem Lett*, vol. 11, no. 3, pp. 1038–1044, Feb. 2020, doi: 10.1021/acs.jpclett.9b03575.

[65] J. E. D. Davies, “Solid state vibrational spectroscopy—III[1] The infrared and raman spectra of the bismuth(III) oxide halides,” *Journal of Inorganic and Nuclear Chemistry*, vol. 35, no. 5, pp. 1531–1534, May 1973, doi: 10.1016/0022-1902(73)80242-8.

CHAPTER-6

Summary & Conclusions

The current thesis focuses on understanding the phonon transport in extended solids using ab-initio molecular dynamics simulations in combination with Boltzmann transport theory. In total 51 extended solids were considered, which consisted of binary systems namely Alkaline Earth Chalcogenides (AEC's) (16 compounds) and Alkali Halides (AH's) (20 compounds) and layered ternary materials like Alkaline Earth halo fluorides (12 compounds) and Bismuth halooxides (03 compounds). The current thesis provides some critical-insights or design principles to obtain low-lattice thermal conductivity (κ_L) materials.

The comprehensive study on AEC's and AH's provides insights on how atomic mass contrast can fine tune the contribution of optical phonons to κ_L and its implications on scattering rates by either enhancing or suppressing κ_L. These insights would aid in the selection of elements for designing new functional materials with and without atomic mass contrast to achieve relatively high and low κ_L values, respectively. The study on layered ternary materials provides an in-depth understanding on interplay among crystal structure, atomic mass and bonding heterogeneity, rattling phenomenon, which would aid in designing extremely low κ_L materials by manipulating in-plane and out-of-plane bonding for future thermal energy management applications.

Chapter 3:

In summary, lattice dynamics, phonon transport, and mechanical properties of Alkaline Earth Chalcogenides (AEC's) with rocksalt-type structure were systematically investigated. Anomalous trends were observed for κ_L in CaCh (CaS > CaO > CaSe > CaTe), SrCh (SrSe > SrO > SrS > SrTe), and BaCh (BaTe > BaSe > BaS > BaO) (where Ch = O, S, Se, Te) series of compounds. In particular, an opposite trend for κ_L was observed in the BaCh (X = O, S, Se, and Te) series, which contrasts with the expected trend from their atomic mass. A few observations are proposed from this study to design (ultra)low κ_L materials, which are as follows: (1) design a material with a combination of heavy and light elements to have high mass contrast, which produces an acoustic-optic phonon gap, (2) phonon softening of transverse acoustic (TA) modes due to heavy atomic mass element; (3) constituent elements in a material with a high electronegativity difference produce a large LO-TO splitting, resulting in LLO (TO) phonon modes, which might fall into the acoustic mode region, and they are responsible

for the softening of acoustic phonon modes or enhancing the overlap between the LLO and longitudinal acoustic (LA) phonon modes, thereby increasing scattering rates thus resulting in shorter phonon lifetimes; and (4) selection of a material with a relatively high density (ρ). The application of tensile strain further reduces κ_L in binary systems through phonon softening, which increases scattering rates, thereby lowering phonon lifetimes and eventually lowering κ_L.

The detailed study on AH's provides several critical insights regarding the relationship between mass ratio and κ_L: (a) when the difference in atomic mass between elements in a material is minimal, it significantly boosts the contribution of optical phonons to κ_L ultimately resulting in an overall increase in κ_L. (b) Materials with a mass ratio close to unity and low atomic masses within a binary system exhibit more dispersive optical phonons. These optical phonons make a substantial contribution to κ_L. (c) Conversely, materials with a mass ratio close to unity but heavier atomic masses in a binary system display less dispersion optical phonons with sharp peaks in the narrow frequency range, resulting in a relatively less contribution of optical phonons (compared with acoustic phonons) to κ_L. (d) In general, materials with a mass ratio approaching unity tend to feature longer phonon lifetimes, which remain dominant in achieving high κ_L values. These findings suggest that materials composed of elements with similar atomic masses exhibit relatively higher values of κ_L in a given series of compounds.

It is found that low-lying optical phonons contribute significantly to phonon transport to enhance κ_L in materials (NaF, NaCl, KCl, MgO, CaO, MgS, SrSe, SrTe, and BaTe) with a mass ratio close to unity along with their average atomic mass. Relatively low scattering rates for materials with a mass ratio close to unity result in high phonon lifetimes, thereby resulting in an anomalously high κ_L in a given series. Tensile lattice strain-dependent phonon transport properties of BaTe and MgTe reveal that phonon lifetimes play a dominant role in determining the trends in κ_L. Overall, phonon scattering rates (inverse of phonon lifetimes) play a predominant role over phonon group velocities in determining the anomalous trends in κ_L for AHs and AECs with a mass ratio close to one. The present study provides an in-depth understanding of atomic mass and its effect on phonon transport properties of AHs and AECs. Furthermore, this study reveals that by manipulating the atomic masses, one can engineer materials with

both high and low κ_L values, providing exciting possibilities for tailored thermal conductivity in various applications.

Chapter 4:

For the Alkaline earth halo fluorides, MXF (M = Ca, Sr, Ba and X = Cl, Br, I) which are layered ternary materials that crystallize in *P4/nmm* symmetry, these exhibit anisotropy from their crystal structure, which is strongly determined by the axial bond, and it is attributed to large axial ratio (c/a > 2) where halogen atom acts as a rattler as evidenced from potential energy curves and phonon density of states. Low axial (c/a) ratio leads to relatively isotropic κ_L values in BaXF compared to CaXF and SrXF series (X = Cl, Br, I) . The MXF compounds exhibit highly anisotropic (large phonon transport anisotropy ratio 10.95 for CaIF) to isotropic (small phonon transport anisotropy ratio 1.49 for BaBrF) for κ_L values despite their iso-structure. Moreover, ultralow κ_L (<1 W/m-K) values have been predicted for CaBrF, CaIF and SrIF in the out-of-plane direction due to weak van der Waals (vdW) bonding. Overall, the comprehensive study on MXF compounds provides insights on designing low κ_L layered materials by fine tuning in-plane and out-of-plane bonding through chemical intuition.

Chapter 5:

The chemical bonding, lattice dynamics, and phonon transport features of layered matlockite PbClF-type Bismuth halooxides, BiXO (X =Cl,Br,I) were studied. For BiBrO and BiIO, the large axial ratio (c/a > 2) is attributable to the large axial Bi-X1 bond, which determines the structural (c > a) and elastic ($C_{11} > C_{33}$) anisotropy in BiXO compounds. This property is similar to that of BaXF (X =Cl, Br, I) compounds, which have weak van der Waals bonds in the cross-plane direction. The three compounds under investigation i.e. BiClO, BiBrO and BiIO have been predicted to have an ultralow cross-plane κ_L (< 1 W/m-K). Furthermore, the presence of structural and elastic anisotropy leads to a significant phonon transport anisotropy ratio of 13.5 for BiBrO and 15.6 for BiIO at a temperature of 300 K. This indicates a highly anisotropic phonon transport in these two compounds. The computed potential energy curves demonstrate

that Bi and Br/I atoms function as rattlers within the compounds BiBrO and BiIO. The presence of $6s^2$ lone pair electrons cause enhanced Born effective charges are observed along in-plane directions. The comprehensive understanding of crystal structure, chemical bonding, mechanical properties, lattice dynamics and phonon transport properties provides an in-depth understanding of interplay among atomic mass, lone pair induced anharmonicity and bonding heterogeneity, which would aid in the selection of elements or discovery of extremely low κ_L materials for future thermal energy management applications.

Future scope of work:

1. To explore the phonon transport in 2D materials and monolayers.
2. Employing machine learning potentials to investigate materials at higher temperatures.
3. To look for the feasibility of quantifying the contributions of the several factors that play a dominant role in κ_L
4. To explore more families of isostructural compounds so that these could serve as descriptors for designing low κ_L materials for thermal management applications.
5. Compute the electronic contributions as well to thermal conductivity and realize functional materials with a very good figure of merit.
6. To collaborate with experimental groups and realise the applications of low κ_L materials.

List of Publications towards the thesis:

SCI Journal Publications:

1. Anomalous Lattice Thermal Conductivity in Rocksalt IIA–VIA Compounds**, Rakesh Roshan, S. Chand ;** Yedukondalu, Neelam.; Muthaiah, R.; Lavanya, K.; Anees, P.; Rajaboina, Rakesh Kumar; Rao, T., Ehm, Lars; Parise, John B., ***ACS Applied Energy Materials,*** **(2022)** *5(1), 882-896.* **https://doi.org/10.1021/acsaem.1c03310** **[IF : 6.4]**

2. Effect of Atomic Mass Contrast on Lattice Thermal Conductivity: A Case Study for Alkali Halides and Alkaline-Earth Chalcogenides, **Rakesh Roshan, S. Chand** ; Yedukondalu, Neelam; Pandey, Tribhuwan; Kunduru, Lavanya; Muthaiah, Rajmohan; Rajaboina, Rakesh Kumar; Ehm, Lars; Parise, John B., ***ACS Applied Electronic materials*** **(2023),** *5, 11, 5852–5863* **https://doi.org/10.1021/acsaelm.3c00759** **[IF : 4.7]**

Accepted for publication:

3. Highly Anisotropic to Isotropic nature and Ultralow Out-of-plane Lattice Thermal Conductivity of Layered PbClF-type Materials**, Rakesh Roshan, S. Chand;** Yedukondalu, Neelam.; Rajaboina, Rakesh Kumar; Huang, Haw-Tyng; T., E,Lars; Parise, J.B., ***ACS inorganic Chemistry,*** **(Jan 2024). [IF : 4.6]**

List of Publications out of thesis:

1. Lattice Instability and Ultralow Lattice Thermal Conductivity of Layered PbIF, Yedukondalu, N., Shafique, A., **Rakesh Roshan, S. Chand**, Barhoumi, M., Muthaiah, R., Ehm, L., Parise, J. B., & Schwingenschlögl, U, ACS Applied Materials & Interfaces, 14(36), 40738–40748, 2022. https://doi.org/10.1021/acsami.2c01135

2. Effect of Hydrostatic Pressure on Lone Pair Activity and Phonon Transport in Bi_2O_2S, N. Yedukondalu, Tribhuwan Pandey, and **Rakesh Roshan, S. Chand.**, in *ACS Applied Energy Materials*, vol. 6, no. 4, pp. 2401–2411, 2023. https://doi.org/10.1021/acsaem.2c03725

3. Lattice instability, anharmonicity and Raman spectra of BaO under high pressure: A first principles study, Lavanya, K., Yedukondalu, N., **Rakesh Roshan, S. Chand**, Dabhi, S., Sripada, S., Sainath, M., Ehm, L., & Parise, J. *Journal of Physics and Chemistry of Solids*, vol. 170, pp. 110967, 2022. http://dx.doi.org/10.1016/j.jpcs.2022.110967

4. Pressure-Induced Martensitic Phase Transition and Low Lattice Thermal Conductivity of SrClF, Kunduru, L., Yedukondalu, N., **Rakesh Roshan, S. Chand**, Sripada, S., Sainath, M., Ehm, L., & Parise, J. *The Journal of Physical Chemistry C*, 125(31), 17261-17270, 2021. https://doi.org/10.1021/acs.jpcc.1c00800

5. Structural phase transition and electronic structure of binary CaO and SrO under high pressure, Lavanya Kunduru, N. Yedukondalu, **Rakesh Roshan, S. Chand**, Suresh Sripada, & M. Sainath., Materials *Today: Proceedings*, vol. 62, pp. 2744–2747, 2022. http://dx.doi.org/10.1016/j.matpr.2021.12.237

List of International Conferences/schools/workshops where current research work (in parts) was presented:

1. Presentation at 2023 Virtual School on Many-Body Calculations using EPW and BerkeleyGW on June 7, 2023 organized by Center for Computational Study of Excited-State Phenomena in Energy Materials (C2SEPEM) at Lawrence Berkeley National Laboratory, and by the Oden Institute for Computational Engineering and Sciences, The University of Texas at Austin, USA.

2. Presentation at International Workshop on Vienna Abinitio Simulation package eco-system, Feb 6-7 2023, HIGH PERFORMANCE COMPUTING CENTRE - UNIVERSITY OF ÉVORA, Portugal Sponsored by EuroCC2 (European Commission, EuroHPC JU), Foundation for Science & Technology (Portugal), HP High Performance Computing Chair.

3. Presentation at International Conference on Energy Conversion and Storage (ICES-2023) held at Indian Institute of Technology, IIT Madras, India from 18-20 Jan 2023.

4. Presentation at International Interdisciplinary Conference on Energy, Nanotechnology and IoT Feb - 2 to 4, 2023 at National Institute of Technology, NIT Pondicherry, India.

5. Presentation at First International Conference on Technologies for Smart Green Connected Society supported by ACS and ECS, virtual, worldwide, 29-30 Nov 2021 organized by Professors Hidemitsu Furukawa and Ajit Khosla of Yamagata University, Japan.

CV of Mr. S Chand Rakesh Roshan

S Chand Rakesh Roshan

Google Scholar: https://scholar.google.com/citations?hl=en&user=-zT28VwAAAAJ

LinkedIn: https://www.linkedin.com/in/schandrakeshroshan/

ORCID: https://orcid.org/0000-0001-5729-4845

Contact details: roshanscrd@gmail.com , roshan@rgukt.ac.in

Academics:

Ph.D – National Institute of Technology, Warangal (2019-2024)

M.Tech – University of Hyderabad, Hyderabad, India (2008-2010)

(CGPA: 8.88 / 10)

M.Sc – Sri Satya Sai University, Prasanthi Nilayam, India (2006-2008)

(CGPA: 4.85 / 5.00)

Qualified in JEST, All India Percentile 97.7.

Qualified in GATE, All India Rank 244

Qualified in CSIR-UGC NET for LS.

Awarded NASA Teacher Award in 2012.

Employment: Working as Assistant Professor, Department of Physics, RGUKT Basar from October 2010.

Professional membership:

Life Member of Indian Science Congress Association
Life Member of Indian Physics Association
Life Member, IAENG
Life Membership -The Indian Society for Technical Education - ISTE.
ACCMS Member (Asian Consortium on Computational Materials Science)
Life Member, MRSI - Materials Research Society of India (MRSI).
Life Member, SSI – Systems Society of India (SSI).
Community Associate Membership, ACS.

Declaration: I hereby declare that the details and information given above are complete and true to the best of my knowledge.

February 2024 S Chand Rakesh Roshan